THERMAL MECHANICAL ANALYSIS OF APPLICATIONS WITH INTERNAL HEAT GENERATION

A Dissertation

presented to

the Faculty of the Graduate School

at the University of Missouri-Columbia

In Partial Fulfillment

of the Requirements for the Degree

Doctor of Philosophy

---

by

SRISHARAN GARG GOVINDARAJAN

Dr. Gary Solbrekken, Dissertation Supervisor

DECEMBER 2014

The undersigned, appointed by the dean of the Graduate School, have examined the dissertation entitled

THERMAL MECHANICAL ANALYSIS
OF APPLICATIONS WITH
INTERNAL HEAT GENERATION

presented by Srisharan Garg Govindarajan,

a candidate for the degree of doctor of philosophy,

and hereby certify that, in their opinion, it is worthy of acceptance.

Professor Gary Solbrekken

Professor Chung Lung Chen

Professor Robert Winholtz

Professor Hani Salim

ACKNOWLEDGEMENTS

I am grateful to my supervisor Dr. Gary Solbrekken for having guided me through this dissertation with his patience and knowledge, while giving me the independence to work in my own way. My family has been a great source of support through all these years and I would like to thank them for believing in me and making this possible. I am also fortunate to have made some great friends during my time as a graduate student and they have certainly helped me tide over difficult periods with all their encouragement.

Interacting and working with accomplished researchers has greatly benefitted me and I would like to thank Dr. George Vandegrift at the Argonne National Laboratory, Charlie Allen from the Missouri University Research Reactor, Dr. Sherif El-Gizawy at the University of Missouri, Chris Bryan, Dr. James Freels, Dr. Prashanth Jain, Dr. David Chandler, Dr. Paul Williams, Larry Ott, Randy Hobbs, Cliff Hayman, Fred Griffin, and Christopher Hurt at the Oak Ridge National Laboratory.

Finally, I would like to thank my colleagues, Dr. Kyler Turner, John Kennedy, Philip Makarewicz, Casey Jesse, Brian Graybill, Annemarie Hoyer, and Alex Moreland, for offering their perspectives on various issues during the course of this dissertation.

TABLE OF CONTENTS

ACKNOWLEDGEMENTS ii

LIST OF FIGURES vii

LIST OF TABLES xiv

NOMENCLATURE xv

ABSTRACT xvi

Chapter

1. INTRODUCTION 1

    1.1 Molybdenum-99 and Technetium-99m 2

    1.2 Production Methods and Target Development 4

    1.3 Thermal Contact Resistance 8

    1.4 Control Blades 10

    1.5 Objective of Work 12

2. LITERATURE REVIEW 14

    2.1 Target Design and Irradiations 14

    2.2 Thermal Contact Resistance 17

    2.3 Thermal Stresses in Cylinders 20

    2.4 Fission Gas Release and Uranium Swelling 22

3. ANNULAR TARGET THERMAL- MECHANICAL SAFETY ANALYSIS 24

    3.1 Target Design 24

    3.2 Plate Target 24

    3.3 Annular Target 26

4. MODELING WITHOUT RESIDUAL STRESSES 31

4.1 Non-Uniform Heating Numerical Model....31
4.2 Uniform Heating Numerical Model....41
4.3 Uniform Heating Analytical Model- Dimensional Form....43
4.4 Uniform Heating Analytical Model- Sensitivity Studies....58
5. MODELING WITHOUT RESIDUAL STRESSES - RESULTS....61
5.1 Uniform Heating- Analytical and Numerical....61
5.2 Non-Uniform Heating....68
5.3 Uniform and Non-Uniform Heating Comparison....76
5.4 Uniform Heating Sensitivity Studies....81
6. DIMENSIONLESS ANALYTICAL MODEL - UNIFORM HEATING....94
6.1 Dimensionless Thermal-Mechanical Expressions....94
6.2 Dimensionless Model Results....100
7. MODELING WITH RESIDUAL STRESSES....104
7.1 Hydroforming Assembly Description....105
7.2 Draw-Plug Assembly Description....107
8. HYDROFORMING ASSEMBLY AND IRRADIATION ANALYSIS....108
8.1 Material Model....108
8.2 Numerical Finite Element Model....109
8.3 Hydroforming Analysis Results....113
9. DRAW-PLUG ASSEMBLY AND IRRADIATION ANALYSIS....119
9.1 Material Model....119
9.2 Numerical Finite Element Model....120
9.3 Draw-Plug Analysis Results....124

10. INTERFACIAL PHENOMENA AND URANIUM SWELLING 130
10.1 Fission Gas Release and Uranium Swelling Model 130
10.2 Interfacial Conductance Model 136
10.3 Additional Effects 141
10.4 Numerical Model 142
10.5 Results 143
11. REACTOR SPECIFIC ANNULAR TARGET ANALYSIS 149
11.1 Reactor Description 149
11.2 Target Geometry 151
11.3 Calculation of Input 153
11.4 Finite Element Model Development 155
11.5 Results 161
11.6 Technical Adequacy and Independent Review Comments 167
12. BORAL CONTROL BLADE SAFETY ANALYSIS 168
12.1 Control Blade Geometry and Model Development 168
12.2 Heating Profile Development 171
12.3 Numerical Finite Element Model 176
12.4 Results 181
13. CONCLUSIONS AND RECOMMENDATIONS 183
APPENDIX 187
1. Mathematica Code to Determine Heat Flux 187
2. Mathematica Code to Determine Outer Tube Parameters 189
3. Mathematica code to Determine Inner Tube Parameters 190

4. Mathematica Code to Determine Contact Pressure 192

5. Mathematica Code to Calculate Fission Gas Pressure.....194

6. Mathematica Code to Develop a Thermal Conductance Model for Al 6061-T6 and Al 6061-T6 Interface 197

7. Mathematica Code to Develop a Thermal Conductance Model for Al 6061-T6 and Nickel Interface 200

8. Mathematica Code to Develop a Thermal Conductance Model for Uranium and Nickel interface 203

9. Mathematica Code to Develop a Thermal Conductance Model for Al 6061-T4 and Al 6061-T4 interface 206

10. Mathematica Code to Develop a Thermal Conductance Model for Al 6061-T4 and Pure Al interface.....209

11. Abaqus Input File for the Planar Model with Non-Uniform Heating.....212

12. Abaqus Input File for the Hydroforming and Irradiation Model 215

13. Abaqus Input File for the Draw-Plug Based Irradiation Model 227

14. Abaqus Input File for the Control Blade Analysis.....246

REFERENCES 249

VITA 261

LIST OF FIGURES

Figure Page

1. (a) Australian Nuclear Science and Technology Organization's (ANSTO) technetium generator external view. (b) General internal structure of a technetium generator. 3
2. Traditional powder dispersion method using HEU. 5
3. Mo-99 activity vs. uranium density for HEU and LEU dispersion. 6
4. Proposed LEU metal foil based approach for Mo-99 production. 7
5. Hot cells at (a) Comision Nactional de Energia Atomica (CNEA) in Argentina, and (b) Missouri University Research Reactor (MURR).. 8
6. Surface irregularities offering resistance to heat flow through a compound cylinder assembly. 9
7. MURR core showing the reflector, control blade and pressure vessel.. 11
8. Flat plate target with welded edges. 25
9. Curved plate type target with welded edges. 25
10. A simple diagram of the annular target illustrating the position of the foil longitudinally and the location of the circumferential gap. 26
11. A prototype annular target with welded edges. 27
12. Interfacial contact bond formed by solid contact spots and interstitial gaps. 27
13. Sketch depicting the resistances across the interfacial thickness. 28
14. Annular target design using Al 3003-H14 as the cladding.. 30
15. Pictorial representation of the modeling strategy for the analysis of the annular target without initial residual stresses. 32
16. Numerical model assembly showing: (a) The inner tube alone with the recess and (b) The inner tube after the addition of the outer tube. 32
17. Pictorial representation of the position of the annular target in the vertical experimental facility relative to the reactor core. 33
18. Numerical setup of the 2D plane strain model of the annular target modeled without the nickel recoil barrier. 34
19. Annular target assembly procedure in Abaqus FEA. 35

20. Mechanical boundary condition applied to the annular target assembly. 37

21. Representation of the coolant flow internally and through the annulus. 38

22. Finite element mesh used to simulate the non-uniform heating model. 41

23. Setup of the uniform heating 2D plane strain model of the annular target. 42

24. Mechanical boundary conditions used in the uniform heating model. 43

25. Symbolic dimensions and thermal resistance network of the uniform heating annular target case. 44

26. Representation of the simplified solution approach for stresses and displacement. 48

27. Circumferential temperature distribution on the inner and outer cladding for uniform heating with $q'''=1.6 \times 10^{10}$ W/m^3. 61

28. Assembly temperature distribution contour for uniform heating with $q'''=1.6x10^{10}$ W/m^3. 62

29. Radial temperature distribution in the cladding for $q'''=1.6 \times 10^{10}$ W/m^3 and uniform heating. 62

30. Radial stress distribution in the cladding at $\theta=270^{o}$ for uniform heating with $q'''=1.6x10^{10}$ W/m^3. 63

31. Radial stress distribution contour of the assembly for uniform heating with $q'''=1.6x10^{10}$ W/m^3. 64

32. Hoop stress distribution in the cladding at $\theta=270^{o}$ for uniform heating at $q'''=1.6x10^{10}$ W/m^3. 64

33. Hoop stress distribution contour of the assembly for uniform heating with $q'''=1.6x10^{10}$ W/m^3. 65

34. Separation between the foil and the outer tube for uniform heating with $q'''=1.6x10^{10}$ W/m^3. 66

35. Interfacial separation between the foil and the outer tube cladding for uniform heating with $q'''=1.6x10^{10}$ W/m^3. 66

36. Circumferential contact pressure distribution in the inner tube for uniform heating with $q'''=1.6x10^{10}$ W/m^3. 67

37. Assembly temperature distribution contour for non-uniform heating. 68

38. Radial stress and temperature distribution for non-uniform heating. 69

39. Radial displacement contour illustrating the interfacial separation between the foil and the cladding for non-uniform heating. 70

40. Hoop stress and separation along the circumference of the outer tube inner surface for non-uniform heating. 70

41. Assembly hoop stress contour for non-uniform heating. 70

42. Temperature and hoop stresses in the outer tube for non-uniform heating. 72

43. Interfacial separation and contact pressure variation in the inner surface of the outer tube for non-uniform heating. 72

44. Temperature and hoop stresses in the inner tube for non-uniform heating 73

45. Contact pressure in the inner tube outer surface for non-uniform heating. 74

46. Deformed and un-deformed radial distribution contours of the inner tube for non-uniform heating. 75

47. Deformed and un-deformed radial distribution contours of the outer tube for non-uniform heating. 75

48. Deformed and un-deformed radial displacement contours of the LEU foil for non-uniform heating. 75

49. Final deformed shape of the annular target post irradiation for non-uniform heating. 75

50. Assembly temperature distribution comparison for uniform and non-uniform heating. 77

51. Circumferential temperature distribution on the outer surface of the inner tube: comparison between uniform and non-uniform heating. 77

52. Circumferential temperature distribution on the inner surface of the outer tube: comparison between uniform and non-uniform heating. 78

53. Assembly radial stress distribution comparison for uniform and non-uniform heating. 78

54. Comparison of contact pressure on the outer surface of the inner tube for uniform and non-uniform heating. 79

55. Comparison of hoop stresses on the outer surface of the inner tube for uniform and non-uniform heating. 80

56. Comparison of hoop stresses on the inner surface of the outer tube for uniform and non-uniform heating. 80

57. Comparison of the magnitude of separation at the interface of the foil and the outer tube for uniform and non-uniform heating conditions. 80

58. Radial temperature distributionin the inner and outer tubes for varying LEU heat generation rates with T_{wall} =373 K for uniform heating. 82

59. Radial stress distribution in the inner and outer tubes for varying LEU heat generation rates with T_{wall} =373 K for uniform heating. 82

60. Hoop stress distribution in the inner and outer tubes for varying LEU heat generation rates with Twall =373 K for uniform heating. 83

61. Temperature variation on the surfaces of the tubes with varying heat transfer coefficient ratios with T_{wall} = 373 K for uniform heating. 84

62. (a) Radial stress distribution and (b) contact pressure on the outer surface of the inner tube for varying heat transfer coefficient ratios with T_{wall}=373 K for uniform heating. 85

63. Hoop stress distribution in the inner and outer tubes for varying heat transfer coefficient ratios with T_{wall} = 373 K for uniform heating. 85

64. Separation at the interface of the outer tube and LEU foil for varying heat transfer coefficient ratios with T_{wall}= 373 K for uniform heating. 86

65. Hoop stress in the inner tube for varying heat transfer coefficient ratios with T_{wall} =373 K for uniform heating. 87

66. Cladding temperature distribution for varying LEU heat generation rates with the heat transfer coefficient ratio H=1, with no restrictions on wall temperature and for uniform heating. 88

67. Radial stress distribution in the cladding for varying LEU heat generation rates with the heat transfer coefficient ratio H=1, with no restrictions on wall temperatures and for uniform heating. 88

68. Hoop stress distribution in the cladding for varying LEU heat generation rates with the heat transfer coefficient ratio H=1, with no restrictions on wall temperature and for uniform heating. 89

69. Temperature distribution in the cladding with varying heat transfer coefficient ratios for uniform heating with no restrictions on wall temperature. 90

70. Radial stress and contact pressure distribution in the inner tube outer surface with varying heat transfer coefficient ratios for uniform heating with no restrictions on wall temperature. 91

71. Hoop stress distribution in the cladding with varying heat transfer coefficient ratios for uniform heating with no restrictions on wall temperature. 92

72. Separation at the interface of the foil and the outer tube with varying heat transfer coefficient ratios for uniform heating and no restrictions on wall temperature. 92

73. Variation of hoop stress in the inner tube at H=1 for different tube thickness ratios and LEU heat generation rates. 93

74. Hoop stress in the inner tube at q'''=1.6 E10 W/m^3 at various tube thickness and heattransfer coefficient ratios. 93

75. Dimensionless radial temperature distribution in the annular target. 100

76. Dimensionless radial stress distribution in the annular target. 101

77. Dimensionless hoop stress distribution in the inner tube and the outer tube. 102

78. Dimensionless radial displacement in the inner tube and the LEU foil 102

79. Dimensionless radial displacement in the outer tube. 103

80. The draw-plug and the hydroforming assembly techniques. 104

81. Drawing of the geometry in the first analysis step of the assembly simulation model. 106

82. (a) Hydroforming test rig with the annular target in place and (b) assembled hydroforming test rig. 106

83. Pre-assembly state of the annular target. 107

84. Draw-plug assembly device. 107

85. True stress and plastic strain curves for Al 6061-T6 and uranium. 109

86. Finite element mesh used in the assembly and irradiation modeling. 110

87. Loading and mechanical boundary conditions for the assembly hydroforming simulation in the first analysis step. 111

88. Loading and boundary conditions for the irradiation model 112

89. Numerical displacement contour and microscopic images of the annular target after the assembly process. 113

90. Equivalent plastic strain across the radius of the annular target at $\theta=270^{o}$. 114

91. Separation at the interface of the foil and the outer tube after the various modeling steps. 115

92. Radial temperature distribution across the inner and the outer cladding. 116

93. Hoop stress distribution in the inner tube through various modeling steps 117

94. Hoop stress distribution in the outer tube through various modeling steps 118

95. True stress and plastic strain curve for nickel used in the numerical model. 120

96. Pre-assembly target tubes and the plug dimensions. 121
97. The model change command in Abaqus to remove the plug. 122
98. The three-step axisymmetric modeling procedure with boundary and loading conditions. 123
99. Finite element mesh used in the draw-plug based analysis. 124
100. Sectioning locations along the assembled target length. 125
101. Post-assembly views of the sectioned images against the numerical model. 126
102. Longitudinal separation at the outer tube interface. 126
103. Equivalent plastic strain across the thickness at half the target length. 127
104. Hoop stress distribution across the cladding thickness. 128
105. Longitudinal temperature distribution for Target-1 and Target-2. 129
106. Irradiation stress state of Target-1 and Target-2. 129
107. The dependence of swelling on temperature for high purity uranium 136
108. Mechanical and thermal loading during the irradiation step. 142
109. Volumetric swelling strain rate definition location. 143
110. Von Mises stresses in the cladding for case-1 compared against Target-2 values from Figure 107. 145
111. Thermal contact conductance as a function of pressure for various interfacial combinations. 145
112. Radial temperature distribution in the annular target for case-1 146
113. Variation of maximum temperature with the heat generation rate for case-4. 148
114. Variation of von Mises stresses with the heat generation rate for case-5. 148
115. Aerial view of the HFIR facility. 150
116. The HFIR core illustrating the location of the experimental facilities 150
117. Pre-assembly annular target dimensions for HFIR irradiation. 151
118. Dimensions of the draw-plug used to assemble the annular target with the 6061-T4 Al cladding. 152
119. Material models for Al 6061-T4 and uranium. 153
120. Draw-plug assembly model setup for the HFIR annular target. 157

121. Finite element mesh of the assembly model for the HFIR annular target. 158

122. Irradiation model setup for the HFIR annular target. 159

123. Finite element mesh of the irradiation model for the HFIR annular target. 160

124. Von Mises stress distribution in the cladding for the HFIR annular target. 164

125. Radial temperature distribution in the HFIR annular target 164

126. Longitudinal temperature distribution in the inner tube for the HFIR target. 165

127. Longitudinal temperature distribution in the outer tube for the HFIR target. 166

128. Dimensions of the BORAL control blade.....169

129. A cross- sectional view of the MCNP MURR core model.....170

130. Linearized exponential decay function for a given thickness and azimuthal location for alpha heating.....173

131. 'A' and 'B' coefficient variations with thickness in BORAL core for alpha heating at left edge location. 173

132. 'A' and 'B' coefficient variation with thickness in the BORAL core for gamma heating at the left edge location. 173

133. Alpha heat generation data and fit through the BORAL core at the left edge.....175

134. Alpha heat generation data and fit at the fuel-side BORAL face. 175

135. Components of the assembled control blade along with the mechanical boundary conditions.....180

136. Finite element mesh of the (a) BORAL meat and (b) aluminum cladding used in the Abaqus model. 180

137. (a) Temperature distribution contour of the control blade and (b) variation of temperature along the cladding centerline. 182

138. (a) Radial deflection contour and (b) deflection variation on the sides of the control blade.....182

139. Deflection variation along the length of the control blade with varying thermal conductivity of the BORAL.....182

LIST OF TABLES

Table Page

1. Material properties of the foil and the cladding used in the analysis.....34
2. Mesh configuration for the non-uniform heating numerical model without residual stresses.....40
3. LEU heat generation rates used in the sensitivity studies.....58
4. Heat transfer coefficient parametric study for wall temperatures maintained at 373 K.....59
5. Heat transfer coefficient study with no restriction on wall temperature.....60
6. Tube thickness variation study.....60
7. Percent difference comparison between the analytical and numerical models for the inner and the outer tubes. 67
8. Uniform and non-uniform heating comparison summary. 81
9. Material properties used in the draw plug model.....120
10. Post assembly target measurements: Measured vs. model results. 125
11. Properties and of quantity of gases used in the calculations.....131
12. Material and surface properties of the metals. 138
13. Thermophysical properties of the gases in the gap conductance calculations.....140
14. Maximum von Mises stress variation with the addition of constraints. 144
15. Maximum cladding temperature variation with the addition of constraints. 146
16. Material properties used in the calculations.....152
17. Properties of the fission gases used in the reactor specific calculations. 154
18. Assembled dimensions of the annular target: measurement vs. model results. ...162
19. Maximum residual stresses in the inner and outer tubes 162
20. Annular target temperature results for the safety basis analysis. 163
21. Alpha volumetric heat generation data and fit comparison at the left edge.....176
22. Material properties of the BORAL and the aluminum cladding used in the analysis.....180

NOMENCLATURE

C_p	heat capacity	n	number of moles	Subscripts	
B	virial coefficient	q	power	F	foil
D	diameter	q"	heat flux	IF	interface
E	elastic modulus	q‴	volumetric heat generation	IT	inner tube
G	shear modulus	r	radius	OT	outer tube
H	microhardness	u	displacement	cond	conduction
L	length	x	mass fraction	conv	convection
M	molecular mass	y	mole fraction	eff	effective
Nu	Nusselt number	Greek		gen	generation
P	pressure	α	thermal expansion coefficient	fD	fully developed
Pr	Prandtl number	β	accommodation coefficient	in	inner surface
Q	dimensionless heat generation	Δ	quantitative change	out	outer surface
R	dimensionless radius	δ	gap thickness	max	maximum
R'	thermal resistance	ε	strain	Abbreviation	
Re	Reynolds number	γ	ratio of specific heat	ANL	Argonne national lab
T	temperature	κ	bulk modulus	DOE	Department of energy
U	total interference	λ	mean free path	FEA	finite element analysis
V	flow velocity	ϕ	asperity slope	HEU	high enriched uranium
Z	compressibility factor	Ψ	plasticity index	HFIR	high flux isotope reactor
f	fissions	ρ	density	LEU	low enriched uranium
g	temperature jump distance	μ	dynamic viscosity	MURR	Missouri university research reactor
h	heat transfer coefficient	υ	Poisson's ratio	ORNL	Oak ridge national laboratory
h'	thermal conductance	σ	stress (or) roughness	PVD	physical vapor deposition
k	thermal conductivity	θ	dimensionless temperature		

ABSTRACT

The radioactive tracer Technetium-99m is widely used in medical imaging and is derived from its parent isotope Molybedenum-99 (Mo-99) by radioactive decay. The majority of Molybdenum-99 (Mo-99) produced internationally is extracted from high enriched uranium (HEU) dispersion targets that have been irradiated. To alleviate proliferation risks associated with HEU-based targets, the use of non-HEU sources is being mandated. However, the conversion of HEU to LEU based dispersion targets affects the Mo-99 available for chemical extraction. A possible approach to increase the uranium density, to recover the loss in Mo-99 production-per-target, is to use an LEU metal foil placed within an aluminum cladding to form a composite structure. The target is expected to contain the fission products and to dissipate the generated heat to the reactor coolant. In the event of interfacial separation, an increase in the thermal resistance could lead to an unacceptable rise in the LEU temperature and stresses in the target. The target can be deemed structurally safe as long as the thermally induced stresses are within the yield strength of the cladding and welds.

As with the thermal and structural safety of the annular target, the thermally induced deflection of the BORAL®-based control blades, used by the University of Missouri Research Reactor (MURR®), during reactor operation has been analyzed. The boron, which is the neutron absorber in BORAL, and aluminum mixture (BORAL meat) and the aluminum cladding are bonded together through powder metallurgy to establish an adherent bonded plate. As the BORAL absorbs both neutron particles and gamma rays, there is volumetric heat generation and a corresponding rise in temperature. Since the BORAL meat and aluminum cladding materials have different thermal expansion

coefficients, the blade may have a tendency to deform as the blade temperature changes and the materials expand at different rates. In addition to the composite nature of the control blade, spatial variations in temperature within the control blade occur from the non-uniform heat generation within the BORAL as a result of the non-uniform thermal neutron flux along the longitudinal direction when the control blade is partially withdrawn. There is also variation in the heating profile through the thickness and about the circumferential width of the control blade. Mathematical curve-fits are generated for the non-uniform volumetric heat generation profile caused by the thermal neutron absorption and the functions are applied as heating conditions within a finite element model of the control blade built using the commercial finite element code Abaqus FEA. The finite element model is solved as a fully coupled thermal mechanical problem as in the case of the annular target. The resulting deflection is compared with the channel gap to determine if there is a significant risk of the control blade binding during reactor operation.

Hence, this dissertation will consist of two sections. The first section will seek to present the thermal and structural safety analyses of the annular targets for the production of molybdenum-99. Since there hasn't been any detailed, documented, study on these annular targets in the past, the work complied in this dissertation will help to understand the thermal-mechanical behavior and failure margins of the target during in-vessel irradiation. As the work presented in this dissertation provides a general performance analysis envelope for the annular target, the tools developed in the process can also be used as useful references for future analyses that are specific to any reactor. The numerical analysis approach adopted and the analytical models developed, can also be

applied to other applications, outside the Mo-99 project domain, where internal heat generation exists such as in electronic components and nuclear reactor control blades. The second section will focus on estimating the thermally induced deflection and hence establish operational safety of the BORAL control blades used at the Missouri University Research Reactor (MURR) to support their relicensing efforts with the Nuclear Regulatory Commission (NRC). The common theme in both these sections is the nuclear heat source, high heat flux, non-uniform heating, composite structures and differential thermal expansion. The goal is to establish the target and component operational safety, and also provide documented analysis that can be referred to in the future.

Chapter 1: Introduction

In 1934, Marie and Pierre Curie reported the first artificial production of radioactive material, after discovering radioactivity in aluminum foil that was irradiated with a polonium preparation. The discoveries by Wilhelm Konrad Roentgen (X-ray), Marie Curie (radioactive thorium and coining the term 'radioactivity') and Henri Becquerel (radioactive uranium salts), formed the basis for their work. An article [1] published in the Journal of the American Medical Association in 1946 described the successful application of Iodine-131, a radioisotope, to treat a patient with thyroid cancer metastases. This provided the much needed boost to the field of nuclear medicine and led to extensive research and development of non-invasive medical procedures to provide diagnostic treatment to patients. Positron emission tomography (PET), magnetic resonance imaging (MRI), computed X-ray tomography (CT), single-photon emission computed tomography (SPECT), and X-rays, are some of the non-invasive medical techniques. These procedures involving nuclear medicine employ the use of radioactive tracers which emit gamma rays from within the body. The tracers are short lived isotopes linked to chemical compounds which permit specific physiological processes to be examined. For example, PET uses radio nuclides that are isotopes with short half-lives such as fluorine-18 (~110 minutes), carbon-11 (~20 minutes), nitrogen-13 (~ 10 minutes) and oxygen-15 (~2 minutes). These radio nuclides are either injected into the patient's bloodstream or given orally so that they interact with the compounds normally used by the body such as glucose, water, or ammonia. The positron emitting radionuclide accumulates in the area of concern and emits a positron that combines with an electron to emit gamma rays in opposite directions which are picked up by PET gamma cameras.

Apart from being helpful in cardiac and brain imaging, the PET has been found to be very accurate in detecting and evaluating cancers. Despite advances in other imaging methods such as CT and MRI, the ability to image the metabolic abnormalities associated with a disease has made PET one of the most significant diagnostic tools. Amongst all the radio nuclides used in various medical procedures, Technetium-99m is the most commonly used diagnostic radioactive tracer element and more information about the same can be found in the following section.

1.1 Molybdenum-99 and Technetium-99m

Molybdenum, a transition metal found in group 6 in the periodic table, was discovered in 1778 by Carl Wilhelm Scheele. There are approximately 35 recognized isotopes of molybdenum, with atomic mass numbers ranging from 83 to 117. The isotopes with atomic masses 92, 94, 95, 96, 97, 98 and 100 occurs naturally while the isotope with atomic mass of 100 is considered to be unstable [2]. Molybdenum-99 (Mo-99) is obtained as a fission product after neutron irradiation of uranium-235 (U-235). Technetium-99m (Tc-99m) is the daughter isotope of Mo-99, was discovered in 1937 by Carlo Perrier (an Italian mineralogist) and Emilio Gino Segre (a Nobel laureate in physics), to fill space number 43 in the periodic table. In 1940, Emilio Segre and Chien-Wu performed experiments to analyze the fission products of U-235 which contained Mo-99 [3].Their analysis results helped them conclude that the element 43 had a 6 hour half-life. The short half-life of Tc-99m (6 hours) restricts it from being transported. Due to this, the Mo-99 (half-life of 66 hours) is directly shipped to hospitals and radio-pharmacies in radiation shielded containers known as technetium generators (Figure 1). The Mo-99, with its 66 hour half-life, decays to Tc-99m. As shown in Figure 1[9], the Tc-99m can be obtained

by passing a saline solution through the generator. This process removes the Tc-99m but leaves behind the Mo99. Brookhaven National Lab developed the first Mo-99/ Tc-99m generator. Equation (1) describes the 'beta' decay process of Mo-99 to Tc-99m:

$$^{99}\mathrm{Mo} \rightarrow ^{99m}\mathrm{Tc} + e^{-} + \nu_e \qquad (1)$$

where, e^- denotes the beta particle emitted from the nucleus and ν_{ev} represents the electron antineutrino.

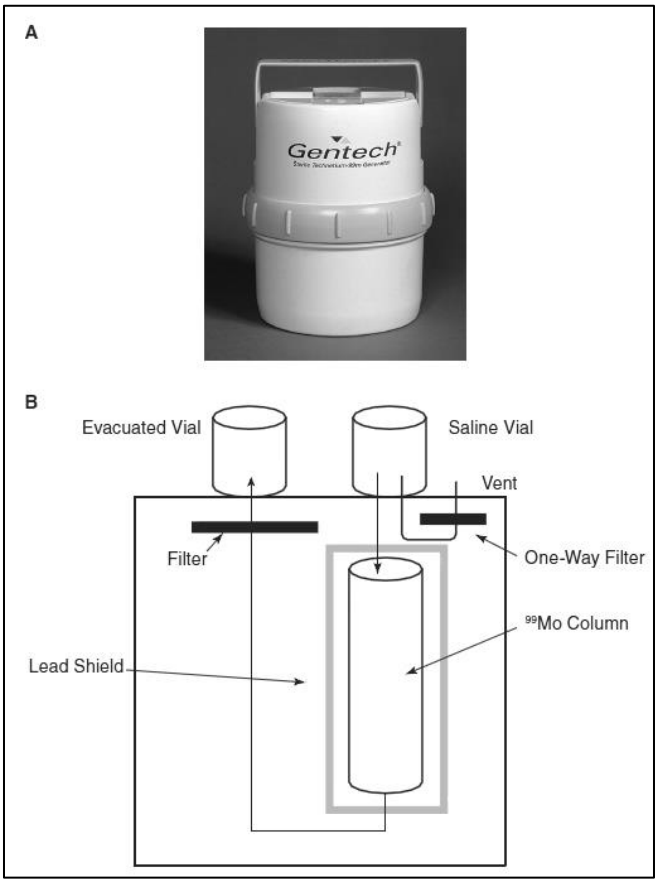

Figure 1. (a) Australian Nuclear Science and Technology Organization's (ANSTO) technetium generator external view. (b) General internal structure of a technetium generator.

The commonly used process to separate the Mo-99/Tc-99m is the column chromatography technique. During this process, the Mo-99 in the form of molybdate (MoO_4^{2-}) is adsorbed onto acid alumina (Al_2O_3). When the Mo-99 decays, it forms

pertechnetate TcO_4^-, which is less tightly bound to the alumina due to its single charge. Application of salt water over the Mo-99 column removes the soluble Tc-99m, resulting in a saline solution containing the Tc-99m as the dissolved sodium salt of the pertechnetate. Further, the Tc-99m undergoes isomeric transition to yield Tc-99m and emits gamma rays as shown below Eq.(2). The sorbed molybdate (MoO_4^{2-}) is washed with ammonium hydroxide solution and then removed from the column using a concentrated saline solution.

$$^{99m}\mathrm{Tc} \rightarrow ^{99}\mathrm{Tc} + \gamma \qquad (2)$$

When a patient has been injected with Tc-99m, the above reaction takes place inside the body and the emission of the gamma rays is picked up by the gamma camera thus paving the way for accurate diagnosis of ailments. The use of Tc-99m gained momentum in the 1960s across the world with the improvements made to the gamma cameras. In 1963, the first report on the use of Tc-99m diagnostic imaging from the USA was published [4]**.** They used an intravenous injection technique for Mo-99 and allowed it to concentrate in the liver, becoming an internal generator of Tc-99m. After sufficient Tc-99m build up they were able to visualize the liver using the emitted gamma rays.

1.2 Production Methods and Target Development

One method of producing Molybdenum-99 is by the neutron irradiation of fissile U-235 contained in high enriched uranium (HEU) or low-enriched uranium (LEU) targets in a nuclear reactor. The other method is by using n-γ based accelerator techniques which is out of the scope of discussion in this dissertation. The neutron irradiation of fission U-235 initiates a nuclear fission reaction, generating a large amount of heat and fission

products. The purpose of these targets is to ensure that the fission products remain well contained, by enduring the thermal stresses induced in the target due to high temperatures. Another function of the target is to effectively dissipate the generated heat to the reactor coolant to ensure that the target temperature remains within the melting point of the cladding material. Majority of the Mo-99 currently produced comes from HEU targets, which contains greater than 20 % of U-235, using a traditional powder dispersion target as illustrated in Figure 2. In this method, a mixture of aluminum and HEU powder is heated and compressed between two plates to form a monolithic structure. This ensures that no gas gaps exist at the uranium and aluminum interfaces. To recover the Mo-99 the entire plate is dissolved in alkaline or acidic solution, resulting in expensive liquid waste.

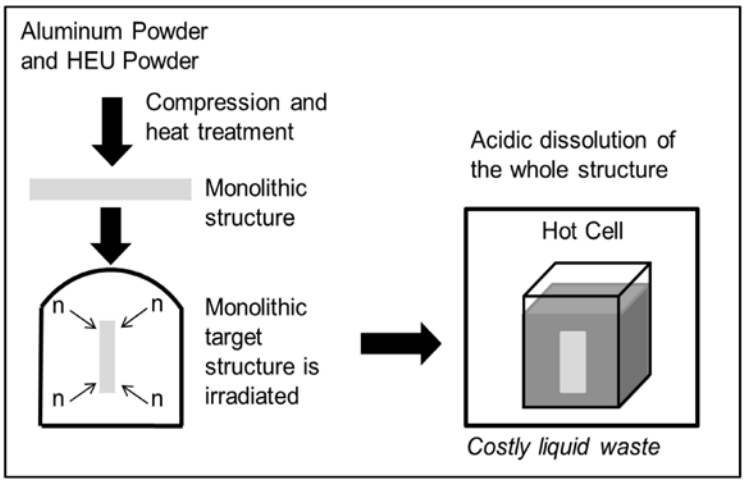

Figure 2. Traditional powder dispersion method using HEU.

Due to the high concentration of U-235 in HEU, it can be used to make nuclear weapons apart from being beneficial to high volume production of Mo-99. In order to alleviate proliferation risks associated with the use of HEU in civilian and nuclear applications the use of LEU targets is being mandated. While the use of LEU will increase the safety, it is

also the motivating factor behind the switch from the dispersion target to the foil target. Since LEU has only a fraction of the U-235 content that HEU has per unit volume, more LEU would be required to achieve the same output of Mo-99. Hence, if LEU were to be used in a dispersion target shown in Figure 2, the volume of the target would increase dramatically. But, by switching to a LEU foil, the mean U-235 density of the foil target is much higher than that of a comparable dispersion target. Figure 3 provides a plot of the molybdenum-99 activity with the LEU dispersion method and the HEU powder dispersion method, under the following irradiation conditions at the Missouri University Research Reactor (MURR): irradiation time of 7 days, a thermal neutron flux of 2.0 x 10^{14} n/cm^{2}s and a molybdenum-99 fission yield of 6%. Figure 3 provides further credence to the fact that the use of LEU in a dispersion target will decrease the Mo-99 yield.

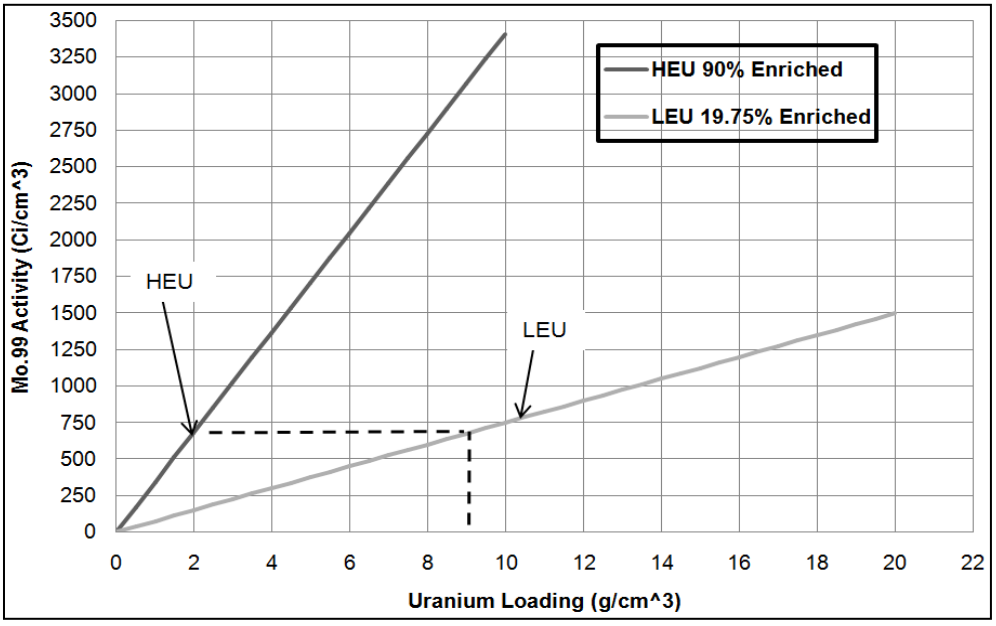

Figure 3. Mo-99 activity vs. uranium density for HEU and LEU dispersion.

The alternative to HEU dispersion targets is to use LEU foil based targets, where the LEU foil is wrapped in a nickel foil and sandwiched between two concentric aluminum tubes to form a composite structure [6]. The role of the nickel foil is to act as a recoil barrier [7] and prevent any bonding between the aluminum cladding and the LEU foil during irradiation. After irradiation the aluminum cladding is cut open to retrieve the LEU foil alone, which is then dissolved to retrieve the Mo-99. A pictorial representation of this process is illustrated in Figure 4 with the annular target and the flat plate target [8].

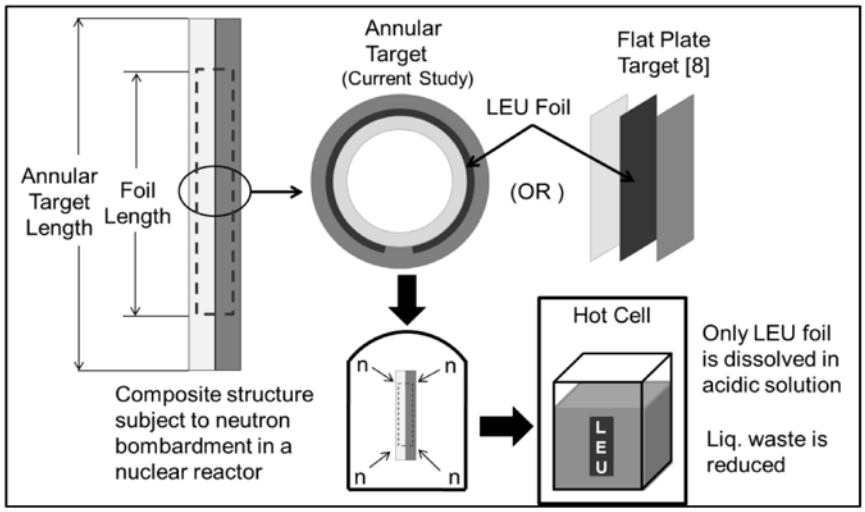

Figure 4. Proposed LEU metal foil based approach for Mo-99 production.

Upon removal of the targets from the reactor after irradiation; they are cooled for about a day before being transported to the processing facilities in radiation shielded containers. The cooling of the targets is a safety measure to reduce the overall irradiation doses in the target processing system, to prevent the target from being damaged due to the high temperatures, and to provide time for short lived fission gases to decay. The chemical processing of the targets takes place inside 'hot cells'. Post-irradiation, approximately 1 % of the Mo-99 produced in the target is lost to radioactive decay every hour. Hence it is important to quickly carry out the processing in the hot cell to recover the Mo-99. The

hot cells are the most expensive part of a processing facility and they consist of a container for dissolving the targets, which is connected to tubing and columns for subsequent chemical separations to isolate the Mo-99. It also consists of remote manipulators to move around the contents of the hot cell as shown in Figure 5[9].

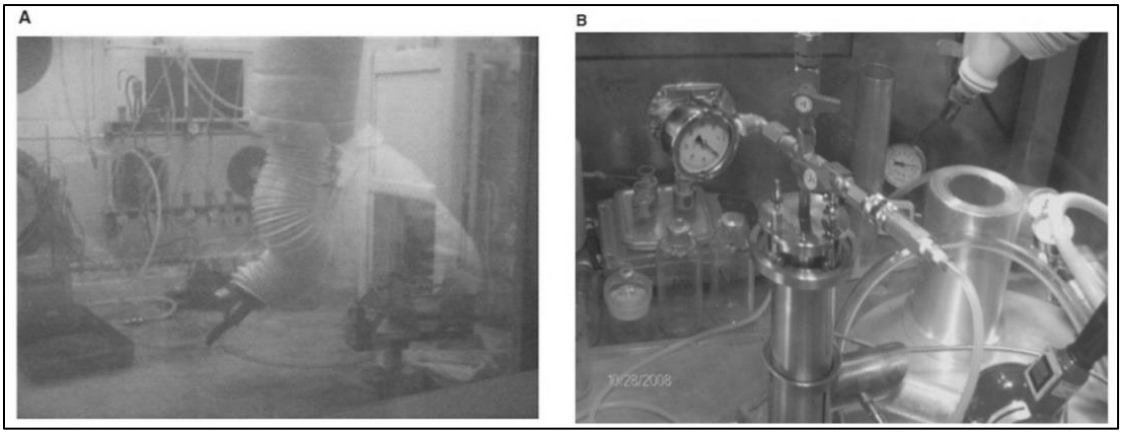

Figure 5. Hot cells at (a) Comision Nactional de Energia Atomica (CNEA) in Argentina, and (b) Missouri University Research Reactor (MURR).

1.3 Thermal Contact Resistance

The proposed LEU foil based approach for Mo-99 production using a composite cylindrical target makes the thermal contact resistance (reciprocal of thermal contact conductance) very important from a thermal and hence a structural standpoint. As in the case of many other high heat flux applications such as electronics cooling and turbine blade cooling, it is necessary to determine the rate of heat transfer across the interfaces formed by components in contact and possibly try to control it to ensure prolonged component life, reliability and safety. Typically most surfaces, though they appear to be 'smooth', are composed of microscopic (roughness) and macroscopic (waviness) surface irregularities due to manufacturing limitations. These irregularities result in interstitial gaps and solid contact spots, where a finite contact pressure exists. The heat flow is

constricted through these solid contact spots and as a result there is some amount of resistance to the flow of heat, and a corresponding temperature drop at the interface as illustrated in Figure 6. For the annular target, the issue is cooling of the LEU foil so that it does not exceed the temperature limits for melting and U-growth. The interfacial heat transfer mechanism consists of conduction through the solid contact spots, conduction through the interstitial gaps and radiation across the interface. The convective heat transfer mechanism is not taken into account as the interfacial gaps, generally of the order of μm, are too small for bulk fluid motion to support convection.

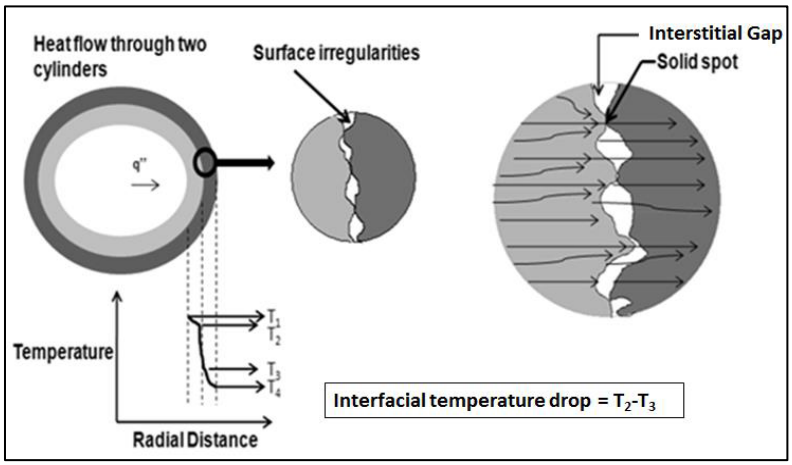

Figure 6. Surface irregularities offering resistance to heat flow through a compound cylinder assembly.

Radiation can also be neglected if the interfacial temperatures are below 573 K [10]. Hence, the interfacial conductance can be expressed as the sum of the conductance through the solid spots (h'_{solid}) and the interstitial gaps (h'_{gap}) as given by Eq.(3). In this equation 'h'' represents the total conductance and 'R'' denotes the total interfacial resistance.

$$h' = \frac{1}{R'} = h'_{solid} + h'_{gap} \tag{3}$$

1.4 Control Blades

The nuclear fission chain reaction is the fundamental process by which nuclear reactors produce usable energy. In this process, a U-235 atom is struck by an incident neutron, causing the atom to fission into smaller fragments. These new neutrons then collide with other U-235 atoms, creating a chain reaction that releases a substantial amount of energy. Hence the key to sustaining a fission chain reaction is to be able to control the amount of neutrons that propagate to the subsequent fission step. The control blades are an important technology for maintaining the desired state of fission reactions within a nuclear reactor. They help with real time control of the fission process, which is crucial to keep the fission chain reaction active and prevent it from accelerating beyond control. The design of a reactor influences the selection of material to be used for control blades. For the control blade to be able to absorb neutrons, it should have a large neutron absorption cross section and should be resilient to quick burn out. The material selection for a control blade is also dependent on the ability of the rod to resonantly absorb neutrons. Cross sections with this quality are usually preferred over cross sections that have a high thermal neutron absorption capability [11].

In a nuclear reactor, the reactor core is enclosed by a thick walled cylindrical pressure vessel. Protecting the inside of the vessel from fast neutrons escaping from the fuel assembly is a cylindrical shield wrapped around the fuel assembly called the reflector. The control blades at the Missouri University Research Reactor (MURR) operate in a gap between the outside of the reactor pressure vessel and the inside of the beryllium reflector as illustrated in Figure 7, obtained from [12]. The outer diameter of the pressure vessel is between 0.318 and 0.319m. The inner diameter of the beryllium reflector is between

0.347 and 0.348m. The gap width is maintained by vertical spacers which are set into the beryllium reflector and cross the gap to the outer diameter of the reactor pressure vessel.

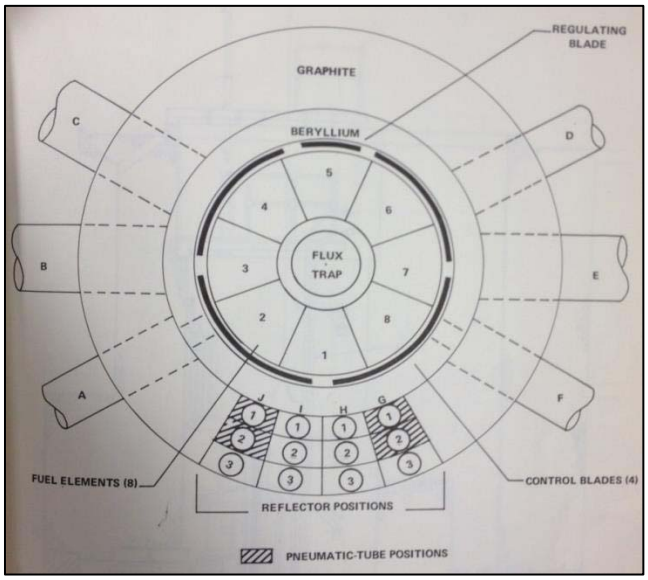

Figure 7. View of the MURR core showing the reflector, control blade and pressure vessel.

The BORAL® control blades used by MURR will experience a thermally induced deflection during reactor operation due to the composite structure of the control blade. The neutron absorber in BORAL is boron. BORAL has an aluminum and boron carbide mixture enclosed in an aluminum cladding. The boron and aluminum mixture (BORAL meat) and the aluminum cladding are bonded together through powder metallurgy to establish an adherent bonded plate. As the BORAL absorbs both neutron particles and gamma rays there is volumetric heat generation and a corresponding rise in temperature. Since the BORAL meat and the aluminum cladding materials have different thermal expansion coefficients, the blade may have a tendency to deform as the blade temperature changes and the materials expand at different rates. In addition to the composite nature of the control blade, spatial variations in temperature within the control blade occur from the non-uniform heat generation within the BORAL meat. The high boron-10 cross section

of the B-10 (n, α) Li-7 thermal neutron reaction produces the vast majority of the heating in the control blade. This reaction primarily occurs within the first 0.051 x 10^{-2} m of the BORAL meat surface and produces about 2.79 MeV of energy, of which 0.84 MeV is the reaction energy of the Li-7 and 1.47 MeV is the alpha particle. The remaining 0.48 MeV is a gamma rays. Hence, about 80 % of the nuclear reaction's energy is deposited within a few millimeters of the reaction location. Consequently, the major heating is in the outer two surfaces of the BORAL meat, making the heat generation through the blade low except for the outer 0.051 x 10^{-2} m of each surface. These combine to produce a variation in the heating profile through the thickness and about the circumferential width of the control blade. The heat generation is also non-uniform along the longitudinal direction because the thermal neutron flux drops off significantly from the leading edge (bottom) of the control blade to the top. Mathematical curve fits are generated for the non-uniform volumetric heat generation profile caused by the thermal neutron absorption in a B-10 (n, α) Li-7 reaction and the gamma heating. The functions are applied as heating conditions within a finite element model of the control blade built using the commercial finite element code Abaqus FEA. A convective heat transfer coefficient is applied to the outer boundaries of the control blade and neutral assembly temperature is assumed to be room temperature. The finite element model is solved as a fully coupled thermal stress analysis, where the temperature distribution is solved for and then used to determine the mechanical deflection of the control blade.

1.5 Objective of Work

For the annular target, since most analysis parameters are reactor specific, the goal is to develop a general performance analysis envelope, using numerical models and simplified

analytical expressions for thermal-stresses in composite cylinders, which covers most operational parameters (heat generation rates, heat transfer coefficients) that are likely to be used by reactors. The importance of the analysis stems from the fact that, though these annular targets have been safely irradiated in the past, there is no documented safety analysis to completely understand the behavior of the targets during irradiation. Hence, the objective of annular target investigation is to analyze its thermal mechanical behavior, develop a general performance analysis envelope and assess the conditions under which the targets could potentially fail.

While the annular target analysis is focused on establishing the magnitude of temperature and thermally induced stresses in the target, relative to the melting temperature and the yield strength of the cladding, the goal of the BORAL control blade analysis for MURR is centered around determining whether the thermally induced deflection of the control blade will be within the specified channel gap limits for safe operation. The results from this reactor-specific control blade analysis were used to help MURR with their reactor relicensing efforts during the summer of 2012. Broadly, it is the thermal-mechanical behavior of the both these internal heat generating applications that is being analyzed.

Hence, this dissertation will seek to provide analysis results based on two internal heat generation applications (annular target for Mo-99 production and the control blade analysis to support MURR relicensing efforts). In both these applications the heat source is nuclear, there exists high heat flux that needs to be managed by effective cooling, non-uniform heating, the presence of composite structures and differential thermal expansion, with the end goal in both these analyses being – component and operational safety.

Chapter 2: Literature Review

2.1 Target Design and Irradiations

Low-enriched uranium foil based annular target design and developmental work was carried out by the Argonne National Lab (ANL) [13]. The design consisted of an LEU foil sandwiched between concentric cylindrical tubes. A recess was cut on the inner tube to accommodate the LEU foil. Their analysis focused on developing a cost effective annular target design that would minimize the thermal contact resistance between the LEU foil and the target tubes. They performed thermal cycling tests, over a period of 7 days in a furnace at 473 K, on the assembled annular targets and established that they would perform well when irradiated. They also established the average value of hoop stress in the outer tube to be 3 MPa. This target design concept was successfully irradiated in 1999 [14]. Good radiation performance and no heat transfer problems were reported based on their test results. During disassembly the targets were easily removed from the irradiation holders and this proved that no significant mechanical distortions existed during in-pile irradiation. Their conclusions, based on the disassembly, were that the nickel recoil barriers perform the best while aluminum and zirconium as target tubes work well.

The thermal mechanical behavior of the LEU foil based annular target developed by [13] was evaluated by Areva-Cerca [15]. They performed their thermal analysis using the numerical code CFX and used experiments to determine the thermal contact resistance. In their experiments they used a perfectly flat rolled LEU foil and did not account for the surface irregularities (macroscopic and microscopic) on the foil surface which is

important in the thermal contact resistance analysis [16]. A feasibility study [17] was carried out by performing a preliminary thermal and fluid flow analysis to estimate the heat removal capability for a 20 g LEU foil annular target irradiated in MURR. In the parametric studies they varied the pressure drop and the thermal load separately. They concluded that a minimum pressure drop of 15 kPa is required, for a 15 kW heat dissipation, to ensure that boiling is suppressed. Their thermal load variation studies were aimed at determining the maximum possible heat dissipation for the target while maintaining the temperature below 373 K. They concluded that for a uniform heating configuration, 30 kW heat can be removed before reaching 373 K, and for the non-uniform heating case, 16 kW heat can be removed before reaching 373 K. Their parametric studies also helped them conclude that the cladding temperatures for the non-uniform heating case can be controlled by optimizing the thickness of the aluminum tubes. The results from the analysis were found to comply with the acceptance criteria established by the MURR operating licensing technical specifications.

Preliminary safety calculations on a prototype LEU foil based annular target can and subsequently trials at HIFAR were carried out by the Australian Nuclear Science and Technology Organization (ANSTO) [18]. In their numerical calculations using CFX4, they used a 125 micro meter foil, with a target mass of 0.4 g and a thermal neutron flux of 0.19 E14 n/cm^{2}s. Their analysis predicted a maximum foil temperature of 138°C and a maximum can wall temperature of 92°C. They also determined the optimum diameter of the coolant exit to be 3 mm as it provided greater flow through the inner channel than through the can-rig channel. This is consistent with the analysis in [17], which also concluded that there is greater flow through the inner flow channel as compared to the

coolant flow between the outer tube and the channel wall. Their trial irradiation results were also found to be consistent with their numerical analysis results.

A physics study [19], using the neutronics code MCNP, was carried out on the target irradiation for fission molybdenum production at the High-Flux Advanced Neutron Application Reactor (HANARO) in Korea. An annulus type of uranium foil (with no circumferential gap), 100 micro meter in thickness and 100 mm in length was used in the analysis. The nickel coated uranium foil was sandwiched between two aluminum tubes. To evaluate the effect of surface roughness, they varied the target foil thickness from 75-125 micro meters. They found the reactivity change due to loading of targets to be much lower than that prescribed by the HANARO safety limits. Thermal hydraulic and neutronics analysis was performed on LEU foil based annular targets for the production of 100 Ci of molybdenum-99 at the Pakistan research reactor-1 (PARR-1) [20, 21]. They used a 125 µm thick uranium foil at 19.99 % enrichment, enveloped in a 15 µm thick Ni foil. This configuration was placed between two aluminum tubes of 162 mm length and the edges were welded. The reactivity of fission molybdenum-99 was analyzed for various power levels between 5.4 kW and 17.41 kW. However, for their analysis, they used the maximum power of 17.41 kW and found the corresponding maximum surface temperature rise of 317 K to be within the saturation temperature (386 K) at the core pressure level. Based on their analysis they reported that the reactor safety will not be compromised in adopting the proposed annular target and holder designs for the molybdenum-99 production.

Thermal mechanical studies were carried out on LEU foil based flat plate targets by varying the boundary conditions applied to the aluminum plates [22]. The focus of the

analysis was to evaluate the impact of changing boundary conditions (fully constrained, partially constrained and free) on the thermal mechanical behavior of these plates. They reported that the variation of stresses and strains induced in the plates was related to the manner in which the plate was constrained. They also showed that the magnitude of deflection through the thickness of the plate was greatest when the plate was fully constrained as opposed to being partially constrained with free edges.

Thermal stress numerical and analytical analyses of annular targets for Mo-99 production using LEU metal foils have recently been analyzed [23, 24]. In [23] the authors did not account for the pre stresses from the assembly process. They assumed that their numerical thermal-mechanical model began from a stress- free state. Their target design was based on the ANL annular target design [13], but the cladding material was Al 6061-T6 as compared to the Al 3003-H14 used in [13, 14]. In [24] the authors included the residual stresses from the hydroforming assembly process and the numerical model was built to simulate the hydroforming assembly process first, followed by the thermal-mechanical irradiation analysis. In both these instances [23, 24] they concluded safe irradiation of these annular targets based on analysis results.

2.2 Thermal Contact Resistance

A good understanding of the interface integrity is an important aspect in high heat flux applications as the presence of surface irregularities and its incorrect evaluation will result in overheating and subsequent failure of components. Typically in thermal contact resistance studies involving flat joints the contact pressure is known and can be taken as the independent variable. In cylindrical joints, the flow of heat causes the expansion of

the tubes which results in the contact pressure [25]. Hence the heat flux is the independent variable in cylindrical joints.

Results from tests on cylindrical joints with varying interface heat fluxes [26] showed that the thermal contact resistance is dependent upon the initial gap, the differential thermal expansion due to an interfacial temperature drop and the differential expansion due to the temperature gradients. Also, due to the contact resistance being dependent on the initial gap, the results illustrate that joints with an interference fit will have negligible thermal contact resistance. This is true as with an interference fit, the interface temperature discontinuity will be negligible. They also report that the there is a dearth of literature based on contact conductance studies of cylindrical joints and often the effects of differential expansion are neglected assuming the thermal contact resistance to be constant. Power law correlations based on previous experimental work were obtained [27], to predict the solid spot thermal conductance at the interface of Zircaloy-2 and Uranium Dioxide. The investigators concluded that more work is required to determine the effect of mean junction temperature on the thermal contact conductance. They also stated that the surface parameters other than the roughness effects must be accounted for future analysis.

Experiments on composite cylinders were performed by Hsu and Tam [28]. They varied the heat flux, microscopic surface properties only on one side of the interface and compared their results with those of Ross and Stoute [29]. They found these experimental results to be much lower than the calculated values and attributed it to the increase in micro-contact area due to the lateral expansion of the flat contacts and thermally induced strain at the interface. A study on the coaxial cylindrical casings in a vacuum

environment was performed [30], taking into account the mechanical and thermo physical properties of the tubes. The investigators report a dependency between the contact pressure, thermal load, initial interference of the tubes and the ratio of thermal expansion coefficients of the tubes without considering the microscopic or macroscopic surface irregularities. They concluded that for a case of radially outward heat flow, if the thermal expansion coefficient of the inner tube is lesser than that of the outer tube then the thermal contact resistance at the interface will increase due to a decrease in the interfacial contact pressure.

An iterative procedure [31] was used, based on a plane stress and interference fit assumption, to predict the contact conductance of cylindrical joints based on flat contact conductance models. The iterative procedure takes into account the surface roughness, microhardness and the contact pressure at the interface. The thermal contact conductance is presented as a function of the contact pressure, thus recommending that accounting for the difference between the circumferential and axial roughness is important. Their model was in good agreement with that of Hsu and Tam [28] and the modified flat contact models of Ross and Stoute [29]. A laser flash technique [32] along with a Gaussian parameter estimation procedure was employed to estimate the thermal contact resistance at the interface of a double layer sample. The investigators provide the analysis of sensitivity coefficients for each parameter of the double-layer sample which can be extended for use in designing experiments. Based on their numerical simulations they concluded that their method could estimate the thermal contact resistance between the layers with high accuracy if any one of the sample materials is a good conductor of heat or if a thin layer assumption is used. They also found that the energy absorbed by the

sample from the laser pulse can be estimated with ease if a high signal to noise ratio exists. An experimental methodology to predict the thermal contact resistance based on the interfacial stresses in a pair of concentric aluminum tubes was identified [33]. The authors showed that for a couple of aluminum tubes in perfect contact, external heating of the outer tube would result in tensile stresses being generated on both the tubes. This opens up a gap between the tubes and increases the thermal contact resistance. Internal heating of the inner tube would result in compressive stresses being generated on the tubes, thus reducing the thermal contact resistance. Thus by controlling the direction of heat flow, contact is either established or withdrawn due to the compressive and tensile stresses respectively.

An expression for the thermal contact conductance (reciprocal of thermal contact resistance) as a function of the contact pressure, at the interface of Al 6061-T6 and uranium was recently developed [34]. The expression is based on a widely used correlation from literature [35] that assumes plastic deformation of the asperities at the interface. The authors assumed the total conductance to be a sum of the solid spot conductance and the gap conductance. In the gap conductance calculations, they assumed that the interstitial gaps would be filled with a mixture of Helium (He), Xenon (Xe), Krypton (Kr) and Iodine (I). The assumption of the existence of these gases in the interstitial gaps was made based on the data available from an irradiation study [36].

2.3 Thermal Stresses in Cylinders

Compound cylinders and composite layered structures have a wide range of applications in gas storage, spacecraft structures, nuclear power plants, nuclear reactor control blades and also in applications for medical isotope production [24]. Compound cylinders are

generally preferred over a single cylinder, as the composite structure provides reinforcement, thereby increasing its capability to withstand a comparatively larger stress state. This is especially beneficial in high heat flux applications, such as in nuclear reactors, where material or component failure due to yielding is undesirable. Over the years many investigators have come up with steady state and time dependent analytical solutions for thermal stresses in compound cylinders. The Laplace transform solution technique has been commonly used to solve the transient problem in compound cylinders [37] and a single hollow cylinder [38]. The transient thermo elastic solution in compound cylinders with traction free boundary conditions [37] was solved by utilizing the Laplace transform and the matrix similarity transform, to obtain a solution that can be applied to the thermal stress estimation in multilayered composite cylinders with non-homogeneous materials. The compound cylinders usually undergo an assembly process to fit them together. This process induces stresses in the material, as a result of which a finite pressure exists at the interface of the cylinders. The thermal stresses in compound cylinders with an initial interface pressure have been solved using the finite difference method in conjunction with the Laplace transform and matrix similarity transform [39]. In compound cylinders with radial heat flow, the thermal expansion coefficient of the materials, along with the direction of the heat flow dictates the integrity of interfacial contact [25]. Earlier work [40] also concluded that local separation occurs at the interface when heat flows into a higher distortivity material. The exact steady state thermo elastic solution for functionally graded cylinders with the thermal expansion coefficient as a function of the radius of the cylinder has also been studied [41]. The authors were able to establish the location of maximum stresses and concluded that the volumetric average of

the thermal expansion coefficient can be used to represent the effective thermal expansion coefficient.

In the nuclear industry there has been an effort to utilize low-enriched uranium metal foil based annular targets [34] to produce molybdenum-99 and hence obtain its daughter element technetium-99m which is used as a radioactive tracer. The annular targets used for this purpose typically consist of a uranium metal foil sandwiched between two aluminum cylinders to form a composite cylindrical structure [23, 42]. The inner and outer aluminum cylinders are collectively referred to as the 'cladding'. Extensive analysis has been performed in this area using other composite geometries as well [8, 43].

2.4 Fission Gas Release and Uranium Swelling

It has been shown [44, 45] that during irradiation the uranium increases in volume by a number of mechanisms (increase in atomic volume, low temperature distortion, swelling by absorption of vacancies and swelling due to fission product gas pressure) each depending on the irradiation temperature. Most of the available literature [46, 47and 48] presents the swelling of uranium fuel pins/ rods and there is no available data (to the knowledge of the author) on swelling of LEU metal foils during irradiation. An available data source for swelling of pure uranium metal [49] indicates that the swelling due to irradiation is an integral function of the neutron damage at temperature and time. The data from this source [49] also indicates that there would be significant swelling at temperatures in excess of 400°C (673 K) but essentially no swelling at temperatures below 350°C (623 K). Hence the current approach to address uranium swelling is to ensure that the LEU temperature remains below 350°C (623 K) at the 100 % power case. In case the temperatures are found to exceed this value while performing analyses at a

higher power (> 100 %), it can be argued that all power ranges above the 100 % power represent end of the cycle situations and is therefore highly transient, where the reactor will be scrammed automatically or manually within minutes of the start of the transient. Irradiation of the LEU foil will produce large amounts of heat along with which fission by-products are created that include fission gases. The irradiation time dictates the quantity of gases (number of moles) that are usually generated and released. The noble gases Xe (Xe-131) and Kr (Kr-84) along with Iodine (I-127) account for the majority of the fission gases generated [36]. However Iodine release is not expected [50] and only Kr and Xe are expected to contribute towards the gas release fraction along with He (if the target was He back filled and the ends were TIG welded). An aspect that needs to be given consideration is the determination of the volume in which these gases are likely to be contained. Difficulty arises in determining this volume due to the surface irregularities. ANSTO in their calculations [18] determined the volume at the elastic limit and used this value in their fission gas pressure calculations. It is usually assumed that the gas mixture is 'ideal' and the ideal gas law is used to estimate the gas pressure. In their safety calculations, the gas mixture was assumed to be ideal and a release fraction [51] was used to determine the fission gas pressure.

Chapter 3: Annular Target Thermal-Mechanical Safety Analysis

3.1 Target Design

Two different types of LEU foil based target geometries have been considered for Mo-99 production – flat plate type [8] and annular target [23, 24 and 34]. Of these, the annular target geometry will be the primary focus area of this dissertation. A brief overview of the flat plate geometry analysis and work will be provided before focusing on the annular target studies and analysis.

3.2 Plate Target

Analysis of LEU foil based plate targets was completed by using numerical and experimental analysis methods [8] at the University of Missouri. The goal of the analysis was to establish the thermal-mechanical response of the plate type targets and assess the probability of target failure by modeling various worst case scenarios. The design consisted of a nickel recoil barrier wrapped around a LEU foil, placed between two aluminum plates and pressed together. The edges were assumed to be welded to provide a completely sealed environment for the fission products. From a mechanical standpoint, the edge welds (Figure 8 and Figure 9 from [8]) prevent the plate from moving apart from each other. Pillowing of the plates was reported, the magnitude of which depends on the boundary condition applied to the edges of the plates and the amount of heat dissipated through the aluminum cladding. The effects of fission gas release and uranium swelling on the thermal mechanical response of the target were also analyzed. The analysis results indicate that the fission gas pressure would contribute more towards the stresses induced

in the cladding as compared to the uranium swelling induced stresses. The magnitude of plate deflection was found to be tolerable and in the micro meter range.

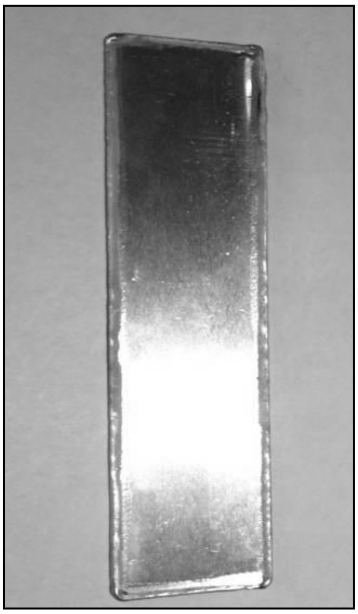

Figure 8. Flat plate target with welded edges.

Figure 9. Curved plate type target with welded edges.

3.3 Annular Target

The geometry of the annular target [23, 24 and 34] consists of an LEU foil, wrapped in a thin (~ 15 µm thick) nickel envelope and placed between two aluminum tubes to form a sandwiched structure. The inner and outer aluminum tubes are collectively referred to as the cladding. The nickel acts as a recoil barrier [5, 6, 7 and 13] to prevent the LEU foil from bonding with the aluminum cladding during irradiation. A recess is cut on the inner tube to facilitate easy assembly of the foil. The geometry of the foil is such that it doesn't wrap completely around the inner tube, leaving a small gap (~11.5 mm) around the circumference as illustrated in Figure 10. This is the region where the inner cladding and the outer cladding are in direct contact and a longitudinal cut is made along this region to extract the LEU foil after irradiation.

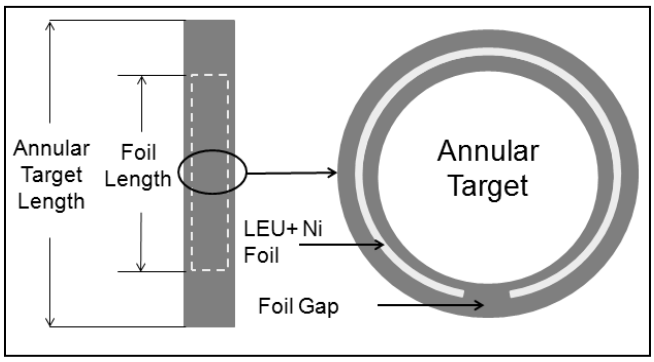

Figure 10. A simple diagram of the annular target illustrating the position of the foil longitudinally and the location of the circumferential gap.

After assembly, the ends of the target are welded (TIG or EB) to provide a completely sealed environment within which the fission products are expected to be contained during irradiation. A picture of a prototype annular target with welded edges is presented in Figure 11. The composite structure of the target creates interfaces which are made up of solid contact spots and interstitial gaps between the adjacent materials in contact. This

discontinuous contact is due to the surface irregularities (macroscopic and microscopic) that exist due to manufacturing limitations. From a heat transfer standpoint, the existence of these discontinuities is undesirable as it offers resistance to the flow of heat as illustrated earlier in Figure 6 and as shown below in Figure 12.

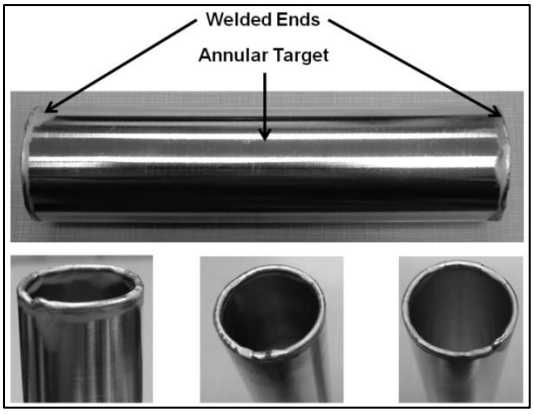

Figure 11. A prototype annular target with welded edges.

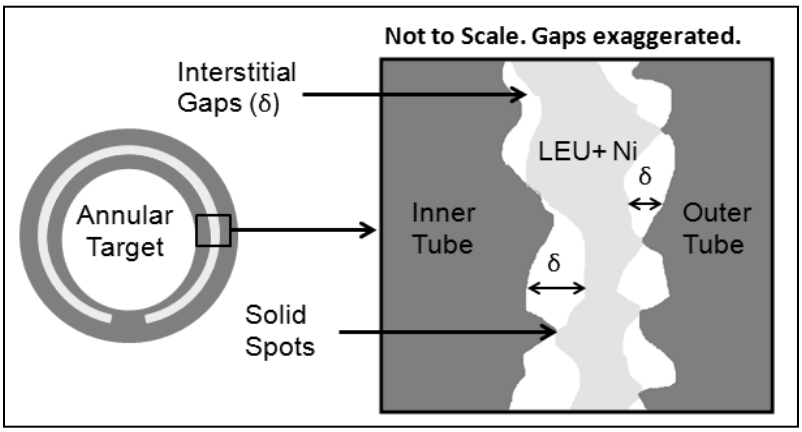

Figure 12. Interfacial contact bond formed by solid contact spots and interstitial gaps.

The thermal contact conductance (h) is the reciprocal of thermal contact resistance (R') and is defined as the ratio of the heat flux (q") to the interfacial temperature (ΔT) drop caused due to surface irregularities. Mathematically it is represented by Eq. (4).

$$h' = \frac{1}{R'} = \frac{q''}{\Delta T} \tag{4}$$

The heat transfer through a joint consists of conduction through the contact spots, the interstitial gaps and through radiation. Since the gap thickness is usually very small (of the order of μm) the convection effects are not considered and the radiation effects can be neglected if the joint temperature is below 573 K [10].Thus, the total conductance (h') can be obtained by solving the solid spot conductance (h'_{solid}) and the gas gap conductance (h'_{gap}) in a parallel resistance network as presented by Eq. (3) in Sec. 1.3. The contribution from the gap conductance is usually negligible when compared to the conductance through the solid spots. However, the gap conductance must be taken into account if the interface medium is a good conductor or the bodies in contact are made up of materials that are relatively poor conductors of heat (e.g. Stainless steel).

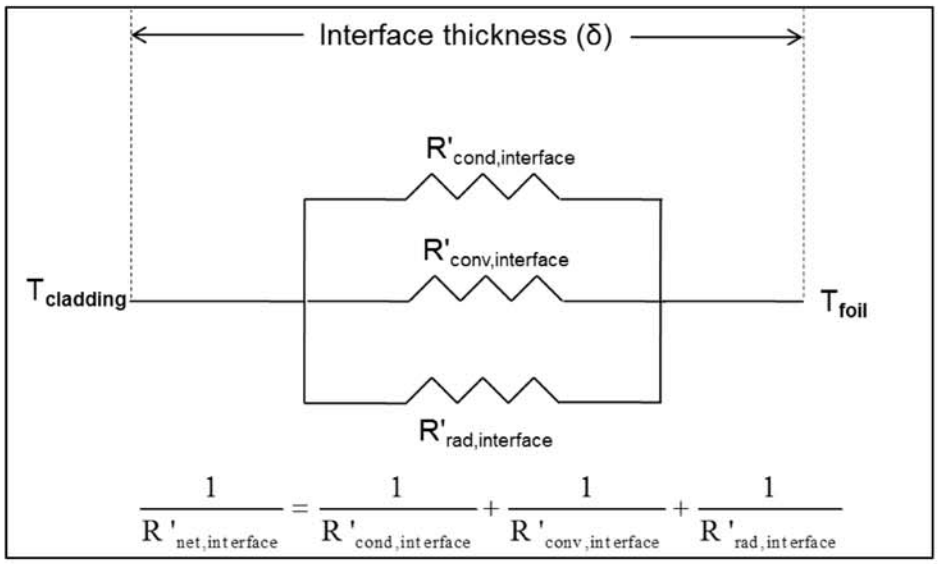

Figure 13. Sketch depicting the resistances across the interfacial thickness.

Though a high value of thermal contact conductance is desirable in nuclear reactors, gas turbine blades, there exist applications involving storing and transportation of cryogenic fluids [52], thermal isolation of space craft components [53] that require a low value of thermal conductance or higher thermal resistance. In the case of nuclear reactors, a

higher thermal conductance is desirable to effectively transfer the heat to the coolant thus preventing overheating which could result in the failure of the part being irradiated and cause unscheduled reactor outages. The large amount of fission heat generated by the LEU during irradiation needs to be dissipated to the coolant. The generated heat increases the target temperature and the increase in temperature causes thermal expansion. Since the LEU and the aluminum have different thermal expansion coefficients, the magnitude of thermal expansion will differ. This thermal expansion mismatch causes pillowing and stresses in the target. Post irradiation, the aluminum cladding and the sandwiched foil are mechanically separated, after which the LEU foil is chemically processed. The separation of the LEU from the cladding before processing reduces the mass of the material to be chemically dissolved in alkaline or acidic solutions.

The advantage of using an annular target is to improve the structural integrity of the target and the heat transfer rate. The LEU foils to be used have been produced by the Korean Atomic Energy Research Institute (KAERI, South Korea) using the casting method (where the metal is melted and poured into a mold) and by Argonne National Lab using the hot and cold rolling technique. In the hot rolling process the metal is heated above its re-crystallization temperature and the foil is then rolled to form sheets while in the cold rolling process the crystalline structure of the foil is retained and the process is carried out at room temperature.

The drawback of using the KAERI foils is that they have a lot of surface irregularities and waviness. These microscopic and macroscopic irregularities will make it difficult to justify the use of these targets as a significant amount of surface irregularities will affect the heat transfer rates due to an increase in the thermal contact resistance at the interfaces.

The cold rolling technique used by the Argonne National Lab, though an expensive and labor intensive method can eliminate the surface irregularities. The annular target design [54] used by the Missouri University Research Reactor (MURR) is presented in the Figure 14. It should be noted that the choice of cladding material for this target presented in Figure 14 is Al 3003-H14, but the current analysis considers Al 6061-T6 to be the cladding material. Aluminum alloy 6061-T6 has higher material yield strength (276 MPa) as compared to Al 3003-H14 (145 MPa).

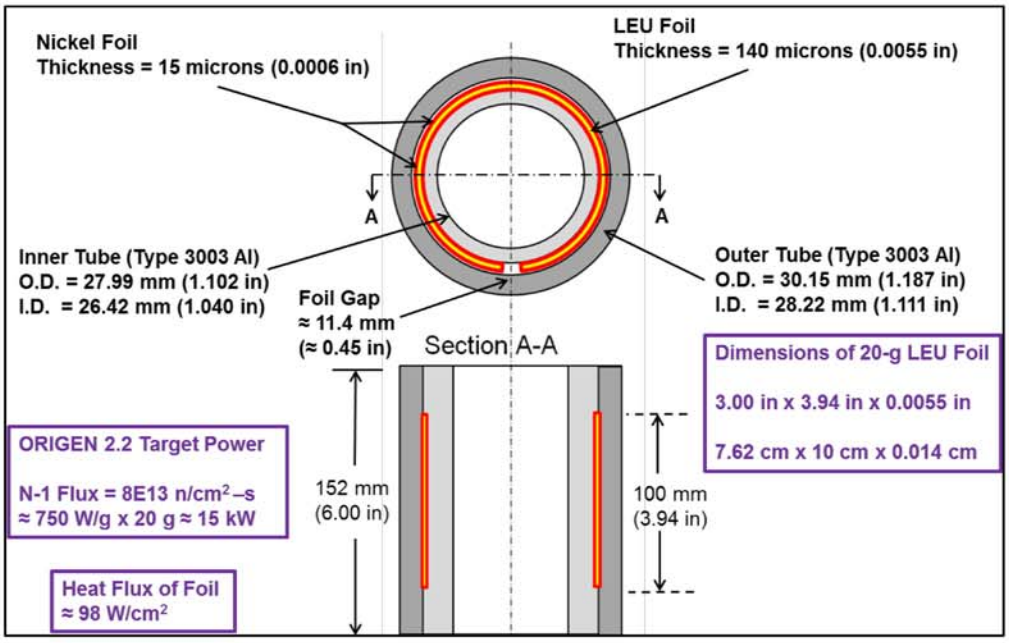

Figure 14. Annular target design using Al 3003-H14 as the cladding with the dimensions.

Chapter 4: Modeling Without Residual Stresses

Prior to being irradiated in a nuclear reactor, the annular targets undergo 'preparation'. This preparation involves assembling the targets [24, 55] and welding the target ends. The assembly process induces residual stresses in the target and these residual stresses remain in the target prior to irradiation. The initial part of the analysis does not account for the residual stresses in the thermal-mechanical irradiation modeling and all the analysis in Sec 4 and its sub-sections will provide analysis and results without the effects of the assembly residual stresses. The analysis results with the residual stresses will be presented in detail in Sec. 7 and its sub-sections.

The commercial finite element code Abaqus FEA [56], version 6.10, was used to perform a thermal-mechanical analysis on the annular foil based target. Originally released in the year 1978, Abaqus FEA is a set of software applications meant for finite element analysis and computer aided engineering. A numerical simulation in Abaqus FEA typically consists of 3 separate stages namely the pre-processing stage, simulation evaluation stage and the post processing stage. The pre-processing stage involves creation of an input file which contains all the constraints under which the model is to be numerically evaluated. In the second stage the numerical analysis is evaluated based on the constraints specified in the pre-processing stage or the Abaqus FEA input file. The post-processing stage involves visualizing the results and extracting data.

4.1 Non-Uniform Heating Numerical Model

Since running full blown 3D finite element simulations is time consuming and not cost effective, it was decided to simplify the analysis and create a 2D model of the heated

portion of the annular target which is located mid-way along the target length as illustrated in Figure 15.

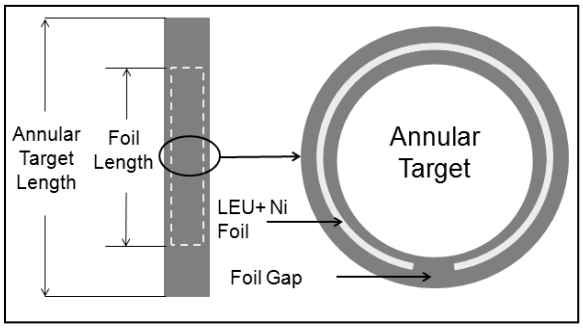

Figure 15. Pictorial representation of the modeling strategy for the analysis of the annular target without initial residual stresses.

The annular target was modeled as a 2-D plane strain (temperature is independent of axial coordinate, no axial strain and length is large as compared to the cross section) analysis that consists of a low enriched uranium foil of open cross section (not a complete circle due to the foil gap) sandwiched between two aluminum tubes (cladding) of material type - Al-6061 T6. While the outer aluminum tube has a uniform circular cross section, the inner tube has a recess cut on its surface as presented in Figure 16, to accommodate the LEU foil. This LEU foil generates heat when irradiated and coolant flows through the inner tube and along the outer tube.

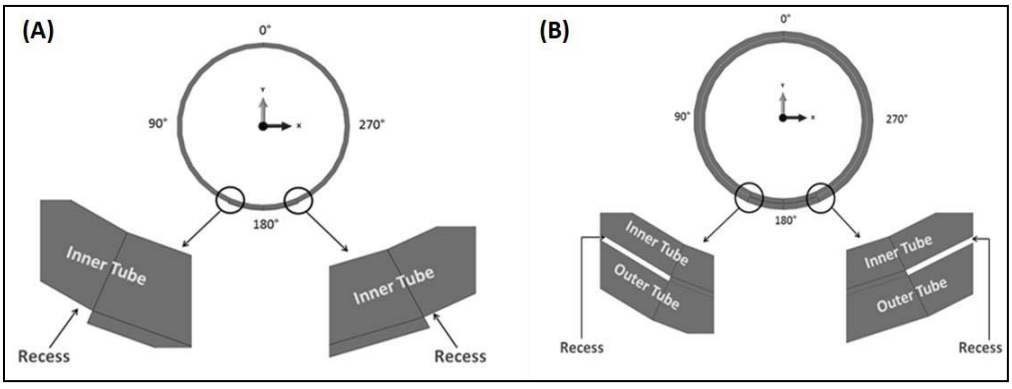

Figure 16. Numerical model assembly showing: (a) The inner tube alone with the recess and (b) The inner tube after the addition of the outer tube.

This LEU foil generates heat when irradiated and coolant flows through the inner tube and along the outer tube. The annular target is usually placed in a target holder and inserted into one of the vertical experimental facilities to be irradiated. The neutron flux in each of these vertical experimental facilities will vary depending upon the reactor configuration. The physical configuration of the annular target in a reactor [57] with coolant flow is illustrated in Figure 17.

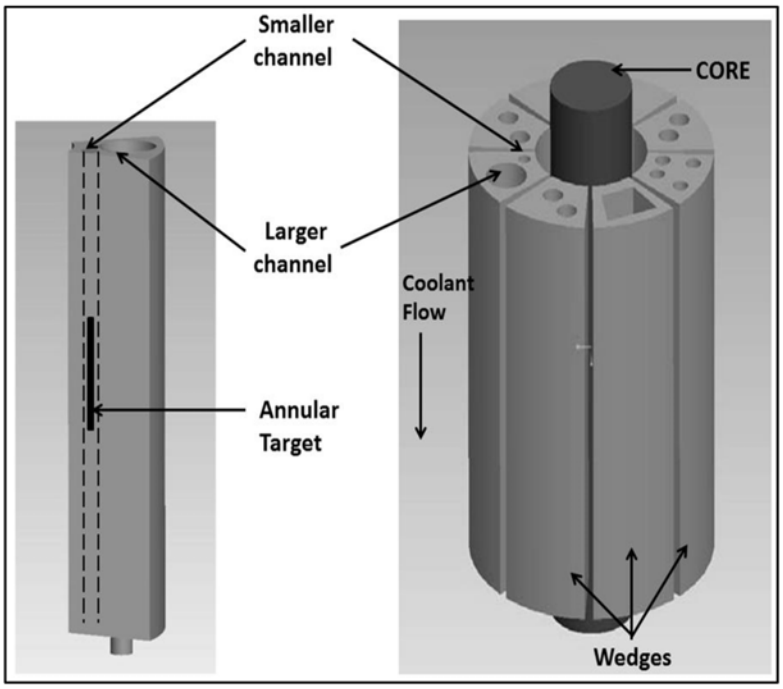

Figure 17. Pictorial representation of the position of the annular target in the vertical experimental facility relative to the reactor core.

The first step in modeling the annular target involves creating the individual parts in Abaqus FEA [56] namely the inner tube, foil and the outer tube using the dimensions given in Figure 18. The nickel recoil barrier was not included in the analysis model as its thickness (~15 µm) is lesser than the LEU foil itself (~125 µm). After this the material properties are created based on the data from Table 1 followed by assigning these material properties to the created parts using sections and sectional assignments.

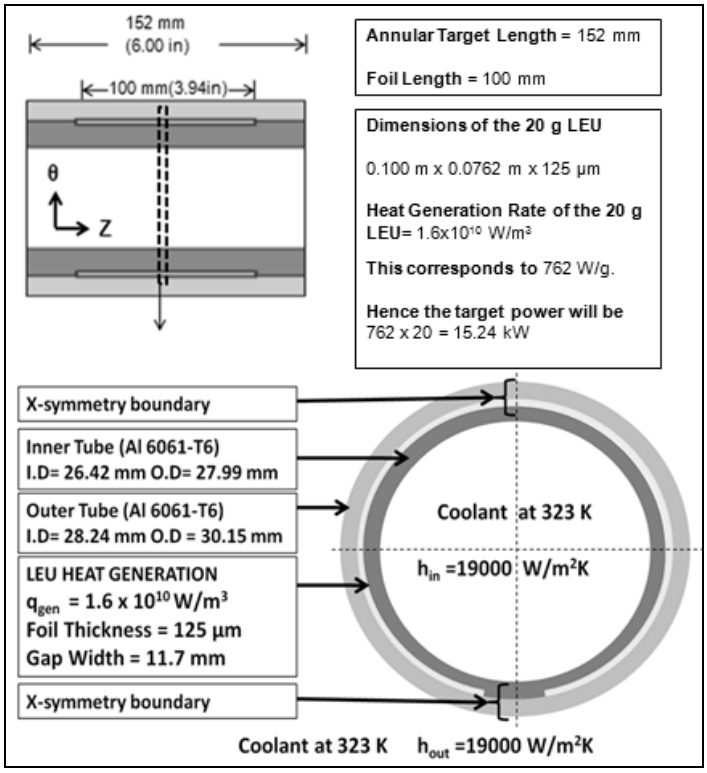

Figure 18. Numerical setup of the 2D plane strain model of the annular target modeled without the nickel recoil barrier.

Table 1. Material properties of the foil and the cladding used in the analysis.

Material Property	Aluminum 6061-T6	Uranium
Density (Kg/m^3)	2700	19100
Elastic Modulus (GPa)	68.9	208
Poisson's Ratio	0.33	0.23
Thermal Conductivity (W/mK)	167	27.5
Thermal Expansion Coefficient (K^{-1})	2.34 x 10^{-5}	1.39 x 10^{-5}

The assembly module in Abaqus FEA [56] provides various options, constraints under which the model can be assembled. The easiest assembly procedure is the 'translation' option which can be found under the 'Instance' toolbar. It requires the user to select the movable instance, input the start point for translation, which is usually on the movable

part and the end point for the translation, which is on the immovable part. The annular target assembly procedure is pictorially presented in Figure 19.

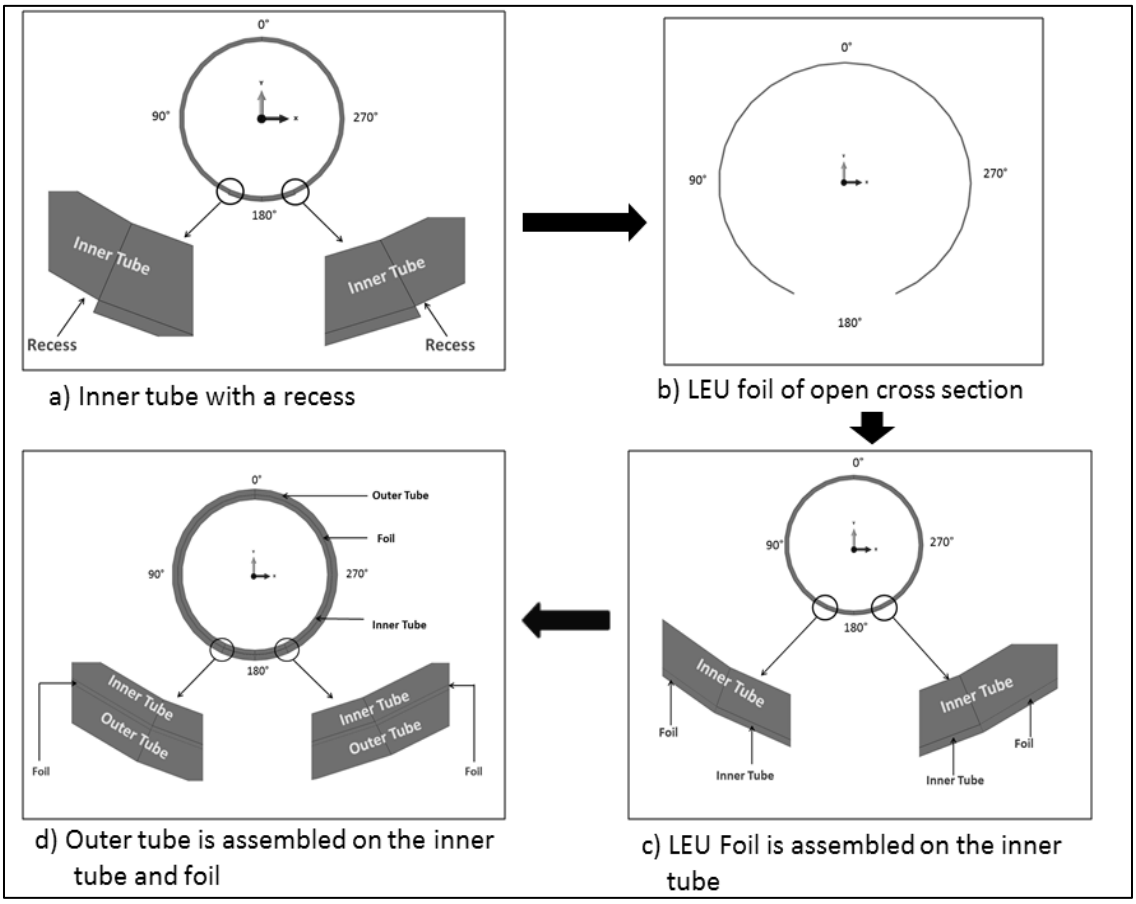

Figure 19. Pictorial representation of the annular target assembly procedure in Abaqus FEA.

The first step is to select the inner tube 'instance'. After this, the LEU foil is assembled on the recess cut in the inner tube. The final step is to assemble the outer tube over the inner tube and the foil. Once the model has been assembled, it is always good to check if the parts are located in the position they are supposed to be in. Abaqus FEA [56] carries out the simulation based on analysis steps. Hence it is required to create the appropriate analysis step(s) based on the type of analysis to be carried out (e.g. heat transfer, static, dynamic, fully coupled thermal stress).

To numerically evaluate the assembly in Abaqus FEA [56], the contact conditions have to be enforced through the interaction properties. The thermal and mechanical interactions properties are specified in this fully coupled thermal stress analysis. The mechanical contact conditions allow the user to specify the normal behavior and tangential behavior of the surfaces that come into contact. A 'frictionless' tangential behavior is chosen while the normal behavior is based on a 'hard contact' formulation where the constraints are enforced by the Lagrange multiplier method. The option of surface separation after contact is selected as this closely represents the behavior in the target during irradiation. The thermal contact conditions require the specification of the thermal conductance, thermal radiation or heat generation due to frictional effects. For this analysis the thermal conductance option is selected and a high value of thermal conductance (10^9 W/m^{2}K) is specified for perfect contact (zero gap).

The thermal stress analysis can be performed in Abaqus FEA [56] in a couple of ways – a fully coupled thermal stress analysis and a sequentially coupled thermal stress analysis. In a fully coupled thermal stress analysis the thermal and the mechanical parts are solved simultaneously. This procedure can be used when the user expects the thermal behavior to affect the mechanical behavior and vice versa. On the other hand a sequentially coupled thermal stress analysis is used when the thermal part influences the mechanical solution and there is no reverse dependence. To execute a sequentially coupled thermal stress analysis, the thermal part is solved first and its values are fed into the stress model after replacing the 'heat transfer' step with a 'static-general' step and using the corresponding meshing elements.

The specification of mechanical boundary conditions plays an important role in the behavior of the model. Since the LEU foil based annular target under consideration is symmetric about the x-axis, an x-symmetric boundary condition is applied to the nodes as illustrated in Figure 20. The x-symmetric boundary condition restricts the translation in the horizontal direction and does not allow any tangential rotation as well. Hence by making use of the geometry of the model, the boundary conditions are enforced without significantly affect the setup.

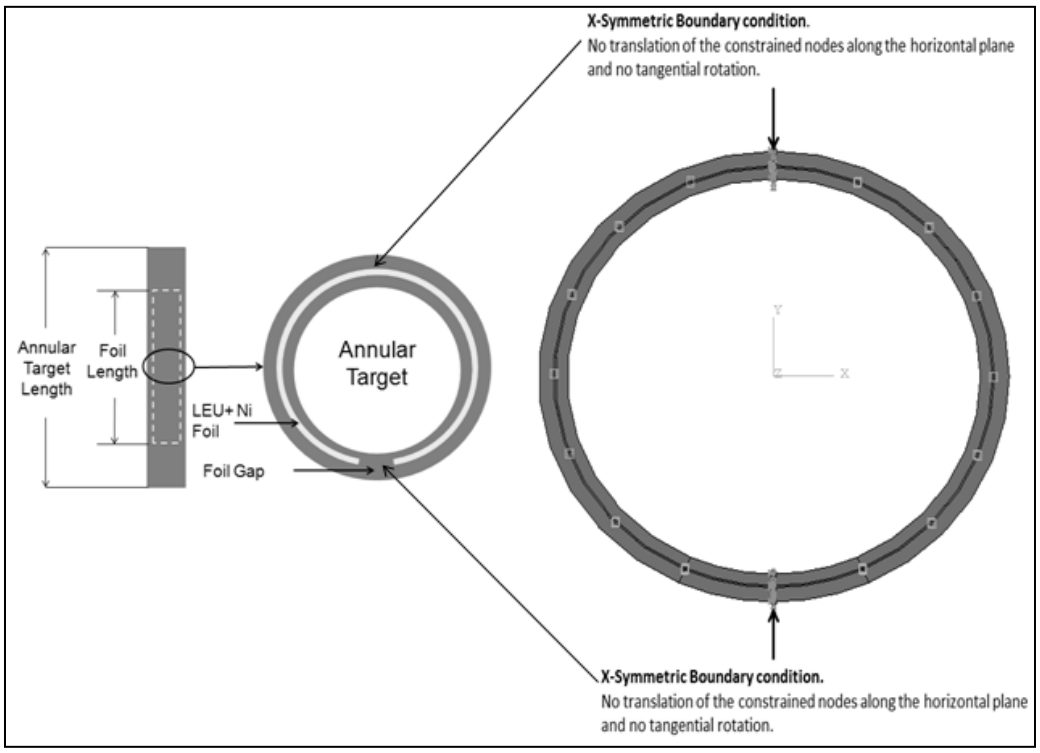

Figure 20. Mechanical boundary condition applied to the annular target assembly.

From a thermal standpoint, it is required to specify the heat transfer coefficient at the inner and the outer regions to effectively dissipate the heat generated by the LEU foil. To simulate water cooling in the reactor, a heat transfer coefficient of 19000 $W/m^2 K$ was used on the inner and outer regions. Subsequently parametric studies were performed by

varying the heat transfer coefficient ratios, the tube thickness ratios and the heat generation rate of the LEU foil. These studies will be presented in subsequent sections. This would provide an insight into the behavior of the target under various conditions and could possibly serve as a useful reference tool for future analysis. Figure 21 illustrates the coolant flow through the inner tube and along the outer tube-channel wall gap.

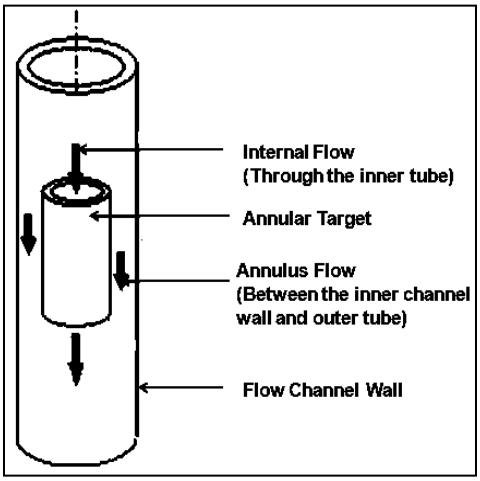

Figure 21. Pictorial representation of the coolant flow internally and through the annulus.

The inner diameter of the inner tube and the outer diameter of the outer tube can be obtained from Figure 18 as 26.42 mm and 30.15 mm respectively. The diameter of the flow channel wall was taken to be 50 mm with a target length of 152 mm. The water coolant properties were calculated at 323 K and were found to be: density (ρ) = 986.870 Kg/m^3, dynamic viscosity (μ) = 488.920 x 10^{-6} Kg/m-s, thermal conductivity (k) = 0.651 W/mK and specific heat (C_p) = 4170.3 J/Kg K. The formula to determine the Reynolds number for flow through a circular tube, in terms of the density (ρ), flow velocity (V), diameter (D) of the tube and dynamic viscosity (μ) of the fluid is given by

$$Re = \frac{\rho V D}{\mu} \qquad (5)$$

In Eq. (5), since the velocity is unknown at this point, the Reynolds number and hence the type of flow (laminar or turbulent) cannot be determined at the moment. However, it is assumed that the flow is turbulent and this assumption will be verified once the velocity has been determined. The following Nusselt number correlation [58] in Eq. (6) with C=1 and m=2/3 was used to determine the flow velocity through the inner tube and along the outer tube.

$$\frac{Nu_D}{Nu_{D,fD}} = 1 + \frac{C}{\left(\frac{L}{D}\right)^m} \qquad (6)$$

$$\text{where, } Nu_D = \frac{hD}{k}$$

In Eq.(6), 'Nu_D' is the Nusselt number averaged over the path length (includes entrance effects), '$Nu_{D,fD}$' is the fully developed Nusselt number, 'L' is the flow path length, and 'D' is the hydraulic diameter of flow area. The fully developed Nusselt number ($Nu_{D,fD}$), as a function of the Reynold's number (Re) and Prandtl number (Pr) can be determined using the Dittus-Boelter correlation[59] given below by Eq. (7).

$$Nu_{D,fD} = 0.023(Re)^{0.8}(Pr)^{0.4} \qquad (7)$$

$$\text{where, } Pr = \frac{\mu C_p}{k}$$

Solving Eq.(6), the flow velocities through the inner tube and along the outer tube were found to be 3.48 m/s and 3.62 m/s respectively. This value falls in the predicted range of flow velocity (3.4 ± 0.8 m/s) at MURR based on a completed experimental study [60]. Back calculating the Reynolds number based on these velocities, for flow through the inner tube Re = 176776 and for flow through the annulus Re = 271605 confirming the

assumption of turbulent flow conditions. The loading source for this problem is the heat generation of the foil to simulate the fission heat generated during irradiation. This value can be specified by selecting the 'body heat flux' option under the 'Load' module.

In any finite element analysis, the choice of the elements that make up the mesh plays a significant role in the solution convergence process. Abaqus FEA [56] has a particular set of elements for its different analysis steps and care should be taken to select the appropriate element. The nature of the element chosen (i.e. linear, quadratic or tetrahedral) entirely depends on the analysis type, geometry of the parts that make up the assembly. Generally for problems involving contact it is recommended to use a fine mesh of linear elements. However, a huge number of linear elements are required to closely model curved surfaces. Hence in this analysis the quadratic reduced integration elements of type CPE8RT were used. The use of these quadratic elements also helps to model the edges on curved surfaces accurately. A lot can be written about the choice of element types in Abaqus FEA [56], but have only been briefly mentioned in this section as it covers the broader picture of the model and analysis setup. Table 2 provides the mesh configuration used in the numerical analysis.

Table 2. Mesh configuration for the non-uniform heating numerical model without residual stresses.

Part	Element Type	Nodes	Elements	Thickness Elements
Inner Tube	Quadratic reduced integration (CPE8RT)	12800	4000	10
Foil	Quadratic reduced integration (CPE8RT)	12800	4000	10
Outer Tube	Quadratic reduced integration (CPE8RT)	12800	4000	10

Due to the open cross of the foil (Figure 18) only a portion of the inner and outer cladding is uniformly heated and the region where the inner and the outer cladding make contact will not receive as much heat as compared to the uniformly heated regions. Hence, it is expected that a cold spot will be formed in this region due to the existence of comparatively lower temperature gradients. In essence, the LEU foil based annular target modeled with an open cross section foil and a recess on the inner tube is a case of non-uniform heating. The finite element mesh used in the numerical model is presented in Figure 22. A 'matched' mesh, with equal number of elements and nodes along the edges and thickness of all the parts, was used to facilitate convergence and easier extraction of radial data across the annular target assembly

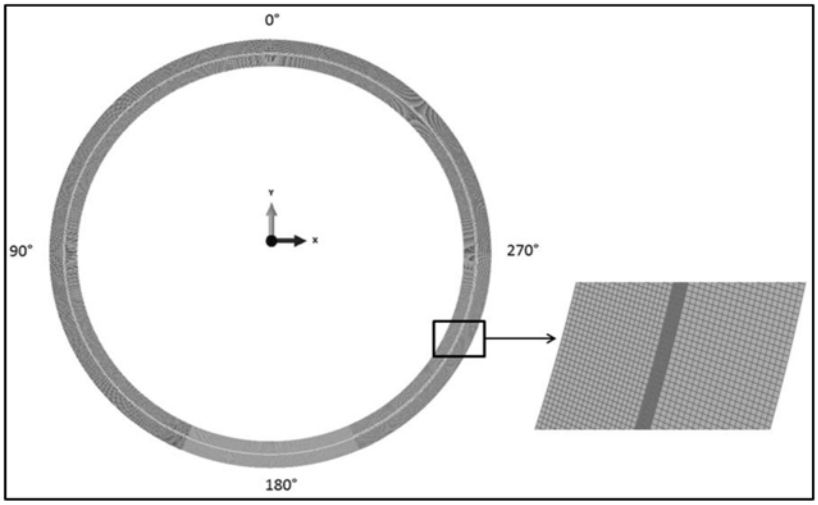

Figure 22. Finite element mesh used to simulate the non-uniform heating model.

4.2 Uniform Heating Numerical Model

The presence of a recess on the inner tube, open cross section of the foil and the non-uniform heating as a result will require a complex analytical model to validate the non-uniform heating numerical model. If the foil is modeled with no circumferential gap, then

this essentially represents a uniform heating case (as long a uniform heat generation thermal loading condition is used). Analytical models can be developed to validate this configuration as illustrated in Figure 23. Once the uniform heating model has been validated, it can be used to validate the non-uniform heating model by comparing the relative order of magnitudes in the uniformly heated portion of the non-uniform heating model (i.e. in the uniformly heated portion of the annular target with a recess). In addition to the x-symmetric boundary condition, a y-symmetric boundary condition can be applied to the nodes as shown in Figure 24.

The use of such an approach might over or under-predict the stresses and temperatures. A similar mesh is used on the uniform and non-uniform heating models to facilitate easier comparison of results at the nodal locations. Except for the foil being modeled as a full circular cylinder and the non-existence of a recess on the inner tube, the model is setup for analysis in a similar way as explained in the previous section for non-uniform heating.

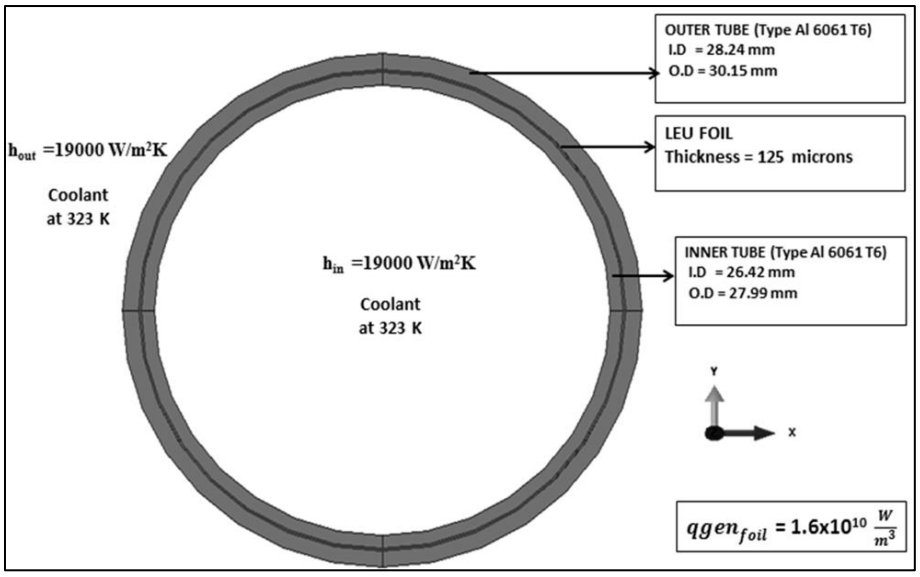

Figure 23. Setup of the uniform heating 2D plane strain model of the annular target.

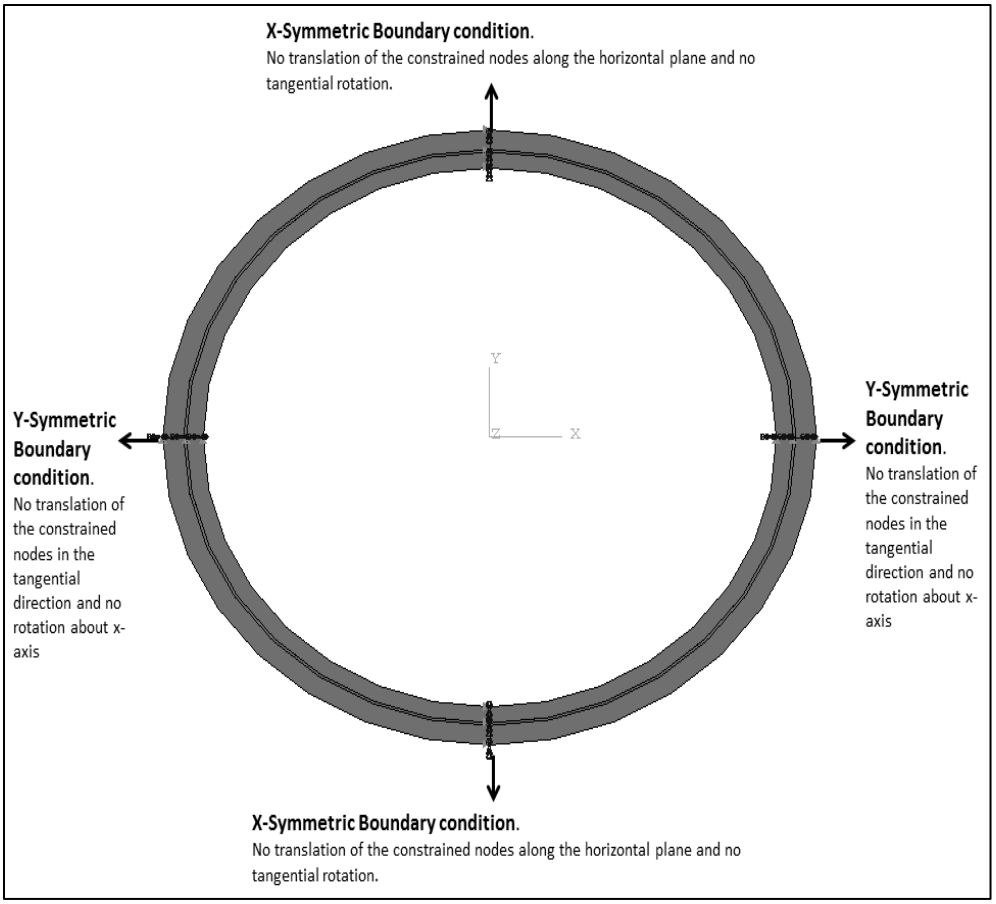

Figure 24. Mechanical boundary conditions used in the uniform heating model.

4.3 Uniform Heating Analytical Model- Dimensional Form

The heat generated by the LEU foil will conduct through the thickness of the inner cladding and outer cladding as illustrated by the thermal resistance network in Figure 25. From Figure 25, the effective series resistance in the radially outward direction ($R'_{eff,\ OT}$) is given by Eq.(8), while the effective series resistance for radially inward heat flow ($R'_{eff,\ IT}$) is given by Eq.(9). The resulting parallel resistance network formed by $R'_{eff,\ OT}$ and $R'_{eff,\ IT}$ can be used to obtain the effective parallel resistance given by Eq.(10).

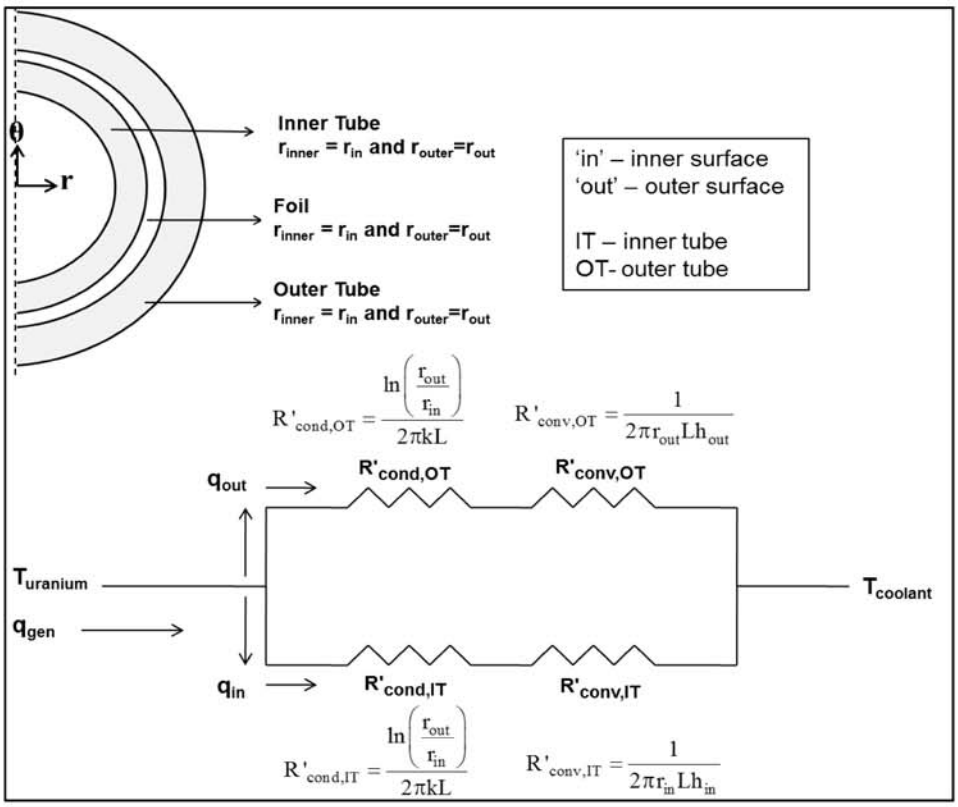

Figure 25. Symbolic dimensions and thermal resistance network of the uniform heating annular target case.

$$R'_{eff,OT} = R'_{cond,OT} + R'_{conv,OT} \tag{8}$$

$$R'_{eff,IT} = R'_{cond,IT} + R'_{conv,IT} \tag{9}$$

$$R'_{eff} = \left(\frac{1}{R'_{eff,OT}} + \frac{1}{R'_{eff,IT}} \right)^{-1} \tag{10}$$

The effective resistance in Eq. (10) can also be expressed as a function of the maximum target temperature (uranium temperature), coolant temperature and the heat transfer rate (q) as given by Eq. (11). Using this equation along with Eq. (10), the uranium temperature can be determined.

$$R'_{eff} = \frac{T_{uranium} - T_{coolant}}{q} \tag{11}$$

The approach in this analytical model is to obtain a single, generalized, temperature distribution solution for a heat generating cylinder with inner radius 'r_{in}' and outer radius 'r_{out}', and use this solution to predict the temperature distribution in the inner tube, foil and the outer tube. It is also assumed in the derivation that the boundary temperatures at the inner and outer surfaces (T_{in} and T_{out} respectively) are known. The equation for one dimensional steady state heat conduction in a cylinder with heat generation (q_{gen}) and temperature independent thermal conductivity (k) is given by

$$\frac{1}{r}\frac{d}{dr}\left(r\frac{dT}{dr}\right) + \frac{q_{gen}}{k} = 0 \tag{12}$$

Integrating Eq. (12) twice with respect to 'r', gives the general solution in terms of the constants 'c_1' and 'c_2' as presented by Eq. (13)

$$T(r) = -\frac{q_{gen}}{4k}r^2 + c_1 \ln(r) + c_2 \tag{13}$$

With the help of the two boundary conditions: at r =r_{in} , T=T_{in} and at r=r_{out}, T=T_{out} , the constants 'c_1' and 'c_2' were determined as

$$\left.\begin{aligned} c_1 &= \frac{q_{gen}\left(r_{in}^2 - r_{out}^2\right) + 4k\left(T_{in} - T_{out}\right)}{k\ln\left(\frac{r_{in}^4}{r_{out}^4}\right)} \\ c_2 &= \frac{q_{gen}\left[r_{out}^2\ln\left(r_{in}\right) - r_{in}^2\ln\left(r_{out}\right)\right]}{4k\ln\left(\frac{r_{in}}{r_{out}}\right)} + \frac{\left[T_{out}\ln\left(r_{in}\right) - T_{in}\ln\left(r_{out}\right)\right]}{\ln\left(\frac{r_{in}}{r_{out}}\right)} \end{aligned}\right] \tag{14}$$

Substituting the constants from Eq. (14) in Eq.(13), the radial temperature distribution in a heat generating cylinder is given by Eq. (15) as

$$T(r) = T_{in} + (T_{in} - T_{out})\frac{\ln\left(\frac{r}{r_{in}}\right)}{\ln\left(\frac{r_{in}}{r_{out}}\right)} + \frac{q_{gen}\left(r_{in}^2 - r_{out}^2\right)}{4k}\left[\frac{\ln\left(\frac{r}{r_{in}}\right)}{\ln\left(\frac{r_{in}}{r_{out}}\right)} - \frac{\left(r^2 - r_{in}^2\right)}{\left(r_{in}^2 - r_{out}^2\right)}\right] \qquad (15)$$

Equation (15) also represents the temperature distribution across the heat generating foil and this expression can be used to determine the temperature distribution through the inner and the outer tubes by setting the heat generation rate to zero (q_{gen}=0).

In the event of perfect interfacial contact between the foil and the inner tube, the interface temperature would have to be determined before trying to obtain the temperature distribution across the inner tube- foil composite. The temperature compatibility conditions at the interface are given by Eq.(16)

$$\begin{aligned} T_{out,IT} &= T_{in,F} \\ &\text{and} \\ \left[k_{IT}\frac{dT(r)_{IT}}{dr}\right]_{interface} &= \left[k_F\frac{dT(r)_F}{dr}\right]_{interface} \end{aligned} \qquad (16)$$

Equation (15) can be directly used for the foil temperature distribution ($T(r)_F$) in Eq. (16) , while q_{gen} is set to zero in Eq. (15) for the inner tube temperature distribution ($T(r)_{IT}$) in Eq. (16). Hence by using Eqs.(15) and (16), the expression for the interface temperature distribution ($T_{interface}$) is given by Eq.(17) as

$$T_{interface} = T_{in,IT} - \frac{\left(T_{in,IT} - T_{out,F}\right)}{\left(1 + \frac{k_{IT} r_F \ln\left(\frac{r_{in,F}}{r_{out,F}}\right)}{k_F r_{IT} \ln\left(\frac{r_{in,IT}}{r_{out,IT}}\right)}\right)} - \frac{q_{gen}\left(r_{in,F}^2 - r_{out,F}^2\right)}{4k_F}\left[\frac{1 - \frac{2r_F^2 \ln\left(\frac{r_{in,F}}{r_{out,F}}\right)}{\left(r_{in,F}^2 - r_{out,F}^2\right)}}{1 + \frac{k_{IT} r_F \ln\left(\frac{r_{in,F}}{r_{out,F}}\right)}{k_F r_{IT} \ln\left(\frac{r_{in,IT}}{r_{out,IT}}\right)}}\right] \quad (17)$$

With the knowledge of the temperature distribution given by Eq. (15), the stresses and displacements in the cladding (inner tube and outer tube) and the foil can be easily obtained. The approach to determine the stresses and displacement is illustrated in Figure 26. Since the interface pressure will be finite when there is perfect contact at the foil and inner tube interface, the radial stress on the outer surface of the inner tube will be equal to the radial stress on the inner surface of the foil. Moreover, as the inner surface of the inner tube and outer surface of the foil are not under the influence of any external load, the radial stress at these surfaces will be zero as illustrated in Figure 26. For one dimensional problems in which the strain and displacement are functions of the radial coordinate alone, the stress equilibrium equation is given by Eq.(18). The radial strain (ε_r) and the hoop strain (ε_θ) can be expressed in terms of the displacement (u) as given by Eq. (19)

$$\frac{\partial \sigma_r}{\partial r} + \frac{\sigma_r - \sigma_\theta}{r} = 0 \quad (18)$$

$$\left.\begin{aligned} \varepsilon_r &= \frac{du}{dr} \\ \varepsilon_\theta &= \frac{u}{r} \end{aligned}\right] \quad (19)$$

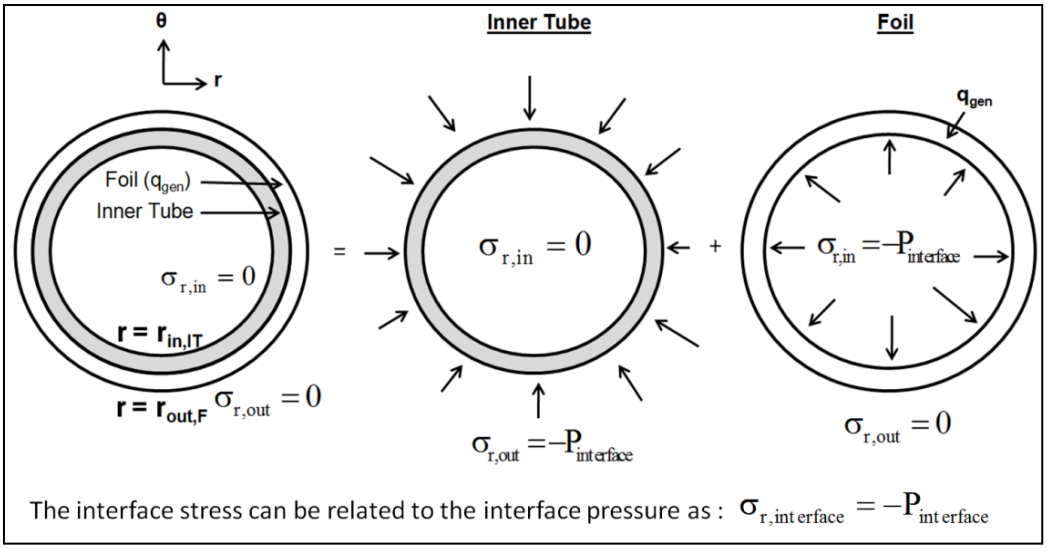

Figure 26. Representation of the simplified solution approach for stresses and displacement.

The stress-strain (radial and hoop) relationship for a plane strain case, using Hooke's law, with zero axial strain is given by Eq(20). In this equation 'E' is the elastic modulus, 'ν' is the Poisson's ratio and 'α' is the thermal expansion coefficient of the material.

$$\left.\begin{aligned}\varepsilon_r &= \frac{1-\nu^2}{E}\left(\sigma_r - \frac{\nu}{1-\nu}\sigma_\theta\right) + (1+\nu)\alpha T(r)\\ \varepsilon_\theta &= \frac{1-\nu^2}{E}\left(\sigma_\theta - \frac{\nu}{1-\nu}\sigma_r\right) + (1+\nu)\alpha T(r)\end{aligned}\right] \tag{20}$$

Using Eqs (19) and (20), the radial stress (σ_r) and the hoop stress (σ_θ) as a function of the displacement can be obtained as provided by Eq (21).

$$\left.\begin{aligned}\sigma_r &= \frac{E}{(1+\nu)(1-2\nu)}\left[(1-\nu)\frac{du}{dr} + \frac{\nu u}{r} - \alpha(1+\nu)T(r)\right]\\ \sigma_\theta &= \frac{E}{(1+\nu)(1-2\nu)}\left[\nu\frac{du}{dr} + (1-\nu)\frac{u}{r} - \alpha(1+\nu)T(r)\right]\end{aligned}\right] \tag{21}$$

Using Eqs.(21) and (18), the displacement formulation of the governing equation is given by Eq. (22), which can be integrated twice to obtain the general solution for displacement, in terms of the constants 'c_3' and 'c_4', given by Eq.(23)

$$\frac{d}{dr}\left(\frac{1}{r}\frac{d(r\,u)}{dr}\right)-\alpha\left(\frac{1+\nu}{1-\nu}\right)\frac{dT(r)}{dr}=0 \tag{22}$$

$$u=\left(\frac{1+\nu}{1-\nu}\right)\left(\frac{\alpha}{r}\right)\int_{r} r\,T(r)\,dr+c_3 r+\frac{c_4}{r} \tag{23}$$

Substituting Eq. (23) in Eq. (21), the general solution for the radial stress and the hoop stress in terms of the integration constants 'c_3' and 'c_4' can be obtained as presented by Eqs. (24) and (25) respectively.

$$\sigma_r=-\frac{\alpha E}{(1-\nu)r^2}\int_{r_{in}}^{r} r\,T(r)\,dr+\frac{c_3 E}{(1+\nu)(1-2\nu)}-\frac{c_4 E}{(1+\nu)r^2} \tag{24}$$

$$\sigma_\theta=-\frac{\alpha E}{(1-\nu)r^2}\left[\int_{r_{in}}^{r} r\,T(r)\,dr-r^2\,T(r)\right]+\frac{c_3 E}{(1+\nu)(1-2\nu)}+\frac{c_4 E}{(1+\nu)r^2} \tag{25}$$

Applying Eq. (24) to the inner tube configuration in Figure 26 with the boundary conditions $\sigma_{r,in}=0$ and $\sigma_{r,out}=\sigma_{r,interface}$,the constants 'c_3' and 'c_4' for the inner tube can be obtained as given by Eqs. (26) and (27) respectively. In these equations the subscript 'IT' refers to the inner tube as mentioned before. The constants 'c_3' and 'c_4' for the foil configuration in Figure 26 , obtained by using Eq. (24), are given by Eqs. (28) and (29) respectively. Using each of the Eqs. (15), (26) and (27), after setting $q_{gen}=0$, in Eqs. (23), (24) and (25), the expressions for radial stress (Eq. (30)), hoop stress(Eq. (31)) and

displacement (Eq. (32)) in the inner tube can be obtained as a function of the interface stress ($\sigma_{r,interface}$).

$$c_{3,IT} = \left[-\frac{r_{out}^2 \sigma_{r,interface}(1+\nu)(1-2\nu)}{E\left(r_{in}^2 - r_{out}^2\right)} - \frac{\alpha(1+\nu)(1-2\nu)\int_{r_{in}}^{r_{out}} r\,T(r)\,dr}{\left(r_{in}^2 - r_{out}^2\right)(1-\nu)} \right]_{IT} \tag{26}$$

$$c_{4,IT} = \left[-\frac{r_{in}^2 r_{out}^2 \sigma_{r,interface}(1+\nu)}{E\left(r_{in}^2 - r_{out}^2\right)} - \frac{\alpha r_{in}^2(1+\nu)\int_{r_{in}}^{r_{out}} r\,T(r)\,dr}{\left(r_{in}^2 - r_{out}^2\right)(1-\nu)} \right]_{IT} \tag{27}$$

$$c_{3,F} = \left[\frac{r_{in}^2 \sigma_{r,interface}(1+\nu)(1-2\nu)}{E\left(r_{in}^2 - r_{rout}^2 - \nu^2 r_{in}^2\right)} - \frac{\alpha(1+\nu)(1-2\nu)\int_{r_{in}}^{r_{out}} r\,T(r)\,dr}{(1-\nu)\left(r_{in}^2 - r_{rout}^2 - \nu^2 r_{in}^2\right)} \right]_{F} \tag{28}$$

$$c_{4,F} = \left[\frac{r_{in}^2\, r_{rout}^2\, \sigma_{r,interface}(1+\nu)}{E\left(r_{in}^2 - r_{rout}^2 - \nu^2 r_{in}^2\right)} - \frac{\alpha r_{in}^2(1+\nu)^2\int_{r_{in}}^{r_{out}} r\,T(r)\,dr}{\left(r_{in}^2 - r_{rout}^2 - \nu^2 r_{in}^2\right)} \right]_{F} \tag{29}$$

$$\sigma_{r,IT} = \left[\frac{E\alpha\left(T_{in} - T_{out}\right)}{(1-\nu)} \left(\frac{\dfrac{r^2 - r_{in}^2}{r_{out}^2} \dfrac{\sigma_{r,interface}(1-\nu)}{E\alpha\left(T_{in} - T_{out}\right)}}{\dfrac{r^2}{r_{out}^2}\left(1 - \dfrac{r_{in}^2}{r_{out}^2}\right)} + \frac{\dfrac{r_{in}^2}{r_{out}^2}\left(1 - \dfrac{r^2}{r_{out}^2}\right)}{2\dfrac{r^2}{r_{out}^2}\left(1 - \dfrac{r_{in}^2}{r_{out}^2}\right)} - \frac{\ln\left(\dfrac{r}{r_{out}}\right)}{2\ln\left(\dfrac{r_{in}}{r_{out}}\right)} \right) \right]_{IT} \tag{30}$$

$$\sigma_{\theta,IT} = \left[\frac{E\alpha\left(T_{in} - T_{out}\right)}{(1-\nu)} \left(\frac{\dfrac{r^2 + r_{in}^2}{r_{out}^2} \dfrac{\sigma_{r,interface}(1-\nu)}{E\alpha\left(T_{in} - T_{out}\right)}}{\dfrac{r^2}{r_{out}^2}\left(1 - \dfrac{r_{in}^2}{r_{out}^2}\right)} - \frac{\dfrac{r_{in}^2}{r_{out}^2}\left(1 + \dfrac{r^2}{r_{out}^2}\right)}{2\dfrac{r^2}{r_{out}^2}\left(1 - \dfrac{r_{in}^2}{r_{out}^2}\right)} - \frac{1 + \ln\left(\dfrac{r}{r_{out}}\right)}{2\ln\left(\dfrac{r_{in}}{r_{out}}\right)} \right) \right]_{IT} \tag{31}$$

$$u_{IT} = \left[\frac{\alpha\left(T_{in} - T_{out}\right) r \left(1+\nu\right)}{16} \left(\frac{16\, T_{out}}{T_{in} - T_{out}} - \frac{8\left(1-\nu-\ln\left(\frac{r}{r_{out}}\right)\right)}{\left(1-\nu\right)\ln\left(\frac{r_{in}}{r_{out}}\right)} + \frac{16\,\frac{\sigma_{r,interface}}{E\,\alpha\left(T_{in}-T_{out}\right)}}{\frac{r^2}{r_{out}^2}\left(1-\frac{r_{in}^2}{r_{out}^2}\right)}\left(\frac{r^2}{r_{out}^2}\left(1-2\nu\right)+\frac{r_{in}^2}{r_{out}^2}\right) - \frac{8\frac{r_{in}^2}{r_{out}^2}\left(1+\frac{r^2}{r_{out}^2}\left(1-2\nu\right)\right)}{\frac{r^2}{r_{out}^2}\left(1-\frac{r_{in}^2}{r_{out}^2}\right)\left(1-\nu\right)} \right) \right]_{IT} \tag{32}$$

Using each of Eqs.(15), (28) and (29), in Eqs. (23),(24) and (25), the expressions for radial stress (Eq.(33)), hoop stress (Eq. (34)) and displacement (Eq.(35)) in the foil can be obtained as a function of the interface stress ($\sigma_{r,interface}$).

$$\sigma_{r,F} = \left[\frac{E\,\alpha\left(T_{in}-T_{out}\right)}{\left(1-\nu\right)} \left(\frac{\frac{r_{in}^2}{r_{out}^2}\left(1-\frac{r^2}{r_{out}^2}\right)\frac{\sigma_{r,interface}\left(1-\nu\right)}{E\,\alpha\left(T_{in}-T_{out}\right)}}{\frac{r^2}{r_{out}^2}\left(1-\frac{r_{in}^2}{r_{out}^2}\right)} + \frac{\frac{r_{in}^2}{r_{out}^2}\left(1-\frac{r^2}{r_{out}^2}\right)}{2\frac{r^2}{r_{out}^2}\left(1-\frac{r_{in}^2}{r_{out}^2}\right)} - \frac{\ln\left(\frac{r}{r_{out}}\right)}{2\ln\left(\frac{r_{in}}{r_{out}}\right)} + \frac{q_{gen}\left(r_{in}^2-r_{out}^2\right)}{16\,k\left(T_{in}-T_{out}\right)} \left(\frac{\left(1-\frac{r^2}{r_{out}^2}\right)\left(\frac{r_{in}^2}{r_{out}^2}+\frac{r^2}{r_{out}^2}\right)}{\frac{r^2}{r_{out}^2}\left(1-\frac{r_{in}^2}{r_{out}^2}\right)} - \frac{2\ln\left(\frac{r}{r_{out}}\right)}{\ln\left(\frac{r_{in}}{r_{out}}\right)} \right) \right)_{F} \right] \tag{33}$$

Equations (30) and (33) can be combined to provide a general solution for the radial stress distribution as presented by Eq.(36). Similarly, Eqs (31) and (34) can be combined to obtain a general hoop stress distribution solution as given by Eq.(37). A general solution for the displacement (Eq. (38)) can also be obtained by combining Eqs. (32) and (35).

$$\sigma_{\theta,F}=\left[\frac{E\,\alpha\left(T_{in}-T_{out}\right)}{\left(1-\nu\right)}\left(\begin{array}{l}-\dfrac{\dfrac{r_{in}^2}{r_{out}^2}\left(1+\dfrac{r^2}{r_{out}^2}\right)\dfrac{\sigma_{r,interface}\left(1-\nu\right)}{E\,\alpha\left(T_{in}-T_{out}\right)}}{\dfrac{r^2}{r_{out}^2}\left(1-\dfrac{r_{in}^2}{r_{out}^2}\right)}-\dfrac{\dfrac{r_{in}^2}{r_{out}^2}\left(1+\dfrac{r^2}{r_{out}^2}\right)}{2\dfrac{r^2}{r_{out}^2}\left(1-\dfrac{r_{in}^2}{r_{out}^2}\right)}-\dfrac{1+\ln\left(\dfrac{r}{r_{out}}\right)}{2\ln\left(\dfrac{r_{in}}{r_{out}}\right)}\\[2ex]-\dfrac{q_{gen}\left(r_{in}^2-r_{out}^2\right)}{16\,k\left(T_{in}-T_{out}\right)}\left(\dfrac{\dfrac{3r^4}{r_{out}^4}+\dfrac{r_{in}^2}{r_{out}^2}-\dfrac{r^2}{r_{out}^2}\left(1-\dfrac{r_{in}^2}{r_{out}^2}\right)}{\dfrac{r^2}{r_{out}^2}\left(1-\dfrac{r_{in}^2}{r_{out}^2}\right)}+\dfrac{2\left(1+\ln\left(\dfrac{r}{r_{out}}\right)\right)}{\ln\left(\dfrac{r_{in}}{r_{out}}\right)}\right)\end{array}\right)\right]_F \tag{34}$$

$$u_F=\left[\frac{\alpha\left(T_{in}-T_{out}\right)r\left(1+\nu\right)}{16}\left(\begin{array}{l}\dfrac{16\,T_{out}}{T_{in}-T_{out}}-\dfrac{8\left(1-\nu-\ln\left(\dfrac{r}{r_{out}}\right)\right)}{\left(1-\nu\right)\ln\left(\dfrac{r_{in}}{r_{out}}\right)}-\dfrac{8\,r_{in}^2\left(1+\dfrac{r^2}{r_{out}^2}\left(1-2\nu\right)\right)}{r^2\left(1-\dfrac{r_{in}^2}{r_{out}^2}\right)\left(1-\nu\right)}\\[2ex]-\dfrac{16\,r_{in}^2\left(1+\dfrac{r^2}{r_{out}^2}\left(1-2\nu\right)\right)\dfrac{\sigma_{r,interface}}{E\,\alpha\left(T_{in}-T_{out}\right)}}{r^2\left(1-\dfrac{r_{in}^2}{r_{out}^2}\right)}\\[2ex]-\dfrac{q_{gen}\left(r_{in}^2-r_{out}^2\right)}{k\left(T_{in}-T_{out}\right)}\left(\begin{array}{l}\dfrac{2\left(1-\nu-\ln\left(\dfrac{r}{r_{in}}\right)\right)}{\left(1-\nu\right)\ln\left(\dfrac{r_{in}}{r_{out}}\right)}\\[2ex]-\dfrac{\dfrac{r^4}{r_{out}^4}-\dfrac{r_{in}^2}{r_{out}^2}-\dfrac{r^2}{r_{out}^2}\left(3+\dfrac{r_{in}^2}{r_{out}^2}\left(1-2\nu\right)-2\nu\right)}{\dfrac{r^2}{r_{out}^2}\left(1-\dfrac{r_{in}^2}{r_{out}^2}\right)\left(1-\nu\right)}\end{array}\right)\end{array}\right)\right]_F \tag{35}$$

$$\sigma_{r,General} = \frac{E\,\alpha\left(T_{in}-T_{out}\right)}{\left(1-\nu\right)}\left[\left(\frac{\frac{r_{in}^2}{r_{out}^2}\left(1-\frac{r^2}{r_{out}^2}\right)\frac{\sigma_{r,interface}\left(1-\nu\right)}{E\,\alpha\left(T_{in}-T_{out}\right)}}{\frac{r^2}{r_{out}^2}\left(1-\frac{r_{in}^2}{r_{out}^2}\right)}\right)_F + \frac{\frac{r_{in}^2}{r_{out}^2}\left(1-\frac{r^2}{r_{out}^2}\right)}{2\frac{r^2}{r_{out}^2}\left(1-\frac{r_{in}^2}{r_{out}^2}\right)}\right.$$
$$+\left(\frac{\frac{r^2-r_{in}^2}{r_{out}^2}\frac{\sigma_{r,interface}\left(1-\nu\right)}{E\,\alpha\left(T_{in}-T_{out}\right)}}{\frac{r^2}{r_{out}^2}\left(1-\frac{r_{in}^2}{r_{out}^2}\right)}\right)_{IT} - \frac{\ln\left(\frac{r}{r_{out}}\right)}{2\ln\left(\frac{r_{in}}{r_{out}}\right)}$$
$$\left.+\frac{q_{gen}\left(r_{in}^2-r_{out}^2\right)}{16\,k\left(T_{in}-T_{out}\right)}\left(\frac{\left(1-\frac{r^2}{r_{out}^2}\right)\left(\frac{r_{in}^2}{r_{out}^2}+\frac{r^2}{r_{out}^2}\right)}{\frac{r^2}{r_{out}^2}\left(1-\frac{r_{in}^2}{r_{out}^2}\right)} - \frac{2\ln\left(\frac{r}{r_{out}}\right)}{\ln\left(\frac{r_{in}}{r_{out}}\right)}\right)\right] \tag{36}$$

$$\sigma_{\theta,General} = \frac{E\,\alpha\left(T_{in}-T_{out}\right)}{\left(1-\nu\right)}\left[-\left(\frac{\frac{r_{in}^2}{r_{out}^2}\left(1+\frac{r^2}{r_{out}^2}\right)\frac{\sigma_{r,interface}\left(1-\nu\right)}{E\,\alpha\left(T_{in}-T_{out}\right)}}{r^2\left(1-\frac{r_{in}^2}{r_{out}^2}\right)}\right)_F - \frac{\frac{r_{in}^2}{r_{out}^2}\left(1+\frac{r^2}{r_{out}^2}\right)}{2r^2\left(1-\frac{r_{in}^2}{r_{out}^2}\right)}\right.$$
$$+\left(\frac{\left(\frac{r^2+r_{in}^2}{r^2}\right)\frac{\sigma_{r,interface}\left(1-\nu\right)}{E\,\alpha\left(T_{in}-T_{out}\right)}}{\left(1-\frac{r_{in}^2}{r_{out}^2}\right)}\right)_{IT} - \frac{1+\ln\left(\frac{r}{r_{out}}\right)}{2\ln\left(\frac{r_{in}}{r_{out}}\right)}$$
$$\left.-\frac{q_{gen}\left(r_{in}^2-r_{out}^2\right)}{16\,k\left(T_{in}-T_{out}\right)}\left(\frac{\frac{3r^4}{r_{out}^4}+\frac{r_{in}^2}{r_{out}^2}-\frac{r^2}{r_{out}^2}\left(1-\frac{r_{in}^2}{r_{out}^2}\right)}{\frac{r^2}{r_{out}^2}\left(1-\frac{r_{in}^2}{r_{out}^2}\right)} + \frac{2\left(1+\ln\left(\frac{r}{r_{out}}\right)\right)}{\ln\left(\frac{r_{in}}{r_{out}}\right)}\right)\right] \tag{37}$$

$$u_{General} = \frac{\alpha (T_{in} - T_{out}) r (1+\nu)}{16} \left[- \left(\frac{16\, r_{in}^2 \left(1 + \frac{r^2}{r_{out}^2}(1-2\nu) \right) \frac{\sigma_{r,interface}}{E\,\alpha (T_{in} - T_{out})}}{r^2 \left(1 - \frac{r_{in}^2}{r_{out}^2} \right)} \right)_F + \frac{16\, T_{out}}{T_{in} - T_{out}} + \left(\frac{16 \frac{\sigma_{r,interface}}{E\,\alpha (T_{in} - T_{out})}}{\frac{r^2}{r_{out}^2} \left(1 - \frac{r_{in}^2}{r_{out}^2} \right)} \left(\frac{r^2}{r_{out}^2}(1-2\nu) + \frac{r_{in}^2}{r_{out}^2} \right) \right)_{IT} - \frac{8 \left(1 - \nu - \ln \left(\frac{r}{r_{out}} \right) \right)}{(1-\nu) \ln \left(\frac{r_{in}}{r_{out}} \right)} - \frac{8\, r_{in}^2 \left(1 + \frac{r^2}{r_{out}^2}(1-2\nu) \right)}{r^2 \left(1 - \frac{r_{in}^2}{r_{out}^2} \right)(1-\nu)} - \frac{q_{gen} \left(r_{in}^2 - r_{out}^2 \right)}{k (T_{in} - T_{out})} \left(\frac{2 \left(1 - \nu - \ln \left(\frac{r}{r_{in}} \right) \right)}{(1-\nu) \ln \left(\frac{r_{in}}{r_{out}} \right)} - \frac{\frac{r^4}{r_{out}^4} - \frac{r_{in}^2}{r_{out}^2} - \frac{r^2}{r_{out}^2} \left(3 + \frac{r_{in}^2}{r_{out}^2}(1-2\nu) - 2\nu \right)}{\frac{r^2}{r_{out}^2} \left(1 - \frac{r_{in}^2}{r_{out}^2} \right)(1-\nu)} \right) \right] \quad (38)$$

Equations (36), (37) and (38) can be used to determine the radial stress, hoop stress and displacement respectively, in the inner tube, foil and the outer tube. The following are applicable while using Eqs (36), (37) and (38).

$$\left.\begin{array}{l} \text{1) For the inner tube : Set the 1st term on the RHS and } q_{gen} \text{ to zero.} \\ \text{2) For the foil : Set the 3rd term on the RHS to zero.} \\ \text{3) For the outer tube: Set the 1st term and 3rd term on the RHS,} \\ \quad \text{along with } q_{gen}\text{, to zero.} \end{array}\right] \quad (39)$$

The interfacial stress ($\sigma_{r,interface}$) should be known to solve Eqs. (36), (37) and (38). This interfacial stress and hence the contact pressure ($\sigma_{r,\,interface} = -P_{interface}$) can be determined by applying the displacement compatibility requirement at the interface of the inner tube and the foil. This condition is given by Eq.(40). Applying Eq. (39) to Eq. (38), and substituting the respective expressions for inner tube displacement (u_{IT}) and foil

displacement (u_F) in Eq. (40), the interfacial stress can be obtained as given by Eq.(41). To present Eq. (41) in a concise form, suitable groupings have been used as provided by Eqs. (42) and (43).

$$\left(r_{out,IT}+u_{IT}\right)_{interface}=\left(r_{in,F}+u_{F}\right)_{interface} \tag{40}$$

$$\sigma_{r,interface}=\frac{E_F\alpha_F\left(T_{in,F}-T_{out,F}\right)}{M_2+M_3}\left[\begin{array}{l}\dfrac{M_3\left(M_4-1\right)}{2\left(1-\nu_F\right)}+\dfrac{\left(1-\nu_F-\ln\left(\dfrac{r_F}{r_{out,F}}\right)\right)}{2\left(1-\nu_F\right)\ln\left(\dfrac{r_{in,F}}{r_{out,F}}\right)}\left(M_5-1\right)\\ -\dfrac{T_{out,F}}{T_{in,F}-T_{out,F}}\left(M_1\dfrac{T_{out,IT}\left(T_{in,F}-T_{out,F}\right)}{T_{out,F}\left(T_{in,IT}-T_{out,IT}\right)}-1\right)\\ +\dfrac{q_{gen}\left(r_{in,F}^2-r_{out,F}^2\right)}{16\,k_F\left(T_{in,F}-T_{out,F}\right)}\left(M_6-\dfrac{2\left(1-\nu_F-\ln\left(\dfrac{r_F}{r_{out,F}}\right)\right)}{\left(1-\nu_F\right)\ln\left(\dfrac{r_{in,F}}{r_{out,F}}\right)}\right)\end{array}\right] \tag{41}$$

where,

$$\left[\begin{array}{l}M_1=\dfrac{\alpha_{IT}\left(T_{in,IT}-T_{out,IT}\right)\left(1+\nu_{IT}\right)\left(\dfrac{r_{IT}}{r_{out,IT}}\right)\left(\dfrac{r_{in,F}}{r_{out,F}}\right)}{\alpha_F\left(T_{in,F}-T_{out,F}\right)\left(1+\nu_F\right)\left(\dfrac{r_F}{r_{out,F}}\right)}\\ M_2=M1\dfrac{E_F\,\alpha_F\left(T_{in,F}-T_{out,F}\right)\left(\left(\dfrac{r_{in,IT}}{r_{out,IT}}\right)^2+\left(\dfrac{r_{IT}}{r_{out,IT}}\right)^2\left(1-2\nu_{IT}\right)\right)}{E_{IT}\,\alpha_{IT}\left(T_{in,IT}-T_{out,IT}\right)\left(\dfrac{r_{IT}}{r_{out,IT}}\right)^2\left(1-\left(\dfrac{r_{IT}}{r_{out,IT}}\right)^2\right)}\\ M_3=\dfrac{\left(\dfrac{r_{in,F}}{r_{out,F}}\right)^2\left(1+\left(\dfrac{r_F}{r_{out,F}}\right)^2\left(1-2\nu_F\right)\right)}{\left(\dfrac{r_F}{r_{out,F}}\right)^2\left(1-\left(\dfrac{r_{in,F}}{r_{out,F}}\right)^2\right)}\end{array}\right] \tag{42}$$

$$
\begin{aligned}
M_4 &= M_1 \frac{\left(\frac{r_F}{r_{out,F}}\right)^2\left(\frac{r_{in,IT}}{r_{out,IT}}\right)^2(1-\nu_{IT})\left(1-\left(\frac{r_F}{r_{out,F}}\right)^2\right)\left(1+\left(\frac{r_{IT}}{r_{out,IT}}\right)^2(1-2\nu_{IT})\right)}{\left(\frac{r_{IT}}{r_{out,IT}}\right)^2\left(\frac{r_{in,F}}{r_{out,F}}\right)^2(1-\nu_{IT})\left(1-\left(\frac{r_{in,IT}}{r_{out,IT}}\right)^2\right)\left(1+\left(\frac{r_F}{r_{out,F}}\right)^2(1-2\nu_F)\right)} \\
M_5 &= M_1 \frac{\ln\left(\frac{r_{in,F}}{r_{out,F}}\right)\left(1-\nu_{IT}-\ln\left(\frac{r_{IT}}{r_{out,IT}}\right)\right)}{\ln\left(\frac{r_{in,IT}}{r_{out,IT}}\right)(1-\nu_{IT})\left(1-\nu_F-\ln\left(\frac{r_F}{r_{out,F}}\right)\right)} \\
M_6 &= \frac{\left(\frac{r_F}{r_{out,F}}\right)^4-\left(\frac{r_{in,F}}{r_{out,F}}\right)^2-\left(\frac{r_F}{r_{out,F}}\right)^2\left(3+\left(\frac{r_{in,F}}{r_{out,F}}\right)^2(1-2\nu_F)-2\nu_F\right)}{\left(\frac{r_F}{r_{out,F}}\right)^2\left(1-\left(\frac{r_{in,F}}{r_{out,F}}\right)^2\right)(1-\nu_F)}
\end{aligned}
\qquad (43)
$$

The interfacial contact pressure can be obtained from Eq. (41) which is derived based on the model developed in this section, or by using Madhusudhana's model from literature [25] which considers the contact pressure to be dependent on the total interference between the cylinders in contact. As defined in his paper [25], this total interference (U) depends on the interference due to temperature gradients, (u_A), interference due to contact resistance (u_B) and the initial interference (u_C). Equation (44) from [63] provides the dimensionless form of the expression for total interference (U) as a function of the contact pressure, material properties and dimensions of the tubes.

$$
\begin{aligned}
\frac{U}{r_{interface}} &= \frac{P_{interface}}{E_{IT}}\left[\frac{E_{IT}}{E_F}\left(\frac{r_{out,F}^2+r_{interface}^2}{r_{out,F}^2-r_{interface}^2}+\nu_F\right)+\left(\frac{r_{interface}^2+r_{in,IT}^2}{r_{interface}^2-r_{in,IT}^2}+\nu_{IT}\right)\right] \\
U &= u_A+u_B+u_C
\end{aligned}
\qquad (44)
$$

The interference due to temperature gradients from [25] is given by Eq. (45) as

$$\frac{u_A}{r_{interface}} = \frac{\alpha_{IT}\Delta T_{IT}}{2\ln\left(\frac{r_{interface}}{r_{in,IT}}\right)}\left[\left(1-\frac{2r_{in,IT}^2\ln\left(\frac{r_{interface}}{r_{in,IT}}\right)}{r_{interface}^2-r_{in,IT}^2}\right)-\left(\frac{\alpha_F k_{IT}}{\alpha_{IT}k_F}\right)\left(1-\frac{2r_{out,F}^2\ln\left(\frac{r_{out,F}}{r_{interface}}\right)}{r_{out,F}^2-r_{interface}^2}\right)\right] \quad (45)$$

The interference due to contact resistance from [25] is given below by Eq.(46):

$$\frac{u_B}{r_{interface}} = \left(\alpha_{IT}-\alpha_F\right)\left(T_{in,IT}-\Delta T_{IT}\right)+\frac{\alpha_F k_{IT}\Delta T_{IT}}{r_{interface}\ln\left(\frac{r_{interface}}{r_{in,IT}}\right)}\left[\frac{1}{h'_{solid}+\left(\frac{k_{gas}}{3\sigma}\right)}\right] \quad (46)$$

In Eq. (46) 'ΔT_{IT}' is the temperature rise in the inner tube, 'h_{solid}' is the solid spot conductance and the ratio of the gas thermal conductivity (k_{gas}) to three times the surface roughness (σ) represents the interstitial gas gap conductance. The widely used correlation from literature for solid spot conductance [35], assuming plastic deformation of the asperities is given by Eq.(47) :

$$h'_{solid} = 1.13\tan(\phi)\frac{k_{eff}}{\sigma}\left(\frac{P_{interface}}{H}\right)^{0.94} \quad (47)$$

In Eq. (47) 'ϕ' represents the asperity slope in radian, 'k_{eff}' is the harmonic average thermal conductivity, 'σ' is the root mean square (RMS) value of surface roughness, '$P_{interface}$' is the interfacial contact pressure and 'H' is the micro-hardness of the softer material. If Eq. (47) is to be considered in Eq. (46) and to solve Eq.(44), an iterative procedure is required to determine the contact pressure. Since the uranium foil and the inner tube cladding are in perfect contact in the model under consideration, an infinite total conductance (a high value of total conductance) was used in the calculations for this

analysis. Considering Eqs.(44), (45) and (46), with the assumption of an infinite total conductance, the contact pressure can be obtained.

4.4 Uniform Heating Analytical Model- Sensitivity Studies

Parametric studies were performed using the developed uniform heating analytical model described in the previous section to assess the sensitivity of the target to various operating conditions. Three parameters, likely to influence the behavior of the target and hence the annular target safety, were identified to be: heat generation rate of the LEU (Table 3), the ratio of heat transfer coefficients (Table 4 and Table 5) and the ratio of the tube thickness as provided in Table 6. These parameters were varied in two different studies: (1) when the inner surface of the inner cladding and outer surface of the outer cladding are maintained at 373 K and (2) when there is no restriction on surface temperatures on the inner surface of the inner cladding and outer surface of the outer cladding.

Table 3. LEU heat generation rates used in the sensitivity studies.

Dimensions of the 20g LEU foil	LEU Heat Generation Rate (x 10^{10} W/m^3)	Power per gram of LEU (W/g)
Length : 0.100 m	1.6	762
Width: 0.0762 m	4.0	1905
Thickness: 125 x 10^{-6} m	6.4	3048

The rate of heat convection from the inner and outer surfaces of the inner and outer tubes respectively will depend on the dissipation of heat from these surfaces to the reactor coolant pool. Moreover the surface heat transfer coefficient will influence the wall temperature of the cladding as well. Since a part of this sensitivity study analyses the target behavior when the wall temperatures are fixed at 373 K (100 Celsius) it was

decided to look into the heat transfer coefficient ratios of the inner and the outer tubes that would maintain the wall temperatures at 373 K.

Applying newton's law of cooling to the inner surface of the inner tube, by keeping the wall temperature fixed at 373 K and the coolant temperature at 323 K, the heat transfer coefficient was found for the inner surface of the inner tube as 22122.60 W/m^2K (for $q'''= 1.6 \times 10^{10}$ W/m^3). This is the heat transfer coefficient that would maintain the inner surface of the inner tube at 373 K. The outer heat transfer coefficient was determined based on the 'H' value presented in Table 4. Next the heat transfer coefficient of the outer wall of the outer tube was determined using the same method and was found to be 17863.98 W/m^2K (for $q'''= 1.6 \times 10^{10}$ W/m^3). This is the heat transfer coefficient of the outer wall that would maintain the surface at 373 K. The inner surface heat transfer coefficient was then determined based on the 'H' value presented in Table 4. Based on the above discussion the value of 'H' required to maintain the inner and outer wall at 373 K at the same time is found to be 1.24.

Table 4. Heat transfer coefficient parametric study for wall temperatures maintained at 373 K.

$q'''= 1.6 \times 10^{10}$ W/m^3		$q'''= 6.4 \times 10^{10}$ W/m^3		Ratio
h_{in} (W/m^2K)	h_{out} (W/m^2K)	h_{in} (W/m^2K)	h_{out} (W/m^2K)	$H=h_{in}/h_{out}$
22122.60	44245.20	88524.40	177048.80	0.5
22122.60	29496.80	88524.40	118032.53	0.75
22122.60	22122.60	88524.40	88524.40	1
23759.09	17863.98	95073.72	71484	1.33
35727.96	17863.98	142968	71484	2

Note: The listed heat transfer coefficients were calculated by maintaining the wall temperatures at 373 K.

Table 4 also provides the range of heat transfer coefficients used to perform a parametric study at a higher heat generation rate of the LEU (6.4×10^{10} W/m^3). The heat transfer

coefficient values provided in Table 5were used in the general parametric study (no restriction on wall temperatures). Since the annular target will operate in a high temperature environment and the magnitude of the thermally induced stresses in the material also depends on the thickness of the cladding tubes, the tube thickness study (Table 6) will provide direction in assessing the minimum thickness of these tubes for varying LEU heat generation rates. Of course, the ability of the tubes to withstand the stresses will depend on their yield strengths. It is expected that Al 6061-T6 (yield strength = 276 MPa) is likely to withstand larger magnitude of stresses until its yield point as compared to Al 3003-H14 (yield strength = 145 MPa) or Al 6061-T4 (yield strength = 145 MPa).

Table 5. Heat transfer coefficient parametric study with no restriction on wall temperature.

h_{in} (W/m^2K)	h_{out} (W/m^2K)	$H=h_{in}/h_{out}$
9500	19000	0.50
14250	19000	0.75
19000	19000	1
19000	14250	1.33
19000	9500	2

Table 6. Tube thickness variation parametric study.

t_{in} (x 10^{-4} m)	t_{out} (x 10^{-4} m)	t_{in}/t_{out}
7.85	8.30	0.96
7.85	9.55	0.82
4.85	9.55	0.51
2.85	9.55	0.30
0.85	9.55	0.09

Chapter 5: Modeling Without Residual Stresses- Results

5.1 Uniform Heating Analytical and Numerical Results

All the results for chapter 3 have been included in this section. This includes the non-uniform heating numerical model, uniform heating numerical model, the dimensional uniform heating analytical model and its sensitivity studies. The dimensionless analytical modeling results will be included once the work is complete. The uniform heating results will be presented first, followed by the non-uniform heating model and the sensitivity studies. For the uniform heating case, where the foil is modeled as a complete cylinder, the temperature distribution along the circumference of the inner and outer tubes at their respective interfaces is a constant as illustrated in Figure 27. This is expected due to uniform heating along the circumference of the tubes and no circumferential variation in temperature exists.

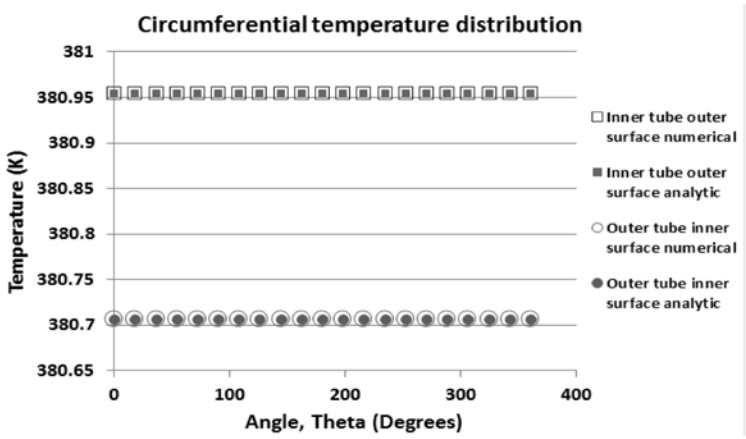

Figure 27. Circumferential temperature distribution on the inner and outer cladding for uniform heating with $q'''=1.6 \times 10^{10}$ W/m^3.

The assembly temperature distribution contour for uniform heating is presented as a contour plot in Figure 28.The radial temperature drop due to radially inward heat flow into the inner tube cladding and radially outward heat flow into the outer tube cladding is

illustrated in Figure 29. The coolant flowing along the inner surface of the inner tube and over the outer surface of the outer tube creates the required temperature gradient for effective heat dissipation. The analytical and numerical temperature values are in good agreement with each other.

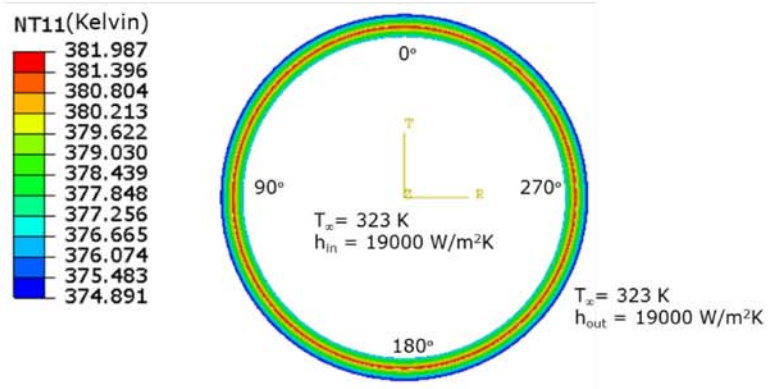

Figure 28. Assembly temperature distribution contour for uniform heating with q'''=1.6x10^{10} W/m^3.

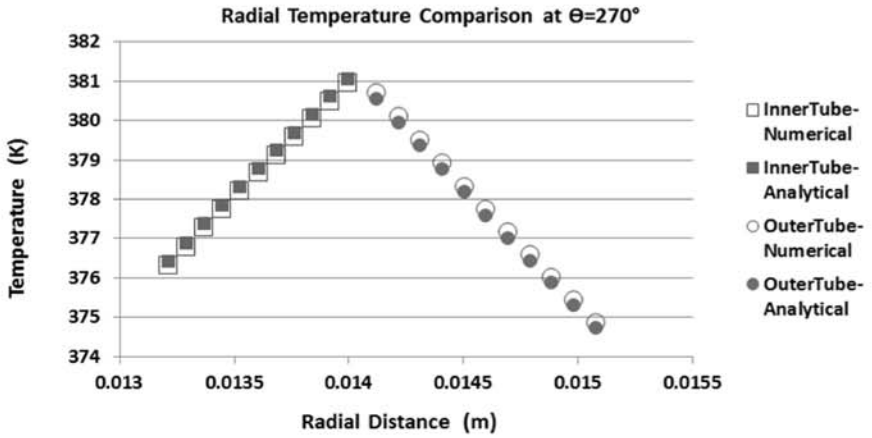

Figure 29. Radial temperature distribution in the cladding for q'''=1.6 x 10^{10} W/m^3 and uniform heating.

Figure 30 provides the compressive radial stress distribution in the inner and outer cladding. The thermal expansion coefficient of uranium ($\alpha = 1.39 \times 10^{-5}\ K^{-1}$) is lesser than that of aluminum ($\alpha = 2.34 \times 10^{-5}\ K^{-1}$). Hence, for radially inward heat flow into the inner tube, due to a higher thermal expansion coefficient, the outer surface of the inner tube tends to expand a lot more than the inner surface of the foil. As a result, the foil acts as a

barrier to the expansion of the inner tube, resulting in compressive stresses being generated. Similarly the stresses in the outer tube are compressive in nature as the temperature gradient at the outer tube-foil interface is greater than at its outer surface. Hence the inner surface of the outer tube tends to move outward by expanding, but the outer surface doesn't expand as much due to a comparatively lower temperature gradient. Hence, compressive stresses are generated in the outer tube with radially outward heat flow from a material of lower thermal expansion coefficient (uranium) to a material of higher thermal expansion coefficient (aluminum).

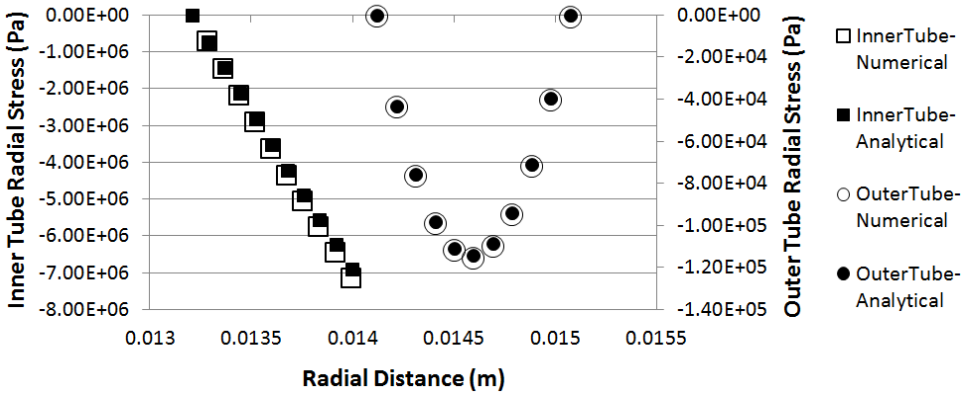

Figure 30. Radial stress distribution in the cladding at θ=270^{0}for uniform heating with q'''=1.6x10^{10} W/m^3.

The magnitudes of compressive stresses on the outer tube are comparatively lower as compared to that of the inner tube. This is because contact is relaxed between the outer tube and the foil while it is reinforced between the inner tube and the foil (due to heat flow direction and thermal expansion coefficient of the materials under consideration). Hence the stresses in the outer tube can be determined by considering the material properties of the outer tube alone. However for the inner tube the composite structure of the inner tube and the foil must be considered due to reinforced contact as pointed out during the development of the uniform heating analytical model in Sec. 4.3. The radial

stress distribution contour plot of the annular target assembly is presented in Figure 31. Figure 32 presents the hoop stress contour of the annular target assembly and Figure 33 hoop stress distribution across the radius of the cladding.

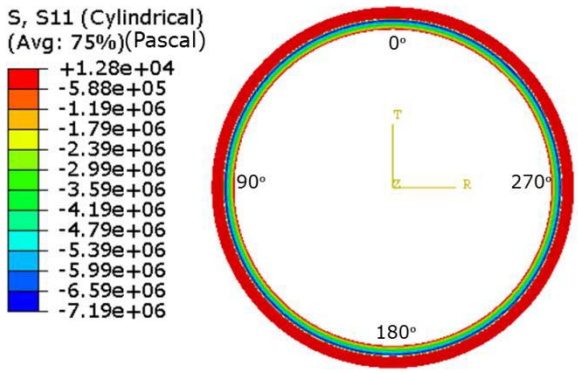

Figure 31. Radial stress distribution contour of the assembly for uniform heating with q'''=1.6x10^{10} W/m^3.

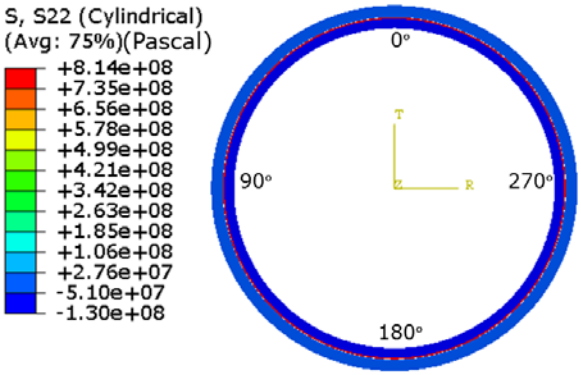

Figure 32. Hoop stress distribution contour of the assembly for uniform heating at q'''=1.6x10^{10} W/m^3.

In the inner cladding the hoop stresses are compressive in nature due to the radially inward heat flow into the inner tube and due to the foil which acts as a barrier to the expansion of the inner tube. A lower temperature gradient on the inner surface of the inner tube and the fact that the expansion of the outer surface of the inner tube is restricted by the foil results in compressive hoop stresses across the inner tube. The hoop stresses on the outer tube move from being compressive to tensile across the radius. This

can be attributed to radially outward heat flow through the outer tube and the outer surface of the outer tube is free to expand. The expansion of the outer surface of the outer tube results in tensile stresses being generated across the outer half of the tube. Now the expansion of the inner surface is resisted by the elements across the thickness of the tube. This is why the hoop stress moves from being compressive to tensile across the radius of the outer tube. From Figure 30 and Figure 33 it can be concluded that there is a good agreement between the numerical and the developed analytical model. It is also worth noting that the predicted hoop stresses in Figure 33 are about 2 orders of magnitude greater than the radial stresses (Figure 30). Also, the hoop stresses in the inner tube are greater than the hoop stresses in the outer tube. This gives some direction in establishing the first point of failure (if any) in the annular target safety analysis.

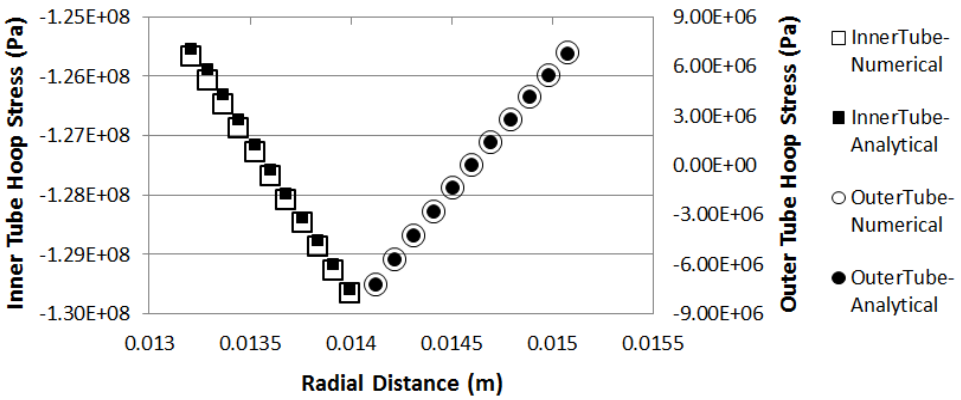

Figure 33. Hoop stress distribution in the cladding at θ=270° for uniform heating at q'''=1.6x10^{10} W/m^3.

Figure 34 and Figure 35 show that a uniform gap opens up at the interface of the outer tube and the foil due to thermal expansion mismatch and radially outward heat flow. The analytical value for separation between the foil and the outer tube was obtained by subtracting the displacement of the foil outer surface from that of the outer tube inner

surface. The contact pressure on the inner tube due to the contact between the foil and the inner cladding is shown in Figure 36.

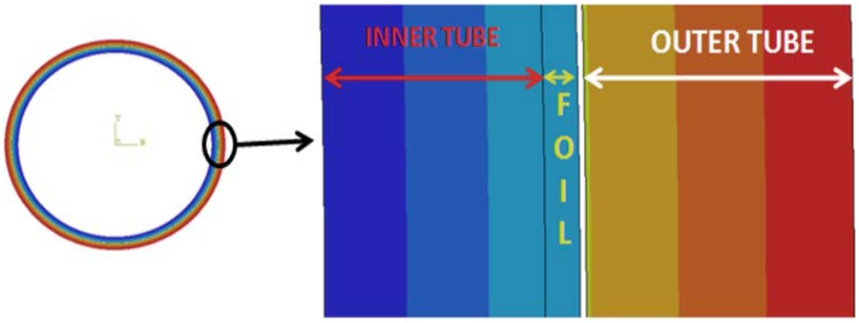

Figure 34. Separation between the foil and the outer tube for uniform heating with q'''=1.6x10^{10} W/m^3.

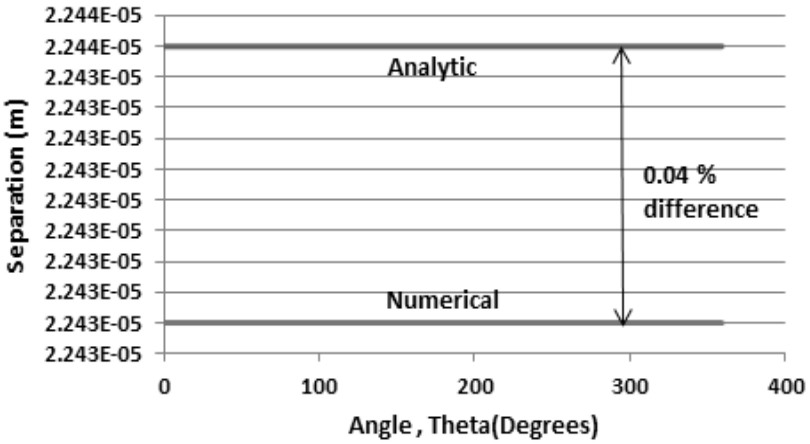

Figure 35. Separation between the foil and the outer tube for uniform heating with q'''=1.6x10^{10} W/m^3.

Table 7 provides the comparison between the analytical and numerical results for temperature and stresses in the cladding. The difference between the numerical temperatures obtained from Abaqus FEA [56] and the analytical temperatures is within 0.05 %. Also, the developed analytical model is able to predict the stresses to within 3 % while also showing good agreement with numerical results.

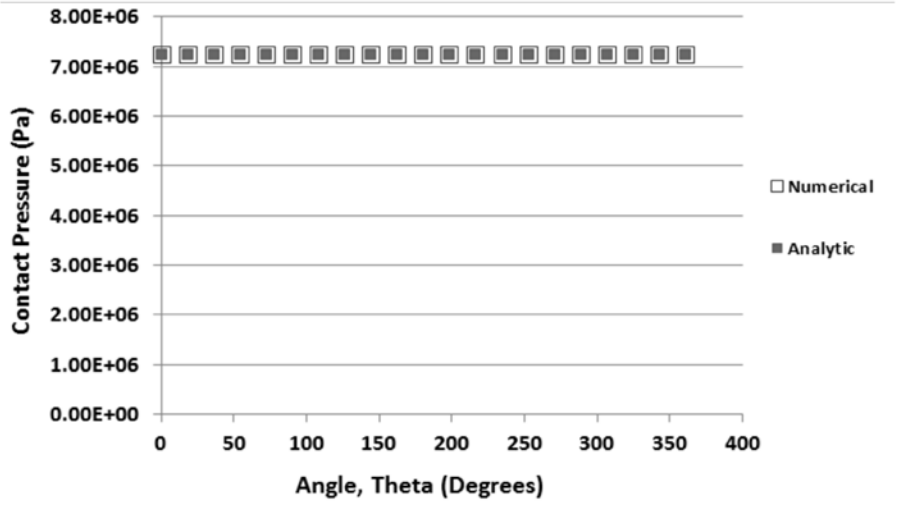

Figure 36. Circumferential contact pressure distribution in the inner tube with $q'''=1.6x10^{10}$ W/m^3.

Table 7. Percent difference between the analytical and numerical models for the inner and the outer tubes.

Part	Radial Distance (x 10^{-3} m)	Temperature (% difference)	Radial Stress (% difference)	Hoop Stress (% difference)
Inner Tube	13.210	0.028	--------	1.643
	13.289	0.029	1.618	1.638
	13.367	0.029	1.104	1.862
	13.446	0.030	1.954	1.928
	13.524	0.030	1.488	1.378
	13.603	0.031	1.134	1.370
	13.681	0.030	1.572	1.852
	13.759	0.031	1.922	1.078
	13.838	0.031	1.134	1.083
	13.917	0.032	2.282	2.599
	13.995	0.030	1.654	2.065
Outer Tube	14.120	0.039	--------	0.235
	14.216	0.040	1.005	0.442
	14.311	0.039	1.038	0.321
	14.407	0.039	0.823	0.354
	14.502	0.038	0.893	0.452
	14.498	0.039	0.934	0.893
	14.693	0.038	1.013	0.089
	14.789	0.038	1.573	0.172
	14.884	0.037	1.191	0.216
	14.979	0.037	1.743	0.201
	15.075	0.036	--------	0.387

5.2 Non-Uniform Heating Results

The difference between the geometry of non-uniform heating model and the uniform heating model validated in the previous section is the open cross section of the foil. Hence, this section will focus on presenting the non-uniform heating results to understand the behavior of the target. Figure 37 provides the assembly temperature distribution contour. The region on either side of 180° represents the tube-tube contact region. There is a temperature drop in this region due to absence of the heat generating LEU foil.

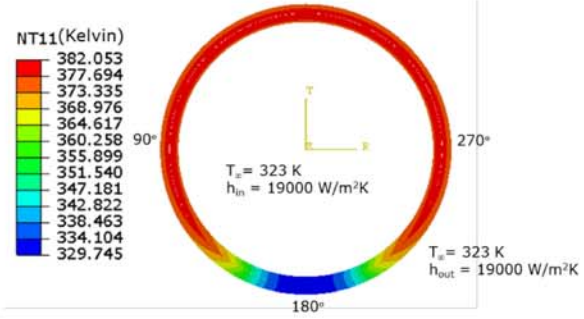

Figure 37. Assembly temperature distribution contour for non-uniform heating.

Figure 38 illustrates the radial stress and temperature distribution across the thickness of the assembly. It is to be noted here that the thermal expansion coefficient of the Uranium foil ($\alpha = 1.39 \times 10^{-5}\ K^{-1}$) is lesser than that of Aluminum ($\alpha = 2.34 \times 10^{-5}\ K^{-1}$). Hence, for radially inward heat flow into the inner tube, due to a higher thermal expansion coefficient, the outer surface of the inner tube tends to expand more than the inner surface of the LEU foil. As a result, the foil acts as a barrier to the expansion of the inner tube, resulting in compressive stresses being generated. Similarly the radial stresses in the outer tube are compressive in nature as the temperature gradient at the outer tube-foil interface is greater than at its outer surface. Hence the inner surface of the outer tube tends to move outward by expanding, but the outer surface doesn't expand as much due

to a comparatively lower temperature. Compressive stresses are generated in the outer tube with radially outward heat flow from a material of lower thermal expansion coefficient (Uranium) to a material of higher thermal expansion coefficient (Aluminum).

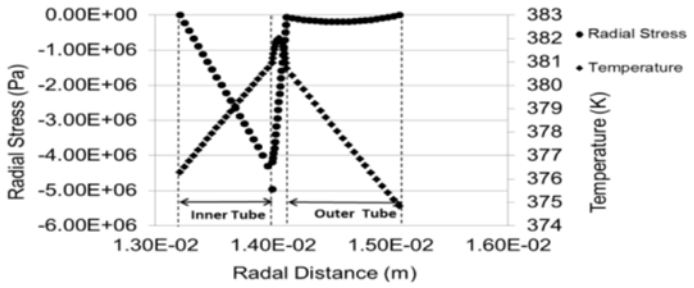

Figure 38. Radial stress and temperature distribution for non-uniform heating.

The radial displacement contour of the target is shown in Figure 39. Beginning at 0°, there is no separation between the foil and the inner tube. A gap between the outer tube and the foil exists due to thermal expansion coefficient mismatch and radially outward heat flow through the outer tube. At 90 ° there is no separation between the foil and the inner tube. However, the magnitude of separation between the foil and the outer tube is lesser than at 0°. This shows that the maximum displacement occurs at the 0° location in Figure 39. Between 90° and 180° a separation transition region exists. This transition region is formed because the ends of the foil move away from the recess (Figure 48) and flap out as they expand. This causes the foil to pull away from the inner tube and make contact with the outer tube. This opens up a gap between the foil and the inner tube. After the separation transition region, the foil separates from the outer tube and gradually moves closer to the inner tube and eventually makes contact. Now a gap opens up between the outer tube and the foil. This behavior is symmetric about the X-axis and hence the pattern repeats itself from 180° to 360°. The separation explained in Figure 39 is illustrated by plotting the separation along the circumference of the outer tube –LEU

foil interface (Figure 40). The assembly hoop stress distribution contour is shown below in Figure 41

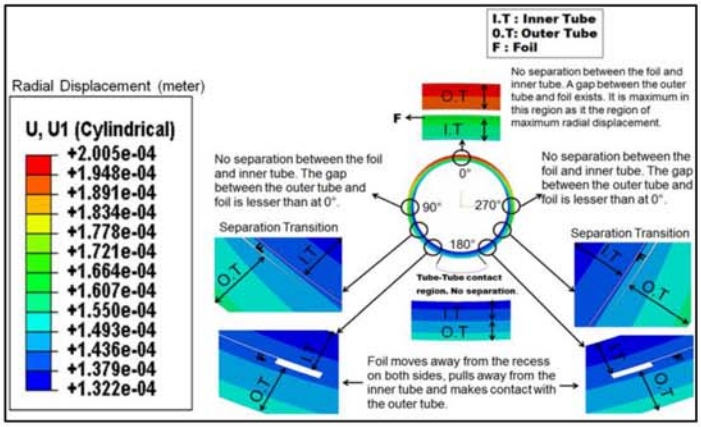

Figure 39. Radial displacement contour illustrating the interfacial separation between the foil and the cladding for non-uniform heating.

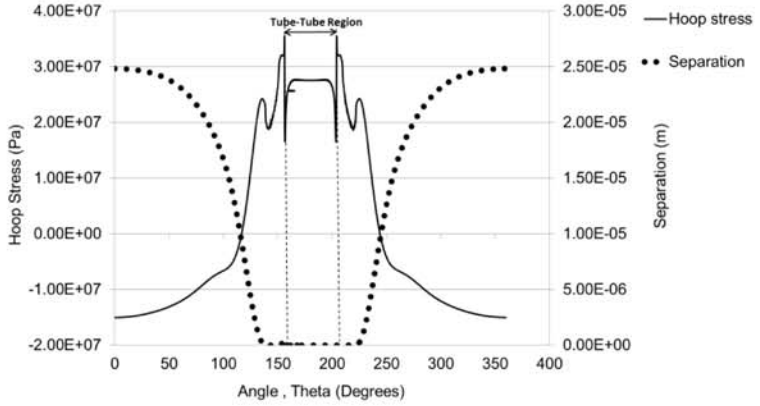

Figure 40. Hoop stress and separation along the circumference of the outer tube inner surface for non-uniform heating

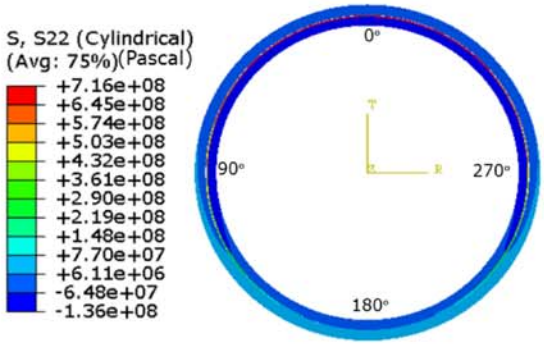

Figure 41. Assembly hoop stress contour for non-uniform heating.

As explained previously, the magnitude of separation between the foil and the outer tube gradually begins to decrease from 0° towards the tube-tube region at 180°. Figure 40 shows that zero separation exists to the left of 150° and a little after 200°. This implies that the LEU foil is in contact with the outer tube and a gap has opened up between the foil and the inner tube. Also, looking closely at the separation plot, a finite separation exists just after 150° and 200°. This is because the foil pulls away from the recess region resulting in finite separation. Figure 40 also illustrates the circumferential variation of hoop stress along the inner surface of the outer tube. Between 0° and 120° the hoop stresses are compressive in nature. This is because the elements across the thickness of the outer tube resist the expansion of the inner surface due to radially outward heat flow inducing compressive stresses. Between 120° and 140° the hoop stresses move from being compressive to tensile. This can be attributed to the separation transition region and the foil making contact with the outer tube. The expansion of the foil due to radially outward heat flow pushes the inner surface of the outer tube causing tensile hoop stresses to form in this region. Between 140° and 160° the tensile hoop stresses fluctuates as the foil pulls away from the recess. This behavior is symmetric from 200°-360°.. Figure 42 shows the temperature distribution along the circumference of the inner surface of the outer tube. From 0°-120° the temperature remains a constant in the uniformly heated region and begins to drop closer to the tube-tube location. The behavior is symmetric from 200°-360°. Though the temperature drives the thermal stresses, Figure 40 illustrates that the separation at the interface influences the magnitude and behavior of the hoop stresses. Figure 43 illustrates the contact pressure and separation along the circumference of the inner surface of the outer tube. From 0 ° onwards the contact pressure is zero when

the separation is finite as shown in Figure 43. A finite contact pressure exists just before 150° as this is the region where the foil makes contact with the outer tube. There is a small region after 150° and 200° where the contact pressure is zero. This is because the foil completely pulls away from the recess on either side (Figure 39) and results in zero contact pressure. The huge spikes in contact pressure are due to the edges of the recess which are regions of high stress concentration and hence result in high contact pressures. The behavior is symmetric from 200°-360°.

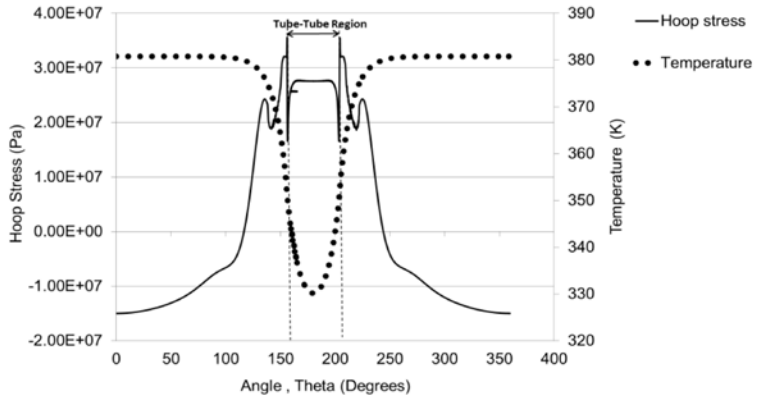

Figure 42. Temperature distribution and hoop stresses in the outer tube for non-uniform heating.

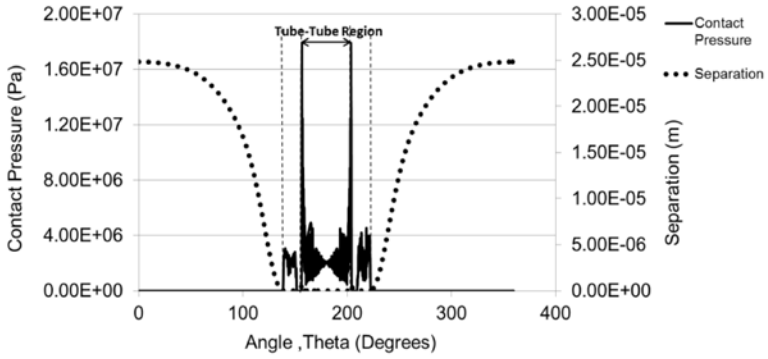

Figure 43. Interfacial separation and contact pressure variation in the inner surface of the outer tube for non-uniform heating.

Figure 44 illustrates the hoop stress and temperature variation along the circumference of the outer surface of the inner tube. From 0°-120° the temperature remains a constant in

the uniformly heated region and begins to drop closer to the tube-tube location. The behavior is symmetric from 200°-360°. The hoop stresses on the outer surface of the inner tube are compressive in nature due to radially inward heat flow and because the foil acts as a barrier to the free expansion of the outer surface of the inner tube. The magnitude of compressive hoop stress decreases from 0° towards the tube-tube region and this behavior is symmetric. This decrease in compressive stress results from the contact between the LEU foil and the inner tube being reinforced and relaxed. Hence the magnitude of compressive hoop stress is maximum at 0° and 360° and decreases by an order of magnitude beyond the separation transition region. The contact pressure at the interface of the inner tube and the LEU foil is illustrated in Figure 45. There is a lot of noise in the contact pressure distribution on either side of the tube to tube region and this is due to the foil separating from the inner tube as illustrated in Figure 39 and this result in nodal mismatch at the interface in the numerical model.

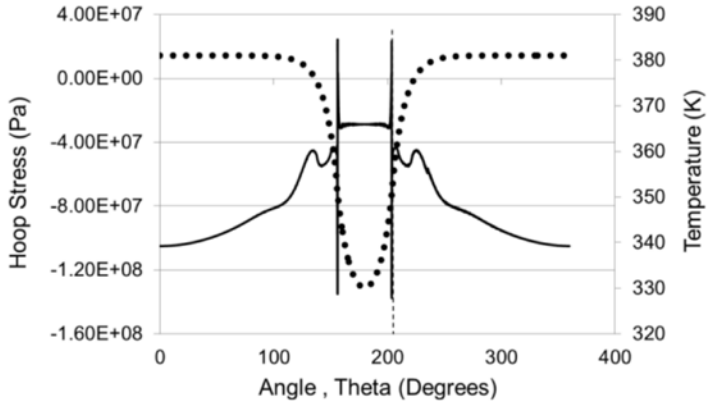

Figure 44. Temperature distribution and hoop stresses in the inner tube for non-uniform heating.

Figure 46 compares the radial displacement contours of the deformed inner tube with the un-deformed inner tube. The maximum radial displacement occurs at 0° on the inner tube. Comparing the deformed inner tube contour with a 10x magnification to that of the

un-deformed inner tube shows that the inner tube thermally expands and hence the inner and outer surfaces of the inner tube are radially displaced as illustrated in Figure 46.

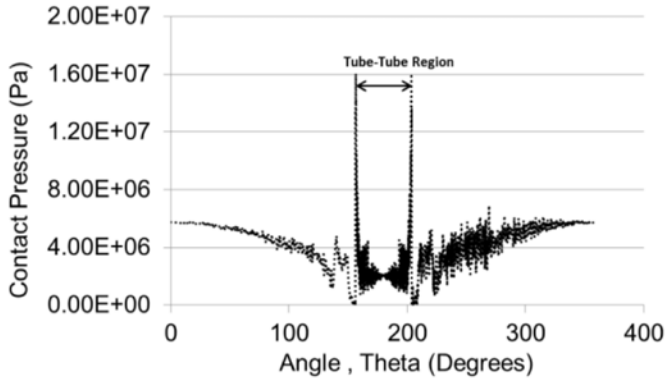

Figure 45. Contact pressure distribution in the inner tube outer surface for non-uniform heating.

Figure 47 compares the radial displacement contours of the deformed outer tube to that of the original un-deformed shape. The maximum radial displacement occurs at 0° on the outer tube. At 0° the magnitude of radial displacement of the outer tube is greater than the inner tube. This is because the LEU foil is in perfect contact with the inner tube at this location (Figure 39 and Figure 40). Hence the foil acts as a barrier to the radial displacement of the inner tube at this location. Comparing the deformed outer tube contour with a 10x magnification to that of the un-deformed outer tube shows that the outer tube thermally expands and hence the inner and outer surfaces of the outer tube are radially displaced as illustrated in Figure 47.

Figure 48 illustrates radial displacement of the foil while the final deformed shape of the annular target assembly is illustrated in Figure 49 as a radial displacement contour plot with a 40x magnification.

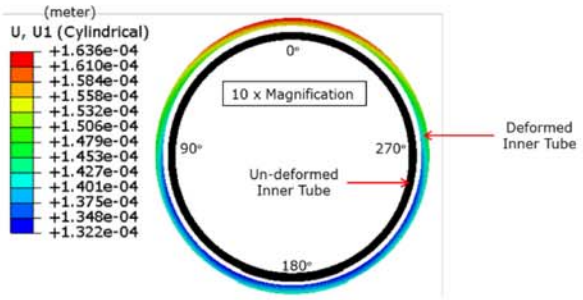

Figure 46. Deformed and un-deformed radial distribution contours of the inner tube for non-uniform heating.

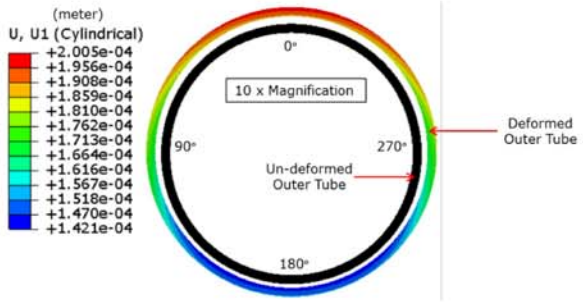

Figure 47. Deformed and un-deformed radial distribution contours of the outer tube for non-uniform heating.

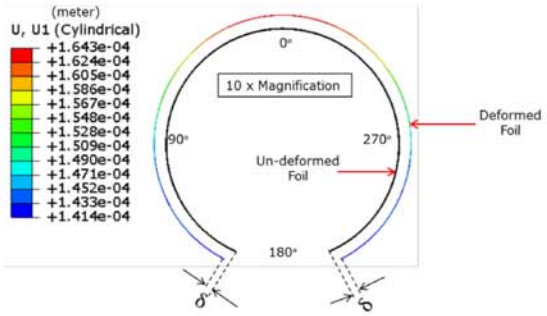

Figure 48. Deformed and un-deformed radial displacement contours of the LEU foil for non-uniform heating.

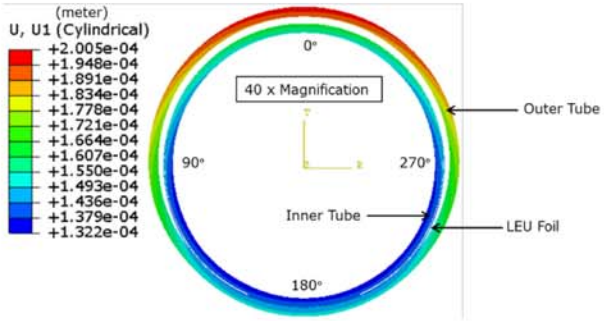

Figure 49. Final deformed shape of the annular target post irradiation for non-uniform heating.

In Figure 48, the deformed contour of the LEU foil clearly shows that the open ends of the foil are pulled inwards by 'δ' and this will result in zero contact pressure on the inner and outer tubes in the regions where the foil exhibits this behavior. This is explains why the contact pressure on the edges of the recess is zero. The final deformed shape of the annular target assembly is illustrated in Figure 49 as a radial displacement contour plot with a 40x magnification. A higher magnification was used to provide a clear picture of how the target would look after irradiation. The gap that opens up between the foil and the outer tube and the foil and the inner tube closer to the tube-tube contact region can be seen. From Figure 40 the maximum magnitude of this gap between the LEU foil and the outer tube is in the micrometer range. Experiments need to be performed to check if the thermal contact resistance is significant for this magnitude of separation. Also, perfect contact is maintained in the tube-tube region at 180°. This coupled with the fact that the maximum magnitude of displacement of the outer tube at 0° is greater than that of the inner tube, the final shape of the target will be oval and not circular.

5.3 Uniform and Non-Uniform Heating Results Comparison

Recall that one goal behind developing a uniform heating model is to validate the non-uniform heating model (annular target with a recess and a foil of open cross section) by comparing the results of the uniformly heated region in the non-uniform heating model with that of the uniform heating model developed in Abaqus FEA and validated using analytical expressions as explained previously. It is expected that the values will be of the same order of magnitude. Figure 50 -Figure 57 provide a comparative study between the uniform and non-uniform heating conditions. The temperature distribution across the radius of the assembly at 270° is illustrated in Figure 50. In Figure 51, the uniform

heating model under predicts the circumferential temperature on the outer surface of the inner tube by 0.02 % while in

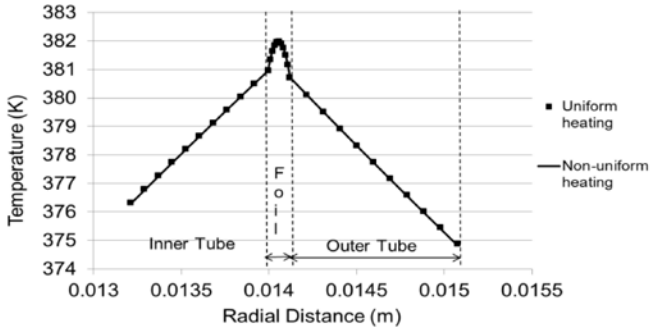

Figure 50. Assembly temperature distribution comparison for uniform and non-uniform heating.

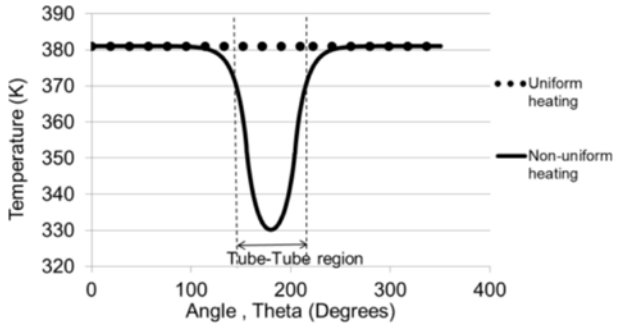

Figure 51. Circumferential temperature distribution on the outer surface of the inner tube: comparison between uniform and non-uniform heating.

Figure 52 the uniform heating model under predicts the circumferential temperature on the inner surface of the outer tube by 0.21 %. The error is within 1% and there exists good agreement between the circumferential temperatures of the uniform and non-uniform heating models. Figure 53 illustrates the comparison of the assembly radial stresses for the uniform and non-uniform heating cases at 270°. The uniform heating numerical model over predicts the compressive radial stress in the inner tube while it under predicts the compressive radial stress in the outer tube. The maximum error on the inner tube is 40 % and on the outer tube is 60 %. In the uniformly heated region of the

non-uniform heating model, the radial stresses across the target assembly are of the same order of magnitude as that of the uniform heating model.

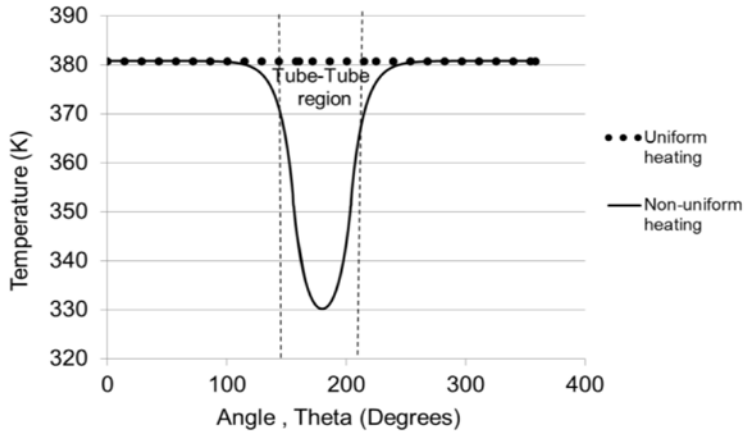

Figure 52. Circumferential temperature distribution on the inner surface of the outer tube: comparison between uniform and non-uniform heating.

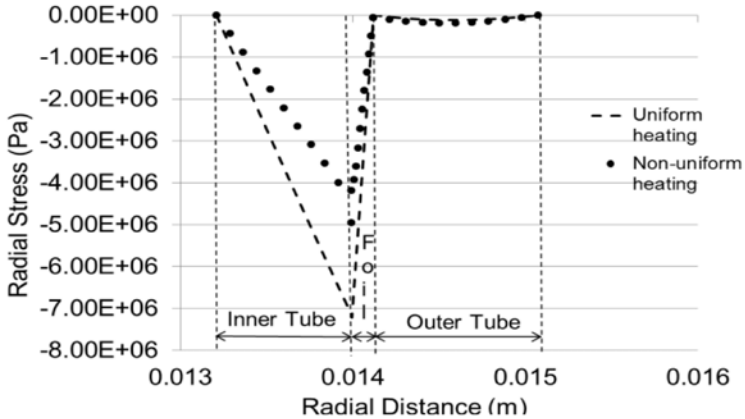

Figure 53. Assembly radial stress distribution comparison for uniform and non-uniform heating.

The contact pressure comparison is illustrated in Figure 54. The uniform heating numerical model over predicts the contact pressure by 20 % when compared to the uniformly heated region of the non-uniform heating model. Also, the contact pressure in the uniformly heated region of the non-uniform heating model is of the same order of magnitude as the contact pressure from the uniform heating model. The hoop stresses on the outer surface of the inner tube and on the inner surface of the outer tube are illustrated

in Figure 55 and Figure 56 respectively. Figure 57 provides the magnitudes of separation at the interface of the LEU foil and the outer tube. For the outer surface of the inner tube (Figure 55), the uniform heating model over predicts the compressive hoop stresses by 20 % as compared to the hoop stresses in the uniformly heated region of the non-uniform heating model. However, the uniform heating model under predicts the compressive hoop stresses on the inner surface of the outer tube by

40 %.

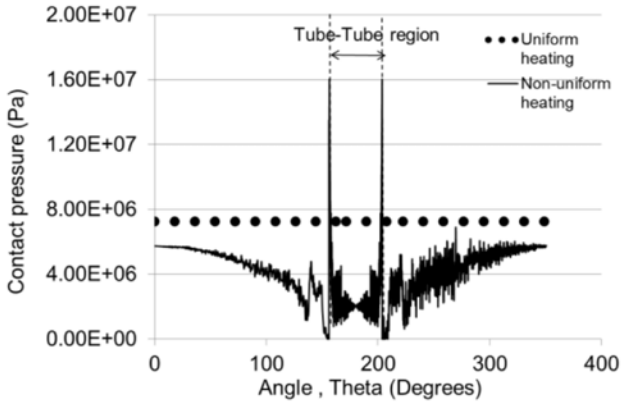

Figure 54. Comparison of contact pressure on the outer surface of the inner tube for uniform and non-uniform heating.

In Figure 55 and Figure 56 the compressive hoop stresses in the uniformly heated region of the non-uniform heating model is of the same order of magnitude as the compressive hoop stresses from the uniform heating model. Thus the temperature distributions, in the circumferential and radial directions for the uniform and non-uniform heating cases, are in good agreement with each other (in the uniformly heated region). The radial, hoop stresses on the inner and outer tubes, the contact pressure and magnitude of separation between the foil and the outer tube are within the same order of magnitude as expected earlier. Hence the uniform heating model with a simple analytic solution can be used effectively for design and to evaluate the risk of target failure.

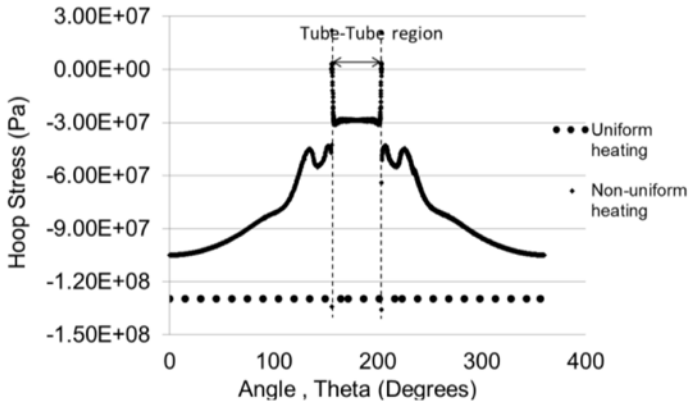

Figure 55. Hoop stresses on the outer surface of the inner tube for uniform and non-uniform heating.

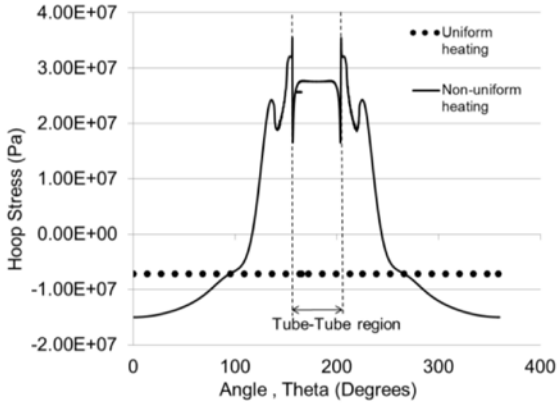

Figure 56. Hoop stresses on the inner surface of the outer tube for uniform and non-uniform heating.

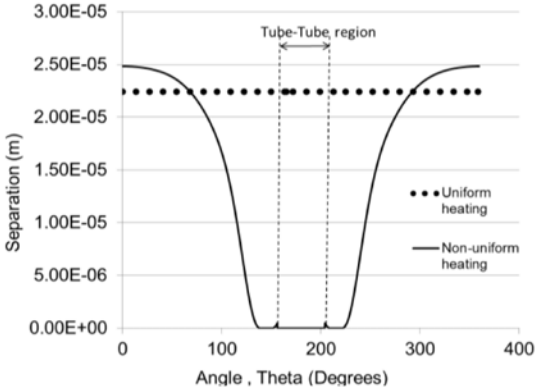

Figure 57. Comparison of the magnitude of separation at the interface of the foil and the outer tube for uniform and non-uniform heating conditions.

Table 8 provides the summary of the uniform and non-uniform heating results comparison for the temperature, stresses, contact pressure and interfacial separation. It is important to note that even though Table 8 suggests that a 60 % difference in outer tube

radial stress results exist, it is the hoop stresses in the inner tube that are likely to dictate the failure of the target (based on Figure 30 and Figure 32). The variation between the uniform and non-uniform heating hoop stresses in the inner tube based on Table 8 is 20 % and within the same order of magnitude.

Table 8. Uniform and non-uniform heating comparison summary (a negative value indicates that the uniform heating model under predicts the results).

Parameter	Inner Tube Maximum Percent Difference (%)	Outer Tube Maximum Percent Difference (%)	Same Order of Magnitude
Temperature	-0.20	-0.21	Yes
Radial Stress	40	-60	Yes
Hoop Stress	20	-40	Yes
Contact Pressure	20	-----	Yes
Separation	-----	-10	Yes

5.4 Uniform Heating Sensitivity Studies

Parametric studies were performed using the developed uniform heating analytical model as explained earlier in Sec. 4.4. First, the analysis results for the case where the wall temperature is maintained at 373 K have been presented by Figure 58 -Figure 65.

Figure 58 provides the radial temperature distribution at $\theta=270^{\circ}$ for varying LEU heat generation rates as given in Table 3.An increase in heat generation rate will result in an increase in heat flux and a corresponding rise in temperature as well. This behavior is well represented in Figure 58. The temperatures originate and converge at a common point. This is because the inner wall of the inner tube and the outer wall of the outer tube are maintained at 373 K. Figure 59 illustrates the radial stress distribution on the inner

and outer tubes for varying heat generation rates of the LEU. In the outer tube the magnitude of stresses increases with increasing heat generation rates. This is because the stresses are driven by the temperature gradients and a higher heat generation rate would imply higher temperature gradients in the target tubes.

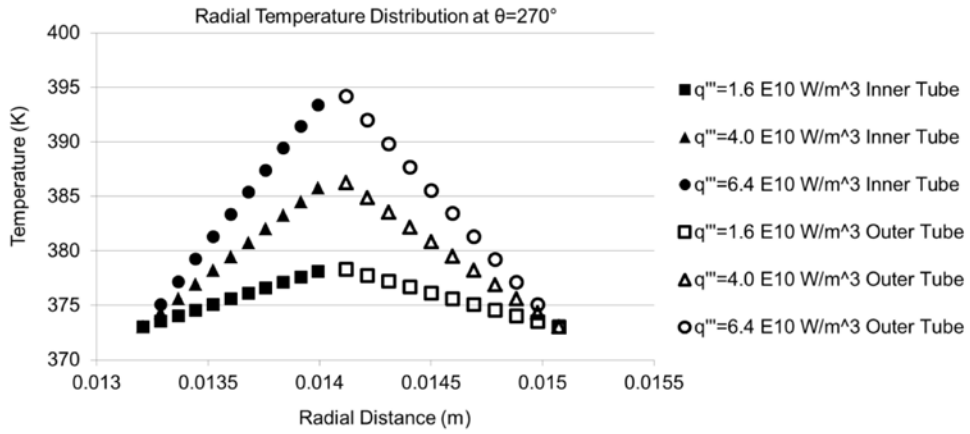

Figure 58. Radial temperature distribution in the inner and outer tubes for varying LEU heat generation rates with T_{wall} =373 K for uniform heating.

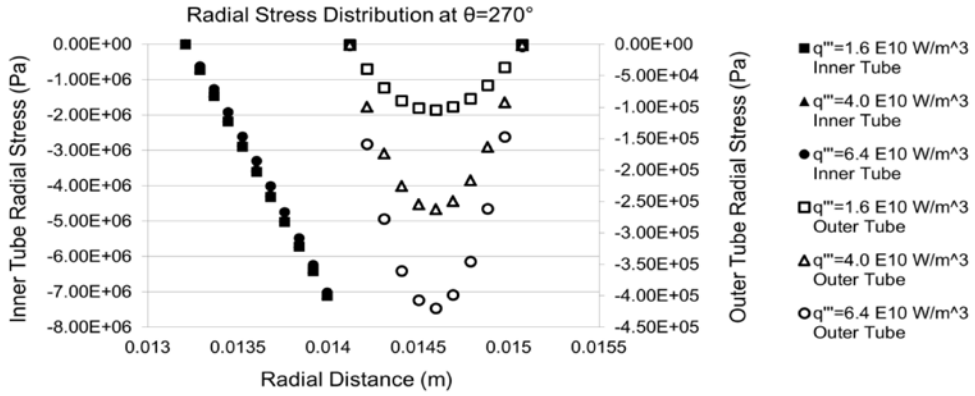

Figure 59. Radial stress distribution in the inner and outer tubes for varying LEU heat generation rates with T_{wall} =373 K for uniform heating.

Figure 60 illustrates the hoop stress distribution on the inner tube and outer tube respectively. The magnitude of compressive stresses increases across the inner tube as there is an increase in temperature across the radius of the inner tube. Since the stresses in the inner tube are compressive in nature, a higher temperature will result in a higher

compressive stress state. An increase in the LEU heat generation rate will increase the magnitude of temperature gradients (Figure 58) and results in a higher compressive stress.

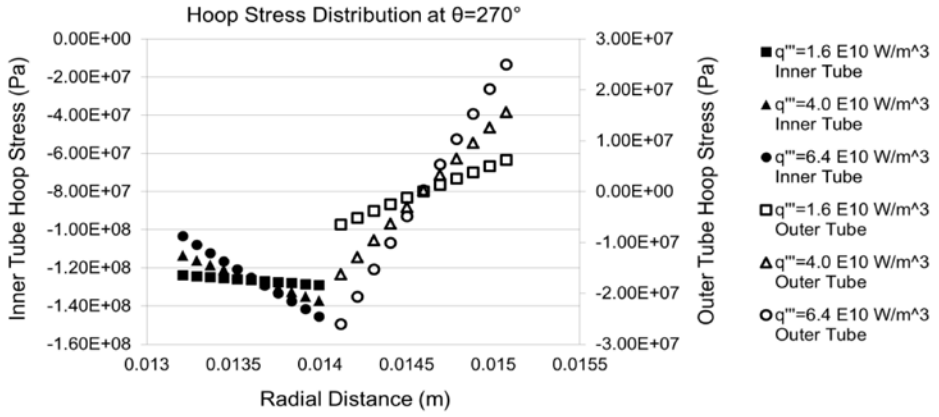

Figure 60. Hoop stress distribution in the inner and outer tubes for varying LEU heat generation rates with Twall =373 K for uniform heating.

Figure 60 also shows that the maximum compressive hoop stress is induced on the inner surface of the outer tube. This is because the inner surface of the outer tube is the surface closer to the heat generating LEU and the temperature of the outer tube will be the highest at this point as shown in Figure 58. Next, the inner to outer heat transfer coefficient ratio was varied based on Table 4 and the results are provided by Figure 61-Figure 64. Figure 61 shows the variation of temperature at the outer and inner surfaces of the tubes for various heat transfer coefficient ratios and at the lowest and highest heat generation rate of the LEU. A heat transfer coefficient ratio of below 1 implies that the outer surface heat transfer coefficient is greater than that of the inner surface while a heat transfer coefficient ratio greater than 1 implies a higher inner surface heat transfer coefficient. In Figure 61, for a heat transfer coefficient ratio of 0.5 the outer surface of the inner tube is at a higher temperature than the inner surface of the outer tube. This is because the inner tube inner surface is at a comparatively lower heat transfer coefficient

than the outer tube. Hence the temperature on the inner tube is higher. With increasing 'H' the difference gradually decreases and at H=2 the outer tube inner surface is at a higher temperature than the inner tube outer surface. This is because for H=2, the outer heat transfer coefficient is lesser than the inner heat transfer coefficient. This also explains why the inner tube inner surface is at a lower temperature at H=2 than for H < 1.

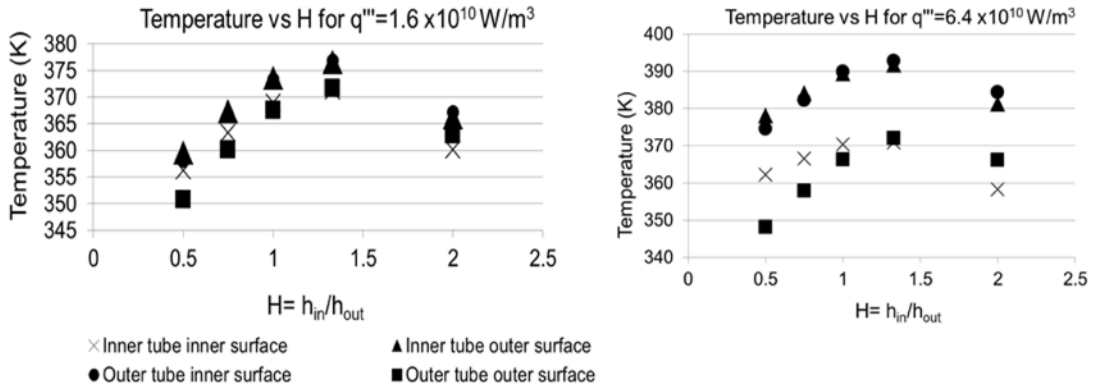

Figure 61. Temperature variation on the surfaces of the tubes with varying heat transfer coefficient ratios with T_{wall} = 373 K for uniform heating.

The radial stress and contact pressure distribution on the inner tube outer surface is illustrated in Figure 62. This behavior can be explained based on the radial temperature distribution on the inner tube outer surface as illustrated in Figure 61. The radial stress increases with increasing H ratios due to an increase in temperature. The maximum temperature on the inner tube outer surface occurs for an H ratio between 1 and 1.50. Since the temperatures drive the stresses, the maximum compressive radial stress occurs between H ratios of 1 and 1.50 as well. The hoop stress in the tubes for a lower and a higher LEU generation rate is provided in Figure 63. Similar to Figure 62, where the radial stress distribution is influenced by the temperature, the variation of hoop stresses with varying heat transfer coefficient ratios is dependent on the temperatures as well. The

magnitude of compressive stresses will be the highest on the surface with higher temperature.

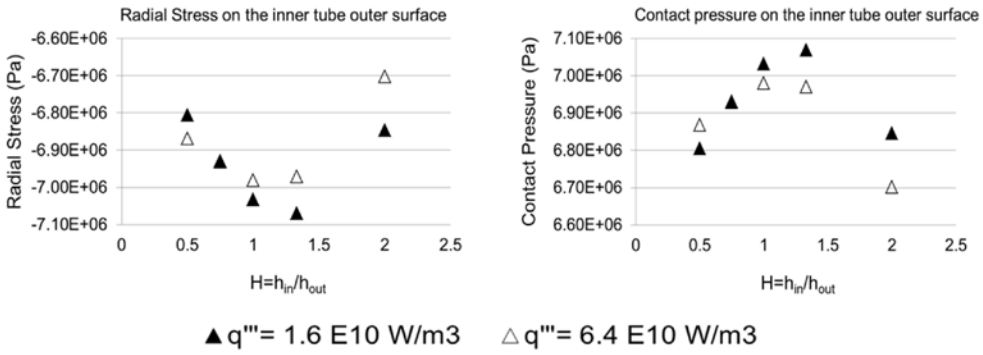

Figure 62. Radial stress distribution and contact pressure on the outer surface of the inner tube for varying heat transfer coefficient ratios with T_{wall}=373 K for uniform heating.

From Figure 61, the maximum temperature on the inner tube outer surface occurs for a H ratio between 1 and 1.50 and also the temperatures on the inner tube outer surface are higher than on the inner surface of the inner tube (due to closer proximity to the heat generating LEU). Hence the magnitude of compressive hoop stresses on the inner tube will be maximum between H=1 and H=1.50.

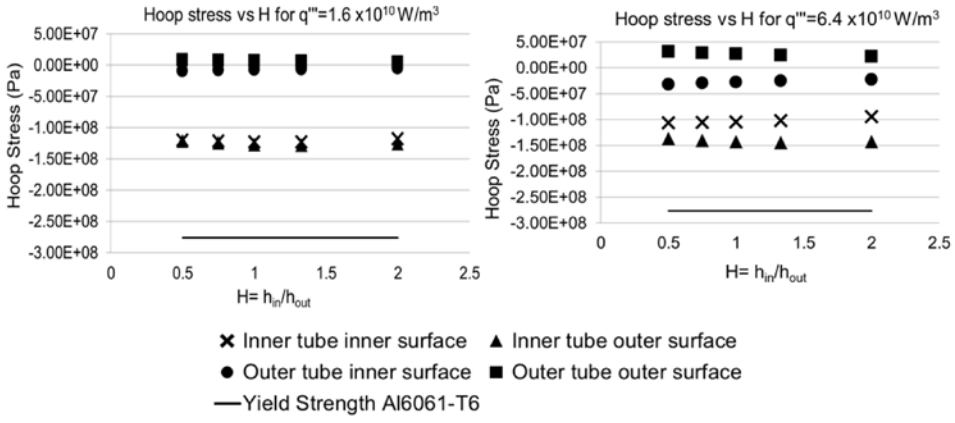

Figure 63. Hoop stress varying heat transfer coefficient ratios with T_{wall} = 373 K for uniform heating.

Figure 64 shows that the separation between the LEU foil and the outer tube cladding can be controlled by varying the heat transfer coefficient ratio. Greater separation will occur

for H > 1. This implies that the inner heat transfer coefficient ratio is greater than the outer tube. The final parameter of interest is the ratio of thickness of the inner tube to the outer tube. From Figure 60, the maximum compressive stress generated in the outer tube is about 30 MPa and this is within the yield strength of Aluminum 6061-T6. A comparison between Figure 60 and Figure 61 shows that the magnitude of compressive hoop stress on the inner tube is higher than the compressive hoop stresses on the outer tube by an order of magnitude. Hence failure of the inner tube will dictate the failure of the target. Due to this it was decided to analyze the hoop stresses on the inner and outer surfaces of the inner tube. This tube thickness ratio study was carried out with the inner surface of the inner tube and the outer surface of the outer tube kept at 373 K. The thickness ratios were varied according to Table 6.

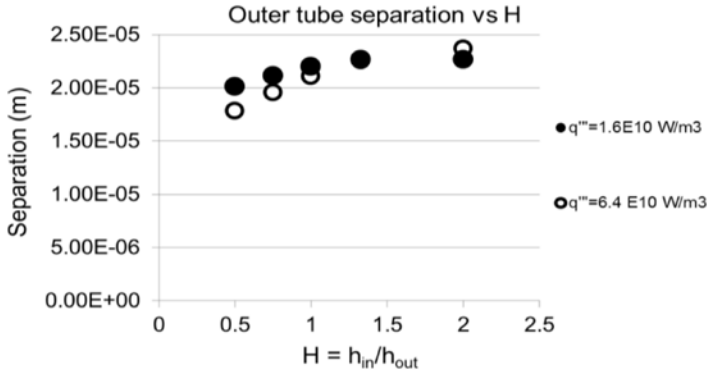

Figure 64. Separation at the interface of the outer tube and LEU foil for varying heat transfer coefficient ratios with T_{wall}= 373 K for uniform heating.

Figure 65 provides the variation of hoop stresses with tube thickness ratio. For a given heat generation rate of the LEU the magnitude of compressive hoop stresses is greater for lower thickness ratios. This is because the thickness of the inner tube is much smaller than that of the outer tube. Hence for a given heat generation rate the magnitude of compressive hoop stresses will be greater.

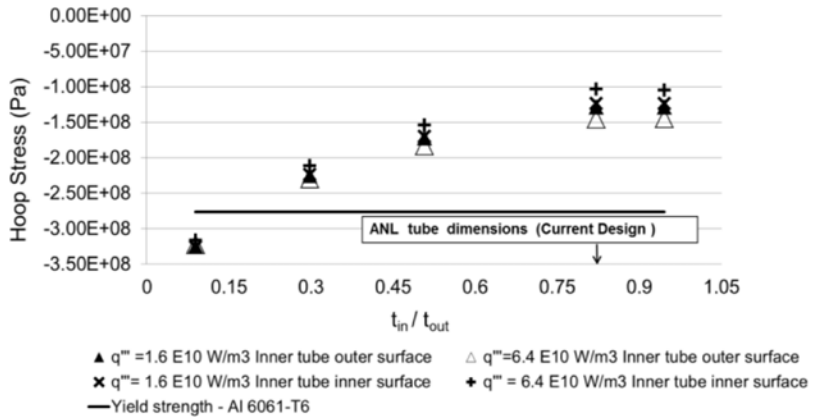

Figure 65. Hoop stress in the inner tube for varying heat transfer coefficient ratios with T_{wall} =373 K for uniform heating.

The tube thickness study plots also confirm that the annular target design of Argonne National Lab falls in the safe operating zone (since its stresses are within the material yield strength) with a thickness ratio of 0.82. The general parametric studies (no restriction on wall temperature) will be presented now. Though most of the trends are likely to be the similar to the results where the wall temperature was maintained at 373 K, the magnitudes will be different. Figure 66- Figure 68 provide the trends for the temperatures, radial and hoop stresses in the cladding for varying LEU heat generation rates according to Table 3. Since the explanation for the behavior of these trends has already been provided previously, they will be explained only briefly to maintain conciseness. The temperature distribution in Figure 66 shows higher temperature magnitudes as compared to when the wall temperatures are held constant as in Figure 58. The trends however remain the same. Figure 67 shows the radial stress distribution on the inner tube for various heat generation rates of LEU. A common trend noticed here is that the magnitude of stresses increases with increasing heat generation rates. This is because the stresses are driven primarily by the temperature gradients and a higher heat flux

would imply comparatively higher temperature gradients in the inner and the outer aluminum cladding.

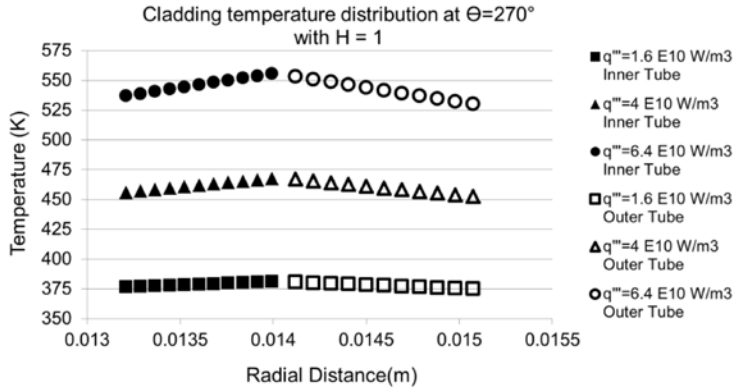

Figure 66. Cladding temperature distribution for varying LEU heat generation rates with the heat transfer coefficient ratio H=1, with no restrictions on wall temperature and for uniform heating.

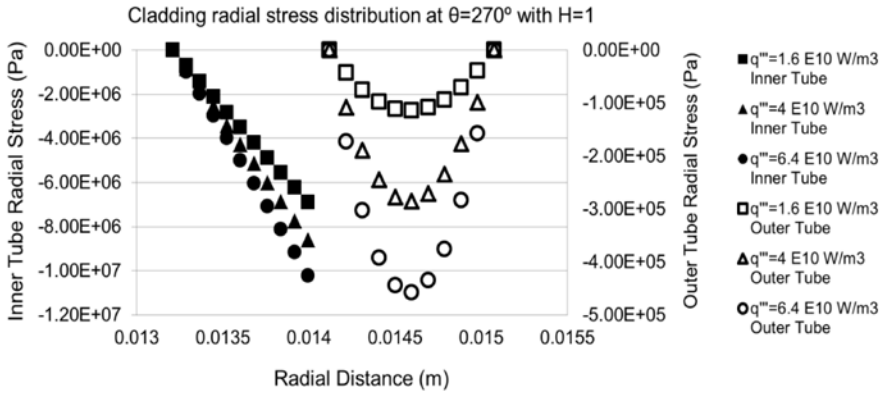

Figure 67. Radial stress distribution in the cladding for varying LEU heat generation rates with the heat transfer coefficient ratio H=1, with no restrictions on wall temperatures and for uniform heating.

Figure 68 provides the hoop stresses across the radius of the inner and outer tubes. As explained earlier the hoop stresses across the radius of the outer tube change from being compressive to tensile due to the expansion of the inner surface being resisted by the outer surface and in expanding the inner surface tries to push the outer surface thus generating tensile stresses. The stresses are compressive on the inner tube due to the direction of heat flow which influences the way in which the inner and outer surfaces of the inner tube expands. The next parameter to be varied is the ratio of the inner to outer

heat transfer coefficient ratio according to Table 5 and the results for this study have been provided by Figure 67-Figure 72.

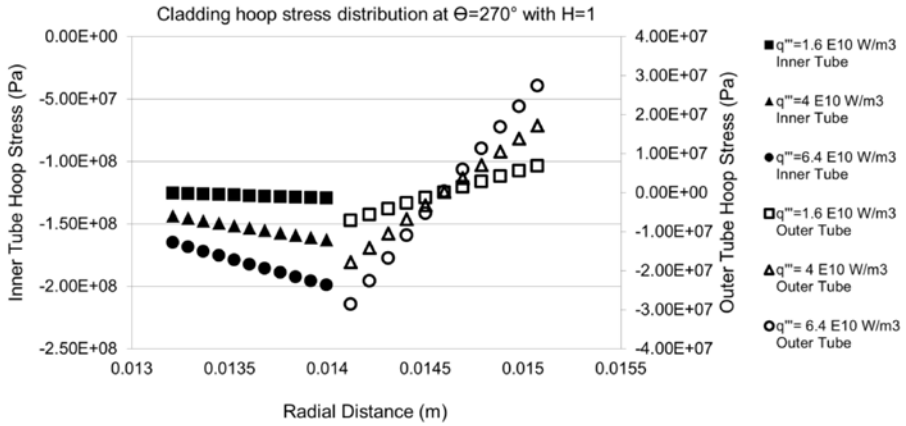

Figure 68. Hoop stress distribution in the cladding for varying LEU heat generation rates with the heat transfer coefficient ratio H=1, with no restrictions on wall temperature and for uniform heating.

Figure 69 illustrates the variation of temperature at the outer and inner surfaces of the tubes for various heat transfer coefficient ratios. A heat transfer coefficient ratio below 1 implies that the outer surface heat transfer coefficient is greater than that of the inner surface while a heat transfer coefficient ratio greater than 1 implies a higher inner surface heat transfer coefficient. Figure 69 shows that as the heat generation rate increases, for a given heat transfer coefficient ratio, the magnitude of temperature at a given location is comparatively larger. Also, when the inner surface of the inner tube is at a lower heat transfer coefficient than the other tube, then the outer surface of the outer tube is at a higher temperature than the inner surface of the inner tube. This is due to an inverse relationship that exists between the heat transfer coefficient and the temperature gradient. For a given heat flux, a lower heat transfer coefficient will result in a higher temperature gradient as compared to when a higher heat transfer coefficient exists. At a heat transfer coefficient ratio of 1 (H=1) the inner tube inner surface is at a higher temperature than the outer tube outer surface. This is because the surface area of the inner tube is smaller

compared to that of the outer tube. Hence for a given heat flux and heat transfer coefficient, a smaller area will result in a larger temperature gradient. Figure 70 illustrates the effect of varying the heat transfer coefficient ratio, on the radial stresses and contact pressure on the outer surface of the inner tube. The inner surface of the inner tube is free from any loading and hence the radial stress on this surface is zero. Similarly the inner and outer surfaces of the outer tube are free from external loading as the outer tube separates from the foil. As a result the radial stresses on these surfaces are zero as well.

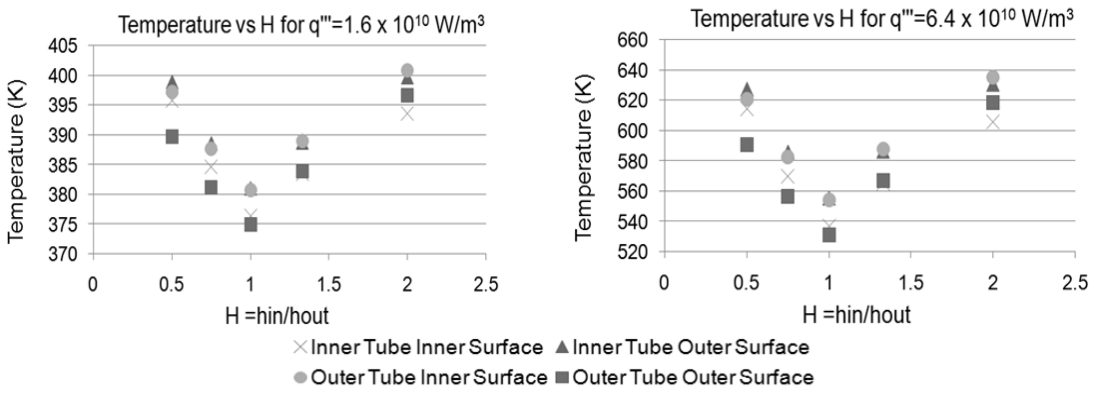

Figure 69. Temperature distribution in the cladding with varying heat transfer coefficient ratios for uniform heating with no restrictions on wall temperature.

From Figure 70 it is evident that the radial stresses are comparatively higher at a higher heat flux, due to higher temperature gradients for the same heat transfer coefficient ratio. Also, the outer surface of the inner tube experiences a higher compressive stress when the inner tube heat transfer coefficient is lower than that of the outer tube. This is because a lower heat transfer coefficient will increase the temperature gradient at that point as seen in Figure 69.

A heat transfer coefficient ratio of 1 (H=1) provides the least compressive stress. A higher contact pressure will exist when the inner tube thermally expands a lot more due to a higher temperature gradient. This is why at H=0.5 in Figure 70, the contact pressure

is the highest as the inner tube heat transfer coefficient takes its lowest value at this ratio. The hoop stress distribution in the tubes for a lower and a higher heat generation of LEU are provided in Figure 71. Figure 69 showed that the temperature increases on either side of H=1. Since the hoop stresses are driven by the temperature gradients, the magnitude of compressive hoop stresses will correspondingly increase on either side of H=1. At a higher heat generation rate the magnitude of compressive hoop stresses are larger than at a comparatively lower heat generation rate due to higher temperature gradients for the same heat transfer coefficient ratio. The inner surface of the inner tube is at a lower temperature compared to the outer surface of the inner tube, hence the magnitude of compressive stresses are lower.

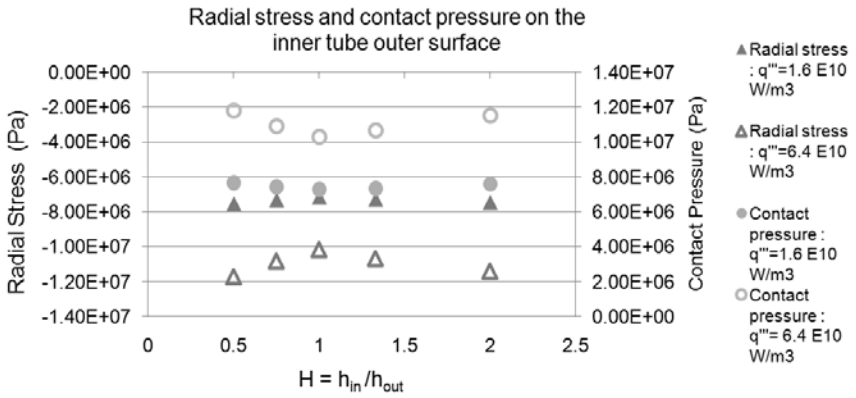

Figure 70. Radial stress and contact pressure distribution in the inner tube outer surface with varying heat transfer coefficient ratios for uniform heating with no restrictions on wall temperature.

Figure 72 shows that the separation that occurs between the foil and the outer tube can be controlled by varying the heat transfer coefficient ratio. It is observed that at higher heat generation rates, the magnitude of separation increases as the surfaces expand more due to comparatively higher temperature gradients. It is also shown that, for a given heat generation rate, greater separation occurs when the inner tube heat transfer coefficient is twice that of the outer tube. In Figure 72 for H<1 the separation is approximately a

constant. Hence a cooling scheme can be designed in such a way that there is more outer cooling if there is a coolant imbalance. The final parameter to be varied in the sensitivity studies with no restriction on wall temperatures was the ratio of the inner tube thickness to the outer tube thickness based on Table 6. Since this particular study imposes no restrictions on wall temperatures, it can be treated as a 'relief depth study' where the idea would be to see what minimum thickness is required in the inner tube to withstand the stresses at varying LEU heat generation rates and heat transfer coefficient ratios. The results have been provided by Figure 73 and Figure 74. Figure 73 provides the inner tube hoop stress variation for different tube thickness ratios and varying LEU heat generation rates with the heat transfer coefficient ratio H=1 ($h_{in}=h_{out}=19000$ W/m^{2}K).

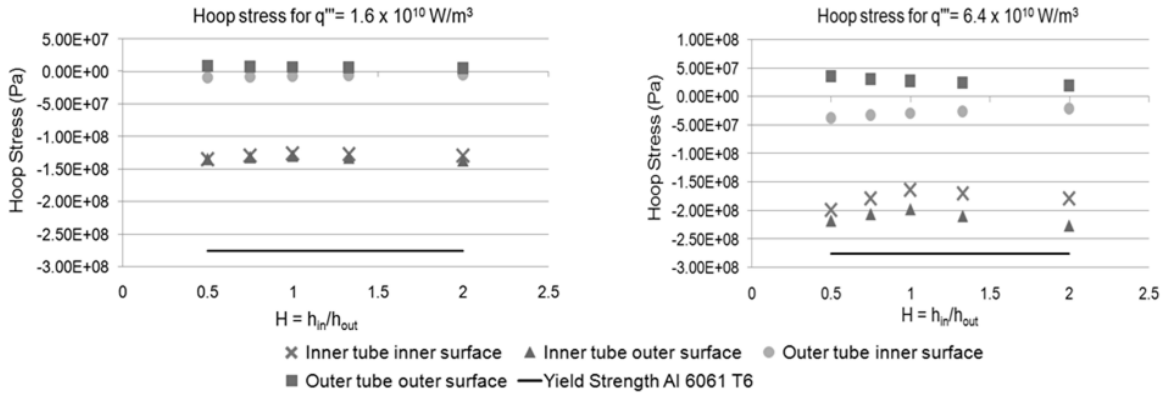

Figure 71. Hoop stress distribution in the cladding with varying heat transfer coefficient ratios for uniform heating with no restrictions on wall temperature.

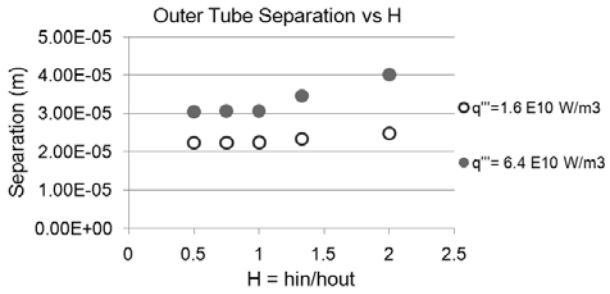

Figure 72. Separation at the interface of the foil and the outer tube with varying heat transfer coefficient ratios for uniform heating and no restrictions on wall temperature.

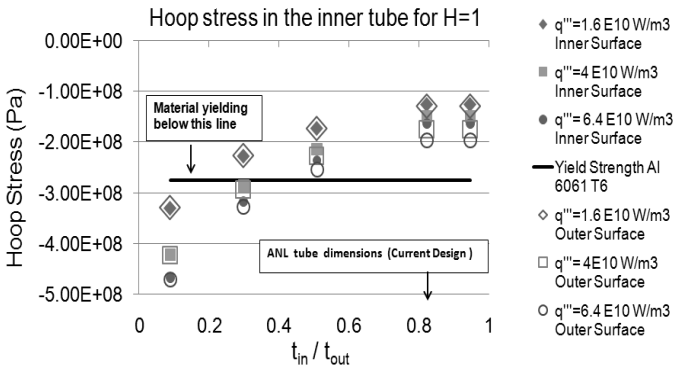

Figure 73. Variation of hoop stress in the inner tube at H=1 for different tube thickness ratios and LEU heat generation rates.

Figure 74 presents the inner tube hoop stress variation as the tube thickness ratio varies while considering a variation in heat transfer coefficient ratio to account for any uncertainties. From Figure 73 and Figure 74 it can be concluded that the current annular target design is unlikely to fail due to material yielding and for any tube thickness ratio < 0.3, the target is likely to fail due to the inability of the inner tube (cladding) to withstand the thermally induced stresses.

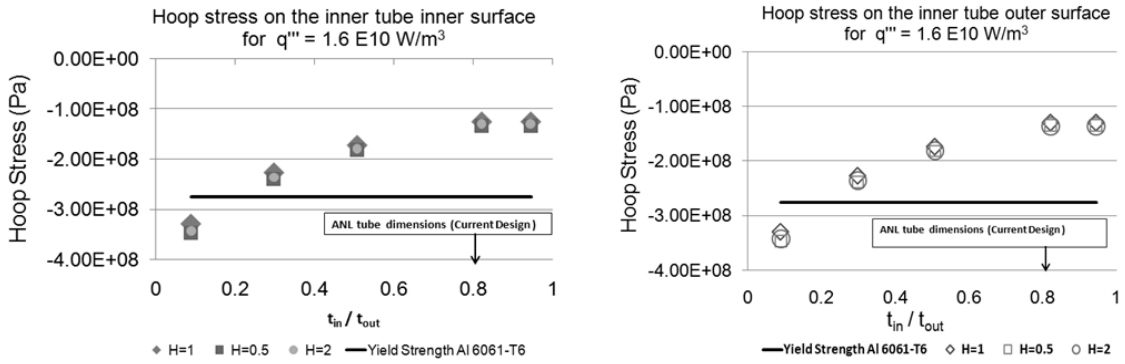

Figure 74. Hoop stress in the inner tube at q'''=1.6 E10 W/m^3 at various tube thickness and heat transfer coefficient ratios.

It should be noted that the results presented in this chapter and section are based on a purely elastic analysis, without considering the assembly residual stresses. The effects of the assembly residual stresses on the target will be addressed in subsequent chapters.

Chapter 6: Dimensionless Analytical Model- Uniform Heating

The dimensional form of the analytical model for uniform heating in a three layer annular cylinder in Sec. 4.3 is difficult to reproduce considering the length of the equations presented. It was decided to present those models in dimensionless form, which would make them more general and usable for design purposes, irrespective of the geometry and heat generation rates. The concept of thermal expansion mismatch has been used to develop an axisymmetric, non-dimensional, analytic solution, to predict the thermal mechanical behavior in a three layer composite cylinder. The middle cylinder represents the heat generating source and its thermal expansion coefficient being lesser than that of the two cylinders enclosing it. The development of the solution is based on the assumption that the separation occurs at the interface of the middle cylinder and the outer cylinder, while contact is reinforced between the middle cylinder and the inner cylinder. If the middle cylinder is assumed to be the uranium foil and the two cylinders enclosing it as the aluminum cladding, this dimensionless model can be applied to the current annular target configuration for a uniform heating condition.

6.1 Dimensionless Thermal-Mechanical Expressions

The dimensional form of the temperature and stresses, for the approach presented in Figure 26, is given by Eqs.(18)-(43). The following dimensionless quantities, given by Eq. (48), are used in developing the dimensionless expressions for the temperature distribution, interface temperature, radial stress, hoop stress, displacement and interface stress as given by Eqs. (49)- (54) respectively.

$$\left.\begin{aligned} R = \frac{r}{r_{out}};\ R_t = \frac{r_{in}}{r_{out}};\ Q = \frac{q_{gen}\left(r_{out}^2 - r_{in}^2\right)}{k\left(T_{in} - T_{out}\right)};\ \varepsilon_{th} = \alpha\left(T_{in} - T_{out}\right);\ U_{General} = \frac{u_{General}}{r_{out}} \\ \theta = \frac{T - T_{in}}{\left(T_{in} - T_{out}\right)};\ \sigma_{(R/H)General} = \frac{\sigma(1-\nu)}{E\,\varepsilon_{th}};\ \sigma_{IF,General} = \frac{\sigma_{Interface}\left(1-\nu_F\right)}{E_F\ \varepsilon_{th,F}} \end{aligned}\right\} \tag{48}$$

$$\theta_{General} = \frac{\ln\left(\frac{R}{R_t}\right)}{\ln\left(R_t\right)} + \frac{Q}{4}\left[\frac{\left(R_t^2 - R^2\right)}{\left(1-R_t^2\right)} - \frac{\ln\left(\frac{R}{R_t}\right)}{\ln\left(R_t\right)}\right] \tag{49}$$

$$\left.\begin{aligned} \theta_{IF} = \left[-\frac{\left(\frac{T_{in,IT} - T_{out,F}}{T_{in,F} - T_{out,F}}\right)}{1 + h_{ratio}\left(\frac{\ln\left(R_t\right)_F}{\ln\left(R_t\right)_{IT}}\right)} + \frac{Q}{4}\left(\frac{1 - 2\left(\frac{R^2\ln\left(R_t\right)}{\left(R_t^2 - 1\right)}\right)_F}{1 + h_{ratio}\left(\frac{\ln\left(R_t\right)_F}{\ln\left(R_t\right)_{IT}}\right)}\right)\right] \\ \text{where,} \\ h_{ratio} = \left(\frac{\left(\frac{k}{r}\right)_{IT}}{\left(\frac{k}{r}\right)_F}\right) \end{aligned}\right\} \tag{50}$$

$$\sigma_{R,General} = \left[\begin{aligned} &\left(\frac{R_t^2\left(1-R^2\right)\sigma_{IF}}{R^2\left(1-R_t^2\right)}\right)_F + \frac{R_t^2\left(1-R^2\right)}{2R^2\left(1-R_t^2\right)} + \left(\frac{\left(R^2 - R_t^2\right)\sigma_{IF}}{R^2\left(1-R_t^2\right)}\right)_{IT} - \frac{\ln\left(R\right)}{2\ln\left(R_t\right)} \\ &-\frac{Q}{16}\left(\frac{\left(1-R^2\right)\left(R_t^2 + R^2\right)}{R^2\left(1-R_t^2\right)} - \frac{2\ln\left(R\right)}{\ln\left(R_t\right)}\right) \end{aligned}\right] \tag{51}$$

$$\sigma_{H,General} = \left[\begin{aligned} &-\left(\frac{R_t^2\left(1+R^2\right)\sigma_{IF}}{R^2\left(1-R_t^2\right)}\right)_F - \frac{R_t^2\left(1+R^2\right)}{2R^2\left(1-R_t^2\right)} + \left(\frac{\left(R^2 + R_t^2\right)\sigma_{IF}}{R^2\left(1-R_t^2\right)}\right)_{IT} - \frac{1+\ln R}{2\ln\left(R_t\right)} \\ &+\frac{Q}{16}\left(\frac{3R^2 + \frac{R_t^2}{R^2} - \left(1-R_t^2\right)}{\left(1-R_t^2\right)} + \frac{2\left(1+\ln\left(R\right)\right)}{\ln\left(R_t\right)}\right) \end{aligned}\right] \tag{52}$$

$$U_{General} = \frac{\varepsilon_{th}\, R}{16}\left[\begin{array}{l} -\left(\frac{16\,\sigma_{IF} R_t^2}{R^2\left(1-R_t^2\right)}\left(\frac{1+\nu}{1-\nu}+\frac{R^2(1-2\nu)(1+\nu)}{(1-\nu)}\right)\right)_F + \frac{16\,T_{out}(1+\nu)}{T_{in}-T_{out}} \\ +\left(\frac{16\,\sigma_{IF}\, R_t^2}{R^2\left(1-R_t^2\right)}\left(\left(\frac{1+\nu}{1-\nu}\right)+\frac{R^2(1-2\nu)(1+\nu)}{R_t^2(1-\nu)}\right)\right)_{IT} \\ -\frac{8(1+\nu)(1-\nu-\ln(R))}{(1-\nu)\ln(R_t)} - \frac{8\,R_t^2\left(\frac{1+\nu}{1-\nu}+\frac{R^2(1-2\nu)(1+\nu)}{1-\nu}\right)}{\Re^2\left(1-\Re_t^2\right)} \\ +Q\left(\begin{array}{l}\frac{2(1+\nu)(1-\nu-\ln(R))}{(1-\nu)\ln(R_t)} - \frac{\left(R^2-\frac{R_t^2}{R^2}\right)(1+\nu)}{\left(1-R_t^2\right)(1-\nu)} \\ +\frac{\left(3\left(\frac{1+\nu}{1-\nu}\right)+\frac{R_t^2(1-2\nu)(1+\nu)}{(1-\nu)}-2\nu\left(\frac{1+\nu}{1-\nu}\right)\right)}{\left(1-R_t^2\right)}\end{array}\right) \end{array}\right] \tag{53}$$

$$\sigma_{IF} = \frac{\left\{\begin{array}{l} -\left(\frac{T_{out}(1+\nu)}{T_{in}-T_{out}}\right)_F\left(Z\left(\frac{T_{out}(1+\nu)}{T_{in}-T_{out}}\right)_{IT}\left(\frac{T_{in}-T_{out}}{T_{out}(1+\nu)}\right)_F-1\right)+ \\ \left(\frac{R_t^2\left(\frac{1+\nu}{1-\nu}+\frac{R^2(1+\nu)(1-2\nu)}{(1-\nu)}\right)}{2R^2\left(1-R_t^2\right)}\right)_F\left(\frac{Z\left(\frac{R_t^2}{1-R_t^2}\right)_{IT}\left(\frac{1-R_t^2}{R_t^2}\right)_F\left(\frac{(1+\nu)}{R^2(1-\nu)}+\frac{(1+\nu)(1-2\nu)}{(1-\nu)}\right)_{IT}}{\left(\frac{(1+\nu)}{R^2(1-\nu)}+\frac{(1+\nu)(1-2\nu)}{(1-\nu)}\right)_F}-1\right) \\ +\left(\frac{(1+\nu)(1-\nu-\ln(R))}{2(1-\nu)\ln(R_t)}\right)_F\left(\frac{Z\left(\frac{(1+\nu)}{(1-\nu)}\frac{(1-\nu-\ln(R))}{\ln(R_t)}\right)_{IT}}{\left(\frac{(1+\nu)}{(1-\nu)}\frac{(1-\nu-\ln(R))}{\ln(R_t)}\right)_F}-1\right) \\ +\frac{Q}{16}\left(\begin{array}{l}\frac{\left(R^2-\frac{R_t^2}{R^2}\right)(1+\nu)}{\left(1-R_t^2\right)(1-\nu)}-\frac{\left(3\left(\frac{1+\nu}{1-\nu}\right)+\frac{R_t^2(1+\nu)(1-2\nu)}{1-\nu}-2\nu\left(\frac{1+\nu}{1-\nu}\right)\right)}{\left(1-R_t^2\right)} \\ -\frac{2(1+\nu)(1-\nu-\ln(R))}{(1-\nu)\ln(R_t)}\end{array}\right)_F \end{array}\right\}}{\left(\begin{array}{l}\left(\frac{R_t^2}{R^2\left(1-R_t^2\right)}\left(\frac{1+\nu}{1-\nu}+\frac{R^2(1+\nu)(1-2\nu)}{(1-\nu)}\right)\right)_F+ \\ E_{ratio}\left(\frac{R_t}{R(1-\nu)}\right)_F\left(\frac{R_t^2(1-\nu)}{R\left(1-R_t^2\right)}\right)_{IT}\left(\frac{(1+\nu)}{(1-\nu)}+\frac{R^2(1+\nu)(1-2\nu)}{R_t^2(1-\nu)}\right)_{IT}\end{array}\right)} \tag{54}$$

where,

$$Z = \varepsilon_{th,ratio}\left(\frac{R_{IT}\, R_{t,F}}{R_F}\right);\ \varepsilon_{th,ratio} = \left(\frac{\varepsilon_{th,IT}}{\varepsilon_{th,F}}\right);\ E_{ratio} = \frac{E_F}{E_{IT}}$$

In Eqs. (49)- (54) the parameters 'R' and 'R_t' represent a dimensionless length scale as given by Eq. (48). Therefore 'R^2' and 'R_t^2' will represent the dimensionless area ratios in Eqs. (49)- (54). In Eq.(50), the parameter 'h_{ratio}' represents the ratios of thermal conductivity to a dimensional length scale for the inner tube and foil. Hence 'h_{ratio}' can be considered to be a thermal conductance ratio of the inner tube to the foil as defined in Eq.(50). The generalized non-dimensional radial stress and hoop stress are given by Eqs. (51) and (52) respectively. The first and third terms represent the product of the non-dimensional interface stress and area ratios given by 'R^2' and 'R_t^2'. The product of the non-dimensional stress and the dimensionless area can be considered to represent a dimensionless force at the interface of the inner tube and the foil.

Equations (53) and (54) represent the radial displacement and the interfacial stress respectively. In these equations the ratio of the poisson's ratio can be represented by the bulk modulus (κ) and the shear modulus (G) of the material as given by Eq. (55).

$$\left.\begin{aligned} \nu &= \frac{3\kappa - 2G}{6\kappa + 2G} \\ \frac{1+\nu}{1-\nu} &= \frac{9\kappa}{3\kappa + 4G} \\ \frac{(1+\nu)(1-2\nu)}{(1-\nu)} &= \frac{27\,\kappa\, G}{(3\kappa + G)(3\kappa + 4G)} \end{aligned}\right\} \tag{55}$$

The bulk modulus (κ) and the shear modulus (G) can also be expressed as functions of the elastic modulus of the material. Based on this definition, the ratio of poisson's ratio can be interpreted as the ratio of the material modulus (bulk, shear or elastic). As the bulk modulus represents the response of a material in a compressive state, it can be effectively used to describe the stresses and displacement given by Eqs. (51)- (54). It should be noted that the substitution of Eq. (55) in each of Eqs. (51)- (54) will present the

expressions as functions of the bulk modulus, shear modulus and the elastic modulus. These represent the material's response to a state of compression, shear stress and linear stress respectively.

Equations (49)- (54) represent generalized expressions for the temperature, stresses and displacement in the foil and the tubes. However, for the purpose of design and analysis, and to represent the trends in the same plot for comparative studies, all the parameters are normalized based on the properties and dimensions of the foil. The definitions for the modified, generalized, non-dimensional temperature, stresses and displacement are now represented by Eq.(56). Using these definitions, the modified temperature, stresses, and displacement are given by Eqs. (57)- (62) respectively.

$$\theta_{\mathbf{modified}} = \frac{\mathbf{T} - \mathbf{T_{coolant}}}{\left(\mathbf{T_{max}} - \mathbf{T_{coolant}}\right)};\ \boldsymbol{\sigma}_{(\Re/\mathbf{H}/\mathbf{IF})\mathbf{modified}} = \frac{\boldsymbol{\sigma}_{\mathbf{Interface}}\left(1-\boldsymbol{\nu}_{\mathbf{F}}\right)}{\mathbf{E_F}\ \boldsymbol{\varepsilon}_{\mathbf{th,F}}};\ \mathbf{U}_{\mathbf{modified}} = \frac{\mathbf{u_{General}}}{\mathbf{r_{out,F}}} \tag{56}$$

$$\theta_{\text{modified}} = \frac{T_{in} - T_{out}}{T_{max} - T_{coolant}}\left[\frac{T_{in} - T_{coolant}}{T_{in} - T_{out}} + \frac{\ln\left(\frac{R}{R_t}\right)}{\ln\left(R_t\right)} + \frac{Q}{4}\left[\frac{\left(R_t^2 - R^2\right)}{\left(1-R_t^2\right)} - \frac{\ln\left(\frac{R}{R_t}\right)}{\ln\left(R_t\right)}\right]\right] \tag{57}$$

$$\theta_{\text{IF,modified}} = \frac{T_{in,F} - T_{out,F}}{T_{max} - T_{coolant}}\left[\frac{T_{in,IT} - T_{coolant}}{T_{in,F} - T_{out,F}} - \frac{\left(\frac{T_{in,IT} - T_{out,F}}{T_{in,F} - T_{out,F}}\right)}{\left(1 + h_{ratio}\left(\frac{\ln\left(R_t\right)_F}{\ln\left(R_t\right)_{IT}}\right)\right)} + \frac{Q}{4}\left(\frac{1 - 2\left(\frac{R^2\ln\left(R_t\right)}{\left(R_t^2 - 1\right)}\right)_F}{1 + h_{ratio}\left(\frac{\ln\left(R_t\right)_F}{\ln\left(R_t\right)_{IT}}\right)}\right)\right] \tag{58}$$

$$\sigma_{\Re,\text{modified}} = \left(\frac{\sigma_{\Delta T,IT}}{\sigma_{\Delta T,F}}\right)_{IT}\left[\left(\frac{R_t^2\left(1-R^2\right)\sigma_{IF}}{R^2\left(1-R_t^2\right)}\right)_F + \frac{R_t^2\left(1-R^2\right)}{2R^2\left(1-R_t^2\right)} + \left(\frac{\left(R^2 - R_t^2\right)\sigma_{IF}}{R^2\left(1-R_t^2\right)}\right)_{IT} - \frac{\ln\left(R\right)}{2\ln\left(R_t\right)} - \frac{Q}{16}\left(\frac{\left(1-R^2\right)\left(R_t^2 + R^2\right)}{R^2\left(1-R_t^2\right)} - \frac{2\ln\left(R\right)}{\ln\left(R_t\right)}\right)\right] \tag{59}$$

$$\sigma_{H,modified} = \left(\frac{\sigma_{\Delta T,IT}}{\sigma_{\Delta T,F}}\right)_{IT}\left[\begin{array}{l} -\left(\frac{R_t^2\left(1+R^2\right)\sigma_{IF}}{R^2\left(1-R_t^2\right)}\right)_F - \frac{R_t^2\left(1+R^2\right)}{2R^2\left(1-R_t^2\right)} + \left(\frac{\left(R^2+R_t^2\right)\sigma_{IF}}{R^2\left(1-R_t^2\right)}\right)_{IT} \\ -\frac{1+\ln(R)}{2\ln(R_t)} + \frac{Q}{16}\left(\frac{3R^2+\frac{R_t^2}{R^2}-\left(1-R_t^2\right)}{\left(1-R_t^2\right)} + \frac{2\left(1+\ln(R)\right)}{\ln(R_t)}\right) \end{array}\right] \tag{60}$$

$$\left(\frac{\sigma_{\Delta T,IT}}{\sigma_{\Delta T,F}}\right)_{IT} = \left(\frac{\frac{E_{IT}\,\varepsilon_{th,IT}}{1-\nu_{IT}}}{\frac{E_F\,\varepsilon_{th,F}}{1-\nu_F}}\right)_{IT} \tag{61}$$

$$U_{modified} = \frac{\left(\frac{\varepsilon_{th}\,R\,r_{out}}{r_{out,F}}\right)_{IT}}{\frac{16}{\left(R\,\varepsilon_{th}\right)_F}}\left[\begin{array}{l} -\left(\frac{16\,\sigma_{IF}R_t^2}{R^2\left(1-R_t^2\right)}\left(\frac{1+\nu}{1-\nu}+\frac{R^2(1-2\nu)(1+\nu)}{(1-\nu)}\right)\right)_F + \frac{16\,T_{out}(1+\nu)}{T_{in}-T_{out}} \\ +\left(\frac{16\,\sigma_{IF}\,R_t^2}{R^2\left(1-R_t^2\right)}\left(\left(\frac{1+\nu}{1-\nu}\right)+\frac{R^2(1-2\nu)(1+\nu)}{R_t^2(1-\nu)}\right)\right)_{IT} \\ -\frac{8(1+\nu)\left(1-\nu-\ln(R)\right)}{(1-\nu)\ln(R_t)} - \frac{8\,R_t^2\left(\frac{1+\nu}{1-\nu}+\frac{R^2(1-2\nu)(1+\nu)}{1-\nu}\right)}{R^2\left(1-R_t^2\right)} \\ +Q\left(\begin{array}{l} \frac{2(1+\nu)\left(1-\nu-\ln(R)\right)}{(1-\nu)\ln(R_t)} - \frac{\left(R^2-\frac{R_t^2}{R^2}\right)(1+\nu)}{\left(1-R_t^2\right)(1-\nu)} \\ +\frac{\left(3\left(\frac{1+\nu}{1-\nu}\right)+\frac{R_t^2(1-2\nu)(1+\nu)}{(1-\nu)}-2\nu\left(\frac{1+\nu}{1-\nu}\right)\right)}{\left(1-R_t^2\right)} \end{array}\right) \end{array}\right] \tag{62}$$

In Eqs.(59) and (60), the terms ' $\sigma_{\Delta T,IT}$' and ' $\sigma_{\Delta T,F}$' represent the thermal stress in the inner tube due to a temperature difference $\Delta T=T_{in}-T_{out}$. Therefore $\left(\sigma_{\Delta T,IT}/\sigma_{\Delta T,F}\right)_{IT}$ represents the ratio of thermal stresses due to a temperature difference ΔT across the inner tube and the outer tube. The definition of this ratio is given by Eq.(61). The subscripts 'IT' or 'F' indicate the applicability of the expression to either the inner tube

or the foil respectively. It should be noted that Eq. (61) is only applicable to the inner tube or the outer tube. Therefore it can be considered as a multiplying factor in Eqs. (59) and (60).

6.2 Dimensionless Model Results

The developed dimensionless model was applied to the current annular target for a uniform heating case, as in Sec 5.1, and the dimensionless numerical and analytical results were compared. The radial temperature distribution in the annular target assembly with Al 6061-T6 as the cladding material has been provided in Figure 75. The temperature distribution across the foil is parabolic since it is the heat generating source, and the temperature linearly decreases across the inner tube and the outer tube.

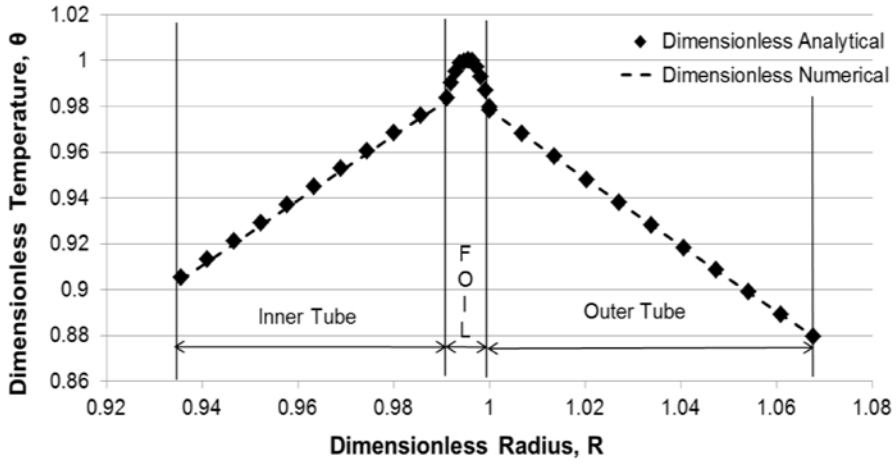

Figure 75. Dimensionless radial temperature distribution in the annular target.

The compressive radial stress distribution across the annular target assembly has been illustrated in Figure 76. It is to be noted here that the thermal expansion coefficient of the LEU foil ($\alpha_{uranium}$) is lesser than the inner tube ($\alpha_{aluminum}$). Hence, for radially inward heat flow into the inner tube, due to a higher thermal expansion coefficient, the outer surface of the inner tube tends to expand a lot more than the inner surface of the LEU foil. As a

result, the LEU foil acts as a barrier to the expansion of the inner tube, resulting in compressive stresses.

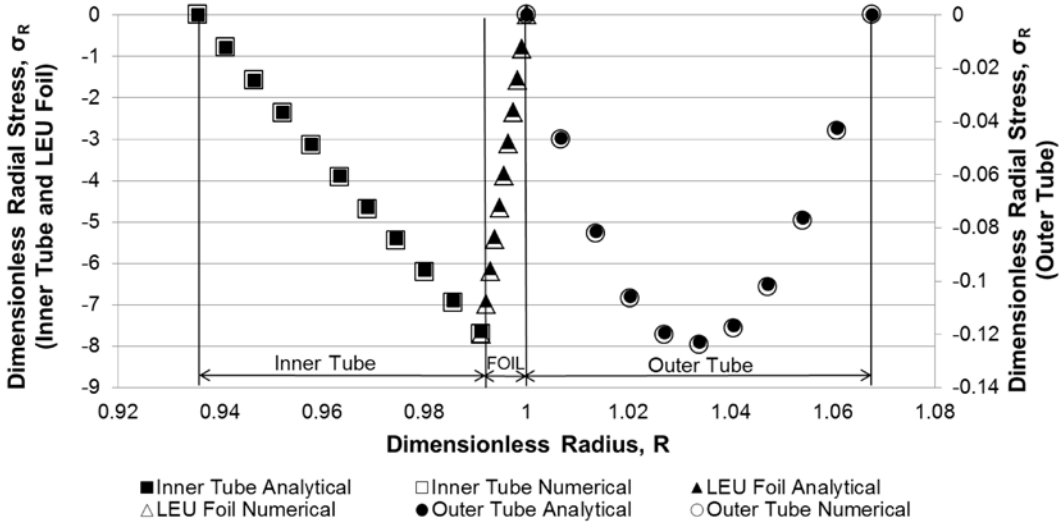

Figure 76. Dimensionless radial stress distribution in the annular target.

The hoop stresses across the inner tube and the outer tube has been provided in Figure 77. Across the radius of the inner tube, the hoop stresses are predominantly compressive in nature, while they move from being compressive to tensile towards the outer surface of the outer tube. A lower temperature gradient on the inner surface of the inner tube and the fact that the free expansion of the outer surface of the inner tube is restricted by the presence of the LEU foil results in compressive hoop stresses in the inner tube. The hoop stress variations in the outer tube can be attributed to radially outward heat flow through the outer tube and the expansion of the outer surface of the outer tube results in tensile stresses being generated across the outer half of the tube. The expansion of the inner surface is resisted by elements across the thickness of the tube and consequently the hoop stresses vary from compressive to tensile across the thickness of the outer tube.

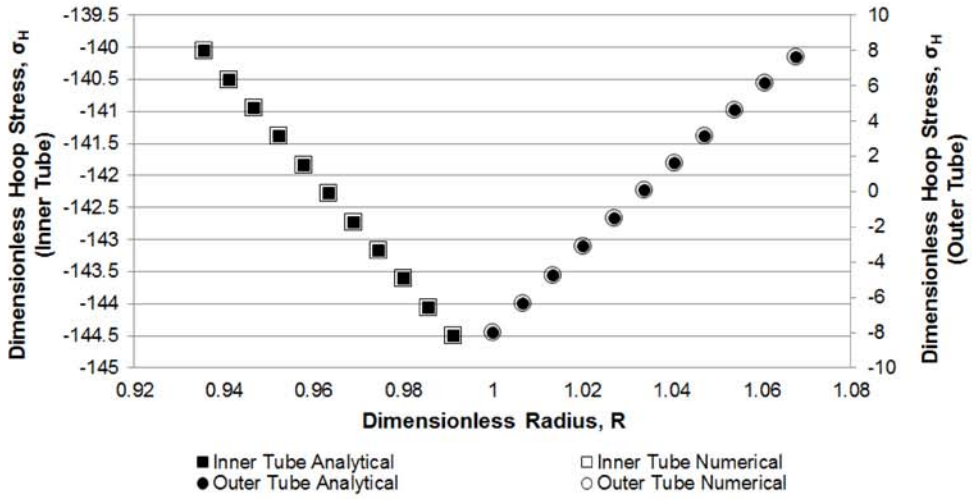

Figure 77. Dimensionless hoop stress distribution in the inner tube and the outer tube.

The radial displacement in the inner tube and the LEU foil has been provided in Figure 78 and that in the outer tube has been provided in Figure 79. Since the outer surface of the inner tube is at a higher temperature, the displacement of this surface is greater than the inner surface of the inner tube. For the inner tube-LEU foil composite, the maximum displacement is on the outer surface of the outer foil.

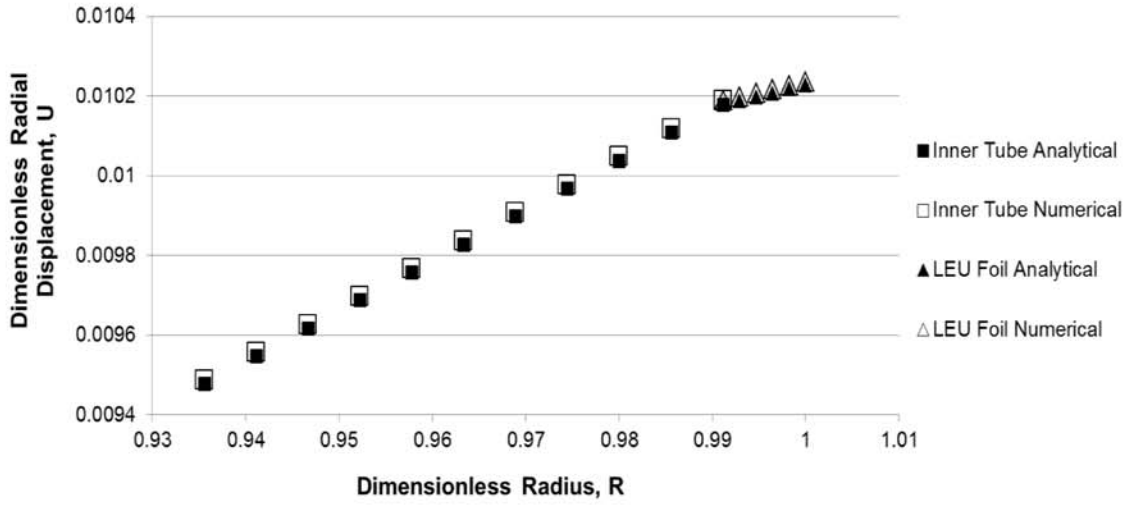

Figure 78. Dimensionless radial displacement in the inner tube and the LEU foil

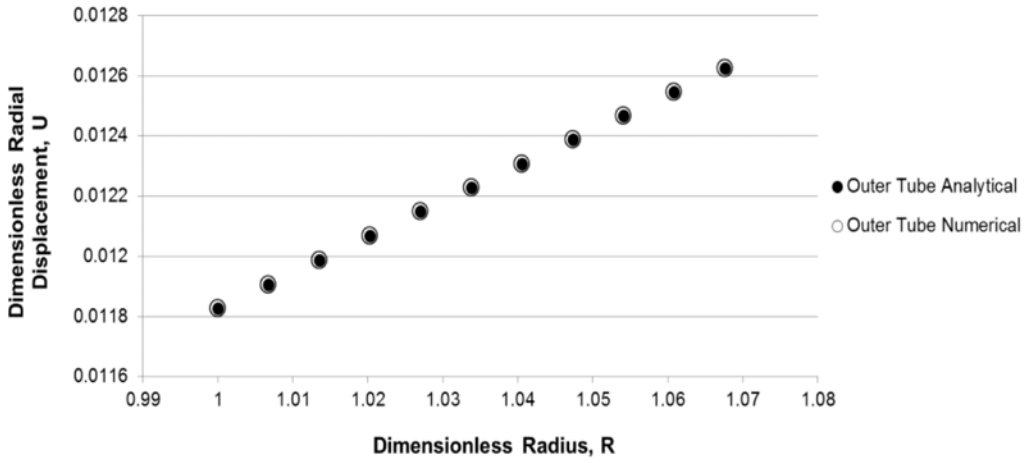

Figure 79. Dimensionless radial displacement in the outer tube.

The developed dimensionless model can be applied to any composite cylinder configuration to predict the temperatures, stresses and displacements. From an annular target standpoint, it can also be used to perform various parametric studies without much effort. Though the cladding material of choice in this analysis is Al 6061-T6, the aluminum alloy 3003-H14 has also been used in the past. The current dimensionless model can also be used to perform a comparative study between Al 3003-H14 and Al 6061-T6. Also, a tube thickness variation study can be performed by varying the dimensionless inner tube thickness '$1-R_t$'. Therefore the developed dimensionless model can be used as a useful design tool for a composite cylinder configuration.

Chapter 7: Modeling With Residual Stresses

While the previous section dealt with the elastic analysis of the annular target in a stress free state, this section will focus on including the assembly residual stresses. For this purpose it is required to develop an assembly model and use it in conjunction with the irradiation model. During the assembly process, an internal pressure is applied to the inner surface of the inner tube to close the gap between the foil and the outer tube. The internal pressure can be applied by either a draw plug or by using a pressurized hydraulic fluid [55]. The internal pressure applied to the inner tube causes it to expand and plastically deforms it. The magnitude of the required internal pressure is calculated by applying the condition that at the end of the process the LEU foil and the outer tube share a common interface.

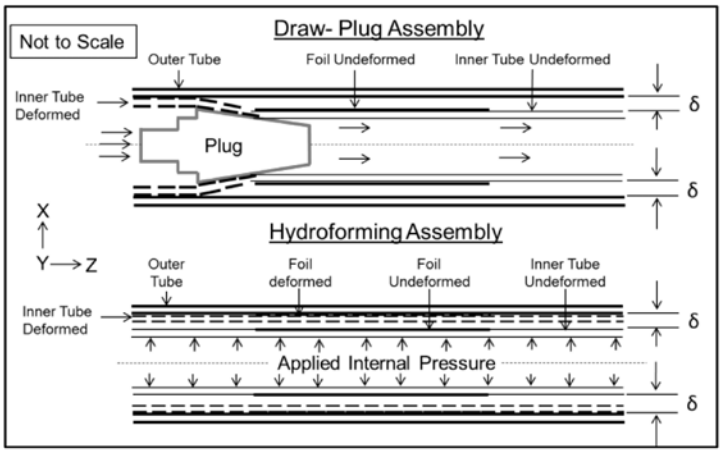

Figure 80. The draw-plug and the hydroforming assembly techniques.

The assembly process creates a sandwich structure where the interfaces between all the target components are in contact with one another. By design, the assembly process leaves residual stresses in the aluminum cladding. Analysis of the annular target without considering the residual stresses in the previous section (Sec 4) indicated that there exists

a natural tendency for a gap to open up between the foil and the outer tube. Hence it is important to model the irradiation process by including the assembly residual stresses and to design the assembly process such that the residual stresses help prevent any gaps from forming.

7.1 Hydroforming Assembly Description

The desired internal pressure for hydroforming was determined through a combined analytical and experimental approach. According to analytical plastic yield theory, the critical pressure which will cause yielding is given by Eq. (63) as

$$P_{crit} = \frac{\sigma_0}{2}\left(\frac{\frac{b^2}{a^2}-1}{\frac{b^2}{r^2}}\right) \tag{63}$$

where 'P_{crit}' is the critical pressure, 'σ_0' is the yield stress, 'b' is the outer diameter of the cylinder, and 'r' is the location of interest through the cylinder wall. Assuming 'r' to be the inner diameter (r =a) reduces Eq. (63) to Eq. (64) as given below. With the help of the inner tube dimensions (Figure 81) and the yield strength of Al 6061-T6 as 276 MPa, the calculated critical pressure using Eq. (64) was found to be 13.75 MPa. This is the pressure that will initiate yielding in the inner tube.

$$P_{crit} = \frac{\sigma_0}{2}\left(1-\frac{a^2}{2b^2}\right) \tag{64}$$

A parametric study is performed to determine the pressure that will nearly close the gap between the foil and the outer tube and is found to be 16.3 MPa. However, this 16.3 MPa does not induce enough plastic deformation to keep the gap closed after unloading. After

analytically determining the proper order for internal pressure, several tests were conducted to precisely determine the internal pressure required to close the gap. This was accomplished using a developed hydroforming test bench (Figure 82) in Dr. Sherif El-Gizawy's lab at the University of Missouri. Using this test bench, experiments were performed to determine the maximum pressure that will not rupture the target. This value was found to be 36.4 MPa. It was found that above this pressure the targets ruptured with both the inner and outer tubes splitting along the longitudinal relief where the inner and outer tubes were in direct contact, without the uranium in between.

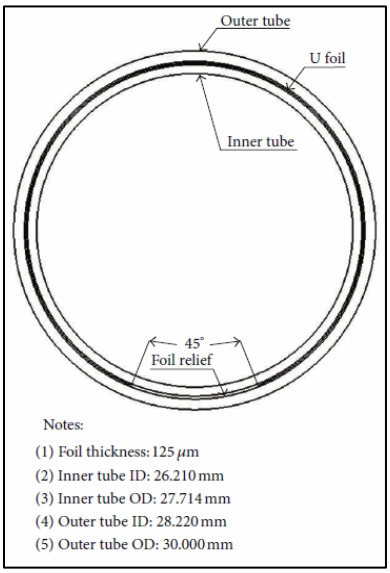

Figure 81. Drawing of the geometry in the first analysis step of the assembly simulation model.

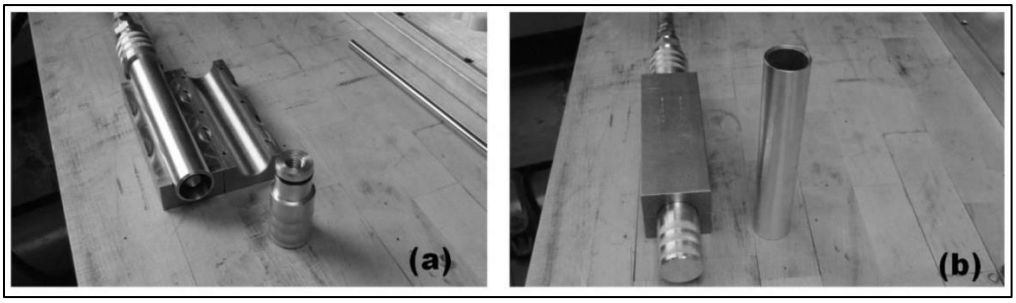

Figure 82. (a) Hydroforming test rig with the annular target in place and (b) assembled hydroforming test rig.

7.2 Draw-Plug Assembly Description

The draw- plug assembly of the annular target begins by wrapping the LEU foil with nickel foil (~ 15 µm thick). The nickel foil, as stated earlier, is used as a recoil barrier to prevent the LEU foil from bonding with the cladding. Various other metal foils (Zn, Al) have also been used as recoil barriers with different combinations of cladding materials [6]. The wrapped LEU foil with the recoil barrier is then inserted between two aluminum tubes (Al 3003-H14 or Al 6061-T6), that serve as the cladding, as illustrated in Figure 83. This combination is then placed inside a draw die and a plug made of D2 tool steel is driven through the inner tube using the setup shown in Figure 84.

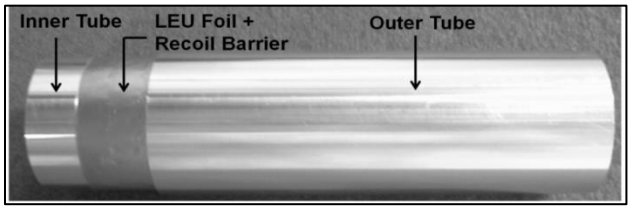

Figure 83. Pre-assembly state of the annular target.

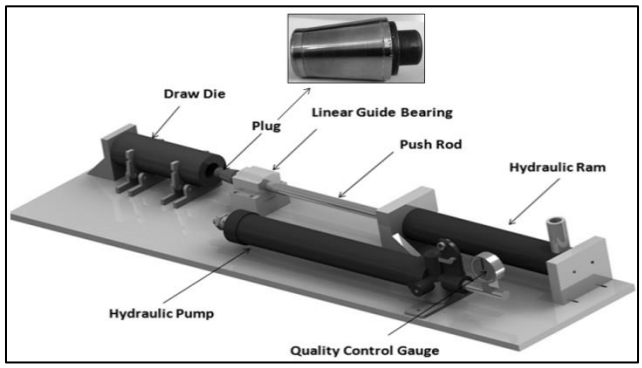

Figure 84. Draw-plug assembly device.

The draw-plug assembly process is expected to plastically deform the inner tube and elastically deform the outer tube. The purpose of the assembly process is to create a bonded composite structure by closing the macroscopic interfacial gaps.

Chapter 8: Hydroforming Assembly and Irradiation Analysis

8.1 Material Model

The assembled stress state of a target is important as it can either aid or hinder the disassembly process. In order to achieve a stress state that encourages the target to open after being cut longitudinally, the inner tube must be plastically deformed and the outer tube must be only elastically deformed. To simulate plastic deformation, a plastic material model must be defined within Abaqus. This data must be given in the form of true stress and plastic strain. In some cases, it may be necessary to convert engineering stress and strain to true stress and plastic strain.

As the tube material being investigated in this dissertation is Al 6061-T6, the true stress and plastic strain data for Al 6061-T6 was obtained from [64] while the flow curve equation based on [65] was used to construct the true stress vs. plastic strain curve for uranium as illustrated in Figure 85.The plasticity data supplied by [65] is in the form of strength coefficients and hardening exponents, *K* and *n* respectively. For unalloyed uranium, the alloy used in this study, *K* and *n* are 1.14 GPa and 0.23, respectively. These values are used in the plastic flow equation given by Eq. (65) as

$$\sigma = K\,\varepsilon^{n} \tag{65}$$

In Eq. (65)'σ' is true stress and 'ε' is plastic strain. It should be noted that according to [65] the values of the strength coefficient and strain hardening exponent are only valid for plastic strains between 0.001 and 0.01. The elastic material definitions are much simpler to create, requiring only the elastic modulus and Poisson's ratio. For the aluminum tubes,

the values used were 68.9 GPa and 0.33, respectively. The elastic modulus for uranium used was 208 GPa and the Poisson's ratio was 0.23 (typical for unalloyed metals). These are consistent with the cladding and foil material properties listed in Table 1.

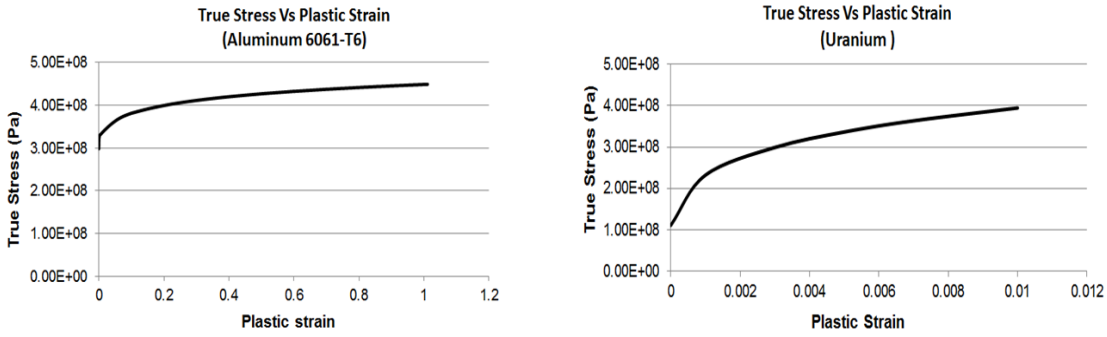

Figure 85. True stress and plastic strain curves for Al 6061-T6 and uranium.

8.2 Numerical Finite Element Model

A numerical model of the annular target assembly was created using the commercial finite element code Abaqus FEA (Figure 81). A three step analysis was created to model, the assembly of the tubes, the residual stresses, and the irradiation process. In the first step, the hydroforming assembly process is simulated by the application of a calculated internal fluid pressure. The second step is a zero pressure step, where the applied internal pressure is removed and the target is allowed to relax. Any remaining stresses in the target are the residual stresses that will help to keep gaps from forming between the LEU and cladding. The final step simulated is the irradiation heat generating process. This step is simulated by applying a volumetric heat generation rate to the LEU foil.

The finite element mesh used in the analysis, consisted of 16000 elements and 51221 nodes with 10 elements through the thickness of each assembly component, is illustrated in Figure 86. Thus, the final assembly consisted of 30 elements through all the

components. It is important to note that the assembly and the residual stress part were modeled as a fully coupled thermal stress problem instead of a static stress analysis. This makes it easier to add a third step to run the irradiation analysis. If a static stress analysis type is used for the first two steps, an Abaqus script file is required to input the residual stress data into the irradiation model which uses a fully coupled thermal stress step. Fully coupled quadratic reduced integration elements of type CPE8RT were used in the analysis.

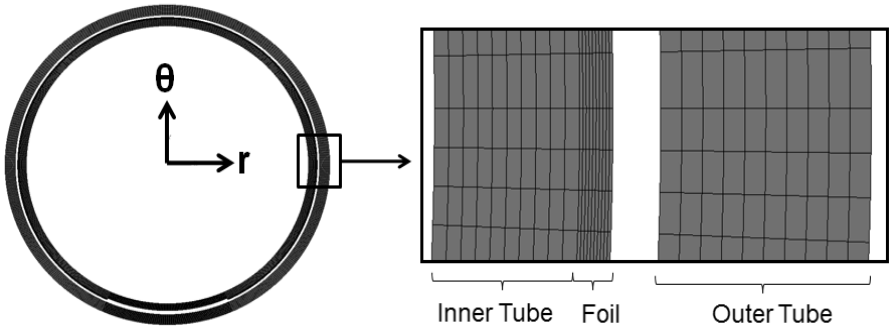

Figure 86. Finite element mesh used in the assembly and irradiation modeling.

The development of the assembly model follows directly from the Argonne National Lab (ANL) target design (Figure 14). Since the mechanical model was constructed in two dimensions, the relevant cross-sectional area of the target occurs at the midpoint of the target's length, such that the inner tube, outer tube, and uranium foil are all present in the model, as illustrated in Figure 81. As the model is based on the ANL target, all the tube dimensions are precisely those described by the technical drawing of that target. Again, because the cross-section occurs at a length along the target that includes the uranium foil, the dimensions of the inner tube correspond to the ANL foil relief specifications. In addition, it should be noted that the foil is assumed to be in perfect initial contact with the inner tube. While this is not necessarily the case with physical specimens, it is an

essential simplification to the model. The loading and boundary conditions for the assembly model have been provided in Figure 87. The calculated maximum allowable pressure using the hydroforming test bench experiments of 36.4 MPa was applied as an internal pressure to the annular target as shown in Figure 87.

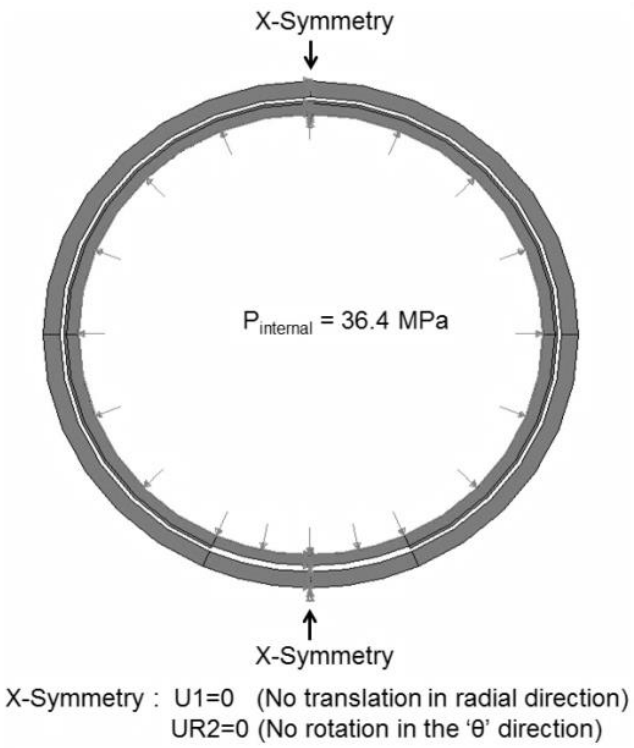

Figure 87. Loading and mechanical boundary conditions for the assembly hydroforming simulation in the first analysis step.

To model the irradiation behavior which takes into account the residual stresses from the assembly process, a fully coupled thermal stress step was added after the residual stress step. The loading conditions and the contact definitions from the first two steps were suppressed. A heat generation rate of 1.6 x 10^{10} W/m^3 was applied to the foil, which corresponds to a heat flux of 100 W/cm^2incident on the outer surface of the inner tube and the inner surface of the outer tube. Water coolant flow at 323 K through the inner and along the outer tubes was simulated by defining a surface heat transfer coefficient and a

sink temperature. A heat transfer coefficient of 19000 W/m^{2}K was used in the inner tube and for flow along the outer tube, maintaining the inner to outer heat transfer ratio at H=1. The loading and boundary conditions for the irradiation model are illustrated in Figure 88.

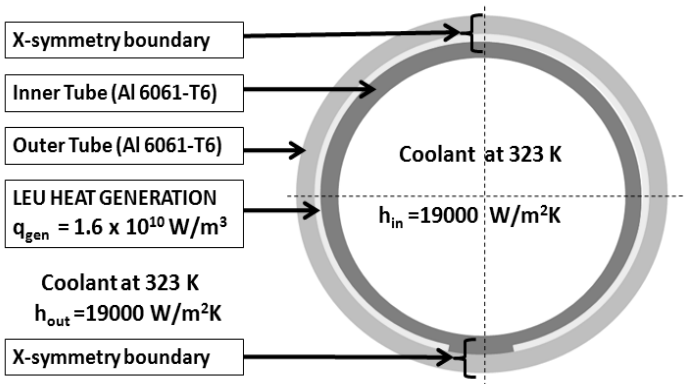

Figure 88. Loading and boundary conditions for the irradiation model in the third analysis step.

New contact definitions had to be made for the irradiation model due to the different contact interaction property for the normal behavior. For the irradiation model it is assumed that the tubes may have a tendency to separate after they come in contact whereas for the hydroforming part, the normal behavior does not allow any separation once the tubes are in contact. This is the main difference in the mechanical contact definition properties for the assembly and the irradiation part. Due to the composite structure of the model and the presence of interfaces, a thermal conductance had to be defined while defining the contact interaction properties. As the magnitude of the thermal conductance is unknown, an infinite conductance was specified at zero clearance and for a clearance of 0.01 m the thermal conductance is assumed to be zero. Abaqus interpolates between these values to obtain the thermal conductance for any interfacial gap in the

model. It is assumed that there is conduction through the air and the effects of heat redistribution haven't been considered in modeling the gap.

8.3 Hydroforming Analysis Results

Figure 8 illustrates the displacement contour after the first assembly step, which simulates the hydroforming process. Though the applied internal pressure closes the gap between the foil and the outer tube, a gap (~ 200 µm) still remains close to the edges of the foil, in the region between the inner and the outer tubes. The maximum displacement occurs in the inner tube at 180° as illustrated in Fig 8.

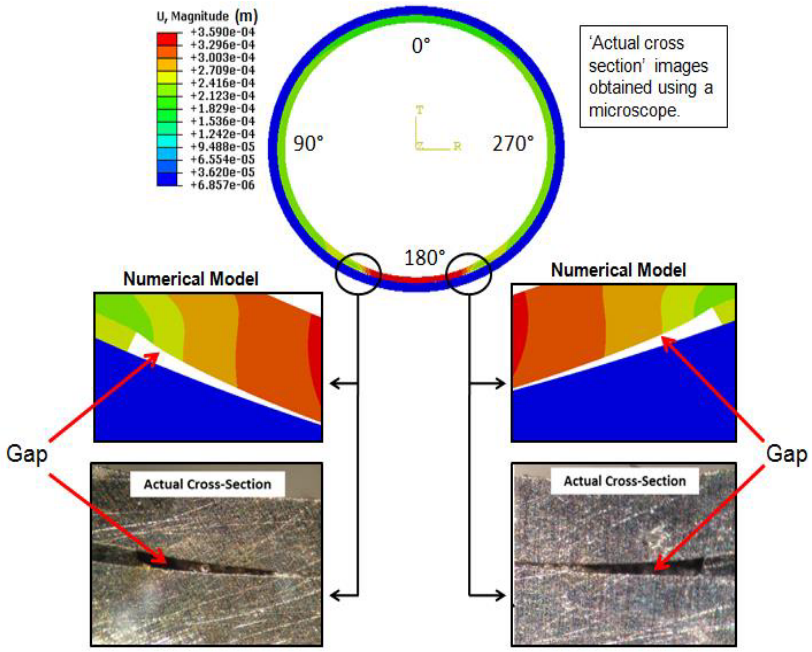

Figure 89. Numerical displacement contour and microscopic images of the annular target after the assembly process.

Figure 90 illustrates the equivalent plastic strain across the thickness of the annular target assembly. The Abaqus parameter name for this is 'PEEQ' and is used to evaluate the yield condition. For isotropic hardening and von Mises plasticity, PEEQ is defined as

$\sqrt{\frac{2}{3}d\varepsilon^{pl}:d\varepsilon^{pl}}$. It is essentially a scalar measure of all components of equivalent plastic strain in a model and a value of PEEQ greater than zero indicates that the material has already yielded. As expected, the combined effects of heating and assembly stresses result in a higher plastic strain at the end of the irradiation step than in the previous steps. Also, the plastic strain remains the same during the pressure relaxation step. This is because, when the applied load is removed the inner tube elastically recovers, but the plastic deformation due to the hydroforming process remains in the inner tube. Figure 90 also illustrates the plastic deformation in the outer tube. For the irradiation step, there is a small amount of plastic deformation in the outer tube while there is zero plastic deformation in the outer tube for the first two steps. This means that the plastic deformation in the outer tube at the end of the irradiation step is purely due to thermal effects.

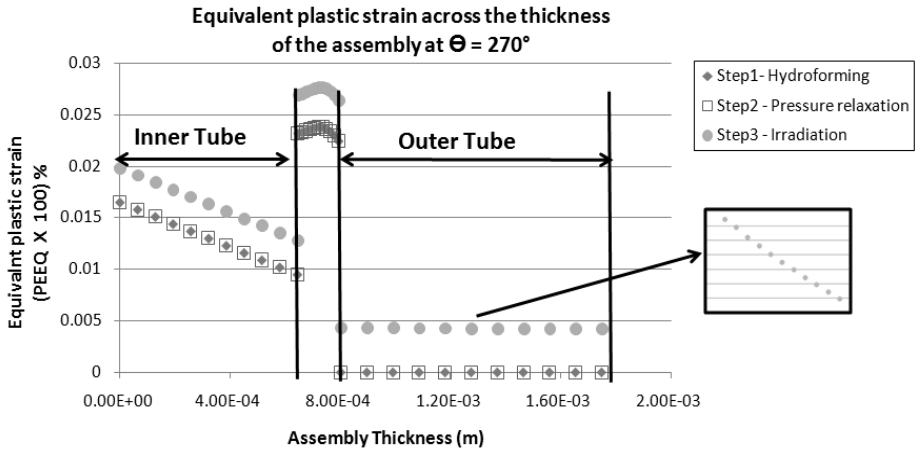

Figure 90. Equivalent plastic strain across the radius of the annular target at 0=270°.

One of the goals of the hydroforming process is to close the gap between the foil and the outer tube by plastically deforming the inner tube. The magnitude of the applied hydroforming pressure should be such that it should be able to close the gap between the

foil and the outer tube, induce sufficient plastic deformation in the inner tube so that even during elastic recovery an interfacial bond is maintained between the foil and the outer tube. Figure 91 illustrates the separation between the outer tube and the foil. For the hydroforming and the pressure relaxation step there is zero separation. This means that the applied hydroforming pressure of 36.4 MPa is sufficient to maintain the contact between the foil and the outer tube when elastic recovery occurs. However, a gap does open up during the irradiation step due to thermal expansion mismatch and radially outward heat flow.

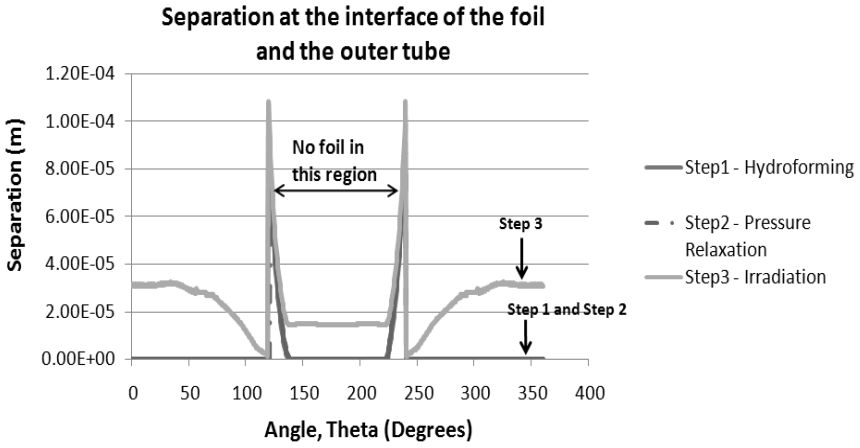

Figure 91. Separation at the interface of the foil and the outer tube after the various modeling steps.

Figure 92 illustrates the radial temperature distribution in the inner tube and outer tube cladding. The temperature decreases from the outer surface to the inner surface for the inner tube for radially inward heat flow and from the inner surface to the outer surface for the outer tube for radially outward heat flow. Due to the separation between the foil and the outer tube, there is a small temperature drop at this interface as illustrated in Figure 92. All the modeling was done by assuming a heat generation value that corresponds to a surface heat flux of 100 W/cm^2. Using this value of heat flux along with the small

temperature drop shown in Figure 92 results in a negligibly small value of thermal contact resistance. However, it remains to be seen if such a small value of thermal contact resistance is significant.

Figure 93 illustrates the hoop stress across the inner tube radius for all the steps in the model. Beginning with the hydroforming step (Figure 93a), the hoop stress is greater on the outer surface than on the inner surface of the inner tube. As the load is removed, the resulting residual hoop stresses drop by an order of magnitude. Figure 93b illustrates the variation of residual hoop stresses during the pressure relaxation step and during the irradiation step. These residual hoop stresses are compressive in the inner surface and the magnitude of compressive stress gradually decreases across the thickness.

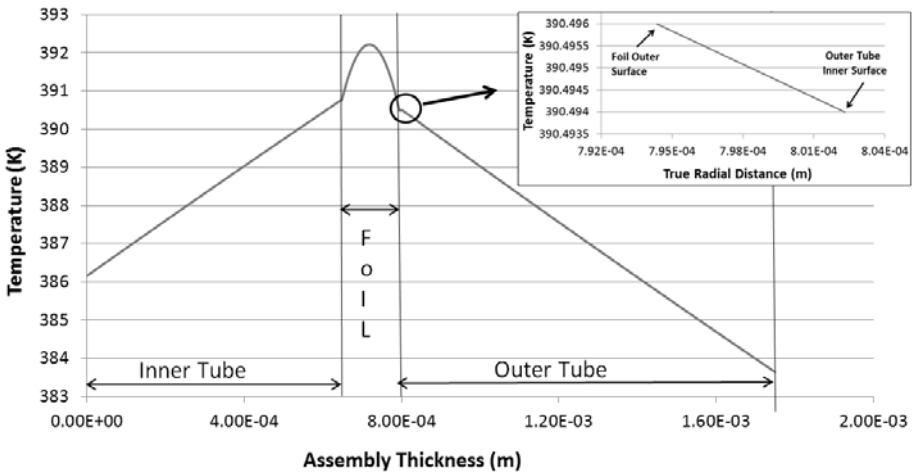

Figure 92. Radial temperature distribution across the inner and the outer cladding.

The maximum compressive stress is on the inner surface as this is where yielding begins. Previous analysis in Sec 4 has shown that for an elastic irradiation model of an annular target that begins from a zero residual stress state, the hoop stresses in the inner tube are completely compressive and increase towards the outer surface of the inner tube. This behavior can be obtained from Figure 93b by subtracting the residual stresses from the

post irradiation hoop stresses. This would effectively give the hoop stresses in a tube for zero residual stress state. Thus the tensile residual stresses reduce the amount of post irradiation hoop stresses in the inner tube.

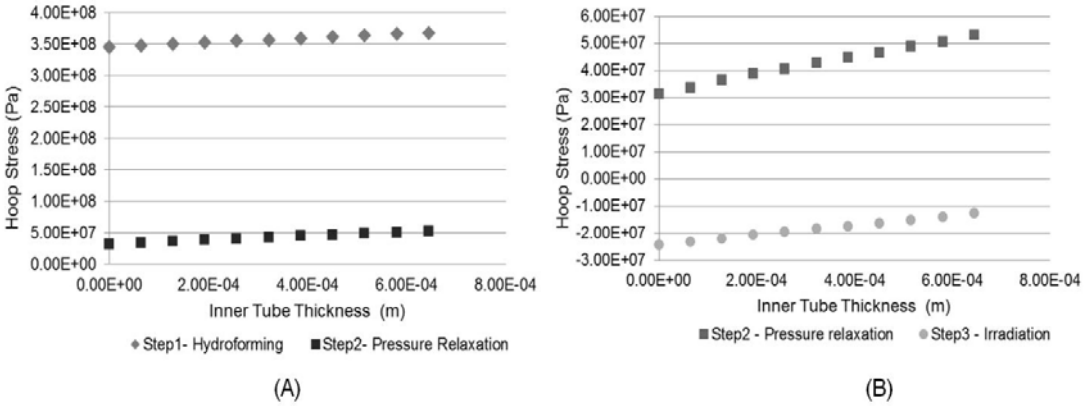

Figure 93. Hoop stress distribution in the inner tube through various modeling steps at θ=270°.

The hoop stresses in the outer tube through the three modeling steps have been illustrated in Figure 94. For the hydroforming process, the hoop stresses are greater on the inner surface than on the outer surface of the outer tube. The internal pressure applied during the hydroforming process causes the outer surface of the foil to be displaced towards the inner surface of the outer tube. When these interfaces meet, the inner surface of the outer tube is displaced outwards resulting in compressive stresses.

The residual stresses from the assembly process are completely compressive in the outer tube with the hoop stresses being higher on the inner surface. The resulting hoop stresses from the final irradiation step are compressive on the inner surface and tensile on the outer surface. This can be attributed to radially outward heat flow through the outer tube. The outer surface of the outer tube is unrestrained and therefore free to expand. The free expansion of the outer surface results in tensile stresses being generated across the outer

half of the tube but expansion of the inner surface is resisted by the elements across the thickness of the tube.

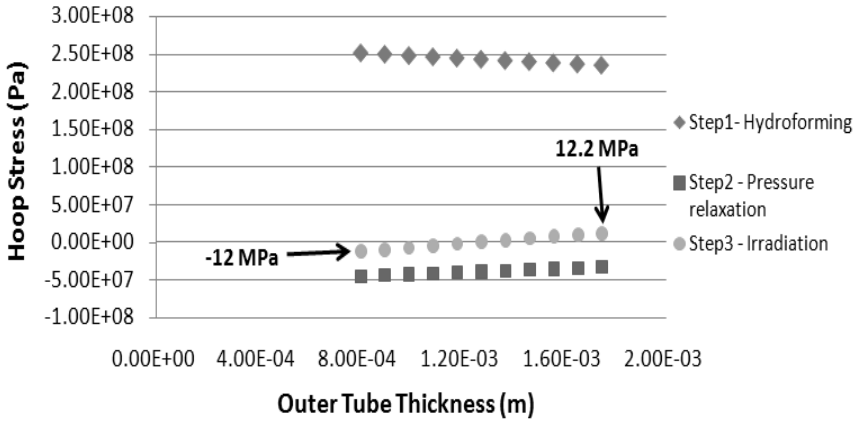

Figure 94. Hoop stress distribution in the outer tube through various modeling steps at θ=270°.

The results from the hydroforming analysis show that the applied internal pressure is adequate to induce enough plastic deformation to maintain the bond at the interface of the foil and the outer tube. The residual stresses from the assembly process tend to negate and decrease the hoop stresses in the inner and outer tubes at the end of the irradiation step. This is favorable from a material standpoint as the inner and outer tubes are unlikely to fail under the applied heat generation of 1.6×10^{10} W/m^3. This corresponds to a heat flux of 100 W/cm^2 incident on the outer surface of the inner tube and the inner surface of the outer tube. The post irradiation hoop stresses in the inner tube are greater than in the outer tube. Hence, the inner tube is likely to dictate the failure of the target.

Chapter 9: Draw-Plug Assembly and Irradiation Analysis

The hydroforming assembly [24] described in Sec 8 is one of the techniques used to assemble the annular target. However, the preferred assembly method for the annular target is the draw-plug technique. In this process, the annular target is placed inside the draw die and a plug made of D2 tool steel is driven through the inner tube using the setup illustrated in Figure 84.

The assembly process is designed to plastically deform the inner tube and elastically deform the outer tube. It is also expected to close the macroscopic interfacial gaps and reinforce the interfacial bond in the process. Similar to the hydroforming analysis, the goal here is to include the assembly residual stresses from the draw plug process into the irradiation model, and hence evaluate the thermal and structural limits of the annular target. While the hydroforming model did not include the nickel foil, the current analysis includes a 10 μm thick Ni foil.

9.1 Material Model

The material models for Al 6061-T6 and uranium, presented in Sec 8.1, were used in the draw-plug analysis as well. In addition to these, a material model for nickel from [66] was used. This is given by Figure 95. The material properties used in the draw plug model have been provided in Table 9 and the properties of the Al 6061-T6 and the uranium are consistent with the values provided in Table 1.

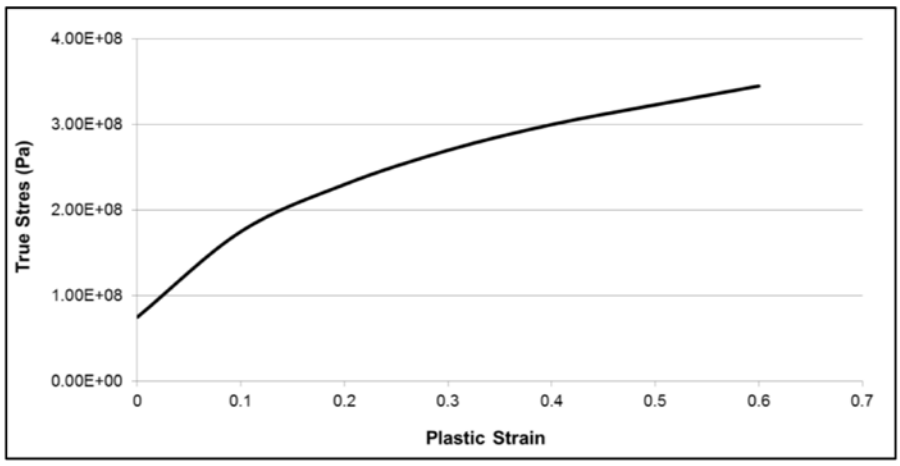

Figure 95. True stress and plastic strain curve for nickel used in the numerical model.

Table 9. Material properties used in the draw plug model.

Property	Al 6061-T6	Uranium	Nickel	D2 Steel
Density (Kg/m^3)	2700	19100	8800	7700
Thermal Conductivity (W/mK)	167	27.50	60.7	20
Elastic Modulus (GPa)	68.90	208	207	210
Poisson's Ratio	0.33	0.23	0.31	0.30
Thermal Expansion Coefficient (K^{-1})	2.34 x 10^{-5}	1.39 x 10^{-5}	1.31 x 10^{-5}	-------

9.2 Numerical Finite Element Model

The numerical modeling procedure consists of simulating the draw-plug assembly process, to obtain the assembled target dimensions and the residual stresses. This is followed by an analysis step where the plug is removed from the simulation. The final analysis step simulates the in-pile irradiation of the annular target. The analysis proceeds in a step-wise approach where the output of the first analysis step is the initial input to the second analysis step. Hence the residual stresses from the draw-plug assembly process

are automatically included as initial inputs in the irradiation model. The dimensions used in the draw plug assembly model are given in Figure 96. These dimensions, along with the stress-strain curves and Table 9 were used to setup the numerical model in Abaqus FEA [56].

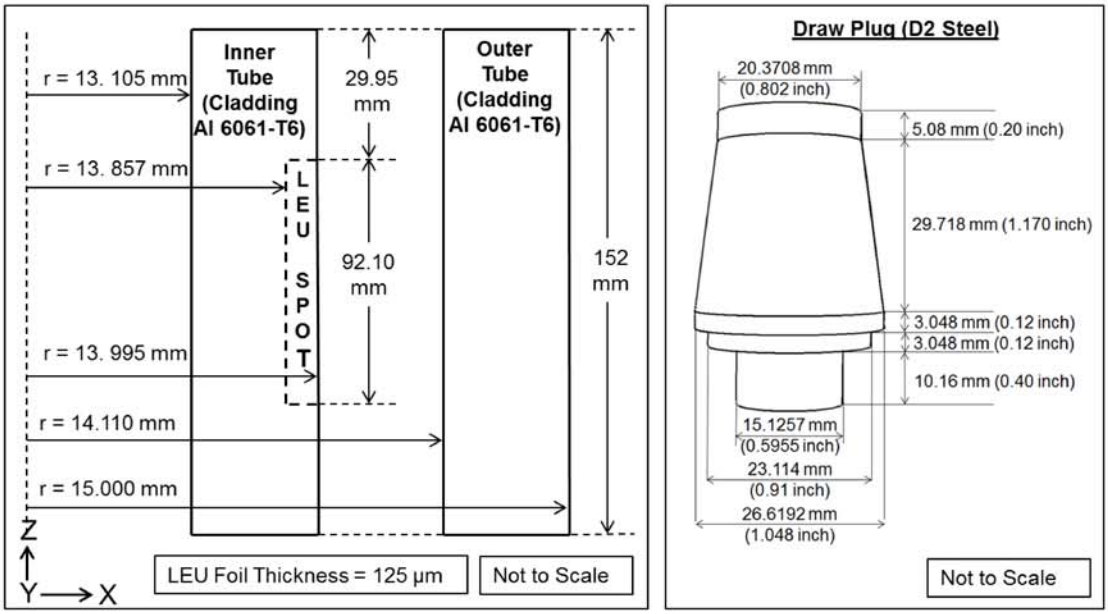

Figure 96. Pre-assembly target tubes and the plug dimensions.

The assembly and irradiation process was simulated using a three-step, steady state, coupled temperature displacement procedure, and has been pictorially represented in Figure 98. In the first analysis step to simulate the assembly of the target, a longitudinal velocity of 0.160726 m/s was applied to the back end of the plug while the radial and rotational velocity components were set to zero. The velocity was applied with the help of an amplitude curve where the longitudinal velocity gradually increases from 0 to 0.160726 m/s for the first 0.001 seconds and remains a constant thereafter from 0.001-1 second. A mechanical boundary condition that constrains the longitudinal displacement of the target was applied to one end of the cladding tubes while the other end was

allowed to remain free. The second step of the analysis was introduced as an intermediate step between the assembly and the irradiation simulation procedures. In this step the plug was removed from the simulation procedure using the 'model change' command as illustrated in Figure 97, and a contact constraint, that doesn't allow the edge surfaces to separate, was applied to both the ends of the assembled annular target to simulate a weld condition.

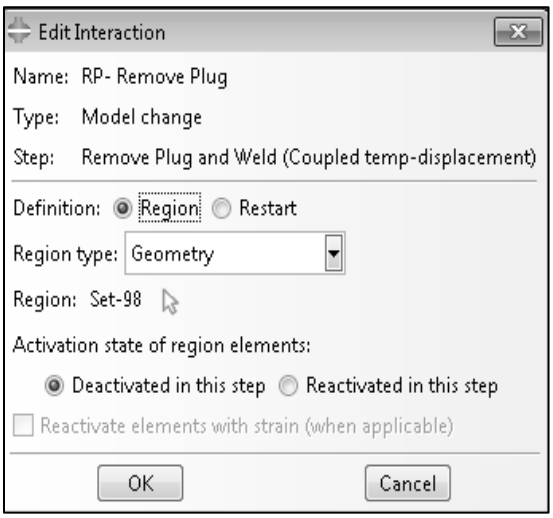

Figure 97. The model change command in Abaqus to remove the plug from the simulation.

The third and final analysis step simulates the in-vessel irradiation of the annular target by applying internal heat generation to the LEU foil and convection boundary conditions to the outer target surfaces. The boundary conditions and constraints from step-2 are carried over to this irradiation step. The thermal boundary conditions applied to the model are identical to those used in the hydroforming procedure [24] presented in Sec 8, and are provided in Figure 98. In the first two analysis steps, the normal-mechanical contact condition does not allow the tubes to separate once they have made contact. However, for the irradiation model the normal-mechanical contact condition allows the tubes to separate during the irradiation process.

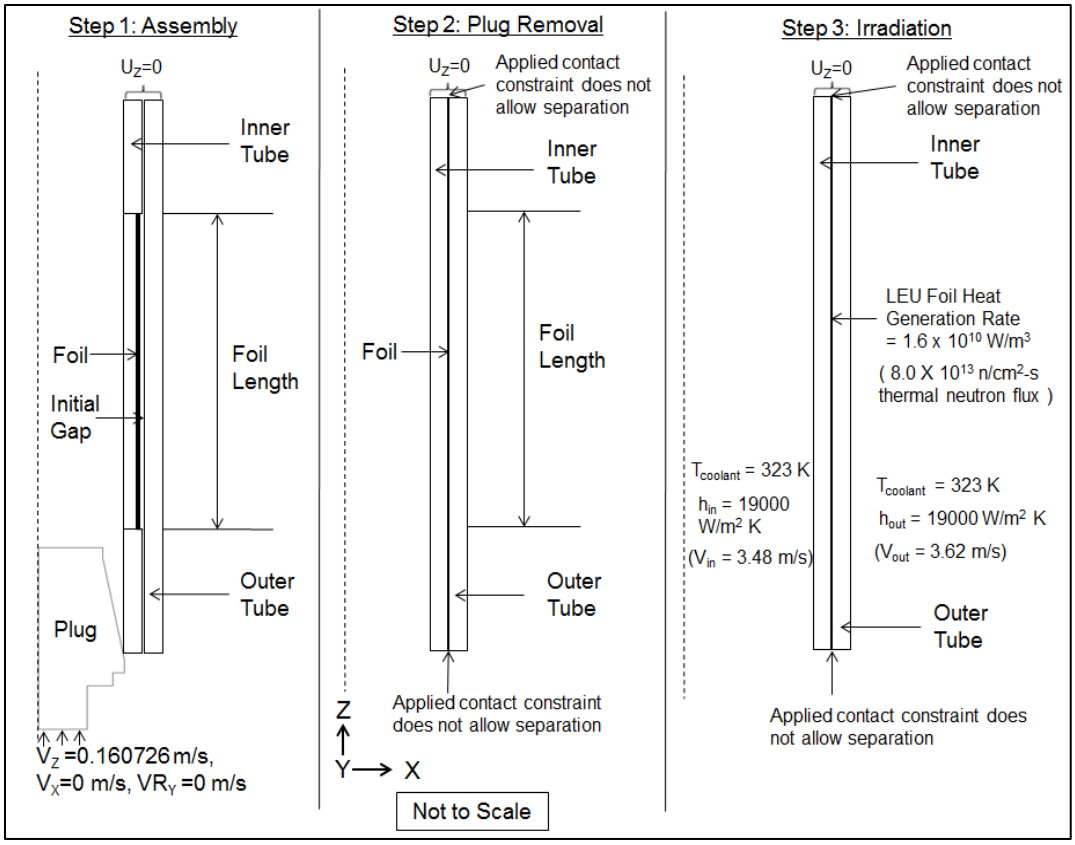

Figure 98. The three-step axisymmetric modeling procedure with boundary and loading conditions.

An infinite interfacial thermal conductance value was assumed at zero clearance, and for a clearance of 0.01 m it was assumed that the thermal conductance would tend to zero. The finite element mesh used in the draw-plug analysis has been provided in Figure 99. As the target configuration used in the hydroforming model did not include the nickel foil, two different target configurations were considered in the draw plug simulations. The first configuration did not consider the nickel foil (Target-1) and the second configuration contains the 10 µm nickel foil (Target-2). This was done to enable comparison between the hydroforming and the draw plug results, as the hydroforming analysis did not consider the nickel foil.

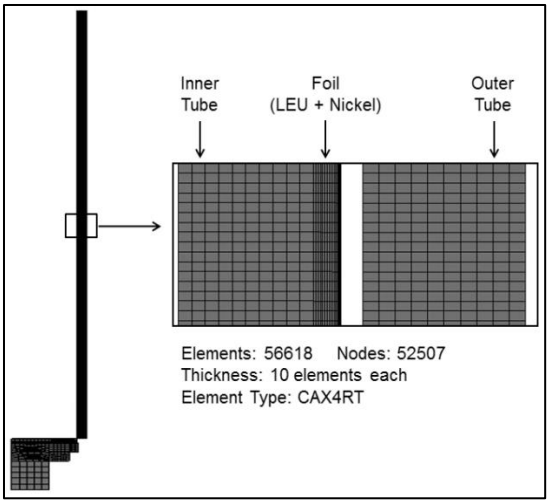

Figure 99. Finite element mesh used in the draw-plug based analysis.

9.3 Draw-Plug Analysis Results

This section will first present the post-assembly target examination results, compare them against the FEA results, and then present the irradiation FEA results. The melting point and the yield strength of the Al 6061-T6 were assumed to be the thermal and the structural safety limits for the irradiation analysis results. As it was not possible to use a LEU foil, a stainless steel 304 (SS-304) surrogate foil was used. Target-1 and Target-2 were assembled using the draw plug given in Figure 96. Target 1 was only comprised of a 76.2 mm by 88.9 mm SS-304 sheet, with a thickness of 125 µm. Target 2 consisted of a nickel foil of thickness 10 µm, enclosing the SS-304 foil with dimensions similar to that of the first target. The total thickness of the foil for the second target was 145 µm. Both the targets were sectioned at locations noted in Figure 100. Each sectioned part was viewed under the microscope to locate any microscopic gaps and to compare it with the assembly numerical model. Table 10 provides the post deformation measurements of the annular target, compared against the finite element model results. There is good agreement between the measured values and the numerical model values. Table 10 also

indicates a dimensional difference between the ‘front’ and the ‘end’ longitudinal positions.

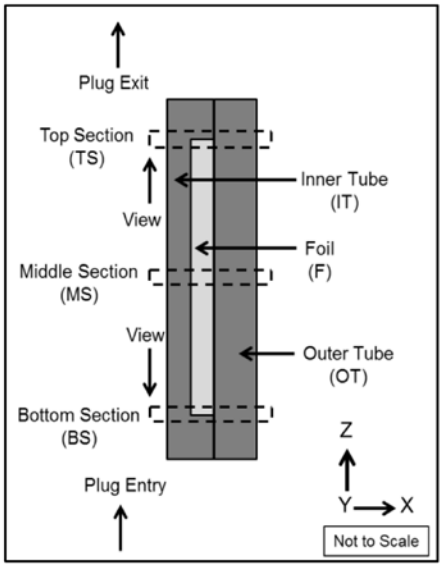

Figure 100. Sectioning locations along the assembled target length.

Table 10. Post assembly target measurements: Measured vs. model results.

	Measured Values (Using SS-304 Surrogate Foil)				Finite Element Model Values (Using LEU Foil)			
	Inner Tube ID (mm)		Outer Tube OD (mm)		Inner Tube ID (mm)		Outer Tube OD (mm)	
	Plug Exit	Plug Entry	Plug Exit	Plug Entry	Plug Exit	Plug Entry	Plug Exit	Plug Entry
Target 1 (Without Ni Foil)	26.543	26.467	30.132	30.168	26.534	26.516	30.044	30.064
Target 2 (With Ni Foil)	26.499	26.513	30.170	30.185	26.480	26.607	30.105	30.146

The post-assembly planar cross sectional views and the corresponding axisymmetric view from the numerical model are illustrated in Figure 101. This figure shows that gaps exist closer to the edges of the recess after the assembly process is complete. The sectioned images and the FEA results confirm the same.

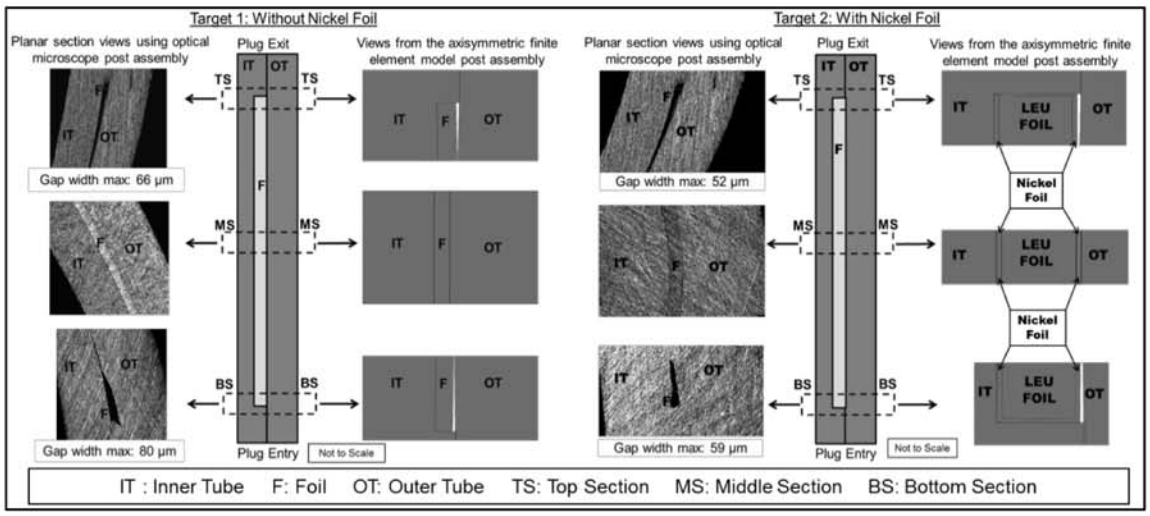

Figure 101. Post-assembly views of the sectioned images against the numerical model.

Figure 102 provides the magnitudes of separation for 'Target-1' and 'Target-2' based on the numerical finite element model. It also shows that finite gaps exist at the top section and bottom section, while there is zero separation in the middle section.

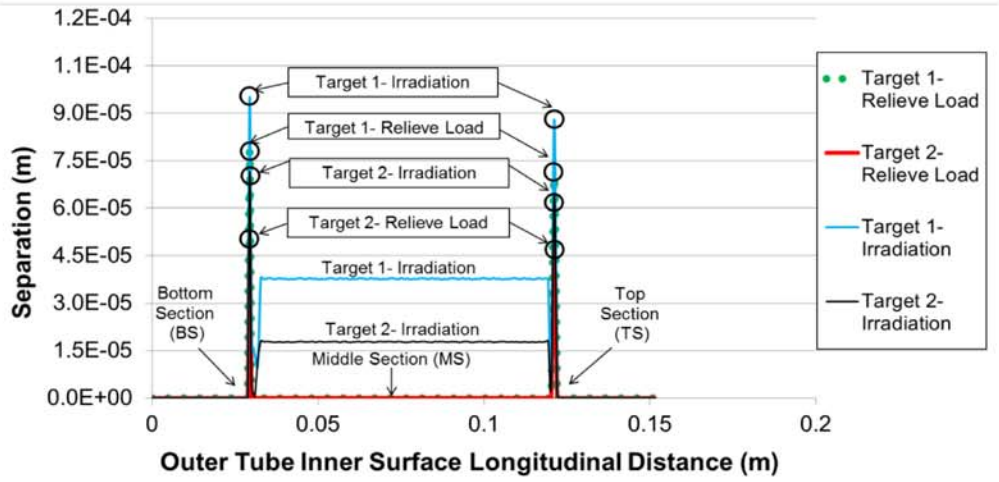

Figure 102. Longitudinal separation at the outer tube interface.

Based on Figure 101, the top section and bottom section correspond to the locations covering the edges of the recess. The magnitude of separation for 'Target-1' is greater than that of 'Target-2'. This can be attributed to the absence of the nickel foil in 'Target-

1'. The separation magnitudes for all cases are different at the top and bottom sections. This can be ascribed to the different mechanical end-boundary conditions closer to the top and bottom sections as illustrated in Figure 98. Figure 103 illustrates the equivalent plastic strain variation across the thickness of the annular target assembly. The results from the current analysis for 'Target-1' and 'Target-2' are compared against the results from the hydroforming analysis [24] from Sec 8. Target-2, with the nickel foil, has the highest plastic strain in the inner cladding and the outer cladding. The strain in the outer tube is zero for both the targets in the post-assembly state. This indicates that the outer tube undergoes only elastic deformation while the inner tube is plastically deformed during the assembly process. The irradiation process increases the plastic strain in the inner tube and induces a finite plastic strain in the outer tube.

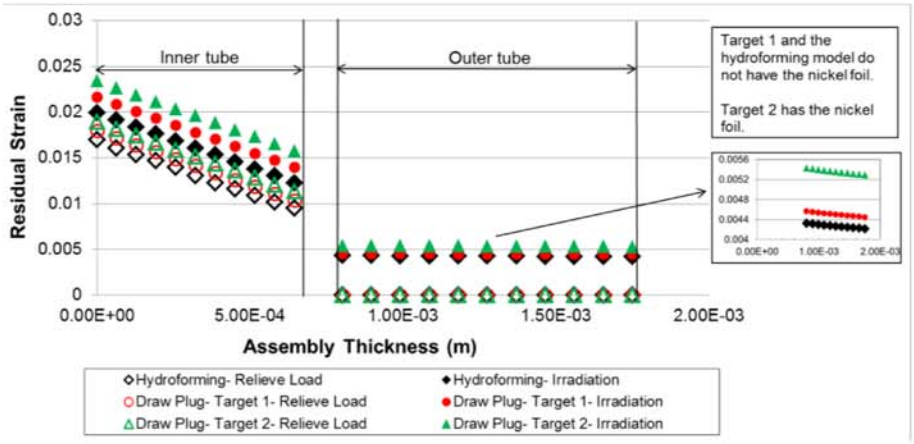

Figure 103. Equivalent plastic strain across the thickness at half the target length.

Figure 104 provides the hoop stress variation across the cladding thickness for the targets deformed by the draw-plug process (Target-1 and Target-2) and the hydroforming analysis [24] from Sec 8. Of these, based on Figure 104, 'Target-2' has the maximum post-assembly and irradiation hoop stress in the inner tube and the outer tube. For the inner tube the maximum hoop stress after the load has been removed is tensile and occurs

on the outer surface, while the maximum irradiation hoop stress is compressive and occurs on the inner surface. In the outer tube, the maximum post-load-removal hoop stress occurs on its inner surface and is compressive, while the irradiation hoop stresses move from being compressive to tensile across the thickness of the outer tube. In general, the inner tube is in a higher compressive stress state during irradiation as compared to the outer tube.

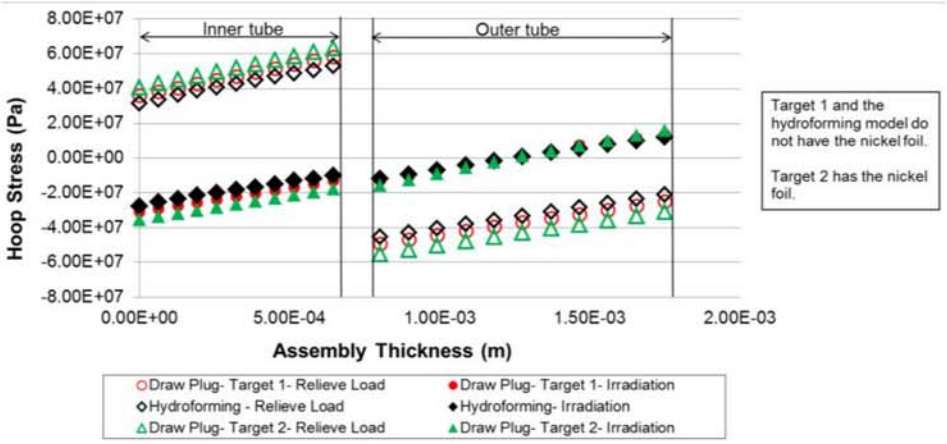

Figure 104. Hoop stress distribution across the cladding thickness at half the target length.

The longitudinal temperature distribution for Target-1 and Target-2 has been presented in Figure 105. For the inner tube, the outer surface is at a higher temperature than its inner surface, while for the outer tube the inner surface is at a higher temperature than the outer surface. The difference in temperatures at these surfaces for both the targets is not easily identifiable in the plots and Target 2 predicts slightly lower temperatures than Target 1 for the same thermal boundary conditions. The maximum temperature of the cladding is well below the melting temperature of the Al 6061-T6 (855 K) and this satisfies the thermal safety criteria. Therefore it is unlikely that the cladding would melt and cause the fission products to escape from the target.

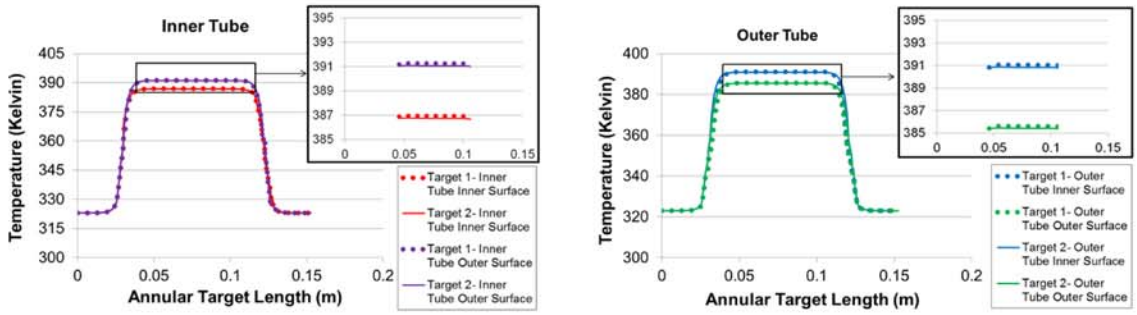

Figure 105. Longitudinal temperature distribution for Target-1 and Target-2.

The variation in von Mises stresses as a function of the longitudinal position has been illustrated in Figure 106. The inner surface of the inner tube for Target-1 predicts higher von Mises stresses than the inner surface of the inner tube for Target-2, while for all other surfaces of the inner and outer tubes, Target-2 predicts higher von Mises stresses. For all cases, the stresses were found to be within the yield strength of the Al 6061-T6 cladding material, thereby satisfying the structural safety criteria.

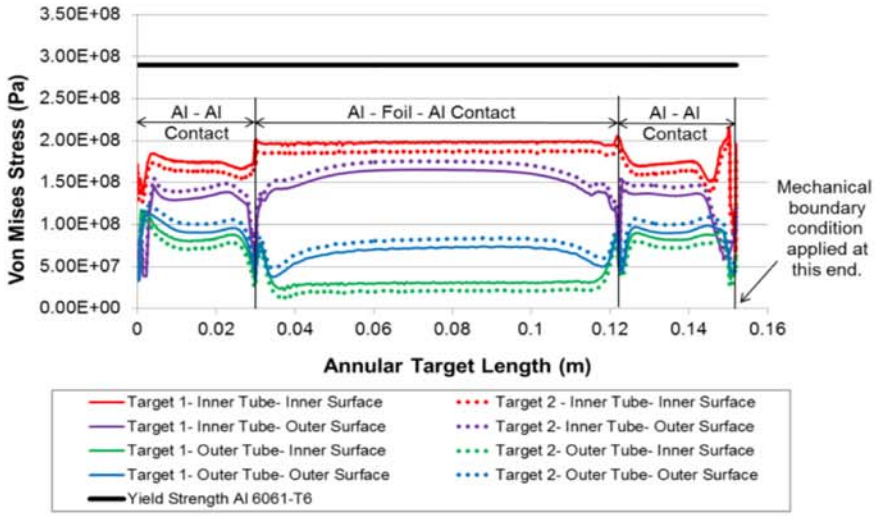

Figure 106. Irradiation stress state of Target-1 and Target-2.

Chapter 10: Interfacial Phenomena and Uranium Swelling

The analysis presented in Sec 9 did not account for the thermal contact conductance, the fission gas pressure, uranium swelling effects, the effect of the internal heat generation within the cladding itself, and the effect of the pressure exerted by the flowing coolant on the cladding walls. The significance of all these parameters on the thermal and structural safety of the target will form the core of this chapter.

10.1 Fission Gas Release and Uranium Swelling Model

It has been shown [44, 45] that during irradiation the uranium increases in volume by a number of mechanisms (increase in atomic volume, low temperature distortion, swelling by absorption of vacancies and swelling due to fission product gas pressure) each depending on the irradiation temperature. Most of the available literature [46, 47 and 48] presents the swelling of uranium fuel pins/ rods and there is no available data (to the knowledge of the author) on swelling of LEU metal foils during irradiation. Irradiation of the LEU foil will produce large amounts of heat along with which fission by-products are created that include fission gases. The irradiation time dictates the quantity of gases (number of moles) that are usually generated and released. The noble gases Xe (Xe-131) and Kr (Kr-84) along with Iodine (I-127) account for the majority of the fission gases generated [36]. However Iodine release is not expected [50] and only Kr and Xe are expected to contribute towards the gas release fraction along with He (if the target was helium back filled and the ends were TIG welded). An issue that needs to be given consideration is the determination of the volume in which these gases are likely to be contained. Difficulty arises in determining this volume due to the surface irregularities.

ANSTO in their calculations [18] determined the volume at the elastic limit and used this value in their fission gas pressure calculations. It is usually assumed that the gas mixture is 'ideal' and the ideal gas law is used to estimate the gas pressure. In their safety calculations, the gas mixture was assumed to be ideal and a release fraction [51] was used to determine the fission gas pressure. Hence the goal is to determine a fission gas pressure and volumetric swelling strain rate for uranium swelling, and use the values as inputs in the numerical model using Abaqus FEA [56]. The total quantity of fission gases (Xr, Kr and He) for a 20 g LEU foil was found from [36] and to be 1.255 x 10^{-4} moles. While calculations in the past [18] have assumed the fission gas mixture to be ideal, in this analysis it was decided to determine the compressibility factor (Z_{mix}) of the gas mixture using Eq.(66). The quantity of gases along with their properties is listed in Table 11.

$$Z_{mix} = 1 + \frac{B_{mix} P}{RT} \tag{66}$$

Table 11. Properties and of quantity of gases used in the calculations.

Gas	From [67]				From [36]
	Critical Temperature T_C (K)	Critical Pressure P_C (MPa)	Critical Volume V_C (m^3/mol)	Eccentricity Factor ω	Moles of gas for 20 g of LEU n (moles)
Xenon	289.70	5.84	11.84 x 10^{-5}	0.008	1.09 x 10^{-4}
Krypton	209.40	5.50	9.12 x 10^{-5}	0.005	1.67 x 10^{-5}
Helium	5.19	0.23	5.74 x 10^{-5}	-0.365	5.30 x 10^{-11}
System temperature, T = 415 K (from [34]) ; Gas constant, R = 8.3144 J/mol K Volume at elastic limit, V = 2.315 x 10^{-7} m^3 (from numerical simulations relating to [34])					

In equation Eq.(66), B_{mix} is the virial coefficient of the mixture, P is the total pressure of

the mixture, R is the ideal gas constant, and T is the system temperature. The current approach to determine the compressibility factor and the fission gas pressure was obtained from [67]. The first part of the calculation is to estimate all the individual virial coefficients, B_i, using Eq. (67). The critical compressibility factor, Zc_i, for each component (i=He, Xe, Kr) can be calculated using Eq.(68).

$$\frac{B_i P_{C,i}}{RT_{C,i}} = 0.083 - \frac{0.422}{\left(\frac{T}{T_{C,i}}\right)^{1.6}} + \omega_i \left[0.139 - \frac{0.172}{\left(\frac{T}{T_{C,i}}\right)^{4.2}} \right] \tag{67}$$

$$Z_{C,i} = 1 + \frac{B_i P_{C,i}}{RT_{C,i}} = 1 + \frac{B_i}{V_{C,i}} \tag{68}$$

Since the fission gas mixture in this analysis consists of three components, the mixing rule for a two component interaction is extended. The formulas that apply to a two component interaction to determine the critical temperature, critical compressibility factor, critical volume, eccentricity factor, critical pressure and temperature, are given by Eqs. (69)-(72) respectively. The subscripts 'i' and 'j' individually refer to any of the three gases (Xe, Kr, He).

$$T_{C,ij} = \sqrt{T_{C,i} T_{C,j}} \tag{69}$$

$$Z_{C,ij} = \frac{Z_{C,i} + Z_{C,j}}{2} \tag{70}$$

$$V_{C,ij} = \left[\frac{V_{C,i}^{1/3} + V_{C,j}^{1/3}}{2} \right]^3 \tag{71}$$

$$\left.\begin{aligned} \omega_{ij} &= \frac{\omega_i + \omega_j}{2} \\ P_{C,ij} &= \frac{Z_{C,ij} R T_{C,ij}}{V_{C,ij}} \end{aligned}\right\} \tag{72}$$

The second virial coefficient, which accounts for the interactions between a component pair can be determined using Eq.(73). With the knowledge of all the second virial coefficients and the individual component mole fractions (y_i or y_j) the virial coefficient of the mixture (B_{mix}) can be determined using Eq.(74). Once B_{mix} has been determined, the gas mixture compressibility factor can be found using Eq.(66).

$$\frac{B_{ij} P_{C,ij}}{R T_{C,ij}} = 0.083 - \frac{0.422}{\left(\frac{T}{T_{C,ij}}\right)^{1.6}} + \omega_{ij}\left[0.139 - \frac{0.172}{\left(\frac{T}{T_{C,ij}}\right)^{4.2}}\right] \tag{73}$$

$$\left.\begin{aligned} B_{mix} &= \sum_i \sum_j y_i y_j B_{ij} \\ B_{ij} &= B_{ji} \end{aligned}\right\} \tag{74}$$

The compressibility factor, using the above equations and the information provided in Table 11, was found to be 0.83 implying that the gas mixture is non-ideal. Hence the gas pressure can be determined using Eq.(75). Using Table 11 and Eq.(75), the gas pressure was found to be 1.59 MPa.

$$P = \frac{Z_{mix} * n_{total} * R * T}{V_{elastic\ limit}} \tag{75}$$

This pressure of 1.59 MPa corresponds to a 100 % gas release situation. However, a 100 % gas release situation is unrealistic and typically lesser than 1 % of the generated gas is

released from the foil by the mechanism of recoil [68, 69]. It has been shown in literature [51] that this recoil depth can be taken as 5 µm and a factor of 0.25 [70] be used to account for the gas atoms that fail to make contact with the surface. Using the LEU foil thickness of 125 µm, taking into consideration the recoil factor of 0.25, a recoil depth of 5 µm and multiplying by a factor of two to account for two sides of the foil, the gas pressure was determined to be 47.74 kPa using Eq.(76).

$$P_{interfacial} = P\left[2 * \frac{\text{recoil depth}}{\text{foil thickness}} * (1 - \text{recoil factor})\right] \tag{76}$$

Uranium swelling is the increase in volume of uranium during irradiation without undergoing any change in shape. The noble fission gases (Xe and Kr) precipitate into small gas bubbles due to their insolubility. A macroscopic increase of these gas bubbles occurs with increasing temperature and the uranium tends to swell as a result. It is expected that most of the gases are contained inside the bubbles, and remain constrained by the surface tension of the metal. The surface tension effects are usually neglected in the swelling calculations unless the bubble sizes are small [44].

Factors such as the composition of the specimen, irradiation temperature, fission rate and external restraint have been reported [48] to influence the swelling of uranium. The majority of the available swelling data in literature, to the author's knowledge, are correlations for U-Mo monolithic fuel, with little available data for swelling of low-enriched uranium foils. Hence, the correlations for a U-Mo fuel will be used to determine the swelling percentage and the corresponding volumetric strain rate. Work done by [71] showed that the overall fuel swelling measured by the post irradiation dimensions is a function of the fission density, and provided an empirical correlation for the percentage

volumetric swelling strain as a function of fission density for temperatures below 523 K. This correlation has been provided by Eq.(77). For an irradiation time of 150 hours, thermal power ~ 15 kW, and assuming that a single atom of U-235 releases 3.2 x 10^{-11} J of energy, the number of fissions was calculated to be 2.36 x 10^{20}. For an LEU foil of thickness 125 µm, length 92.10 mm and width 76.2 mm, the fission density was calculated to be 0.27 x 10^{27} fissions/m^3. Applying this to Eq.(77), the volumetric swelling strain was calculated to be 1.35 %. The volumetric swelling strain rate was calculated using Eq.(78) to be 2.48 x 10^{-8} s^{-1}.

$$\left.\begin{array}{l} \left(\frac{\Delta V}{V_0}\right)_{overall} = 5 f_d \\ \text{for } f_d \le 3x10^{27} \frac{\text{fissions}}{m^3} \quad \text{and } T < 523\,K \\ \left(\frac{\Delta V}{V_0}\right)_{overall} \text{ is the volumetric swelling strain in [\%]} \\ f_d \text{ is the fission density in } 10^{27}\ [\frac{\text{fissions}}{m^3}] \end{array}\right\} \quad (77)$$

$$\text{Volumetric swelling strain rate} = \frac{\ln\left[1+\left(\frac{\left(\frac{\Delta V}{V_0}\right)_{overall}}{100}\right)\right]}{\text{Time}_{irradiation}} \quad (78)$$

An alternate approach to assess the significance of volumetric swelling would be to estimate the temperature levels in the target and compare against a swelling versus temperature curve for uranium. The temperature dependence of swelling in uranium metal from [49] has been provided in Figure 107. The swelling data from [49] presented in Figure 107, along with data from [44], indicates significant swelling at temperatures in excess of 673 K (400 °C) and small to no swelling at temperatures below 623 K (350 °C).

Both the approaches discussed in this section will be considered in analyzing the effects of swelling on the thermal-mechanical safety analysis of the annular target.

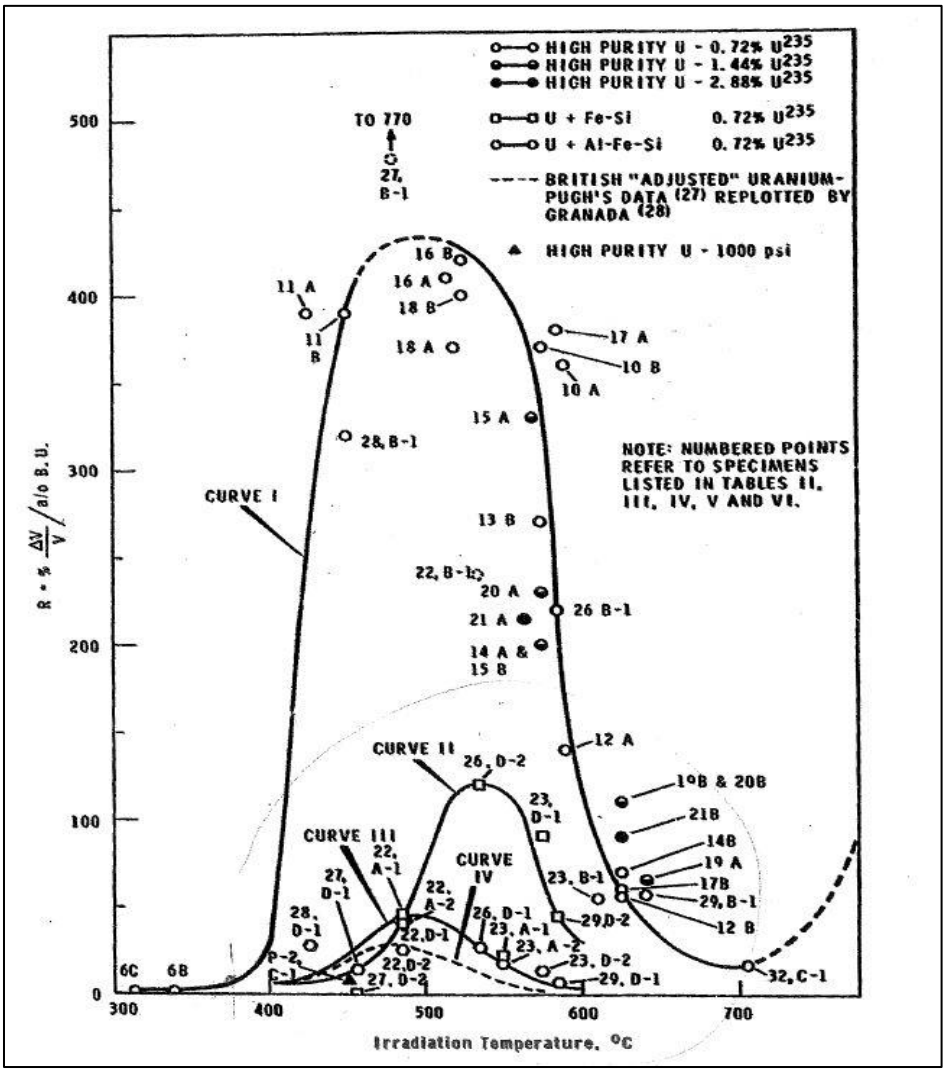

Figure 107. The dependence of swelling on temperature for high purity uranium.

10.2 Interfacial Conductance Model

As explained previously in Figure 12, microscopic interstitial gaps exist between the foil and the cladding which will offer resistance to the flow of heat. In the absence of any interstitial fluid, the predominant mode of conduction will be through the solid contact spots. In the event of fission gas release during irradiation, it is likely that these

interstitial gaps are filled mostly with a mixture of Xe (Xe-131), Kr (Kr-84), and He (Helium). Hence the thermal conductivity of the gas in the interstices will depend on the quantity of this gas mixture which can be obtained from neutronics calculations. It should be noted that the quantity of fission gases will depend on the reactor, the neutron flux, irradiation time and burn up. Calculation of the solid spot conductance will require knowledge of the surface parameters asperity slope, surface roughness apart from the material properties such as the harmonic average thermal conductivity, hardness of the softer material.

The total conductance can be expressed as in Eq.(3), with the solid spot conductance being expressed as a function of the contact pressure and the gap conductance being expressed as a function of the interface thickness. The goal here is to develop an expression for the total conductance as a function of the contact pressure and the interfacial gap. To account for the temperature drop across the interfaces, a thermal contact conductance model was setup and included in the analysis. The presence of the nickel foil necessitates the calculation of the contact conductance at the aluminum 6061 T6 - nickel and nickel-uranium interfaces. The aluminum 6061 T6- aluminum 6061 T6 contact conductance model has been provided for reference. Due to the composite target structure, interfaces exist between the parts in contact. Discontinuities exist at these interfaces due to microscopic (surface roughness) and macroscopic (waviness) irregularities on the surfaces of the parts in contact. This results in the formation of solid contact spots and gas gaps. At the interface of the two surfaces in contact, the expressions for the harmonic average thermal conductivity (k_{eff}), effective modulus of elasticity (E), combined surface roughness ($\sigma_{combined}$) and the effective asperity slope ($\tan\phi$), from [10],

are given by Eqs.(79)- (82) respectively. The properties provided in Table 12 were used to determine the quantities given by Eqs.(79)- (82).

$$k_{eff} = \frac{2k_1 k_2}{k_1 + k_2} \tag{79}$$

$$E = \frac{2}{\left[\frac{1-\nu_1^2}{E_1} + \frac{1-\nu_2^2}{E_2}\right]} \tag{80}$$

$$\sigma = \sqrt{\left(\sigma_1^2 + \sigma_2^2\right)} \tag{81}$$

$$\tan\phi = \sqrt{\left(slope_1^2 + slope_2^2\right)} \tag{82}$$

Table 12. Material and surface properties of the metals.

Property	Al 6061-T6	Uranium	Nickel	D2 Steel
Density (Kg/m^3)	2700	19100	8800	7700
Thermal Conductivity (W/mK)	167	27.50	60.70	20
Thermal Expansion Coefficient (K^{-1})	2.34×10^{-5}	1.39×10^{-5}	1.31×10^{-5}	--------
Elastic Modulus (GPa)	68.90	208	207	210
Poisson's Ratio	0.33	0.23	0.31	0.30
Asperity Slope (Radian)	0.18	0.12	0.14	--------
Roughness (μm)	1.15	1.50	1.27	--------
Hardness (MPa)	1080	1960	2750	--------

The correlation to be used for the solid spot conductance depends on the mode of deformation of the asperities. The mode of deformation can be either elastic or plastic depending on a parameter called the plasticity index [72] denoted by 'Ψ'. The plasticity

index can be determined using Eq.(83), and a value greater than 1 implies plastic deformation of the asperities.

$$\psi = \left(\frac{E}{H}\right)\tan\phi \tag{83}$$

For all the interfacial material combinations considered in this analysis, the asperity deformation mechanism was found to be plastic. The corresponding solid spot conductance correlation for plastic deformation of asperities, from [35], is given by Eq.(84). In Eq. (84), 'P' denotes the interfacial contact pressure, 'H' is the Meyer hardness of the softer material, and all the other parameters are as defined previously. The gas conductance, as a function of the gas mixture thermal conductivity (k_{mix}), temperature jump distance (g_{mix}), and the gap thickness 'δ', can be determined using Eq.(85).

$$\left.\begin{aligned} h'_{solid\ spot} &= C(P)^{0.94} \\ C &= 1.13\left(\frac{\tan\phi}{H^{0.94}}\right)\left(\frac{k_{eff}}{\sigma}\right) \end{aligned}\right\} \tag{84}$$

$$h'_{gas} = \frac{k_{mix}}{\delta + 2g_{mix}} \tag{85}$$

The expressions for the temperature jump distance [73] is given by Eq. (86), and for the gas mixture thermal conductivity [74] is given by Eq. (87). In these equations, 'x' represents the mass fraction, 'M' represents the molecular mass, 'λ' is the mean free path, 'β' is the accommodation coefficient,'μ' is the dynamic viscosity, 'γ' is the ratio of specific heats, 'c_v' is the specific heat at constant volume and the subscript 'i' refers to the constituent gas (He, Kr, Xe, I). The mole fractions have been provided in Table 11

and the thermophysical properties used in the gap conductance calculations can be found in Table 13.

$$g_{mix} = \frac{\sum\left(\frac{x_i\left(\frac{2\lambda_i k_{gas,i}(2-\beta_i)}{\beta_i\,\mu_i\,c_{v,i}(\gamma_i+1)}\right)}{M_i^{0.5}}\right)}{\sum\left(\frac{x_i}{M_i^{0.5}}\right)} \tag{86}$$

$$k_{mix} = \sum_{i=1}^{n} \frac{x_i k_i}{\sum_{j=1}^{n} x_j \left(\frac{\left(1+\left(\frac{\mu_i}{\mu_j}\right)^{0.5}\left(\frac{M_j}{M_i}\right)^{0.25}\right)^2}{\sqrt{8}\left(1+\frac{M_i}{M_j}\right)^{0.5}}\right)} \tag{87}$$

Table 13. Thermophysical properties of the gases used in the gap conductance calculations.

Property	He	Xe	Kr
M (Kg/mol)	3.02×10^{-3}	131.30×10^{-3}	83.80×10^{-3}
μ (Kg/ms)	21.70×10^{-6}	26.17×10^{-6}	28.6×10^{-6}
k (W/mK)	0.170	0.006	0.011
$\gamma = c_p/c_v$	1.67	1.66	1.68
c_v (J/KgK)	3120	97	151
λ (m)	0.193×10^{-6}	0.038×10^{-6}	0.052×10^{-6}
β	0.53	0.86	0.86

For the various interfacial material combinations (Al 6061-T6 and Al 6061-T6, Al 6061-T6 and Ni, Ni and LEU), the expression for the total conductance can be expressed as a sum of the solid spot conductance and the gap conductance as given by Eq.(88).

$$
\left.
\begin{aligned}
& h' = C(P)^{0.94} + \frac{0.007}{\delta + \left(3.566 \times 10^{-7}\right)} \\
& \text{where,} \\
& C = 0.036 \text{ for an interfacial combination of Al 6061-T6 and Nickel} \\
& C = 0.006 \text{ for an interfacial combination of Nickel and Uranium} \\
& C = 0.088 \text{ for an interfacial combination of Al 6061-T6 and Al 6061-T6} \\
& \text{'P' is in Pascal, '}\delta\text{' is in meter and ' h' ' is in W/m}^2\text{K.}
\end{aligned}
\right\} \quad (88)
$$

The value of 'C' in Eq.(88) will depend on the factors that influence the solid spot conductance, such as the surface roughness, asperity slope, material hardness and the thermal conductivity. When the gap thickness is lesser than the temperature jump distance, the gas conductance is effectively the ratio of the gas mixture thermal conductivity to the temperature jump distance. Also, at very low contact pressures the conductance of the gas mixture in the gaps will dominate the solid spot conductance.

10.3 Additional Effects

In addition to the fission gas pressure, uranium swelling and the thermal contact conductance, there are two more parameters that need to be accounted for. The first of these is the pressure exerted by the coolant flow on the walls of the inner tube and the outer tube. From Figure 98, the flow velocities, through the inner and along the outer tubes, are in the predicted flow velocity range (3.4 ± 0.8 m/s) at MURR [60]. Therefore it was decided to use the primary coolant pressure from the MURR safety analysis report [75] and this value was found to be 0.59 MPa. The second parameter that needs to be included in the analysis is the internal heat generation in the cladding, to account for the gamma heating effects that would exist in the cladding, after the target has been placed in the irradiation holder. It is expected that the maximum power generated per gram of the

cladding would be approximately 10 W/g. Multiplying 10 W/g by the density of the Al 6061-T6 from Table 12, the volumetric heat generation in the Al 6061-T6 cladding due to gamma heating was found to be 2.7×10^7 W/m^3.

10.4 Numerical Model

The numerical model of the annular target used in Sec 9.2 was used in this analysis as well, to maintain consistency in the geometry, mesh, boundary conditions, loads, and provide continuity in the analysis sequence. The target geometry in Figure 96 and the finite element mesh presented in Figure 99 are applicable to the analysis present in this section as well. A three-step simulation procedure as presented in Figure 98 of Sec 9.2 was adopted, and the additional constraints were added to the irradiation model as illustrated by Figure 108.

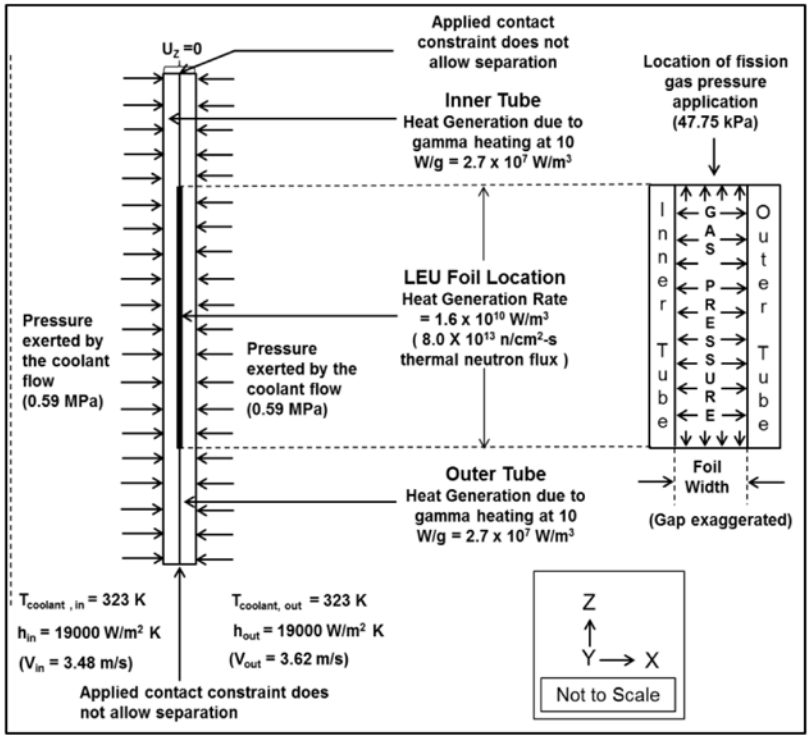

Figure 108. Mechanical and thermal loading of the annular target during the irradiation step.

The developed thermal conductance model given by Eq. (88) was input into Abaqus FEA [56] and applied to the appropriate interfaces. The normal and tangential mechanical contact definitions were kept the same as in Sec 9.2. The calculated fission gas pressure of 47.75 kPa (based on fractional gas release) was applied as a pressure loading condition to the surfaces of the inner and outer tubes as illustrated in Figure 108. The calculated volumetric swelling strain rate of 2.48 x 10^{-8} s^{-1} was included under the plastic material property definition for uranium as illustrated in Figure 109.

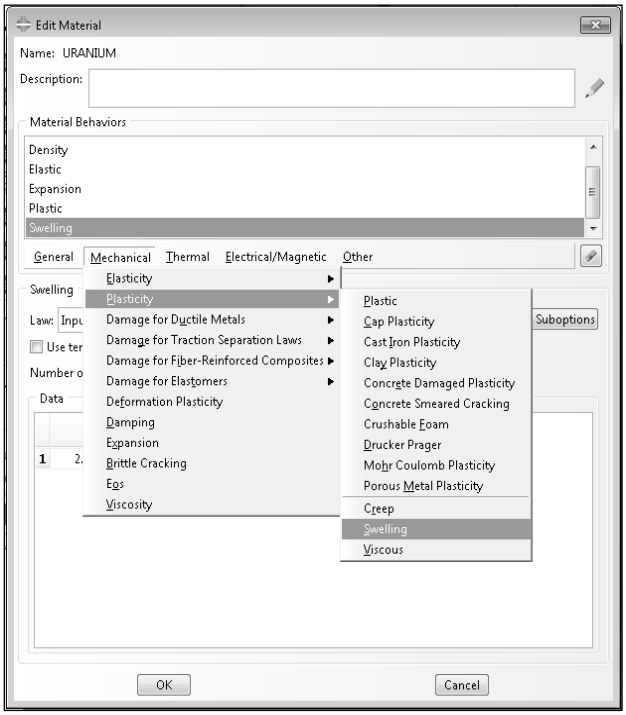

Figure 109. Volumetric swelling strain rate definition location.

10.5 Results

The results will focus on the von Mises stresses and the temperature distribution in the cladding, and provide comparisons against the yield strength and the melting point of the Al 6061-T6. The various applied constraints have been split into 5 cases, as shown in

Table 14. The goal was to estimate the conditions or constraints that provide the worst case scenario for temperature and von Mises stresses. Case-1 represents the 'base' case and all the comparisons made in Table 14 are with respect to the base case. The irradiation von Mises stress distribution for case-1 has been provided in Figure 110. The inner tube is in a higher stress state as compared to the outer tube, based on Figure 110 and Table 14.

Table 14. Maximum von Mises stress variation with the addition of constraints.

Case #	Applied Constraints or Loads	Inner Tube		Outer Tube	
		Inner Surface Max von Mises	Outer Surface Max von Mises	Inner Surface Max von Mises	Outer Surface Max von Mises
1	TCC	216.85 MPa	205.32 MPa	50.74 MPa	112.02 MPa
2	TCC + Swell	Negligible change	Negligible change	Negligible change	Negligible change
3	TCC + Swell + FGP	0.06 % decrease	0.07 % increase	0.09 % increase	0.02 % decrease
4	TCC + Swell + FGP + HGC	0.04 % decrease	0.08 % increase	0.04 % increase	0.05 % decrease
5	TCC + Swell + FGP + HGC + PC	0.32 % increase	0.47 % decrease	1.43 % increase	0.84 % decrease

(TCC – Thermal contact conductance; FGP – Fission gas pressure; HGC- Heat generation in the cladding; PC- Pressure exerted by the coolant)

The effects of the addition of various constraints such as swelling, fission gas pressure, cladding heat generation and the coolant pressure on the cladding, have been provided in Table 14. From the table it can been concluded that case-5 presents the worst case scenario for the stress distribution as it results in the greatest increase in von Mises stresses in the inner surface of the inner tube. However, the maximum percent increase above the base case (case-1) is only 0.32 % (~218 K) and this is unlikely to cause the von Mises stresses to exceed the yield strength of the Al 6061-T6 cladding (~290 K).

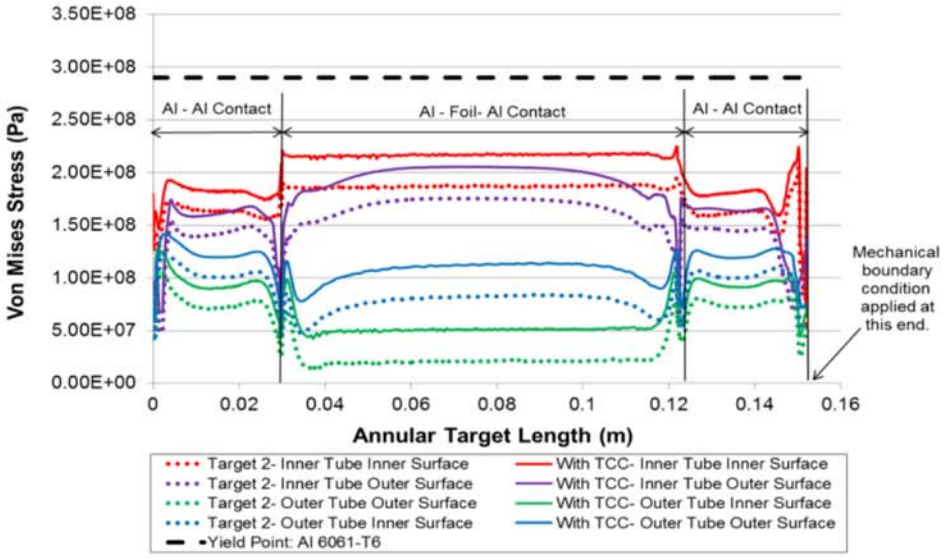

Figure 110. Von Mises stresses in the cladding for case-1 compared against Target-2 values from Figure 106. (Note: The Target-2 model does not have a thermal conductance model and assumes an infinite conductance as discussed in Sec 9.2)

Figure 111 illustrates the variation of the contact pressure with the thermal conductance when the interfacial gap (δ) ~ 0 m. This plot illustrates that the Ni-Uranium interface offers the least favorable heat conductance path of the three interfaces, and is reflected in Figure 112 where this interface experiences the highest interfacial temperature drop ~ 35 K. The radial temperature distribution at half the target length has been provided in Figure 112 and it also illustrates the temperature drop at each interface.

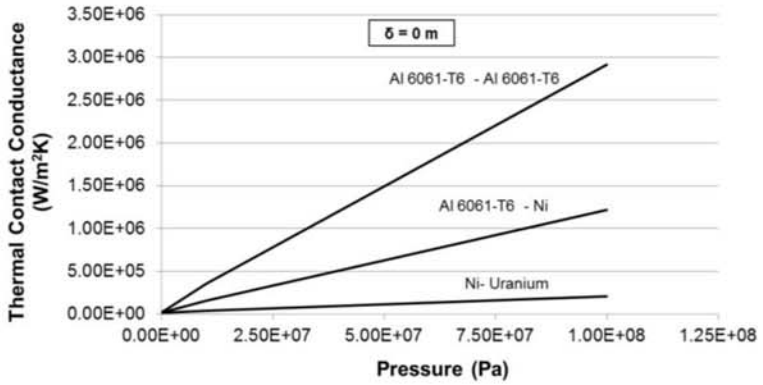

Figure 111. Thermal contact conductance as a function of pressure for various interfacial combinations.

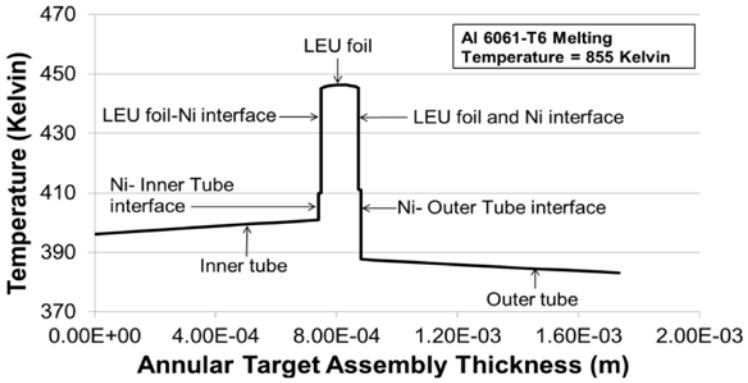

Figure 112. Radial temperature distribution in the annular target for case-1 at half the target length.

While case-5 presented the worst case scenario for the von Mises stresses in Table 14, Table 15 indicates that the pressure exerted by the coolant flow doesn't significantly impact the temperatures. The combined effects of the thermal contact conductance, uranium swelling, fission gas pressure and the internal heat generation in the cladding, present the worst case scenario for the temperature. Accounting for the 0.32 % maximum increase in temperature, the maximum cladding temperature for case-4 is ~ 402 K. This temperature is well below the melting temperature of the Al 6061-T6 cladding at 855 K.

Table 15. Maximum cladding temperature variation with the addition of constraints.

Case #	Applied Constraints or Loads	Inner Tube		Outer Tube	
		Inner Surface Max Temp	Outer Surface Max Temp	Inner Surface Max Temp	Outer Surface Max Temp
1	TCC	396.12 K	400.96 K	387.66 K	382.87 K
2	TCC + Swell	Negligible change	Negligible change	Negligible change	Negligible change
3	TCC + Swell + FGP	0.015 % increase	0.015 % increase	0.013 % decrease	0.014 % decrease
4	TCC + Swell + FGP + HGC	0.31 % increase	0.32 % increase	0.32 % increase	0.31 % increase
5	TCC + Swell + FGP + HGC + PC	0.15 % increase	0.14 % increase	0.15 % increase	0.15 % increase

(TCC – Thermal contact conductance; FGP – Fission gas pressure; HGC- Heat generation in the cladding; PC- Pressure exerted by the coolant)

From Figure 112, the maximum LEU foil temperature is ~ 446 K, justifying the use of the swelling model given by Eq. (77) which is valid for temperatures < 523 K. The negligible changes in von Mises stress or temperature for case-2 with the addition of the volumetric swelling strain rate support the conclusions from [44, 49] that indicate substantial swelling at temperatures in excess of 673 K and small to no swelling at temperatures below 623 K. The effects of varying the LEU heat generation rates on the temperature has been illustrated in Figure 113, and on the von Mises stress has been provided in Figure 114. The parametric studies on the heat generation rate were performed using case-4 for the temperature and on case-5 for the von Mises stresses as these were previously identified to be the worst case scenarios.

The temperatures in the cladding and the LEU foil were found to increase with increasing LEU heat generation rates. The von Mises stresses also increase with increasing heat generation rates of the LEU as illustrated in Figure 114. For LEU heat generation rates greater than 6.4 $x10^{10}$ W/m^3 the maximum von Mises stress in the inner tube approaches the yield strength of the Al 6061-T6 and the target failure is likely to occur around this point. However, this heat generation rate is about 4 times the baseline heat generation rate designed for a heat flux of 100 W/cm^2 and is not realistically attainable in the current situation. Moreover, it represents an 'over-100 % power' scenario and in such a case the reactor would be scrammed automatically or manually.

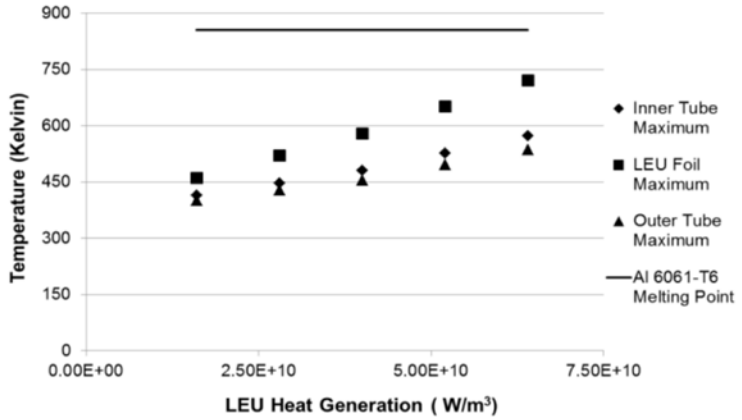

Figure 113. Variation of maximum temperature with the heat generation rate for case-4.

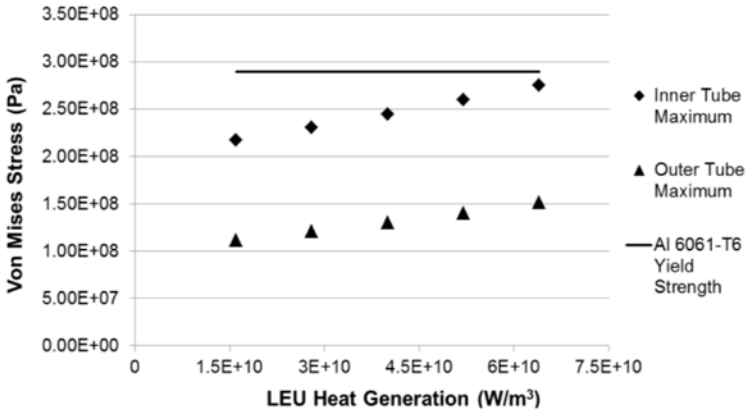

Figure 114. Variation of von Mises stresses with the heat generation rate for case-5.

The analysis presented in this chapter includes all the possible safety case parameters such as the thermal contact conductance, the uranium swelling, fission gas pressure, heat generation in the cladding due to gamma heating, and the pressure exerted by the coolant flow on the cladding wall, that directly or indirectly influence the temperatures and von Mises stresses in the cladding. Based on the results it can be concluded that the temperatures and von Mises stresses in the cladding are unlikely to exceed the melting point and the material yield strength respectively.

Chapter 11: Reactor Specific Annular Target Analysis

The section details the analysis that was performed in the summer of 2013, during my time as a thermal-stress safety analysis intern at the Oak Ridge National Laboratory. The analysis provides the thermal-stress safety calculations of low-enriched uranium (LEU) foil based annular targets to support their safe irradiation at the High Flux Isotope Reactor (HFIR) in Oak Ridge, Tennessee. The analyses presented in the previous chapters provide a general performance analysis envelope for the annular target irradiation and isn't specific to any reactor configuration. However, the results and analysis presented in this chapter are specific to the HFIR configuration. The annular target assembly configuration in this analysis includes the LEU foil, coated with pure aluminum by the physical vapor deposition (PVD) method, sandwiched between two Al 6061-T4 cylinders (or tubes) that serve as the cladding.

11.1 Reactor Description

The High Flux Isotope Reactor (Figure 115) located at the Oak Ridge National Laboratory in Oak Ridge Tennessee, is a nuclear research reactor operating at 85 MWth power. It is a light water cooled and moderated, flux type reactor, utilizing uranium-235 as the fuel, with a beryllium reflector. The average thermal neutron flux at HFIR is 2.3 x 10^{15} n/cm^2-seconds. It provides a constant power density and steady neutrons to help with several research activities and neutron scattering experiments. Experimental irradiations take place in any of the vertical experimental facilities (VXF) shown in Figure 116. There are about 16 small VXFs and 6 large VXFs located in the permanent reflector. The small VXFs are usually used for non-instrumented experiments.

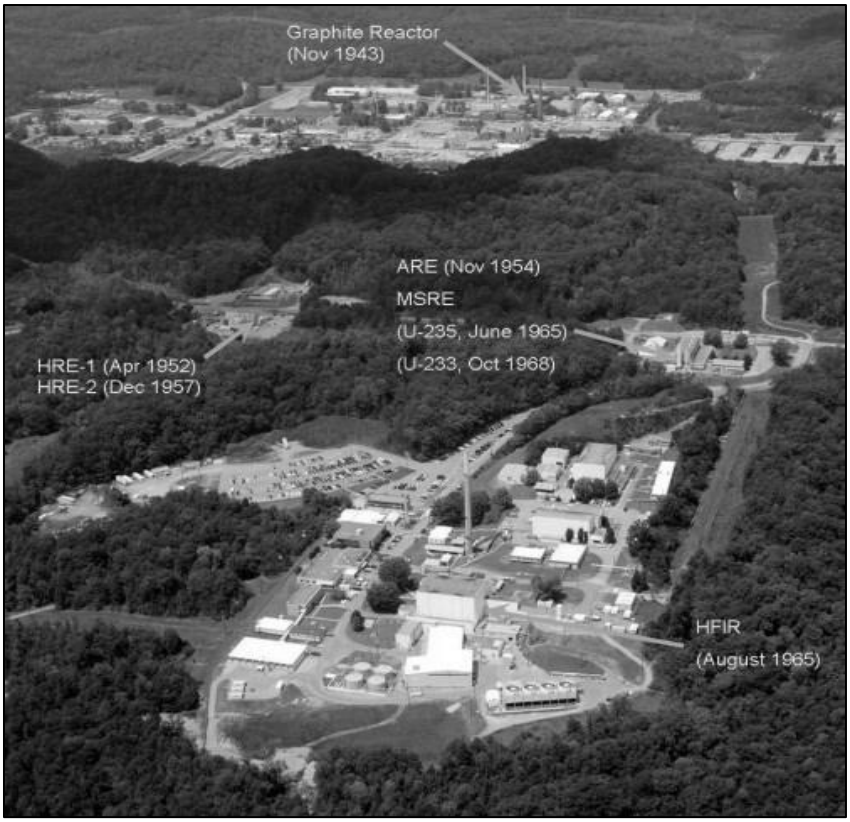

Figure 115. Aerial view of the HFIR facility. (SOURCE: http://energyfromthorium.com/wp-content/uploads/2012/06/ORNL-aerial-labeled-500x534.jpg)

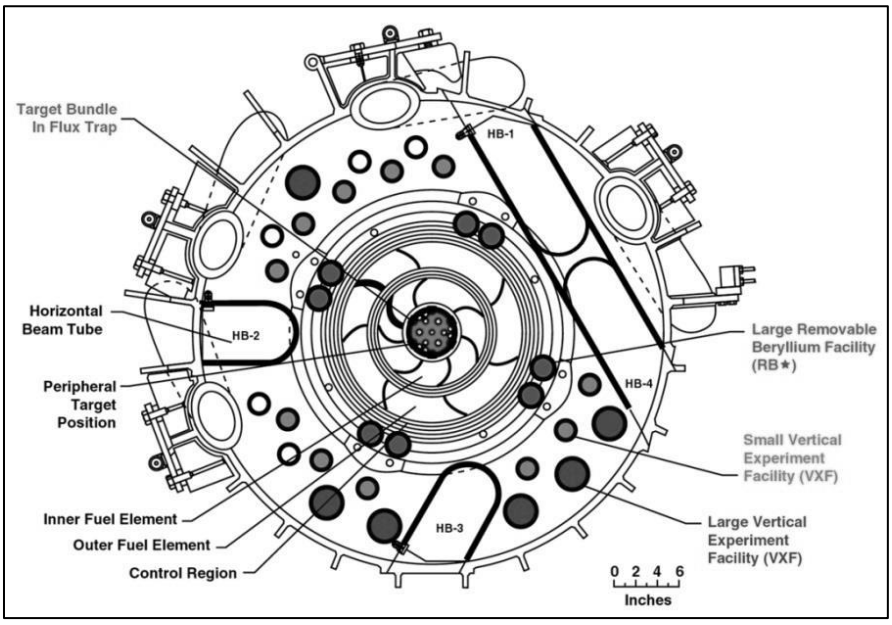

Figure 116. The HFIR core illustrating the location of the experimental facilities. (SOURCE: http://upload.wikimedia.org/wikipedia/commons/4/48/High_Flux_Isotope_Reactor_Core_Cross_Section.jpg)

11.2 Target Geometry

The pre-assembly geometry of the annular target for the HFIR irradiations is illustrated in Figure 117, and the dimensions of the draw-plug used for the assembly process have been provided in Figure 118. The cladding material used for this annular target is Al 6061-T4, which is 'softer' than the Al 6061-T6 used for the annular target analysis through this dissertation. The LEU foil coated with pure aluminum by the physical vapor deposition (PVD) method replaces the LEU foil and Ni foil combination previously used with the Al 6061-T6 based annular target. The size of the draw plug was determined by taking into account the deformation required to close the gap between the foil and the outer cladding, while plastically deforming the inner cladding and only elastically deforming the outer cladding [55].

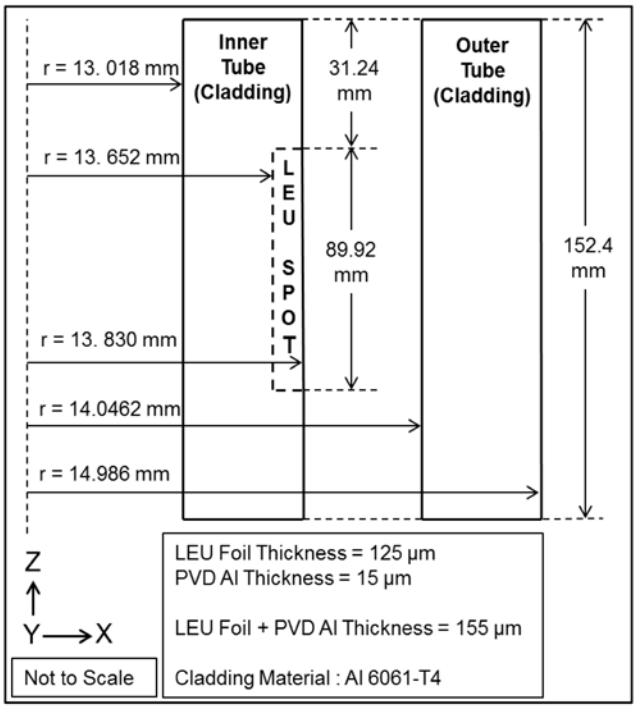

Figure 117. Pre-assembly annular target dimensions for HFIR irradiation.

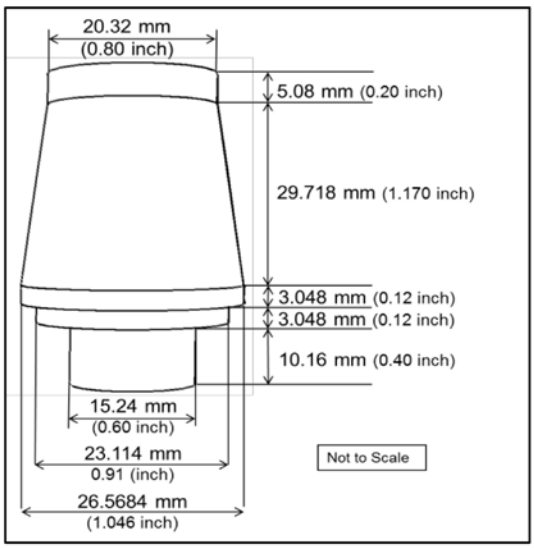

Figure 118. Dimensions of the draw-plug used to assemble the annular target with the 6061-T4 Al cladding.

The properties of the cladding, LEU foil, pure aluminum used in the PVD, and the D2-steel draw-plug, have been provided in Table 16. It should be noted that the properties of the LEU foil and the D2 steel plug are identical to the values used for the annular target analysis with Al 6061-T6 as the cladding material (Table 9).

Table 16. Material properties used in the calculations.

Property	Al 6061-T4	Pure Aluminum	Uranium	D2 Steel
Density (Kg/m^3)	2700	2698.9	19100	7700
Thermal Conductivity (W/mK)	154	210	27.50	20
Thermal Expansion Coefficient (K^{-1})	2.36×10^{-5}	2.40×10^{-5}	1.39×10^{-5}	--------
Elastic Modulus (GPa)	68.90	68	208	210
Poisson's Ratio	0.33	0.36	0.23	0.30
Asperity Slope (Radian)	0.18	0.03	--------	--------
Roughness (μm)	1	0.1	--------	--------
Hardness (MPa)	1080	--------	--------	--------

The true stress and plastic strain curves for the Al 6061-T4 and uranium have been provided in Figure 119. The stress and strain data for the Al 6061-T4 was obtained from [76], while the uranium stress-strain data was obtained from [65].

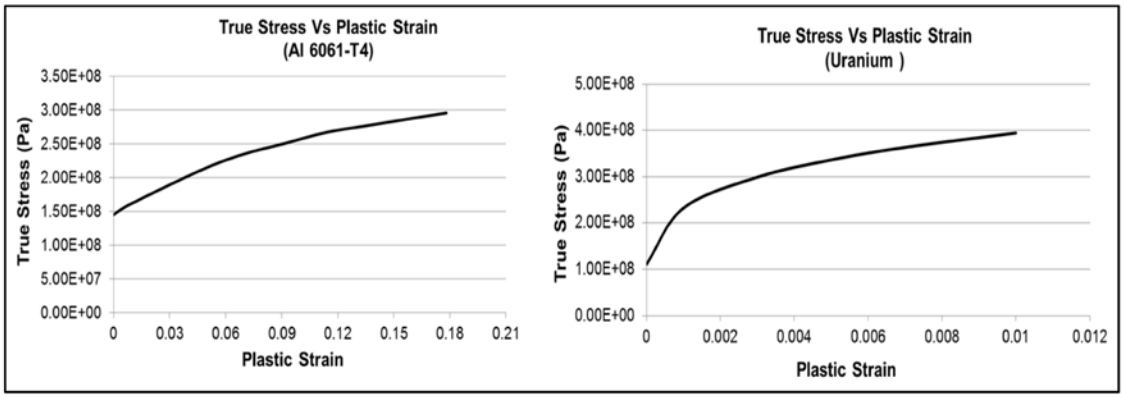

Figure 119. Material models for Al 6061-T4 and uranium.

11.3 Calculation of Input

This section will provide the calculation procedure along with the assumptions involved in determining various input parameters such as the thermal contact conductance and fission gas pressure. A detailed calculation procedure to determine the thermal contact conductance, as the sum of the solid spot conductance and the gas gap conductance has already been provided by Eqs. (79)- (88) in Sec 10.2. Therefore, the calculation procedure will not be repeated in this section. The current configuration has two different interfacial material combinations- Al 6061 T4 and pure Al, Al 6061 T4 and Al 6061 T4. Using the surface properties of the metals listed in Table 16, the fission gas properties from Table 17, and by using Eqs. (79)- (88), the expression for the total conductance was obtained. This is given by Eq.(89).

Table 17. Properties of the fission gases used in the reactor specific calculations.

Property	Helium	Xenon	Krypton	Iodine
Critical Temperature, T_c (K)	5.19	289.7	209.4	819
Critical Pressure, P_c (MPa)	0.23	5.84	5.5	11.7
Critical Volume, V_c (m^3/mol)	5.74×10^{-5}	11.84×10^{-5}	9.12×10^{-5}	15.5×10^{-5}
Eccentricity Factor, ω	-0.365	0.008	0.005	0.12
Mol. Mass x 10^{-3} (Kg/mol)	4.003	131.293	83.80	253.809
Dynamic Viscosity (Kg/m s)	21.7×10^{-6}	26.17×10^{-6}	28.6×10^{-6}	23×10^{-6}
Heat Cap. Const Vol.(J/Kg K)	3120	97	151	226.02
Ratio of Specific Heats	1.667	1.656	1.667	1.299
Mean Free Path (μm)	0.193	0.038	0.052	0.042
Thermal Conductivity (W/mK)	0.169	0.006	0.0107	0.449
Quantity of Fission Gas (moles)	3.28×10^{-10}	3.12×10^{-4}	4.35×10^{-5}	2.70×10^{-5}
Accommodation Coefficient	0.530	0.860	0.861	0.730

$$h' = C(P)^{0.94} + \frac{0.053}{\delta + \left(4.75 \times 10^{-6}\right)}$$

where,

C = 0.094 for an interfacial combination of Al 6061-T4 and Pure Al

C = 0.081 for an interfacial combination of Al 6061-T4 and Al 6061-T4

'P' is in Pascal, 'δ' is in meter and 'h'' is in W/m^2K. (89)

For the irradiation safety case analysis it was assumed that all the generated fission gases would be released, and exert pressure on the walls of the cladding. Even though the target is unlikely to experience a 100% fission gas release, it was reasoned that this conservative assumption would help in modeling the worst-case scenario for the annular target as the fission gas pressure corresponding to a 100% gas release state would predict

a higher irradiation thermal stress margin as compared to when the percentage of gas release, and hence the fission gas pressure is lower. The procedure to calculate the fission gas pressure has already been outlined in Sec 10.1 and is given by Eqs. (66)-(75). Using these equations along with the fission gas data given in Table 17, the fission gas pressure corresponding to a 100 % gas release situation was found to be 7.5 MPa. Uranium swelling effects were not included in the model as there was a lot of uncertainty, at that point, over selecting the best approach to model the swelling effects. Therefore, this aspect was left to the independent reviewer of the calculation to address.

The coolant flow velocity for this irradiation experiment was to be 6.09 m/s. Taking the density of water as 984.55 Kg/m^3, the dynamic viscosity as 487 x 10^{-6} Kg/m-s, thermal conductivity as 0.650 W/mK, Prandtl number as 3.1348, along with the dimensions from Figure 117, and the Nusselt number correlations for fully developed turbulent flow given by Eqs. (6)-(7), the surface heat transfer coefficient for the inner tube was found to be 30118.3 W/m^2K, and for flow over the outer tube was 32220.5 W/m^2K.

11.4 Finite Element Model Development

The commercial finite element code Abaqus FEA [56] was used to first model the draw-plug assembly process of the annular target, and then use the residual stress results in a separate irradiation model. It should be noted that the successive three-step analysis procedure, outlined in Sec.9 and Sec. 10, was developed towards the later part of 2013. The safety analysis was completed using the procedure outlined in this section. The draw-plug assembly process was the preferred method to assemble the annular targets for the HFIR irradiation. In this process, pure aluminum is deposited on the edges of the LEU

foil using a process known as physical vapor deposition (PVD). Following this, the foil with Al coating is wrapped around the inner Al 6061-T4 tube and slid into the outer Al 6061-T4 tube. This combination is placed inside a draw-die and a tapered plug is driven through the inner tube. This expands the inner tube, which in-turn pushes the foil towards the outer tube and enforces interfacial contact. The draw plug assembly process is designed to plastically deform the inner tube and elastically deform the outer tube. After assembly, the ends of the target are welded to provide a completely sealed environment.

Due to the difficulty associated with physically measuring certain dimensions of the annular target assembly, it was decided to simulate the assembly process by means of an axisymmetric stress analysis, using the commercial finite element code Abaqus FEA. The dimensions of the annular target obtained from the assembly were used to build an irradiation model, by including the assembly residual stresses as an initial input. The purpose of the irradiation model is to simulate the in-vessel irradiation by accounting for the volumetric heat generation in the LEU foil, gamma heating in the cladding, fission gas release.

The draw-plug assembly model was setup using the dimensions of the annular target from Figure 117 and the material properties from Table 16. The end of the target, away from the plug, was not allowed to translate in the longitudinal direction, as this is the case during the draw-plug assembly procedure. The assembly model does not have any external loading conditions imposed on it. As the plug moves through the inner tube, a velocity boundary condition was applied to the based of the plug. The radial and rotational velocity components were set to zero, while the longitudinal velocity component was enabled. As the applied drawing force to the plug was unknown to the

author, a simple calculation was performed to determine the velocity required to the move the plug along the length of the inner tube (152.4 mm). Assuming a time period of 1 second, the velocity was found to be 0.1524 m/s, However, this velocity, when applied instantaneously, created a large amount of wrinkling in the tubes. To alleviate this problem, an amplitude curve was created in Abaqus FEA [56] by assuming the gradual increase in velocity for the first 0.001 seconds, after which the velocity was maintained a constant. Based on this amplitude curve the velocity required for the plug to travel the length of the tube was found to be 0.158064 m/s, and this was used an as input for the assembly model given in Figure 120.

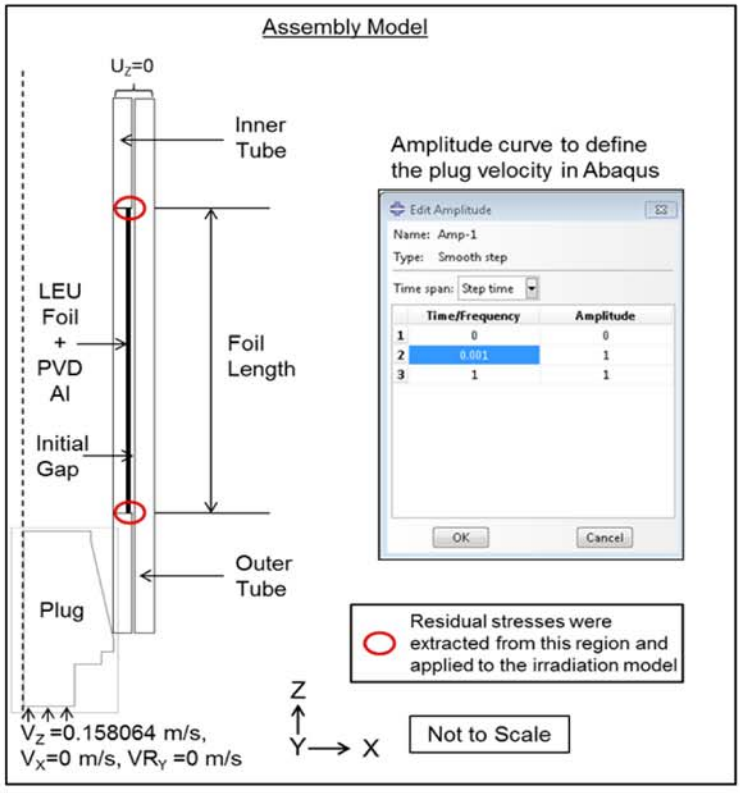

Figure 120. Draw-plug assembly model setup for the HFIR annular target.

After the assembly model, the maximum residual stresses which occur at the edges of the recess, were extracted and these were to be applied as initial inputs to a separate

iradiation model. The contact definitions play an important role in obtaining a converged solution. The tangential behavior and normal behavior contact definitions are applied to the model through the interaction properties module. For the tangential and normal behavior the defaults were used and the 'allow separation after contact' box was unchecked to ensure that the surfaces remain in contact after they have been assembled using the draw-plug process. Figure 121 provides the finite element mesh of the annular target assembly mode. Axisymmetric elements of type CAX4R, with 38630 linear quadrilateral elements and 40205 nodes, were to mesh the annular target assembly.

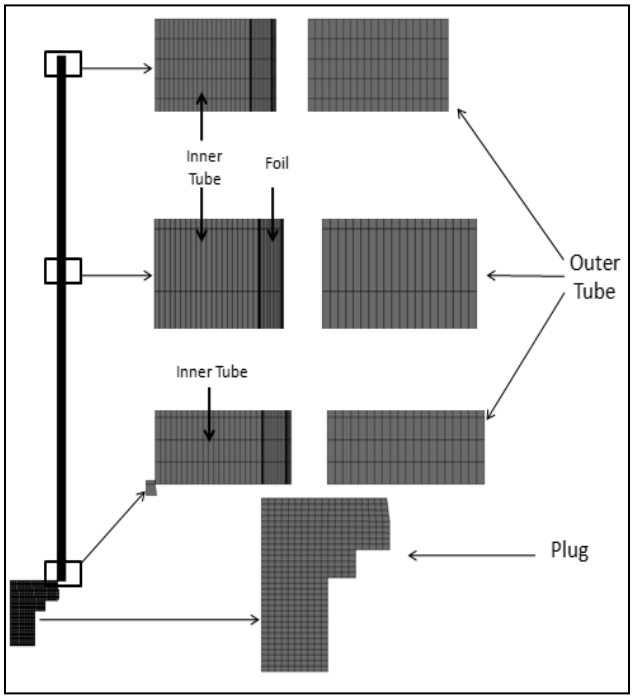

Figure 121. Finite element mesh of the assembly model for the HFIR annular target.

Figure 122 illustrates the setup of the irradiation model in Abaqus FEA [56]. The calculated input parameters such as the thermal contact conductance, fission gas pressure (from Sec 11.2) were included in the irradiation model. The material properties,

mechanical contact definitions remain the same for the irradiation model. The residual stress that remains in the material after the assembly process was taken as the initial condition for the irradiation model and included in the model with the help of a predefined field definition.

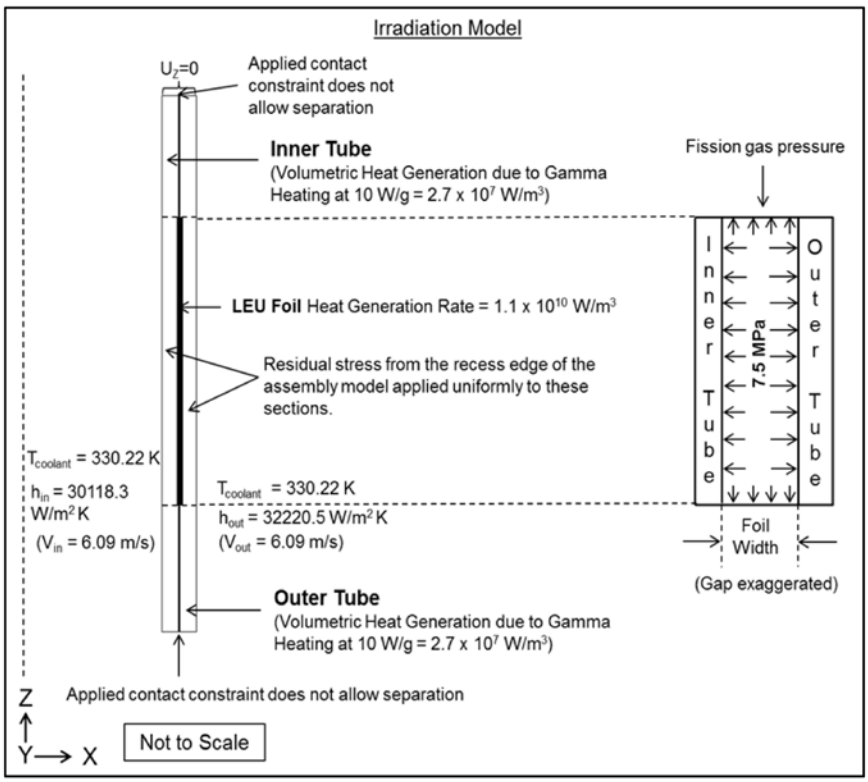

Figure 122. Irradiation model setup for the HFIR annular target.

The developed thermal conductance expression (Eq. (89)) is used in the model by selecting the thermal conductance option from the interaction properties module. The loading conditions for the irradiation model include the volumetric heat generation rate of the LEU foil with the PVD Al coating. Based on the dimensions of the foil (89.916 mm x 78 mm x 0.155 mm), the volumetric heat generation of the foil for a design basis power of 11 kW was found to be 1.01 x 10^{10} W/m^3. A volumetric heating rate was calculated for the inner and the outer Al 6061-T4 cladding to simulate the gamma heating that

would initially exist in the cladding. Taking this heating rate to be 10 W/g, and multiplying by the density of the Al 6061-T4 from Table 16, the volumetric heating rate was found to be 2.7 x 10^7 W/m^3. The calculated fission gas pressure of 7.5 MPa for a 100 % gas release situation was applied to the walls of the cladding as illustrated in Figure 122. The coolant temperature was 330.22 K, the inner and outer heat transfer coefficients, for a flow velocity of 6.09 m/s, were found to be 30118.3 W/m^2K and 32220.5 W/m^2K respectively (Sec 11.3). Figure 123 provides the finite element mesh used in the irradiation model. Fully coupled axisymmetric temperature-displacement elements of type CAX4RT, with 21200 linear quadrilateral elements and 22023 nodes, were used to mesh the irradiation model.

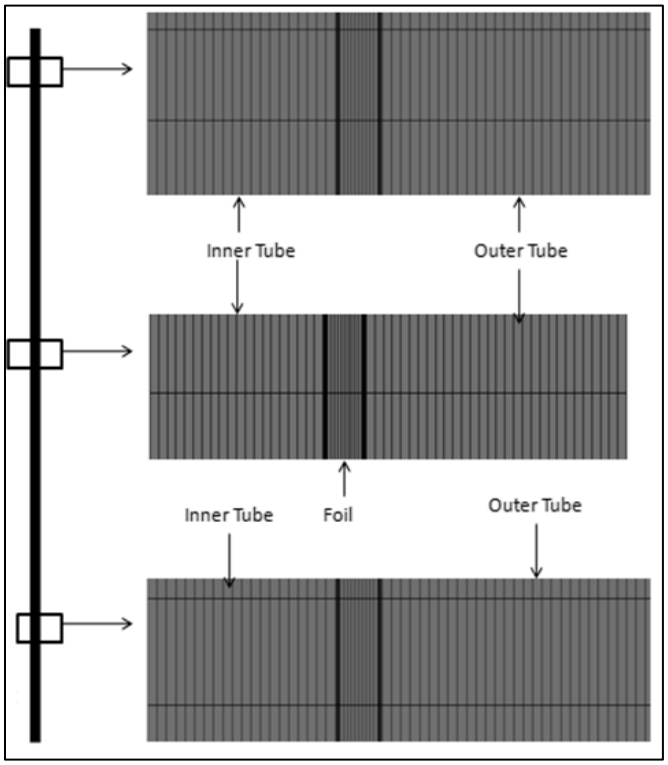

Figure 123. Finite element mesh used in the irradiation model for the HFIR annular target.

The melting point of the cladding was taken to be the thermal safety limit while the von Mises yield criteria for ductile materials as applied to the cladding was used as the structural safety limit. The thermal safety limit criterion is assumed to be met when it can be demonstrated by analysis that cladding temperatures do not exceed the melting temperature of the cladding material, 923 K (650 °C), during irradiation.

The structural safety limit criterion is assumed to be met when it can be demonstrated by analysis that the cladding experiences no plastic yielding during irradiation. The true stress at the onset of plastic deformation (as measured in a uniaxial round-bar tensile test) is assumed to be 145 MPa for the Al 6061-T4 cladding material. The von Mises yield surface model, based on J_2 flow theory, is applied in this analysis to determine the presence of any plastic yielding in the cladding.

The power margin criterion for safety calculations requires that safe operation of the target at reactor power levels of 130% above design-basis must be demonstrated by sensitivity studies performed as a part of the analysis. It is assumed that the reactor power level and the target heat generation rate (including gamma heating of the cladding and volumetric heating of the LEU foil) are linearly proportional, which implies that using a heat generation range from 11-17 kW in the sensitivity studies satisfies this requirement since this range bounds the 14.3 kW heat generation rate that corresponds to the 130% power safety margin.

11.5 Results

The safety basis calculations were not performed for the assembly model as all the assembly process takes place outside the reactor vessel and does not involve any

irradiative heating as well. However, one requirement to be fulfilled after the assembly process is to weld the edges of the target to provide a completely sealed environment. Accurately simulating the welded edges falls outside the scope of this analysis, as it requires information about the geometry of the weld. The edges of the inner and the outer cladding were 'tied' together in the irradiation simulation. This 'tie' constraint, as the name suggests, prevents the edges from separating. The assembled dimensions of the annular target were obtained from the assembly simulation and were compared against the measured values. Table 18 summarizes these results while Table 19 provides the maximum residual stresses in the recess region of the inner and outer tubes.

Table 18. Assembled dimensions of the annular target: measurement vs. model results.

Part	I.D (mm) Measured	I.D (mm) Model	Relief (mm) Measured	Relief (mm) Model	O.D (mm) Measured	O.D (mm) Model
Inner Tube	26.490	26.542	Not Available	27.793	Not Available	28.103
Outer Tube	Not Available	28.103	----------	----------	30.023	29.982

Table 19. Maximum residual stresses in the inner and outer tubes (region in contact with the foil only)

Part	Radial Stress (Pa)	Longitudinal Stress (Pa)	Hoop Stress (Pa)	Shear Stress (Pa)
Inner Tube	2.460×10^{7}	-2.490×10^{8}	-2.118×10^{8}	4.407×10^{7}
Outer Tube	2.330×10^{7}	6.909×10^{7}	7.928×10^{7}	-2.49×10^{6}

The safety-basis calculations require analysis of the annular target at 130% power. For this purpose a parametric study on the power (converted to a volumetric heat generation

rate based on foil volume) was conducted. Table 20 provides the maximum temperature in the annular target for each heat generation rate. The maximum cladding temperature at the maximum chosen power, for the safety-basis calculations, is 381.94 K. This is much lower than the melting temperature of the cladding (923 K). This allays any thermal safety concerns with the annular target.

Table 20. Annular target temperature results for the safety basis analysis.

Heat Generation Rate of the Foil (x 10^{10} W/m^3)	Power (kW)	Inner clad max temperature (Kelvin)	Foil max. temperature (Kelvin)	Outer clad max temperature (Kelvin)
1.01	11	360.49	584.23	358.41
1.20	13	363.92	621.47	365.57
1.38	15	366.41	649.27	373.47
1.56	17	368.27	675.63	381.94

The von Mises stresses along the length of inner and outer cladding are illustrated in Figure 124. Due to the non-uniform stresses and hence the inability to provide the data in a tabular form, it was decided to provide plots at the lowest and the highest power. The lowest power considered here (11 kW) corresponds to the design-basis power, while the highest power (17 kW) can be used as a bounding value for the safety basis power (14.3 kW). At both 11kW and 17 kW, the maximum von Mises stresses are within the yield strength of the Al 6061-T4. This proves that the annular target is structurally safe. Figure 125 illustrates the radial temperature distribution in the annular target, at half the target length. The maximum temperatures provided in Table 20 were obtained from Figure 125. The longitudinal temperature distributions on the surfaces of the inner and outer tubes have been provided by Figure 126 and Figure 127 respectively.

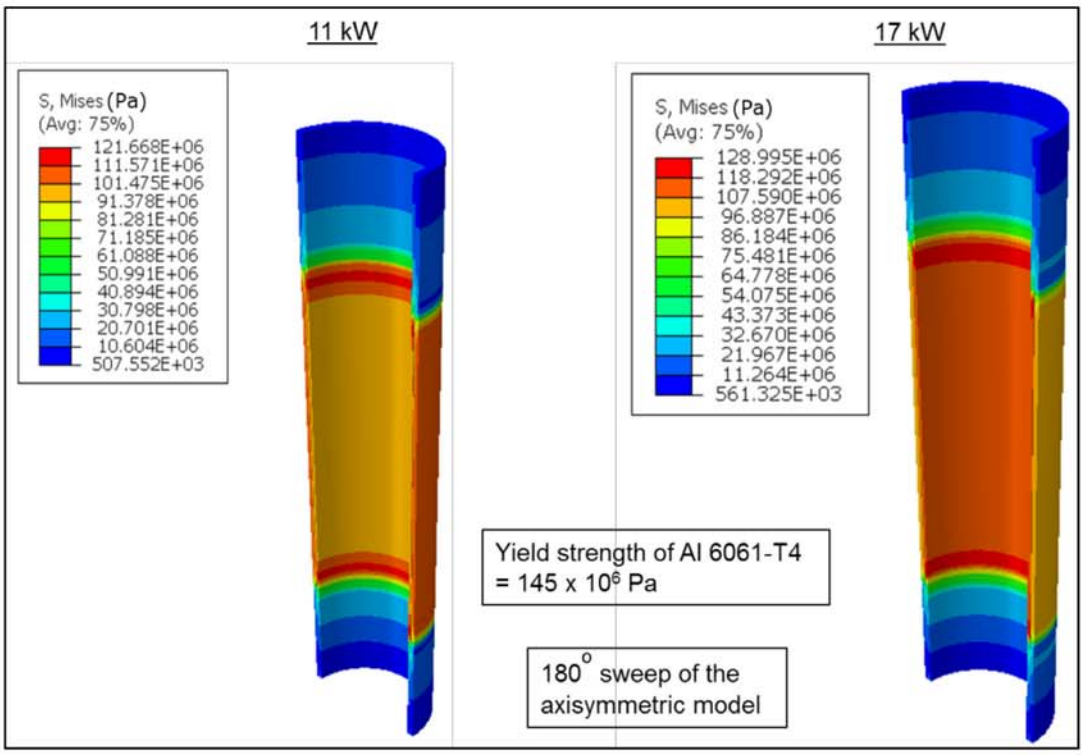

Figure 124. Von Mises stress distribution in the cladding for the HFIR annular target.

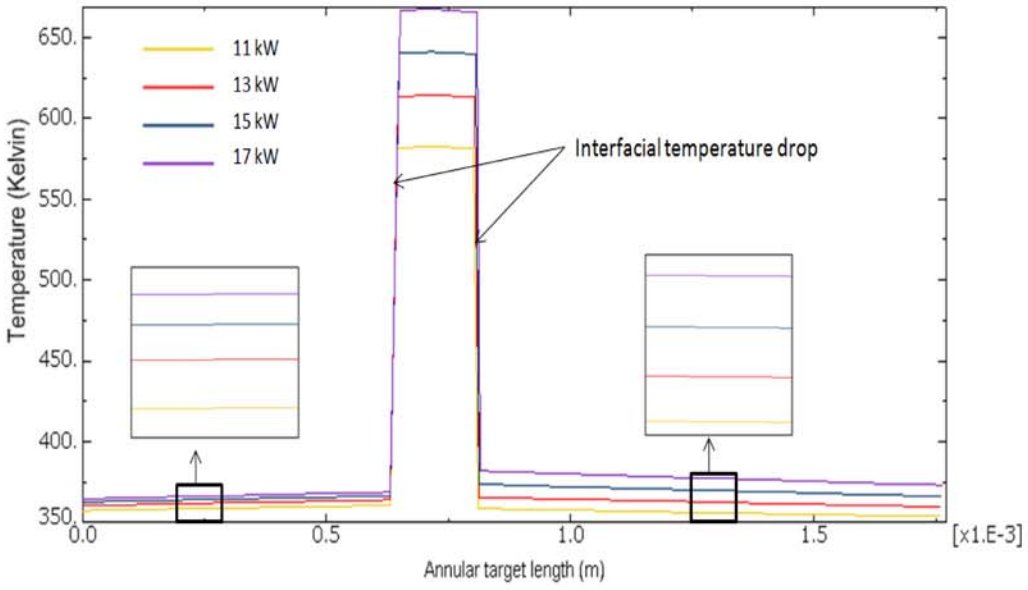

Figure 125. Radial temperature distribution in the HFIR annular target (values extracted at half the target length).

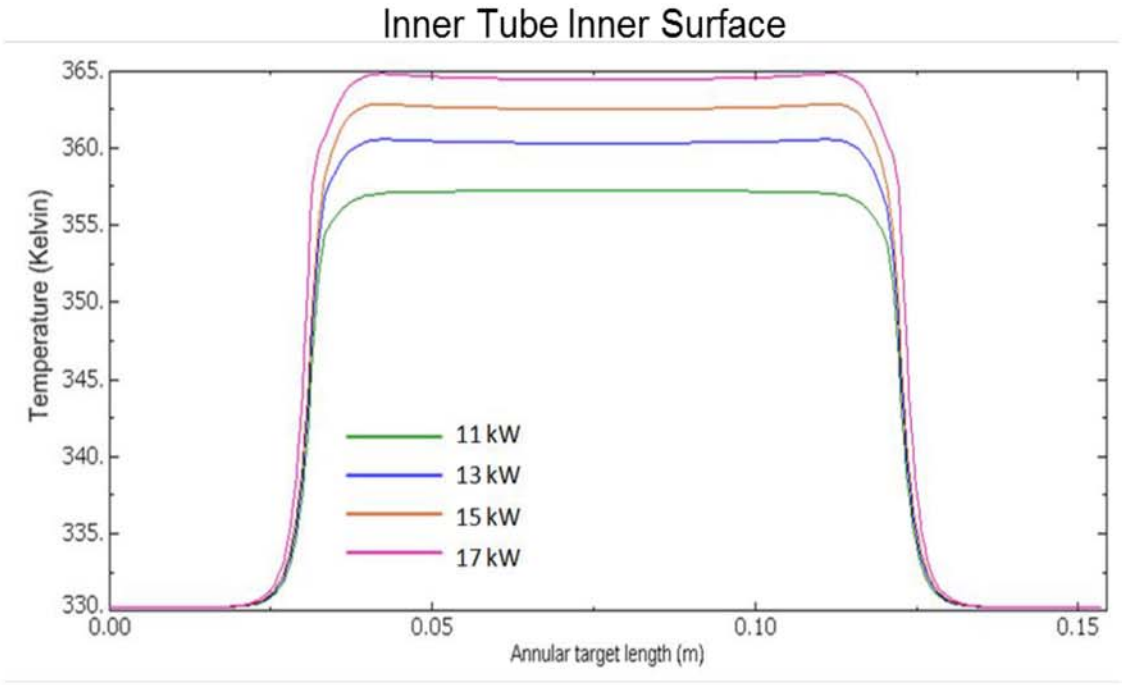

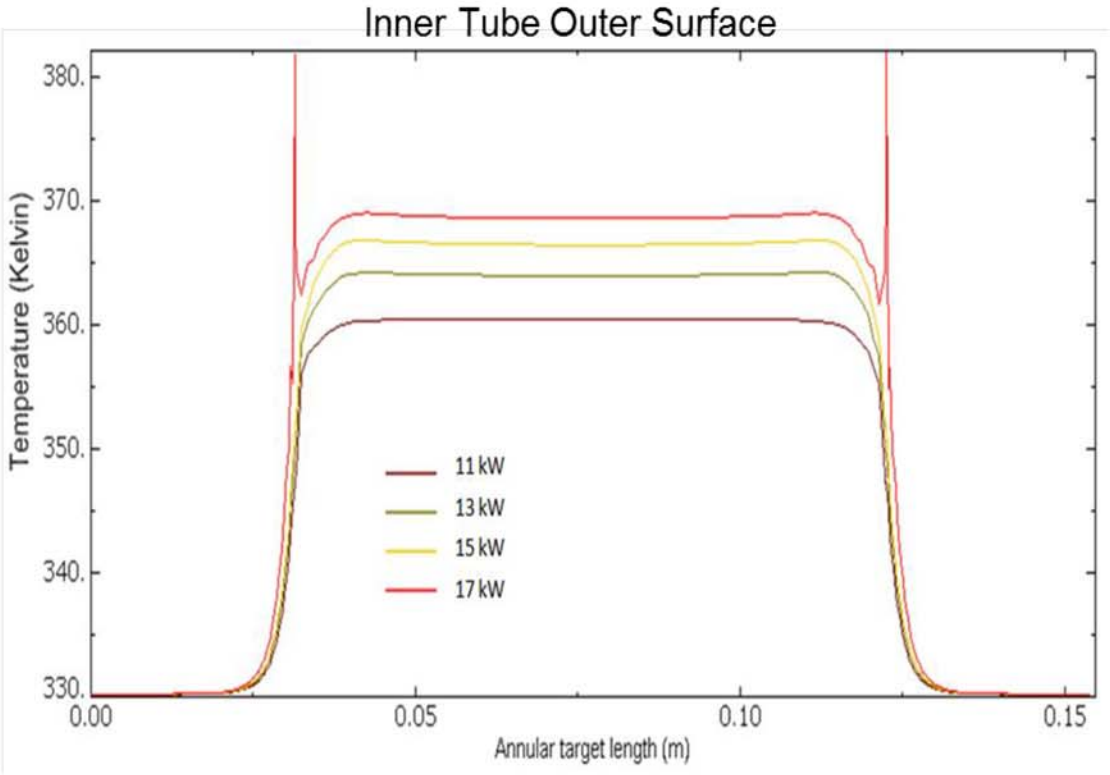

Figure 126. Longitudinal temperature distribution in the inner tube for the HFIR target.

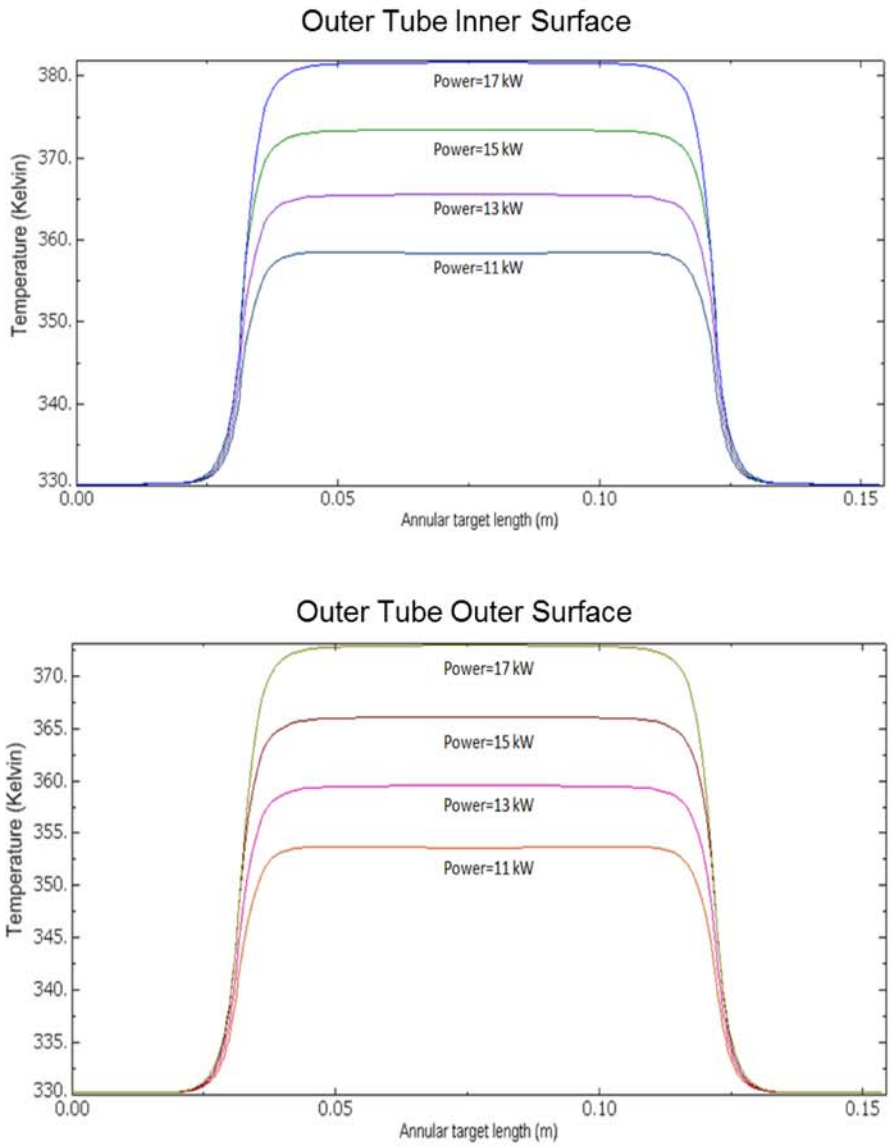

Figure 127. Longitudinal temperature distribution in the outer tube for the HFIR target.

The safety-basis calculations indicate that the annular target temperature will remain below the cladding melting temperature of 923 K for all power levels between 11-17 kW. This range includes the 130% power level at 14.3 kW. The structural results indicate that the von Mises stresses in the cladding are lower than the yield strength of the Al 6061-T4 cladding for all power levels between 11-17 kW.

11.6 Comments from the Technical Adequacy and Independent Review Committee

One of the requirements to be fulfilled before the calculation is formally accepted is that it should pass the technical adequacy review and the independent review. The developed calculation was approved by the committee and their respective conclusions have been provided below in quotations.

"A check and technical adequacy review (TAR) has been carried out for the safety-basis SBP-1000 analysis documented in "Mechanical and Thermal-Stress Analysis of an Annular Target with a Low-Enriched Uranium Foil for HFIR Irradiation," C-HFIR-2013-023, prepared by S.G. Govindarajan. This TAR, guided by the Technical Adequacy Review Checklist (SBPF-1000.1) shown on p. 1 of this document, was performed pursuant to the procedures given in "Preparation, Review, and Handling of Calculations" SBP-1000, rev. 2, and "Configuration Controls of Software for HFIR Safety Basis Calculations," SBP-1300, rev. 1, where applicable. All inputs were checked to ensure that the values reported in C-HFIR-2013-023 correctly reflected the values applied in the Abaqus input files. All significant assumptions were identified and adequately justified in the document. Selected Abaqus baseline cases were re-run by the author of this TAR to check that the results reported in C-HFIR-2013-023 could be easily identified in the Abaqus output by any future re-analysis of the target assembly. A "separate-effects" study was carried out for this TAR for the purpose of checking the sensitivity of the analysis results to small modifications to the input data by identifying and applying different (but still valid) modeling decisions and assumptions. The results of the study indicated that small changes to the inputs produced small changes in the output, and the changes in the results followed trends expected from the physics being simulated by the model."

- *Technical Adequacy Reviewer*

"This independent review of C-HFIR-2013-023/R0 has determined that the calculation is technically adequate (the models employed are generally text-book and have been used extensively in the current fuel performance codes that are available today). Also, a critique (Sections 3.2.2 through 3.2.5, above) of the assumptions employed in the calculation irradiation modeling indicate that these assumptions are overly conservative; that is, the calculated gas gap conductances are probably conservatively low which results in higher calculated foil temperatures."

- *Independent Reviewer*

Chapter 12: Boral Control Blade Safety Analysis

This chapter will focus on the 2nd part of this dissertation – safety analysis of a nuclear reactor component. The analysis presented in this section was performed by the author of this dissertation for MURR to help them with their relicensing efforts. The work [77] was presented at the 5th international symposium for material testing reactors (ISMTR) held in Columbia, Missouri.

12.1 Control Blade Geometry and Model Development

Since a detailed introduction of the BORAL [78] control blades used at MURR has already been provided in Sec 1.4, this section will first introduce the geometry of the control blade followed by the model development.

The neutron absorber in the BORAL [78] control blades at MURR is boron. The control blades operate in a gap between the outside of the reactor pressure vessel and the inside of the beryllium reflector as shown in Figure 7. The BORAL core geometry is 0.863 m long, 0.254 x 10^{-2} m thick and 0.205 m wide. The radius of curvature of the centerline of the blade is 0.166 m. The aluminum cladding thickness of 9.5 x 10^{-4} m on the front and back faces of the BORAL with 0.003 m on both edges. The mounting region of the blade extends to 0.139 m beyond the BORAL cavity. Thus the overall profile of the control blade including the mounting region is 0.211 m wide x 0.004 m thick x 0.101 m long. The geometry of the control blade has been provided in Figure 128. The outer diameter of the pressure vessel is between 0.318m and 0.319m. The inner diameter of the beryllium reflector is between 0.347m and 0.348 m. The gap width is maintained by vertical spacers which are set into the beryllium reflector and cross the gap to the outer diameter of the

reactor pressure vessel. The minimum width of the gap in which the rods operate is 1.4 x 10^{-2} m. The thickness of the control blade is 0.635 x 10^{-2} m, leaving a gap of approximately 0.381 x 10^{-2} m on either side of the blade [79]. The displacement of the blade would be as a result of differential expansion between the inner and outer longitudinal fibers with a radial temperature gradient through the blade.

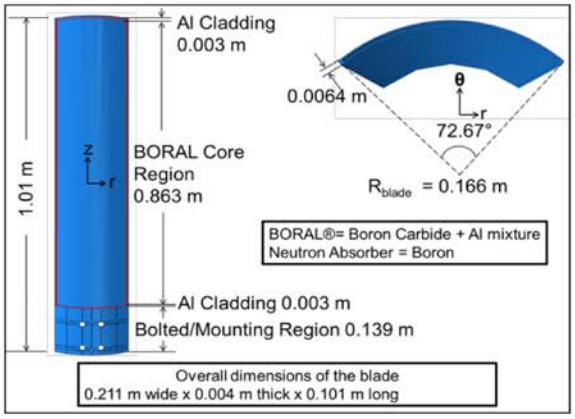

Figure 128. Dimensions of the BORAL control blade at the Missouri University Research Reactor (MURR).

The energy deposition in a highly discretized model of a MURR control blade, that can be in any four possible positions "A", "B", "C" or "D" of the MURR core configuration, was studied using the Monte Carlo N-Particle (MCNP) model [80] by Nickie J. Peters [81] from MURR. A control blade of nominal length 0.863 m, placed in any one of these positions, travels within a narrow annular water channel between the outer surface of the outer reactor pressure vessel and the inner wall of the beryllium reflector, which is 1.42 x 10^{-2} m wide. Figure 129 provides the cross sectional view [82] of the MCNP MURR core model showing the four control blade positions. For the MCNP [80] computations, the control blade was divided into 154 independent zones (cells), which include: (i) 4 azimuthal sections (over the entire length), (ii) 9 radial sections over each of the 4 incremental unit length sections for each azimuthal section, and (iii) 2 radial sections over

each of the next five incremental sections for each azimuthal section. The discretization scheme was chosen to properly account for correct spatial distribution of the energy release from the $^{10}B(n, \alpha)^{6}Li$ reaction, the major component of the energy deposited in the blade. The increase discretization in the (four) lowest portions reflect the most active regions of the control blade.

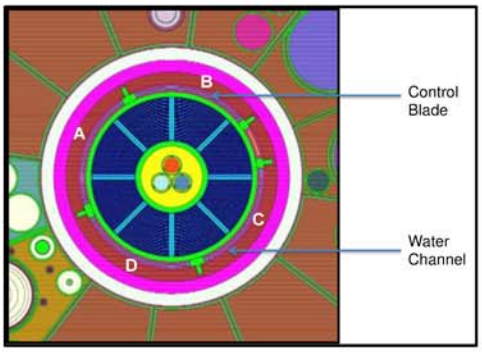

Figure 129. A cross- sectional view of the MCNP MURR core model showing the four positions of the control blades in a narrow water channel between the outer surface of the outer reactor pressure vessel and the inner wall of the beryllium reflector.

The F6 neutron tally in MCNP [80] was used to recover the energy-release from the ^{10}B fission within the blade. Since the second most significant source of energy deposition in the control blade comes from gamma rays, that mostly originate from uranium fission in the fuel and (n, γ) capture interactions throughout the core, the F6 photon tally in MCNP [80] in addition to the method described [81] was used to predict this contribution. Since the energy deposited from the $^{10}B(n, \alpha)^{6}Li$ reaction and the gamma interactions have different origins, their energy deposition profiles throughout the blade are expected to be different. This is important because deflection in the blade is directly related to the magnitudes of thermal stresses across different regions in the blade. The energy deposition profiles (i.e., alpha + gamma) determine how the heating rate varies throughout the blade as it is being irradiated. The bottom of the blade is predicted to be

the region of highest energy deposition. This is expected since the bottom edge of the control blade is always constrained to be within the length of the fuel even at maximum travel.

12.2 Heating Profile Development

The BORAL meat was split into 4 quadrants. The heat generation rate as a function of the thickness and longitudinal position due to radiative heating was calculated. A curve fit was created using the discrete points obtained from the MCNP [80] simulations. The data at the longitudinal locations 0.259 m, 0.432 m, 0.604 m and 0.777 m from the fuel-side aluminum cladding and beryllium side aluminum cladding were used for the heat generation values within the BORAL thickness Fuel-side data points were considered constant through the first four BORAL thickness locations. Beryllium side data points were considered constant through the last four BORAL thickness locations. The data point at the center of the BORAL was averaged from the fuel side and beryllium side points. For a given azimuthal position, the volumetric heat generation data was plotted against thickness and longitudinal position using 3-D plotting software to visualize the general functional trends. Additionally, for a given thickness, the data was plotted against azimuthal and longitudinal position to further aid in visualization. These plots suggested that the volumetric heat generation follows an even polynomial profile in the radial direction, t, and a decaying exponential in the longitudinal direction, z. Hence, a function of the form given by Eq. (90) was assumed, where the functions A(t) and B(t) allow for a different decaying functions to be determined at a given radial position.

$$q''' = f(t,z) = A(t)e^{B(t)z} \tag{90}$$

A function of this form was determined for each of the four partitions the blade was divided into, the left edge, left middle, right middle and right edge quadrants. The equation governing the left edge section was held constant along the azimuthal direction between -36.3˚ and -18.15˚. The equation governing the left middle section was held constant along the azimuthal direction for -18.15˚ to 0˚. Likewise, the right middle section applied to the 0˚ to 18.15˚ portion of the blade and the right edge equation applied to the 18.15˚ to 36.3˚ partition. To derive the functions A(t) and B(t), the natural logarithm of Eq. (90) to obtain Eq. (91).

$$\ln q''' = \ln A(t) + B(t)z + C(t) \tag{91}$$

Using the above equation it is simple to fit a straight line relating the ln (q''') to z at each thickness location. An example of this process can be seen in the Figure 130where $\ln q'''$ is plotted against z at the BORAL fuel-side surface (t = 9.5 x 10^{-4} m) at the left edge location for alpha heat generation. The slope and intercept are provided on the plot, with the slope being the value of B and intercept the value of C. Equations of the form of Eq. (91) were determined for each of the provided thickness and azimuthal locations. These equations were then used as the exponent of the exponential function to return it to the form of Eq.(90). Similar results were obtained for the gamma heating profile. The A and B coefficient variation with thickness was then determined. Due to the discontinuities occurring at the interfaces of the aluminum cladding and BORAL core, the overall function for volumetric heat generation was defined in a piecewise fashion where the A and B coefficients remained constant with thickness through the cladding on the fuel-side and beryllium-side, while the coefficients varied with thickness through the BORAL core. The A coefficient variation followed a 4th order polynomial for the alpha heating

profile and a 2nd order polynomial for the gamma heating profile. The B coefficient followed a 2nd order polynomial curve for both the alpha and gamma heating profiles. Examples of the 'A' and 'B' coefficient variation with thickness through the BORAL core can be seen in Figure 131 and Figure 132.

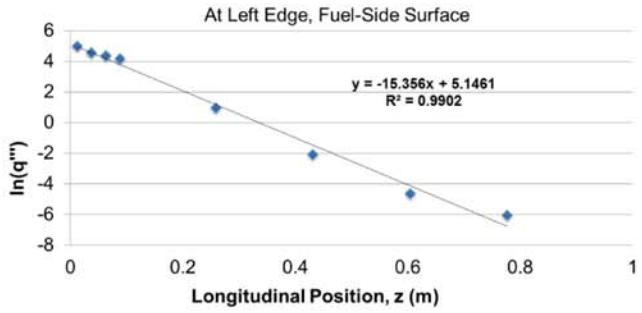

Figure 130. Linearized exponential decay function for a given thickness and azimuthal location for alpha heating.

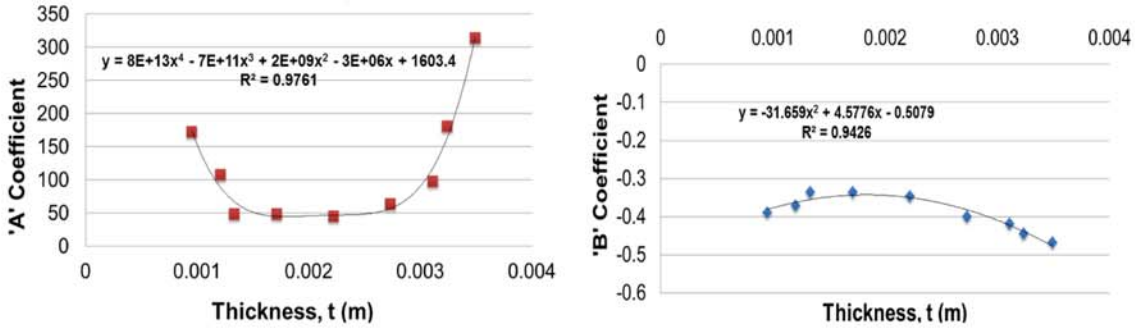

Figure 131.'A' and 'B' coefficient variations with thickness in BORAL core for alpha heating at left edge location.

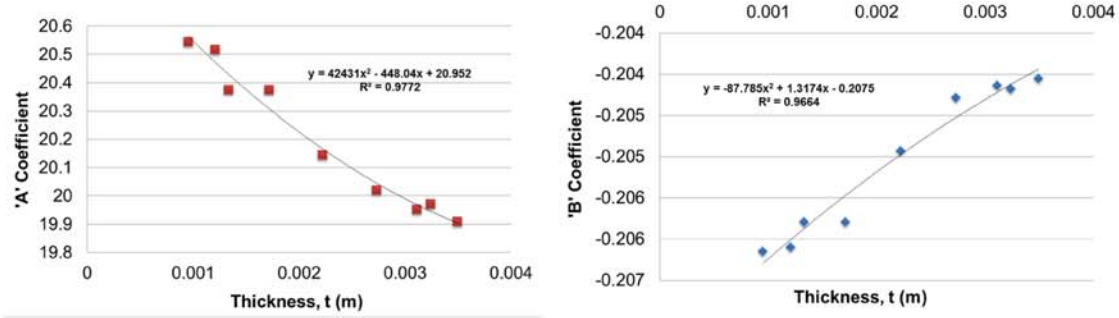

Figure 132. 'A' and 'B' coefficient variation with thickness in the BORAL core for gamma heating at the left edge location.

The resulting functional form for the heat generation rate within the BORAL resembled Eq. (90) where Eqs.(92) and (93) represent the alpha heating profile, while Eqs. (94) and (95) represent the gamma heating profile. The 'c' and 'd' coefficients varied along the azimuthal direction of the blade and were defined for each of the four quadrants.

$$A_{\alpha}(t) = c_{4\alpha}t^4 + c_{3\alpha}t^3 + c_{2\alpha}t^2 + c_{1\alpha}t + c_{0\alpha} \tag{92}$$

$$B_{\alpha}(t) = d_{2\alpha}t^2 + d_{1\alpha}t + d_{0\alpha} \tag{93}$$

$$A_{\gamma}(t) = c_{2\gamma}t^2 + c_{1\gamma}t + c_{0\gamma} \tag{94}$$

$$B_{\gamma}(t) = d_{2\gamma}t^2 + d_{1\gamma}t + d_{0\gamma} \tag{95}$$

Figure 133 illustrates the alpha heat generation through the BORAL core at the left edge (w=-0.079 m) of the control blade data and curve fit surface plots respectively. In Figure 133, the width is held constant as the thickness (t) and longitudinal position (z) are varied.

Figure 134 provides the plots for the alpha heat generation on the fuel-side BORAL face ($t = 9.5 \times 10^{-4}$ m) for the data and curve fit. Thickness (t) has been held constant while the width (w) and longitudinal position (z) have been varied to generate the surface plots. Comparison of the data obtained from MURR and the values obtained from the functional form of the heat generation for the alpha heating profile at discrete points within the control blade has been provided in Table 21.

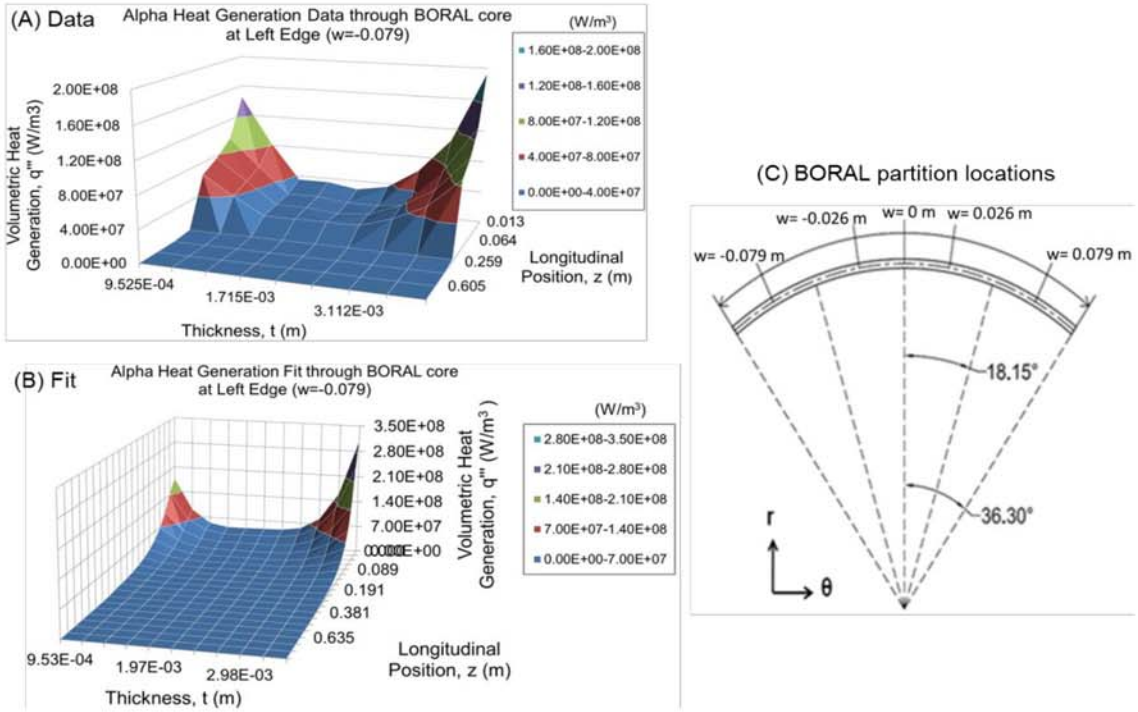

Figure 133. Alpha heat generation data and fit through the BORAL core at the left edge.

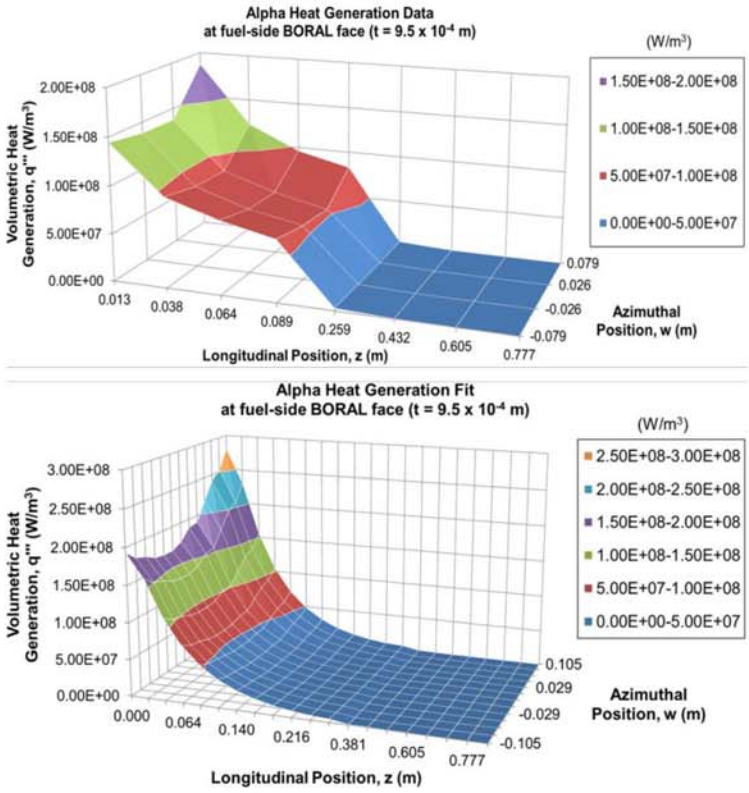

Figure 134. Alpha heat generation data and fit at the fuel-side BORAL face.

Table 21. Alpha volumetric heat generation data and fit comparison at the left edge (w =-0.079m)

Longitudinal Position, z X 10^{-2}(m)	Volumetric Heat Generation Data X 10^{6}(W/m^{3})	Volumetric Heat Generation Fit X 10^{6}(W/m^{3})	Error (%)
t = 0.095			
1.27	144.427	144.884	0.32
3.81	94.874	99.006	4.36
6.35	76.926	67.656	12.05
8.89	64.632	46.232	28.47
25.908	2.612	3.606	38.07
43.18	0.125	0.270	116.11
60.452	0.009	0.020	111.25
77.724	0.002	0.001	34.94
t = 0.222			
1.27	28.419	39.216	37.99
3.81	20.679	27.642	33.67
6.35	17.329	19.484	12.44
8.89	18.241	13.734	24.71
25.908	2.586	1.319	49.01
43.18	0.115	0.122	6.16
60.452	0.007	0.011	45.30
77.724	0.001	0.001	15.93
t = 0.349			
1.27	192.955	248.881	28.98
3.81	132.400	154.462	16.66
6.35	103.999	95.863	7.82
8.89	87.631	59.495	32.11
25.908	2.561	2.435	4.92
43.18	0.105	0.095	9.56
60.452	0.005	0.003	37.99
77.724	0.000	0.000	5.76

12.3 Numerical Finite Element Model

A numerical finite element model of the BORAL control blade was created using the commercial finite element code Abaqus FEA. The curvature of the control blade was created first using the dimensions in the drawings [83, 84] provided by MURR and then

extruded to 0.101 m to form the full length of the control blade. This was followed by creating a partition at 0.869 m to separate the bolted region from the region occupied by the BORAL (Figure 135a). A cavity equivalent in curvature and length of the BORAL was cut-extruded to the length of the BORAL meat. To help simulate the developed heating profile, the BORAL was partitioned into 4 sections along the curvature as illustrated in Figure 135b. Assembly of the model consisted of placing the BORAL meat in the cavity created in the control blade. The 'translation' option in Abaqus was used to perform the assembly by specifying the start and end points for translation. A fully coupled thermal stress step was created and perfect contact was assumed to exist between the BORAL meat and the aluminum cladding. The material properties provided in Table 22 were used in the Abaqus model. It was assumed that all the external surfaces of the aluminum cladding were exposed to coolant at 325 K that provided an effective heat transfer coefficient of 1000 W/m^2K. Perfect interfacial contact between the BORAL and aluminum cladding was assumed. The internal heat generation profile obtained based on the curve fit data was used as the loading condition on the BORAL. Equations (96)- (99) are the expressions for the total heat generation (alpha + gamma) rates (in W/m^3) at the left edge, left middle, right middle and right edge respectively (Figure 133c). An analytic field was created in Abaqus FEA [56] and each of these expressions was input. These analytic fields were used to define the heat generation at each of the 4 partitioned locations on the BORAL meat (Figure 135b). The mechanical boundary conditions were applied to the bolt holes to prevent translation of these holes in the radial and longitudinal direction as illustrated in Figure 135c.

$$q'''_{\text{left edge}} = 1000000\left(\begin{array}{l} e^{39.3701\left(-2.82166-87.7846\left(x^2+y^2\right)+30.3262\sqrt{x^2+y^2}\right)z} \\ \left(1253.36+42431.4\left(x^2+y^2\right)-14469.7\sqrt{x^2+y^2}\right) \\ +e^{39.3701\left(-1369.95-49071.9\left(x^2+y^2\right)+16396.2\sqrt{x^2+y^2}\right)z} \\ \left(\begin{array}{l} 496373-2.99448\,x10^6\sqrt{x^2+y^2}+ \\ 2.14166\,x10^9\left(-0.165227+\sqrt{x^2+y^2}\right)^2 \\ -6.76381\,x10^{11}\left(-0.165227+\sqrt{x^2+y^2}\right)^3 \\ +7.97257\,x10^{13}\left(-0.165227+\sqrt{x^2+y^2}\right)^4 \end{array}\right) \end{array}\right)\frac{W}{m^3} \tag{96}$$

$$q'''_{\text{left middle}} = 1000000\left(\begin{array}{l} e^{39.3701\left(-3.84705-125.048\left(x^2+y^2\right)+42.688\sqrt{x^2+y^2}\right)z} \\ \left(1664.39+57227.8\left(x^2+y^2\right)-19404.1\sqrt{x^2+y^2}\right) \\ +e^{39.3701\left(-1277.24-45666.3\left(x^2+y^2\right)+15272.3\sqrt{x^2+y^2}\right)z} \\ \left(\begin{array}{l} 459575-2.77242\,x10^6\sqrt{x^2+y^2}+ \\ 1.97312\,x10^9\left(-0.165227+\sqrt{x^2+y^2}\right)^2 \\ -6.20434\,x10^{11}\left(-0.165227+\sqrt{x^2+y^2}\right)^3 \\ +7.27138\,x10^{13}\left(-0.165227+\sqrt{x^2+y^2}\right)^4 \end{array}\right) \end{array}\right)\frac{W}{m^3} \tag{97}$$

$$q'''_{\text{right middle}} = 1000000\left(\begin{array}{l} e^{39.3701\left(-4.09969-125.241\left(x^2+y^2\right)+44.241\sqrt{x^2+y^2}\right)z} \\ \left(1234.01+42574.7\left(x^2+y^2\right)-14380\sqrt{x^2+y^2}\right) \\ +e^{39.3701\left(-1317.27-47138.9\left(x^2+y^2\right)+15757.8\sqrt{x^2+y^2}\right)z} \\ \left(\begin{array}{l} 523152-3.15605\ x10^6\sqrt{x^2+y^2}+ \\ 2.26702\ x10^9\left(-0.165227+\sqrt{x^2+y^2}\right)^2 \\ -7.1948\ x10^{11}\left(-0.165227+\sqrt{x^2+y^2}\right)^3 \\ +8.51505\ x10^{13}\left(-0.165227+\sqrt{x^2+y^2}\right)^4 \end{array}\right) \end{array}\right)\frac{W}{m^3} \quad (98)$$

$$q'''_{\text{right edge}} = 1000000\left(\begin{array}{l} e^{39.3701\left(-5.19054-173.182\left(x^2+y^2\right)+58.7592\sqrt{x^2+y^2}\right)z} \\ \left(2850+98956\left(x^2+y^2\right)-33443\sqrt{x^2+y^2}\right) \\ +e^{39.3701\left(-1281.77-45767.5\left(x^2+y^2\right)+15316.4\sqrt{x^2+y^2}\right)z} \\ \left(\begin{array}{l} 655008-3.95133\ x10^6\sqrt{x^2+y^2}+ \\ 2.79157\ x10^9\left(-0.165227+\sqrt{x^2+y^2}\right)^2 \\ -8.70963\ x10^{11}\left(-0.165227+\sqrt{x^2+y^2}\right)^3 \\ +1.01206\ x10^{14}\left(-0.165227+\sqrt{x^2+y^2}\right)^4 \end{array}\right) \end{array}\right)\frac{W}{m^3} \quad (99)$$

The finite element mesh of the BORAL meat and the aluminum cladding are given in Figure 136. Nine thickness elements were specifically used on the BORAL meat to enable the application of the developed heating profile.

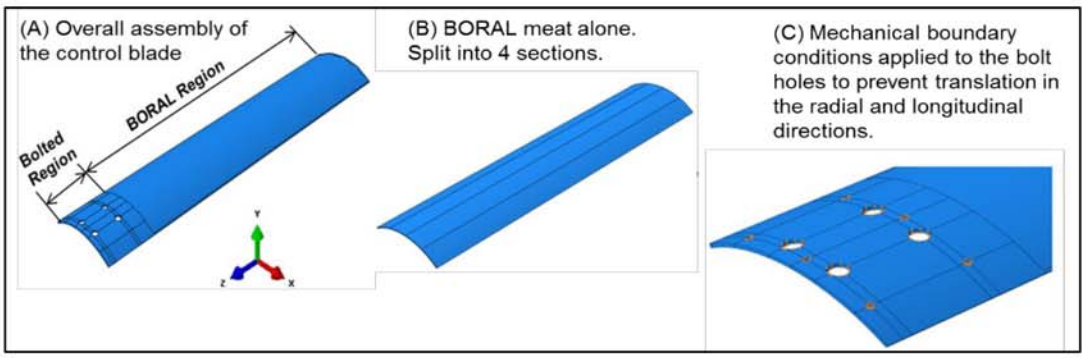

Figure 135. Components of the assembled control blade along with the mechanical boundary conditions.

Table 22. Material properties of the BORAL and the aluminum cladding used in the analysis.

Material Property	Aluminum 1100	BORAL
Thermal Conductivity (W/mK)	186.4	76.8, 98, 132
Density (Kg/m^3)	2713	2481
Elastic Modulus (GPa)	69	62.053
Poisson's Ratio	0.33	0.23
Thermal Expansion Coeff (K^{-1})	2.36E-05	1.97E-05
Specific Heat (J/KgK)	1120	1380

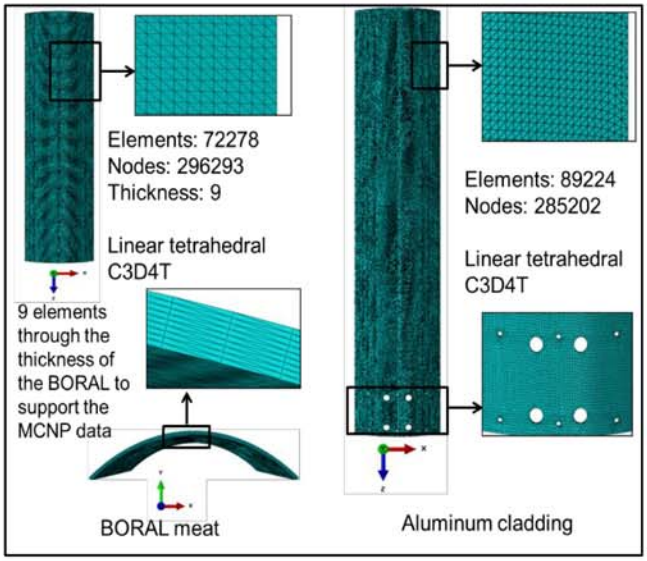

Figure 136. Finite element mesh of the (a) BORAL meat and (b) aluminum cladding used in the Abaqus model.

12.4 Results

Figure 137- Figure 139 illustrates the thermal and corresponding mechanical behavior of the control blade. Figure 137 provides the temperature distribution contour of the control blade along with the temperature distribution along the cladding centerline. The temperature drops off in the longitudinal direction in a manner similar to the heat generation rate. The temperature distribution contour plot in Figure 137a also shows that the right side of the control blade is hotter than the other side and this is consistent with the curve fits (Figure 133 and Figure 134) that were constructed based on the data provided by MURR. The radial deflection of the blade resulting from the temperature is illustrated in Figure 138a. A first look at this figure gives the impression that the deflection is symmetrical when Figure 134 shows that the asymmetry in temperature exists along the curvature of the blade. To verify that asymmetry exists in the radial direction along the curvature, the deflection as a function of the circumference was plotted as shown in Figure 138. This plot shows that the right edge of the blade (which is the hotter side) deflects slightly more than the other side and that the difference in deflection is approximately 30.5 μm.

The thermal conductivity of the BORAL used in the current analysis is 76.8 W/mK as illustrated in Table 22. However, experiments at the University of Missouri suggested that the thermal conductivity of the BORAL was 115±17 W/mK. A parametric study was performed by varying the thermal conductivity of the BORAL with a lower bound of 98 W/mK and an upper bound of 132 W/mK. The change in maximum radial deflection was found to be negligibly small and of the order of 10.2 μm. Figure 139 illustrates that the maximum radial deflection of the blade is within the control blade channel gap even at

the upper bound (132 W/mK) of the BORAL thermal conductivity. It should be noted that the three different thermal conductivity values modeled provide deflections that lie nearly on top of each other making it difficult to distinguish them in the plot.

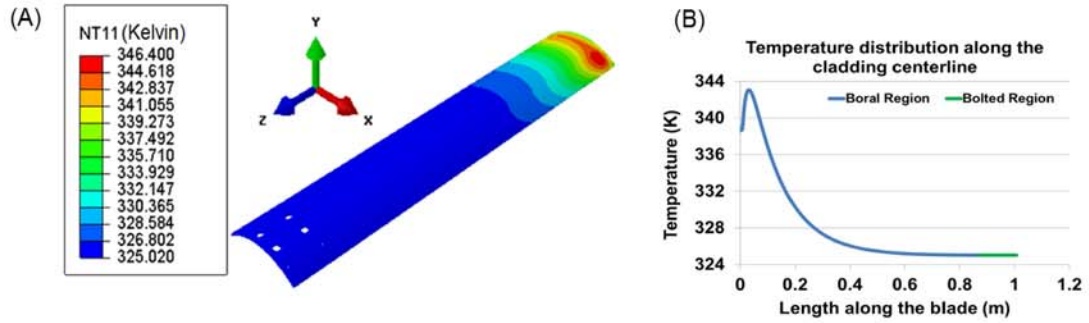

Figure 137. (a) Temperature distribution contour of the control blade and (b) variation of temperature along the cladding centerline.

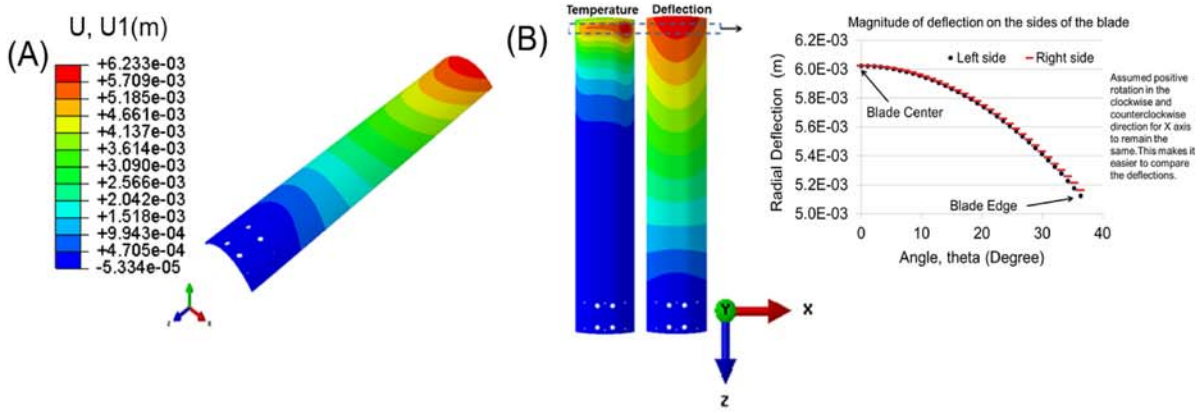

Figure 138. (a) Radial deflection contour and (b) deflection variation on the sides of the control blade.

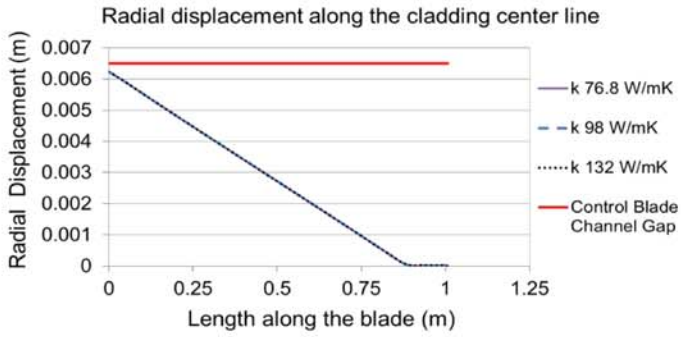

Figure 139. Deflection variation along the length of the control blade with varying thermal conductivity of the BORAL.

Chapter 13: Conclusions and Recommendations

In this dissertation the safety analysis of the annular target and the control blade used at the Missouri University Research Reactor (MURR) has been presented. The main goal in both these investigations is to develop modeling tools to analyze the thermal mechanical behavior of the annular target and the control blade, and establish by means of these developed analysis tools that they would perform safely during irradiation. In the case of the control blade, the analysis was used to support the relicensing efforts of MURR and in the case of the annular target the safety analysis is required to prove that they can be irradiated without any concern for the production of the medical isotope Mo-99. The commercial finite element code Abaqus FEA [56] was used for this purpose.

Initial analysis of the annular target involved development of a 2D uniform heating numerical model. To validate this, an analytical model of a triple layer annular cylinder was constructed. The validated uniform heating model was used to validate the non-uniform heating model using an order of magnitude comparison approach. Based on the analysis of the non-uniform heating model it was found that the inner tube was at a greater risk of failing first (in case the target were to fail) as the magnitude of hoop stresses in the inner tube were greater than on the outer tube. The uniform heating model was able to match the inner tube hoop stresses in the non-uniform heating model to within 20 %. Parametric studies were performed using the uniform heating analytical model to assess the sensitivity of the target to varying LEU heat generation rates, heat transfer coefficient ratios and tube thickness ratios. The analysis results indicate that the annular target with Al 6061-T6 as the cladding material is reliable at high heat generation rates of the LEU (upper bound of 6.4 x 10^{10} W/m^3 ~ 400 W/cm^2 heat flux) and the

magnitude of separation can be controlled by adjusting the heat transfer coefficient split between the inner and outer surfaces.

The second part of the annular target analysis involved inclusion of the assembly residual stresses by simulating either the hydroforming or the draw-plug assembly process before the irradiation analysis. A three step elasto-plastic model was built. In the hydroforming analysis, the first analysis step simulated the hydroforming process using an internal pressure of 36.4 MPa and this was followed by a pressure relaxation step to simulate the recovery. In the axisymmetric draw-plug analysis, the first step simulated the draw-plug assembly process by applying a velocity of 0.160726 m/s to the base of the plug. This was followed by a step where the plug was removed from the simulation. Finally, in both these analyses, the irradiation process was simulated by including the residual stresses from the previous step. The results from the hydroforming and the draw-plug analysis procedures indicate that the residual stresses from the assembly process tend to negate and decrease the stresses at the end of the irradiation step. This is favorable from a material standpoint as the inner and outer tubes are unlikely to fail under the applied heat generation of 1.6×10^{10} W/m^3. This corresponds to a heat flux of ~ 100 W/cm^2 incident on the outer surface of the inner tube and the inner surface of the outer tube.

The effects of fission gas release, uranium swelling, thermal contact conductance, heat generation in the cladding, and the pressure exerted by the coolant flow, were studied for the draw-plug based irradiation model. The analysis results indicate very small changes in temperatures and von Mises stresses for each of the cases considered in the analysis. The group of parameters that provide the worst case scenarios for the temperatures and von Mises stresses was found to be different. The combination of thermal contact

conductance, uranium swelling, fission gas pressure and the cladding heat generation represent the worst case scenario for the temperatures, while this combination along with the pressure exerted by the coolant represents the worst case scenario for the von Mises stresses. The swelling of the uranium was found to have no significant impact on the temperatures and von Mises stresses, while the fractional release based fission gas pressure was found to have very small changes on the temperatures and the stresses.

The parametric study results showed that the maximum temperature even at the highest heat generation rate is well within the melting temperature of the Al 6061-T6 cladding material. While there is sufficient margin for the maximum cladding temperature at the highest heat generation rate, the maximum von Mises stress nearly tends towards the yield point of the cladding, providing a very narrow safety margin. However, it should be noted that it is highly unlikely that this heat generation rate of 6.4×10^{10} W/m^3 would be attained during target irradiation as it represents an 'over 100 % power' scenario and the reactor would be scrammed automatically or manually. Therefore, it can be concluded that the annular target is thermally and structurally safe based on the parameters used in the current analysis, and is unlikely to cause a safety concern.

For the BORAL control blades the task was to establish that the deflection of the blade due to heating will be within the control blade channel gap of 6.5 mm. The BORAL meat was split into 4 quadrants and a heat generation profile that varied with thickness and longitudinal position was applied to each quadrant. The magnitude of the resulting thermally induced deflection was found to be within the channel gap limit of 6.5 mm. The heating profile showed some asymmetry in temperature and the corresponding asymmetric deflection along the blade curvature has been discussed. Finally, thermal

conductivity parametric studies on the BORAL suggested that the maximum radial deflection of the blade is still within the control blade channel gap limit even at a BORAL thermal conductivity of 132 W/mK, which was considered to be the upper bound in the thermal conductivity study.

Apart from providing an annular target performance analysis envelope, the ability to successfully apply the developed tool set to other specific problems, such as the BORAL control blade analysis to help with relicensing efforts and the HFIR safety case analysis to support safe irradiation of targets, has also been demonstrated in this dissertation. Analytical work has also been done, by developing a generalized dimensionless thermal-stress model for a compound cylinder configuration. The work completed through the course of this dissertation has been documented, presented in conferences, and published in journals as well.

Recommendations for future work include extension of the dimensionless thermal stress model to include the thermal contact conductance, and developing an experimental test plan for the thermal contact conductance determination in a composite cylindrical structure. As the determination of the surface parameters play a key role in accurate experimental estimation of the thermal contact conductance, it is also recommended that a test methodology to measure the surface roughness be developed.

APPENDIX

APPENDIX 1: Mathematica Code to Determine Heat Flux

```
Clear[r1,r2,r3,r4,Tinf,Kal,h1,h4,L,Rconvout,Rcondout,Rcondin,Rconvin,Reffout,Reffin,
REFF,quranium,qinward,qoutward,qfluxinward,qfluxoutward]

(*Rcondout,Rconvout,Reffout : conduction resistance through the outer aluminum tube ,
convective resistance on the outer tube outer surface and effective series resistance in the
radially outward direction *)

(*Rcondin,Rconvin,Reffin : conduction resistance through the inner aluminum tube ,
convective resistance on the inner tube inner surface and effective series resistance in the
radially inward direction *)

(* Dimensions and other definitions *)

r1=0.01321;    (*meters*)  (*Inner tube inner radius *)
r2= 0.013995;(*meters*) (* Inner tube outer radius = Foil Inner radius *)
r3= 0.01412; (*meters*)(* Foil outer radius =Outer tube Inner radius *)
r4=0.015075;(*meters*) (* Outer tube outer radius *)
foilthickness=125*10^-6;(*meters*)
rcenter=(r2+((r3-r2)/2)); (*meters*) (* Uranium foil center line radius *)

Tinf=323;(*Kelvin*)(* Coolant temperature *)
Kal=167; (*W/mK*)(* Thermal conductivity of Aluminum *)
Ku =27.5; (*W/mK*)(* Thermal conductivity of Uranium *)
h1 = 19000; (*W/m^2K*)(*Inner tube heat transfer coefficient *)
h4 = 19000;(*W/m^2K*)(*Outer tube heat transfer coefficient *)
L=0.100; (*meters*) (* length of the heated section which will be the length of the foil *)


(* Determination of uranium temperature *)

Rcondout= Log[r4/r3] / (2*Pi*Kal*L);(*Kelvin/Watt*) (* Conduction resistance in the
outer tube *)

Rconvout = 1/ (h4*2*Pi*r4*L);(*Kelvin/Watt*)(* Convective resistance outer coolant *)

Reffout=Rcondout+Rconvout;(*Kelvin/Watt*) (* Effective resistance of the outer tube *)

Rcondin= Log[r2/r1] / (2*Pi*Kal*L);(*Kelvin/Watt*)(* Conduction resistance in the
inner tube *)

Rconvin = 1/ (h1*2*Pi*r1*L);(*Kelvin/Watt*) (* Convective resistance inner coolant *)
```

Ruraniumin=Log[rcenter/r2]/(2*Pi*Ku*L);

Reffin =Rcondin+Rconvin(*+ Ruraniumin *);*(*Kelvin/Watt*)*

REFF = (Reffout*Reffin)/(Reffout+Reffin);*(*Kelvin/Watt*) (* resistance in parallel *)*

(*deltaT=Turanium-Tinf; (*Kelvin*) *)

quranium=17665.17 ; (*Watts*) *(* obtain quranium from qgen =1.6*10^10 as follows : quranium=qgen*2*Pi*rcenter*L*foilthickness *)*

Turanium = Tinf + (REFF * quranium); *(* Temperature of uranium *)*

(Now that the uranium temperature has been determined it can be used to calculate the*

*heat fluxes in the radially inward and outward directions *)*

(* quranium = qoutward + qinward *)
qoutward = (Turanium-Tinf)/(Reffout) ;*(*Watts*)*
qfluxoutward=qoutward/(2*Pi*r3*L*) ; (*W/m^2*)(* Radially outward heat flux *)*
qinward=(Turanium-Tinf)/(Reffin) ; (*Watts*)
qfluxinward=qinward/(2*Pi*r2*L)(*W/m^2*) ; *(* Radially inward heat flux *)*

*(*The heat fluxes obtained here are used to determine the analytical radial stress, hoop*

stress , displacements and temperature)*

APPENDIX 2: Mathematica Code to Determine Outer Tube Parameters

```
(* This notebook calculates the stresses, displacement and temperature across the radius
of the outer tube *) (* Plane Strain Formulation Used *)

Clear[r,Tinf,qflux,hb,a,b,Tdist,alpha1,alpha,EAl1,EAl,vAl,k]
Clear[sigmaRplanestrain,R,sigmaTHETAplanestrain,uRplanestrain]

Tinf=323;(* Coolant temperature *)
qflux=1.04972*10^6; (* Obtained based on mathematica notebook in appendix A *)
h=19000;(* outer heat transfer coefficient *)
a=0.01412;(* Outer tube inner radius *)
b=0.015075;(* Outer tube outer radius *)
Tdist= Tinf + ( ((qflux*a)/k)* (Log[b/r] + (k/(b*h))));
Tdistribution=Tinf + ( ((qflux*a)/k)* (Log[b/R] + (k/(b*h))));

alphaAl =2.34*10^-5;(* Used for Plane Stress *)
EAl=69*10^9; (* Used for Plane Stress *)
alphaAl1 = 2.34*10^-5;(* Thermal expansion coefficient .Used for Plane Strain *)
 EAl1=69*10^9; (* Young's modulus.Used for Plane Strain *)

(* For the plane strain case alpha*EAl is replaced by (alpha1*EAl1/(1-vAl)) . See Theory
of thermal stresses ,circular disc or cylinder,  by BOLEY page 290-291 *)

vAl=0.33;(* Poisson's ratio of Aluminum *)
k=167; (* Thermal conductivity of Aluminum *)

R=0.01412; (* Change this value to determine the stresses , displacement and
temperature at each nodal location across the radius *)

Tinteg1=Integrate[Tdist*r ,{r,a,b}];
Tinteg2 =Integrate[Tdist*r,{r,a,R}];

Tdistribution=Tinf + ( ((qflux*a)/k)* (Log[b/R] + (k/(b*h))));

sigmaRplanestrain= ((alphaAl1*EAl1)/((1-vAl)*R^2)) * ( ( ((R^2 -a^2)/(b^2-a^2)) *
Tinteg1 ) - Tinteg2);

sigmaTHETAplanestrain = ((alphaAl1*EAl1)/((1-vAl)*R^2)) * (( ( ((R^2 +a^2)/(b^2-
a^2)) * Tinteg1 ) + Tinteg2)-(Tdistribution*R^2));


 uRplanestrain=(alphaAl/(R*(1-vAl))) * (  ((1+vAl) * Tinteg2) +  (((((1- 3*vAl)*R^2) + (
(1+vAl)*a^2))/(b^2-a^2))*Tinteg1));
```

APPENDIX 3: Mathematica Code to Determine Inner Tube Parameters

```
Clear[m,rhs1,rhs2,rhs3,rhs4,c1,c2,c3,c4,m1,m2,sigmaR,sigmaT,uR,R,deltaTa,Taluminu
m,Turanium,Tdist,Tdist1,deltaTa,EAl,Efoil,alphaAl,alphafoil,vAl,vfoil,a,b,c,m1,m2,Tu,T
u1,Tinfinner,qflux,kAl,kfoil]

(*  Boundary Conditions Used in the Model *)
(*   BC 1 - SigmaR at a=0 *)
(*  BC 2 - SigmaR at c=0 *)
(*  compatibility boundary condition 1 - SigmaR Al at r=b  =   SigmaR U at r=b *)
(*  compatibility boundary condition 2 - U Al at r=b  =  U U at r=b *)
(*  Inner tube - Aluminum and Outer Tube- Uranium *)

a=0.01321;(* Inner tube inner radius in 'm'*)
b=0.013995;(* Inner tube outer radius = Foil inner radius in 'm' *)
c=0.0140575;(* Foil outer radius in 'm'*)

EAl=69*10^9;(* Young's modulus of aluminum in 'Pa' *)
Efoil=208*10^9;(* Young's modulus of uranium in 'Pa' *)
vAl=0.33;(* Poisson's ratio of aluminum *)
vfoil=0.23; (* Poisson's ratio of uranium *)
alphaAl=2.34*10^(-5);(* Thermal expansion coefficient of aluminum in 'K^-1' *)
alphafoil=1.39*10^(-5);(* Thermal expansion coefficient of uranium in 'K^-1' *)

kAl=167;(* Thermal conductivity of aluminum in W/mK*)
kfoil=27.5;(* Thermal conductivity of uranium in W/mK *)
qflux=949836;(*  Heat flux entering the inner tube in W/m^2K. Obtained based on
mathematica notebook in appendix A *)
Tinfinner=323;(* Coolant temperature in Kelvin *)
ha=19000;(*Inner tube heat transfer coefficient  W/m^2K *)

Tdist1= Tinfinner+ ( (qflux*c)* ( ( Log[r/a]/kAl ) + (1/(a*ha))));

Tb= Tinfinner+  ( (qflux*c)* ( ( Log[b/a]/kAl ) + (1/(a*ha))));

Tur = Tinfinner+((qflux*c)*(  (Log[r/b]/kfoil) + (Log[b/a]/kAl)+(1/(a*ha))));

(* Right side of the matrix *)

m = { { (EAl/((1+vAl)*(1-(2*vAl)))) , (-EAl/((1+vAl)*a^2)) , 0,0} , { 0,0, (1/(1-
(2*vfoil))) , (-1/(c^2)) } , { (EAl/((1+vAl)*(1-(2*vAl)))) , (-EAl/((1+vAl)*b^2)), (-
Efoil/((1+vfoil)*(1-(2*vfoil)))), (Efoil/((1+vfoil)*b^2))} , { b , (1/b) , -b , (-1/b) }};

rhs1=0;(* RHS from BC 1 - SigmaR at a=0 *)
```

```
rhs2= ((alphafoil*(1+vfoil)) /((1-vfoil)* (c^2)))*Integrate[Tur*r,{r,a,c}];(* RHS from BC
2 - SigmaR at c=0 *)

rhs3= ((-alphafoil*Efoil / ((1-vfoil)*(b^2)))*Integrate[Tdist1*r,{r,a,b}])+((alphaAl*EAl /
((1-vAl)*(b^2)))*Integrate[Tb*r,{r,a,b}]); (* RHS from compatibility condition 1 -
SigmaR Al at r=b   =   SigmaR U at r=b *)

rhs4= (((1+vfoil)*alphafoil / ((1-vfoil)*(b)))*Integrate[Tdist1*r,{r,a,b}])+((-
(1+vAl)*alphaAl / ((1-vAl)*(b)))*Integrate[Tb*r,{r,a,b}]);(* RHS from compatibility
condition 2 - U Al at r=b=U U at r=b *)

(* Solving the matrix to determine the four constants *)

 Solve[m.{c1,c2,c3,c4} {rhs1,rhs2,rhs3,rhs4},{c1,c2,c3,c4}]
m1=c1; (* replace c1 with m1 just for convenience*)
m2=c2;  (* replace c2 with m2 just for convenience*)

Clear[sigmaR,sigmaT,Tdist,R]

R=0.0132885;(* Change R to determine the stresses and temperature at any nodal
location across the radius of the tube *)

Tdist=Tinfinner+  ( (qflux*c)* ( ( Log[R/a]/kAl ) + (1/(a*ha))))

sigmaR = -(((alphaAl*EAl)/((1-vAl)*R^2))*Integrate[Tdist1*r ,{r,a,R}] )+ (
(EAl/(1+vAl))*( (m1/(1-(2*vAl)))-(m2/R^2)))

sigmaT = (((alphaAl*EAl)/((1-vAl)*R^2))*Integrate[ Tdist1*r,{r,a,R}])-
((alphaAl*EAl*Tdist)/(1-vAl))+ ( (EAl/(1+vAl))*( (m1/(1-(2*vAl)))+(m2/R^2)))


 uRplanestrain = (( ((1+vAl)*alphaAl)/((1-vAl)*R))*Integrate[Tdist1*r,{r,a,R}]) +
(m11*R)+(m22/R)
```

APPENDIX 4: Mathematica Code to Determine Contact Pressure.

```
(* This mathematica notebook is to compare the pressure obtained using Abaqus to that
obtained using Madhusudhana's formulation *)
(* The  obtained pressure will be in MPa *)

Clear[delTi,p,Ta]

a=13.21*10^(-3); (* Inner tube inner radius in 'm'*)
b=13.995*10^(-3);  (* Inner tube outer radius = Foil inner radius in 'm' *)
c=14.12*10^(-3); (* Foil outer radius in 'm'*)

kAl=167; (* Thermal conductivity of aluminum in 'W/mK ' *)
alphaAl1=2.34*10^(-5);(* Thermal expansion coefficient of aluminum in ' W/mK ' *)
EAl1=70*10^9;(* Young's modulus of aluminum in 'Pa' *)
vAl1=0.33; (* Poisson's ratio of aluminum *)
kU=27.5; (* Thermal conductivity of uranium in 'W/mK ' *)
alphaU1=1.39*10^(-5);(* Thermal expansion coefficient of uranium in ' W/mK ' *)
EU1=208*10^9;(* Young's modulus of uranium in 'Pa' *)
vU1=0.23;(* Poisson's ratio of uranium *)

(* Writing E,v and alpha in terms of plane strain *)

Ei1=EAl1/(1-(vAl1^2));vi1=vAl1/(1-vAl1);alphai1=alphaAl1*(1+vAl1);ki=kAl;
E01=EU1/(1-(vU1^2));v01=vU1/(1-vU1);alpha01=alphaU1*(1+vU1);k0=kU;

uC=0.0;  (* Initial interference in 'm' *)

h=10^9; (* Total contact conductance in 'W/m^2K '. A high value implies infinite
conductance and perfect contact *)

(*Ta- Temp at the inner surface of the inner tube *)
(*T1-Temp at the outer surface of the inner tube *)

delTi=Ta-T1; (* Temp rise in the inner tube *)

DELTAT = (ki*delTi )/((b*Log[b/a])*h); (* ie DELTAT= q/h where q=Q/A *)
c1=Ei1/E01;
c2=(c^2+b^2)/(c^2-b^2);
c3=(b^2+a^2)/(b^2-a^2);

(*delT0=(ki/k0)*delTi*(Log[c/b]/Log[b/a]);*)

uAi = (b*alphai1*delTi)* (1-(  (2*a^2)/(b^2-a^2))*Log[b/a])/(2*Log[b/a]);
uA0 =  (b*alphai1*delTi)*  ((alpha01*ki)/(alphai1*k0))*( Log[c/b]/Log[b/a])* ( 1-(
(2*c^2)/(c^2-b^2))*Log[c/b]) / (2*Log[c/b]);
```

uA=uAi-uA0; *(* Interference due to heat flux in 'm' *)*

uB = b*(T1*(alphai1-alpha01) + (alphai1*DELTAT)); *(* Interference due to contact resistance in 'm'*)*

u=uA+uB+uC;*(* Total interference in 'm' *)*

(Solving to obtain the contact pressure in MPa *)*

Solve[u == ((b*p)/(Ei1))*(c1*(c2+v01)+(c3-vi1)),p]

APPENDIX 5: Mathematica Code to Calculate Fission Gas Pressure

```
(* This code calculates the fission gas pressure for the Al 6061-T6 model *)

Clear[T,Tc1,Tc2,Tc3,Vc1,Vc2,Vc3,w1,w2,w3,n1,n2,n3,ntotal,y1,y2,y3,Tr,B1,B2,B3,Bze
ro1,Bzero2,Bzero3,Bone1,Bone2,Bone3,Pc1,Pc2,Pc3,R,Zc1,Zc2,Zc3]
Clear[Tc11,Tc12,Tc13,Tc21,Tc22,Tc23,Tc31,Tc32,Tc33,Zc11,Zc12,Zc13,Zc21,Zc22,Zc
23,Zc31,Zc32,Zc33,Vc11,Vc12,Vc13,Vc21,Vc22,Vc23,Vc31,Vc32,Vc33]
Clear[w11,w12,w13,w21,w22,w23,w31,w32,w33,Pc11,Pc12,Pc13,Pc21,Pc22,Pc23,Pc31,
Pc32,Pc33,B11,B12,B13,B21,B22,B23,B31,B32,B33]
Clear[Bzero11,Bzero12,Bzero13,Bzero21,Bzero22,Bzero23,Bzero31,Bzero32,Bzero33,B
one11,Bone12,Bone13,Bone21,Bone22,Bone23,Bone31,Bone32,Bone33,Bmix,Zmix,Pfi
ssion,compressibilityfactor, Pfissiongas, volume, Prelease]

T=425;  (* Actual system temperature *)
R=8.3144; (* J/mol K *)
volume= 2.315 *10^-7 ;

(* 1- Xenon ; 2- Krypton; 3- Helium*)

(* Critical temperature in Kelvin *)
Tc1=289.7;
Tc2=209.4;
Tc3=5.19;
(* Critical pressure in Pascal *)
Pc1=5840000;
Pc2=5500000;
Pc3=227000;
(* Critical Volume in m^3 /mol *)
Vc1 =0.0001184;
Vc2=0.0000912;
Vc3=0.0000574;
(* Eccentricity Factor *)
w1=0.008;
w2=0.005;
w3=-0.365;
(* Mole fraction yi. ni is the number of moles *)
n1=20*5.44* 10^-6;
n2=20*8.34 * 10^-7;
n3= 20*2.65 * 10^-12;

ntotal=n1+n2+n3;

y1=n1/ntotal;
y2=n2/ntotal;
y3=n3/ntotal;
```

```
(* Individual virial coefficients calculation *)
Bzero1=0.083- (0.422 / ( (T/Tc1)^1.6));
Bone1=0.139-( 0.172 / ((T/Tc1)^4.2));

Bzero2=0.083- (0.422 / ( (T/Tc2)^1.6));
Bone2=0.139-( 0.172 / ((T/Tc2)^4.2));

Bzero3=0.083- (0.422 / ( (T/Tc3)^1.6));
Bone3=0.139-( 0.172 / ((T/Tc3)^4.2));

B1=(((Bzero1 + (w1 * Bone1))*(R*Tc1)) /Pc1);
B2=(((Bzero2 + (w2 * Bone2))*(R*Tc2)) /Pc2);
B3=(((Bzero3+ (w3 * Bone3))*(R*Tc3)) /Pc3);

(* Individual component critical compressibility factor Zci *)

Zc1= (1 + ( B1/Vc1));
Zc2= (1 + ( B2/Vc2));
Zc3= (1 + ( B3/Vc3));

(* Mixing rules for 2 component interactions *)
Tc11= Sqrt[ Tc1 * Tc1];Tc12= Sqrt[ Tc1 * Tc2];Tc13= Sqrt[ Tc1 * Tc3];
Tc21=Sqrt[Tc2*Tc1];Tc22=Sqrt[Tc2*Tc2];Tc23=Sqrt[Tc2*Tc3];
Tc31=Sqrt[Tc3*Tc1];Tc32=Sqrt[Tc3*Tc2];Tc33=Sqrt[Tc3*Tc3];

Zc11=0.5*(Zc1+Zc1);Zc12=0.5*(Zc1+Zc2);Zc13=0.5*(Zc1+Zc3);
Zc21=0.5*(Zc2+Zc1);Zc22=0.5*(Zc2+Zc2);Zc23=0.5*(Zc2+Zc3);
Zc31=0.5*(Zc3+Zc1);Zc32=0.5*(Zc3+Zc2);Zc33=0.5*(Zc3+Zc3);

Vc11= (0.5*(((Vc1)^1/3)+((Vc1)^1/3)))^3 ; Vc12= (0.5*(((Vc1)^1/3)+((Vc2)^1/3)))^3 ;
Vc13= (0.5*(((Vc1)^1/3)+((Vc3)^1/3)))^3 ;
Vc21= (0.5*(((Vc2)^1/3)+((Vc1)^1/3)))^3 ; Vc22= (0.5*(((Vc2)^1/3)+((Vc2)^1/3)))^3 ;
Vc23= (0.5*(((Vc2)^1/3)+((Vc3)^1/3)))^3 ;
Vc31= (0.5*(((Vc3)^1/3)+((Vc1)^1/3)))^3 ; Vc32= (0.5*(((Vc3)^1/3)+((Vc2)^1/3)))^3 ;
Vc33= (0.5*(((Vc3)^1/3)+((Vc3)^1/3)))^3 ;

w11=0.5*(w1+w1); w12=0.5*(w1+w2);w13=0.5*(w1+w3);
w21=0.5*(w2+w1); w22=0.5*(w2+w2);w23=0.5*(w2+w3);
w31=0.5*(w3+w1); w32=0.5*(w3+w2);w33=0.5*(w3+w3);

Pc11 = (R* Zc11 * Tc11)/Vc11; Pc12 = (R* Zc12 * Tc12)/Vc12;  Pc13 = (R* Zc13 *
Tc13)/Vc13;
Pc21 = (R* Zc21 * Tc21)/Vc21; Pc22 = (R* Zc22 * Tc22)/Vc22;  Pc23 = (R* Zc23 *
Tc23)/Vc23;
Pc31 = (R* Zc31 * Tc31)/Vc31; Pc32 = (R* Zc32 * Tc32)/Vc32;  Pc33 = (R* Zc33 *
Tc33)/Vc33;
```

```
(* Calculate Bij *)
Bzero11=0.083 - (0.422/(T/Tc11)^1.6);Bzero12=0.083 -
(0.422/(T/Tc12)^1.6);Bzero13=0.083 - (0.422/(T/Tc13)^1.6);
Bzero21=0.083 - (0.422/(T/Tc21)^1.6);Bzero22=0.083 -
(0.422/(T/Tc22)^1.6);Bzero23=0.083 - (0.422/(T/Tc23)^1.6);
Bzero31=0.083 - (0.422/(T/Tc31)^1.6);Bzero32=0.083 -
(0.422/(T/Tc32)^1.6);Bzero33=0.083 - (0.422/(T/Tc33)^1.6);

Bone11=0.139- (0.172/(T/Tc11)^4.2);Bone12=0.139-
(0.172/(T/Tc12)^4.2);Bone13=0.139- (0.172/(T/Tc13)^4.2);
Bone21=0.139- (0.172/(T/Tc21)^4.2);Bone22=0.139-
(0.172/(T/Tc22)^4.2);Bone23=0.139- (0.172/(T/Tc23)^4.2);
Bone31=0.139- (0.172/(T/Tc31)^4.2);Bone32=0.139-
(0.172/(T/Tc32)^4.2);Bone33=0.139- (0.172/(T/Tc33)^4.2);

B11 = ((Bzero11 + (w11 * Bone11))*(R * Tc11 ))/Pc11; B12 = ((Bzero12 + (w12 *
Bone12))*(R * Tc12 ))/Pc12;B13 = ((Bzero13 + (w13 * Bone13))*(R * Tc13 ))/Pc13;
B21 = ((Bzero21 + (w21 * Bone21))*(R * Tc21 ))/Pc21; B22 = ((Bzero22 + (w22 *
Bone22))*(R * Tc22 ))/Pc22;B23 = ((Bzero23 + (w23 * Bone23))*(R * Tc23 ))/Pc23;
B31 = ((Bzero31 + (w31 * Bone31))*(R * Tc31 ))/Pc31; B32 = ((Bzero32 + (w32 *
Bone32))*(R * Tc32 ))/Pc32;B33 = ((Bzero33 + (w33 * Bone33))*(R * Tc33 ))/Pc33;

Bmix = (B1 * y1^2)+(B2* y2^2)+ (B3 * y3^2) + (2*y1*y2*B12) +
(2*y1*y3*B13)+(2*y2*y3*B23);

(*Compressibility factor*)

Zmix = 1+ (Bmix/( (Vc1+Vc2+Vc3) ))
0.830825

(* 100 % gas release pressure *)

Pfissiongas= Zmix* ntotal *R*T / (volume)
1.5913×10^6

(* Fractional gas release pressure *)

Prelease = Pfissiongas *(5/125)*(1-0.25)
47739.1
```

APPENDIX 6: Mathematica Code to Develop a Thermal Conductance Model for Al 6061-T6 and Al 6061-T6 Interface.

```
Clear[mew_He,mew_Xe,mew_Kr,mew_I,Ms,Mg,Mg_He,Mg_Kr,Mg_Xe,Mg_I,Ts,T0,C
0,C1,g1,g2,g3,g4,alpha1,alpha2,alpha3,alpha4,gamma1,gamma2,gamma3,gamma4,kg1,k
g2,kg3,kg4,visc1,visc2,visc3,visc4,cv1,cv2,cv3,cv4,lambda1,lambda2,lambda3,lambda4,
gm,bt,sigma,X,Y,deltaeff,phi11,phi12,phi13,phi14,phi21,phi22,phi23,phi24,phi31,phi32,
phi33,phi34,phi41,phi42,phi43,phi44,kgmix,x1,x2,x2,x3,k1,k2,k3,k4,hgmix,CLAsigmaN
i,CLAsigmaU,kNi,kU,ENi,EU,slopeNi,slopeU,vNi,vU,keff,sigmaeff,tantheta,Eeff,si,hs,P
,htotal,delta, CLAsigmaAl, CLAsigmaU, kAl, kU,EAl,EU,slopeAl,slopeU,vAl,vU]

(* ------------------------------------------------------------------------------------------*)
(* Mg and Ms - Molecular weight of gas and solid respectively  in 'g/mol'*)
(* mew - ratio of molecular weights *)
(* alpha - accomodation coefficient *)
(* Ts and T0 - Temp of the solid and reference temp respectively *)
(* g and gm - Temperature jump distance for an individual component and a mixture
respectively *)
(* visc - dynamic viscosity *)
(* kg - thermal conductivity of the individual gas in W/mK *)
(* lambda - mean free path in 'm'*)
(* sigma - surface roughness *)
(* deltaeff - effective gap thickness = delta+2gm *)
(* kgmix - thermal conductivity of the gas mixture in W/mK*)
(* x and y - mass fraction and mole fraction respectively *)
(* gamma - ratio of specific heats *)
(* cv - specific heat at constant volume in J/Kg K *)
(* ------------------------------------------------------------------------------------------*)

(* Input values *)

(* 1- Helium;  2- Xenon  ; 3- Krypton;  *)

Ms=26.981538 *10^-3 ; (* Al *)
Mg1=3.017*10^-3;
Mg2=131.293*10^-3;
Mg3=83.8*10^-3;(* Kg/mol *)


visc1=21.7*10^-6;
visc2=26.17*10^-6;
visc3=28.6*10^-6;  (* Kg/m s *)

kg1=0.1696;
kg2=0.00625;
kg3=0.01067;  (* W/m K*)
```

```
gamma1=1.667;gamma2=1.656;gamma3=1.667;

cv1=3120;cv2=97;cv3=151; (* J/Kg K *)

lambda1=0.19266*10^-6;lambda2=0.03788*10^-6;lambda3=0.05234*10^-6;  (* meter *)

y1=4.22378*10^-7;y2=0.86707;y3=0.132929;

x1=Mg1/(Mg1+Mg2+Mg3);x2=Mg2/(Mg1+Mg2+Mg3);x3=Mg3/(Mg1+Mg2+Mg3);

H=1080*10^6; (*Pa Hardness of Al the softer material obtained from *)
bt=6*sigma;

CLAsigmaAl=1*10^-6;
slopeAl=0.18; (*rad*)
kAl=167;
EAl=68.9*10^9;
vAl=0.33;

(* 1- Helium;  2- Xenon  ; 3- Krypton; *)

(*Accomodation coefficients from literature *)

alpha1=0.53;alpha2=0.86;alpha3=0.861;

(* Temperature jump distance calculation *)
g1=((2-alpha1)/alpha1)*( 2/(gamma1+1))*( kg1/(visc1*cv1))*lambda1;
g2=((2-alpha2)/alpha2)*( 2/(gamma2+1))*( kg2/(visc2*cv2))*lambda2;
g3=((2-alpha3)/alpha3)*( 2/(gamma3+1))*( kg3/(visc3*cv3))*lambda3;

gm =
((x1*g1/(Mg1^0.5))+(x2*g2/(Mg2^0.5))+(x3*g3/(Mg3^0.5)))/((x1/(Mg1^0.5))+(x2/(Mg
2^0.5))+(x3/(Mg3^0.5)))
1.78288×10^-7

(* Gap thickness calculation *)

X= bt/ (2*gm);
Y= 1/(0.305+(1/X));
deltaeff = (X/Y)*(2*gm);

(* Thermal conductivity of a mixture calculation using Wilke's mixture rule*)

phi11=1;phi22=1;phi33=1;phi44=1;
phi12=(( 1+(visc1/visc2)^0.5 ( Mg2/Mg1)^0.25)^2)/( Sqrt[8]*( 1+(Mg1/Mg2))^0.5);
phi13=(( 1+(visc1/visc3)^0.5 ( Mg3/Mg1)^0.25)^2)/( Sqrt[8]*( 1+(Mg1/Mg3))^0.5);
```

```
phi21=(( 1+(visc2/visc1)^0.5 ( Mg1/Mg2)^0.25)^2)/( Sqrt[8]*( 1+(Mg2/Mg1))^0.5);
phi23=(( 1+(visc2/visc3)^0.5 ( Mg3/Mg2)^0.25)^2)/( Sqrt[8]*( 1+(Mg2/Mg3))^0.5);

phi31=(( 1+(visc3/visc1)^0.5 ( Mg1/Mg3)^0.25)^2)/( Sqrt[8]*( 1+(Mg3/Mg1))^0.5);
phi32=(( 1+(visc3/visc2)^0.5 ( Mg2/Mg3)^0.25)^2)/( Sqrt[8]*( 1+(Mg3/Mg2))^0.5);


kgmix = ( y1*kg1 / ((y1*phi11) + (y2*phi12)+ (y3*phi13)  ))+  ( y2*kg2 / ((y1*phi21) +
(y2*phi22)+ (y3*phi23)  ))+  ( y3*kg3 / ((y1*phi31) +(y2*phi32)+ (y3*phi33)  ));

hgmix= FullSimplify[kgmix/(delta + (2*gm)) ](* W/m2 K *)
```

$$\frac{0.00672368}{3.56575\times10^{-7} + \text{delta}}$$

```
(* Solid spot conductance Calculations *)

keff= 2*kAl*kAl/(kAl+kAl);

sigmaeff=1.25* Sqrt[ CLAsigmaAl^2 + CLAsigmaAl^2];

tantheta= Sqrt[ slopeAl^2 + slopeAl^2];

Eeff = 2*(( ((1-vAl^2)/EAl)+ ((1-vAl^2)/EAl))^-1);
si= (Eeff/H)*tantheta
18.2245

(* plasticity index 'si' > 1 =>Mikic's correlation can be used for plastic deformation of
asperities *)

hs= 1.13* (keff/ (H^0.94))*(tantheta/sigmaeff)* (P^0.94)
```

$$0.0876474\ P^{0.94}$$

```
(* Total conductance Calculations *)

htotal=FullSimplify[ Factor[hs + hgmix], P>0]
```

$$\frac{0.00672368}{3.56575\times10^{-7} + 1.\ \text{delta}} + 0.0876474\ P^{0.94}$$

APPENDIX 7: Mathematica Code to Develop a Thermal Conductance Model for Al 6061-T6 and Nickel Interface.

```
Clear[mew_He,mew_Xe,mew_Kr,mew_I,Ms,Mg,Mg_He,Mg_Kr,Mg_Xe,Mg_I,Ts,T0,C
0,C1,g1,g2,g3,g4,alpha1,alpha2,alpha3,alpha4,gamma1,gamma2,gamma3,gamma4,kg1,k
g2,kg3,kg4,visc1,visc2,visc3,visc4,cv1,cv2,cv3,cv4,lambda1,lambda2,lambda3,lambda4,
gm,bt,sigma,X,Y,deltaeff,phi11,phi12,phi13,phi14,phi21,phi22,phi23,phi24,phi31,phi32,
phi33,phi34,phi41,phi42,phi43,phi44,kgmix,x1,x2,x2,x3,k1,k2,k3,k4,hgmix,CLAsigmaN
i,CLAsigmaU,kNi,kU,ENi,EU,slopeNi,slopeU,vNi,vU,keff,sigmaeff,tantheta,Eeff,si,hs,P
,htotal,delta, CLAsigmaAl,CLAsigmaU,kAl,kU,EAl,EU,slopeAl,slopeU,vAl,vU]

(* ------------------------------------------------------------------------------------------*)
(* Mg and Ms - Molecular weight of gas and solid respectively  in 'g/mol'*)
(* mew - ratio of molecular weights *)
(* alpha - accomodation coefficient *)
(* Ts and T0 - Temp of the solid and reference temp respectively *)
(* g and gm - Temperature jump distance for an individual component and a mixture
respectively *)
(* visc - dynamic viscosity *)
(* kg - thermal conductivity of the individual gas in W/mK *)
(* lambda - mean free path in 'm'*)
(* sigma - surface roughness *)
(* deltaeff - effective gap thickness = delta+2gm *)
(* kgmix - thermal conductivity of the gas mixture in W/mK*)
(* x and y - mass fraction and mole fraction respectively *)
(* gamma - ratio of specific heats *)
(* cv - specific heat at constant volume in J/Kg K *)
(* ------------------------------------------------------------------------------------------*)

(* Input values *)

(* 1- Helium;  2- Xenon  ; 3- Krypton;  *)

Ms=26.981538 *10^-3 ; (* Al *)
Mg1=3.017*10^-3;
Mg2=131.293*10^-3;
Mg3=83.8*10^-3;(* Kg/mol *)

visc1=21.7*10^-6;visc2=26.17*10^-6;visc3=28.6*10^-6;  (* Kg/m s *)

kg1=0.1696;kg2=0.00625;kg3=0.01067;  (* W/m K*)

gamma1=1.667;gamma2=1.656;gamma3=1.667;

cv1=3120;cv2=97;cv3=151; (* J/Kg K *)
```

```
lambda1=0.19266*10^-6;lambda2=0.03788*10^-6;lambda3=0.05234*10^-6;  (* meter *)

y1=4.22378*10^-7;y2=0.86707;y3=0.132929;

x1=Mg1/(Mg1+Mg2+Mg3);x2=Mg2/(Mg1+Mg2+Mg3);x3=Mg3/(Mg1+Mg2+Mg3);

H=1080*10^6; (*Pa Hardness of Al the softer material *)
bt=6*sigma;

CLAsigmaNi=1.27*10^-6;CLAsigmaAl=1.15*10^-6;
slopeNi=0.137; (*rad*)slopeAl=0.18; (*rad*) (* Nickel slope from Antonetti and
Yovanovich Table 1 *)
kNi=60.7;kAl=167;
ENi=207*10^9;EAl=68.9*10^9;
vNi=0.31;vAl=0.33;

(* 1- Helium;  2- Xenon  ; 3- Krypton; *)

(*Accomodation coefficients from literature *)

alpha1=0.53;alpha2=0.86;alpha3=0.861;

(* Temperature jump distance calculation *)

g1=((2-alpha1)/alpha1)*( 2/(gamma1+1))*( kg1/(visc1*cv1))*lambda1;
g2=((2-alpha2)/alpha2)*( 2/(gamma2+1))*( kg2/(visc2*cv2))*lambda2;
g3=((2-alpha3)/alpha3)*( 2/(gamma3+1))*( kg3/(visc3*cv3))*lambda3;

gm =
((x1*g1/(Mg1^0.5))+(x2*g2/(Mg2^0.5))+(x3*g3/(Mg3^0.5)))/((x1/(Mg1^0.5))+(x2/(Mg
2^0.5))+(x3/(Mg3^0.5)))
1.78288×10^-7

(* Gap thickness calculation *)

X= bt/ (2*gm);
Y= 1/(0.305+(1/X));
deltaeff = (X/Y)*(2*gm);

(* Thermal conductivity of a mixture calculation using Wilke's mixture rule*)

phi11=1;phi22=1;phi33=1;phi44=1;
phi12=(( 1+(visc1/visc2)^0.5 ( Mg2/Mg1)^0.25)^2)/( Sqrt[8]*( 1+(Mg1/Mg2))^0.5);
phi13=(( 1+(visc1/visc3)^0.5 ( Mg3/Mg1)^0.25)^2)/( Sqrt[8]*( 1+(Mg1/Mg3))^0.5);

phi21=(( 1+(visc2/visc1)^0.5 ( Mg1/Mg2)^0.25)^2)/( Sqrt[8]*( 1+(Mg2/Mg1))^0.5);
```

phi23=((1+(visc2/visc3)^0.5 (Mg3/Mg2)^0.25)^2)/(Sqrt[8]*(1+(Mg2/Mg3))^0.5);

phi31=((1+(visc3/visc1)^0.5 (Mg1/Mg3)^0.25)^2)/(Sqrt[8]*(1+(Mg3/Mg1))^0.5);
phi32=((1+(visc3/visc2)^0.5 (Mg2/Mg3)^0.25)^2)/(Sqrt[8]*(1+(Mg3/Mg2))^0.5);

kgmix = (y1*kg1 / ((y1*phi11) + (y2*phi12)+ (y3*phi13)))+ (y2*kg2 / ((y1*phi21) + (y2*phi22)+ (y3*phi23)))+ (y3*kg3 / ((y1*phi31) +(y2*phi32)+ (y3*phi33)));

hgmix= FullSimplify[kgmix/(delta + (2*gm))](* W/m2 K *)

$$\frac{0.00672368}{3.56575\times10^{-7} + \text{delta}}$$

(* Solid spot conductance Calculations *)

keff= 2*kNi*kAl/(kNi+kAl);

sigmaeff=1.25* Sqrt[CLAsigmaNi^2 + CLAsigmaAl^2];

tantheta= Sqrt[slopeNi^2 + slopeAl^2];

Eeff = 2*((((1-vNi^2)/ENi)+ ((1-vAl^2)/EAl))^-1);
si= (Eeff/H)*tantheta
24.214
(* plasticity index 'si' > 1 =>Mikic's correlation can be used for plastic deformation of asperities *)
hs= 1.13* (keff/ (H^0.94))*(tantheta/sigmaeff)* (P^0.94)
$$0.0342762\ P^{0.94}$$

(* Total conductance Calculations *)

htotal=FullSimplify[Factor[hs + hgmix], P>0]

$$\frac{0.00672368}{3.56575\times10^{-7} + 1.\ \text{delta}} + 0.0342762\ P^{0.94}$$

APPENDIX 8: Mathematica Code to Develop a Thermal Conductance Model for Uranium and Nickel Interface.

```
Clear[mew_He,mew_Xe,mew_Kr,mew_I,Ms,Mg,Mg_He,Mg_Kr,Mg_Xe,Mg_I,Ts,T0,C
0,C1,g1,g2,g3,g4,alpha1,alpha2,alpha3,alpha4,gamma1,gamma2,gamma3,gamma4,kg1,k
g2,kg3,kg4,visc1,visc2,visc3,visc4,cv1,cv2,cv3,cv4,lambda1,lambda2,lambda3,lambda4,
gm,bt,sigma,X,Y,deltaeff,phi11,phi12,phi13,phi14,phi21,phi22,phi23,phi24,phi31,phi32,
phi33,phi34,phi41,phi42,phi43,phi44,kgmix,x1,x2,x2,x3,k1,k2,k3,k4,hgmix,CLAsigmaN
i,CLAsigmaU,kNi,kU,ENi,EU,slopeNi,slopeU,vNi,vU,keff,sigmaeff,tantheta,Eeff,si,hs,P
,htotal,delta, sigma, deltaeff]

(* ------------------------------------------------------------------------------------------*)
(* Mg and Ms - Molecular weight of gas and solid respectively  in 'g/mol'*)
(* mew - ratio of molecular weights *)
(* alpha - accomodation coefficient *)
(* Ts and T0 - Temp of the solid and reference temp respectively *)
(* g and gm - Temperature jump distance for an individual component and a mixture
respectively *)
(* visc - dynamic viscosity *)
(* kg - thermal conductivity of the individual gas in W/mK *)
(* lambda - mean free path in 'm'*)
(* sigma - surface roughness *)
(* deltaeff - effective gap thickness = delta+2gm *)
(* kgmix - thermal conductivity of the gas mixture in W/mK*)
(* x and y - mass fraction and mole fraction respectively *)
(* gamma - ratio of specific heats *)
(* cv - specific heat at constant volume in J/Kg K *)
(* ------------------------------------------------------------------------------------------*)

(* Input values *)

(* 1- Helium;  2- Xenon  ; 3- Krypton;  *)

Ms=58.6934 *10^-3 ; (* Nickel *)
Mg1=3.017*10^-3;Mg2=131.293*10^-3;Mg3=83.8*10^-3;(* Kg/mol *)

visc1=21.7*10^-6;visc2=26.17*10^-6;visc3=28.6*10^-6;  (* Kg/m s *)

kg1=0.1696;kg2=0.00625;kg3=0.01067;  (* W/m K*)

gamma1=1.667;gamma2=1.656;gamma3=1.667;

cv1=3120;cv2=97;cv3=151; (* J/Kg K *)

lambda1=0.19266*10^-6;lambda2=0.03788*10^-6;lambda3=0.05234*10^-6;  (* meter *)
```

y1=4.22378*10^-7;y2=0.86707;y3=0.132929;

x1=Mg1/(Mg1+Mg2+Mg3);x2=Mg2/(Mg1+Mg2+Mg3);x3=Mg3/(Mg1+Mg2+Mg3);

(*sigma=1.28*10^-6; (* Antonetti and Yovanovich Table 1 *)*)
H=1960*10^6; (*Pa Hardness of uranium the softer material*)
bt=6*sigma;

CLAsigmaNi=1.27*10^-6; CLAsigmaU=1.5*10^-6;
slopeNi=0.137; (*rad*)slopeU=0.115; (*rad*) (* Nickel slope from Antonetti and Yovanovich Table 1 *)
kNi=60.7;kU=27.5;
ENi=207*10^9;EU=208*10^9;
vNi=0.31;vU=0.23;

(* 1- Helium; 2- Xenon ; 3- Krypton; *)

(*Accomodation coefficients from literature *)

alpha1=0.53;alpha2=0.86;alpha3=0.861;

(* Temperature jump distance calculation *)

g1=((2-alpha1)/alpha1)*(2/(gamma1+1))*(kg1/(visc1*cv1))*lambda1;
g2=((2-alpha2)/alpha2)*(2/(gamma2+1))*(kg2/(visc2*cv2))*lambda2;
g3=((2-alpha3)/alpha3)*(2/(gamma3+1))*(kg3/(visc3*cv3))*lambda3;

gm =
((x1*g1/(Mg1^0.5))+(x2*g2/(Mg2^0.5))+(x3*g3/(Mg3^0.5)))/((x1/(Mg1^0.5))+(x2/(Mg2^0.5))+(x3/(Mg3^0.5)))

$$1.78288\times10^{-7}$$

(* Gap thickness calculation *)
X= bt/ (2*gm);
Y= 1/(0.305+(1/X));
deltaeff = (X/Y)*(2*gm)

$$6.\left(0.305+\frac{5.94292\times10^{-8}}{\text{sigma}}\right)\text{sigma}$$

(* Thermal conductivity of a mixture calculation using Wilke's mixture rule*)

phi11=1;phi22=1;phi33=1;phi44=1;
phi12=((1+(visc1/visc2)^0.5 (Mg2/Mg1)^0.25)^2)/(Sqrt[8]*(1+(Mg1/Mg2))^0.5);
phi13=((1+(visc1/visc3)^0.5 (Mg3/Mg1)^0.25)^2)/(Sqrt[8]*(1+(Mg1/Mg3))^0.5);

phi21=((1+(visc2/visc1)^0.5 (Mg1/Mg2)^0.25)^2)/(Sqrt[8]*(1+(Mg2/Mg1))^0.5);
phi23=((1+(visc2/visc3)^0.5 (Mg3/Mg2)^0.25)^2)/(Sqrt[8]*(1+(Mg2/Mg3))^0.5);

```
phi31=(( 1+(visc3/visc1)^0.5 ( Mg1/Mg3)^0.25)^2)/( Sqrt[8]*( 1+(Mg3/Mg1))^0.5);
phi32=(( 1+(visc3/visc2)^0.5 ( Mg2/Mg3)^0.25)^2)/( Sqrt[8]*( 1+(Mg3/Mg2))^0.5);

kgmix = ( y1*kg1 / ((y1*phi11) + (y2*phi12)+ (y3*phi13)  ))+  ( y2*kg2 / ((y1*phi21) +
(y2*phi22)+ (y3*phi23)  ))+  ( y3*kg3 / ((y1*phi31) +(y2*phi32)+ (y3*phi33)  ));

hgmix= FullSimplify[kgmix/(delta + (2*gm)) ](* W/m2 K *)
```

$$\frac{0.00672368}{3.56575 \times 10^{-7} + \text{delta}}$$

```
(* Solid spot conductance Calculations *)

keff= 2*kNi*kU/(kNi+kU);

sigmaeff=1.25* Sqrt[ CLAsigmaNi^2 + CLAsigmaU^2];

tantheta= Sqrt[ slopeNi^2 + slopeU^2];

Eeff = 2*(( ((1-vNi^2)/ENi)+ ((1-vU^2)/EU))^-1);
si= (Eeff/H)*tantheta
20.4617
(* plasticity index 'si' > 1 =>Mikic's correlation can be used for plastic deformation of
asperities *)

hs= 1.13* (keff/ (H^0.94))*(tantheta/sigmaeff)* (P^0.94)
```

$$0.00573599\, P^{0.94}$$

```
(* Total conductance Calculations *)

htotal=FullSimplify[ Factor[hs + hgmix], P>0]
```

$$\frac{0.00672368}{3.56575 \times 10^{-7} + 1.\ \text{delta}} + 0.00573599\, P^{0.94}$$

APPENDIX 9: Mathematica Code to Develop a Thermal Conductance Model for Al 6061-T4 and Al 6061-T4 Interface.

```
Clear[mew_He,mew_Xe,mew_Kr,mew_I,Ms,Mg,Mg_He,Mg_Kr,Mg_Xe,Mg_I,Ts,T0,C
0,C1,g1,g2,g3,g4,alpha1,alpha2,alpha3,alpha4,gamma1,gamma2,gamma3,gamma4,kg1,k
g2,kg3,kg4,visc1,visc2,visc3,visc4,cv1,cv2,cv3,cv4,lambda1,lambda2,lambda3,lambda4,
gm,bt,sigma,X,Y,deltaeff,phi11,phi12,phi13,phi14,phi21,phi22,phi23,phi24,phi31,phi32,
phi33,phi34,phi41,phi42,phi43,phi44,kgmix,x1,x2,x2,x3,k1,k2,k3,k4,hgmix,CLAsigmaA
l,CLAsigmaU,kAl,kU,EAl,EU,slopeAl,slopeU,vAl,vU,keff,sigmaeff,tantheta,Eeff,si,hs,P
,htotal,delta,h]

(* ------------------------------------------------------------------------------------------*)
(* Mg and Ms - Molecular weight of gas and solid respectively  in 'g/mol'*)
(* mew - ratio of molecular weights *)
(* alpha - accomodation coefficient *)
(* Ts and T0 - Temp of the solid and reference temp respectively *)
(* g and gm - Temperature jump distance for an individual component and a mixture
respectively *)
(* visc - dynamic viscosity *)
(* kg - thermal conductivity of the individual gas in W/mK *)
(* lambda - mean free path in 'm'*)
(* sigma - surface roughness *)
(* deltaeff - effective gap thickness = delta+2gm *)
(* kgmix - thermal conductivity of the gas mixture in W/mK*)
(* x and y - mass fraction and mole fraction respectively *)
(* gamma - ratio of specific heats *)
(* cv - specific heat at constant volume in J/Kg K *)
(* ------------------------------------------------------------------------------------------*)

H=1080*10^6; (*In Pa *)

CLAsigmaAl=1*10^-6;  kAl=154;
EAl=68.9*10^9;
slopeAl=0.18; (*rad*)
vAl=0.33;

(* Solid spot conductance Calculations *)

keff= 2*kAl*kAl/(kAl+kAl);

sigmaeff=1.25* Sqrt[ CLAsigmaAl^2 +CLAsigmaAl^2 ];

tantheta= Sqrt[ slopeAl^2 +  slopeAl^2 ];
Eeff = 2*(( ((1-vAl^2)/EAl)+ ((1-vAl^2)/EAl))^-1);
si= (Eeff/H)*tantheta
sigmaeff
```

1.76777×10^{-6}
(* plasticity index 'si' > 1 =>Mikic's correlation can be used for plastic deformation of asperities *)
hs= 1.13* (keff/ (H^0.94))*(tantheta/sigmaeff)* (P^0.94)
$0.0808246\, P^{0.94}$

(* Input values For Gap Conductance Model *)

(* 1- Helium; 2- Xenon ; 3- Krypton; 4- Iodine *)

Ms=26.981538 *10^-3 ;Mg1=4.003*10^-3;Mg2=131.293*10^-3;Mg3=83.8*10^-3;Mg4=253.809*10^-3; (* Kg/mol *)

visc1=21.7*10^-6; visc2=26.17*10^-6; visc3=28.6*10^-6; visc4= 23*10^-6; (* Kg/m s *)

kg1=0.1696; kg2=0.00625; kg3=0.01067; kg4=0.449; (* W/m K*)

gamma1=1.667;gamma2=1.656;gamma3=1.667;gamma4=1.299;

cv1=3120;cv2=97;cv3=151;cv4=226.016; (* J/Kg K *)

lambda1=0.19266*10^-6; lambda2=0.03788*10^-6; lambda3=0.05234*10^-6; lambda4=0.0419*10^-6; (* meter *)

y1=8.56*10^-5; y2=0.8146; y3=0.1136; y4=0.0705;

x1=Mg1/(Mg1+Mg2+Mg3+Mg4);
x2=Mg2/(Mg1+Mg2+Mg3+Mg4);
x3=Mg3/(Mg1+Mg2+Mg3+Mg4);
x4=Mg4/(Mg1+Mg2+Mg3+Mg4);

(*Accomodation coefficients from literature *)

bt=6*sigmaeff;

alpha1=0.53;alpha2=0.86;alpha3=0.861;alpha4=0.73;

(* Temperature jump distance calculation *)

g1=((2-alpha1)/alpha1)*(2/(gamma1+1))*(kg1/(visc1*cv1))*lambda1;
g2=((2-alpha2)/alpha2)*(2/(gamma2+1))*(kg2/(visc2*cv2))*lambda2;
g3=((2-alpha3)/alpha3)*(2/(gamma3+1))*(kg3/(visc3*cv3))*lambda3;
g4=((2-alpha4)/alpha4)*(2/(gamma4+1))*(kg4/(visc4*cv4))*lambda4;

gm =
((x1*g1/(Mg1^0.5))+(x2*g2/(Mg2^0.5))+(x3*g3/(Mg3^0.5))+(x4*g4/(Mg4^0.5)))/((x1/(
Mg1^0.5))+(x2/(Mg2^0.5))+(x3/(Mg3^0.5))+(x4/(Mg4^0.5)))

2.37413×10^{-6}

(* Gap thickness calculation *)

X= bt/ (2*gm); Y= 1/(0.305+(1/X));

deltaeff = (X/Y)*(2*gm)

7.98328×10^{-6}

(* Thermal conductivity of a mixture calculation using Wilke's mixture rule*)

phi11=1;phi22=1;phi33=1;phi44=1;
phi12=((1+(visc1/visc2)^0.5 (Mg2/Mg1)^0.25)^2)/(Sqrt[8]*(1+(Mg1/Mg2))^0.5);
phi13=((1+(visc1/visc3)^0.5 (Mg3/Mg1)^0.25)^2)/(Sqrt[8]*(1+(Mg1/Mg3))^0.5);
phi14=((1+(visc1/visc4)^0.5 (Mg4/Mg1)^0.25)^2)/(Sqrt[8]*(1+(Mg1/Mg4))^0.5);

phi21=((1+(visc2/visc1)^0.5 (Mg1/Mg2)^0.25)^2)/(Sqrt[8]*(1+(Mg2/Mg1))^0.5);
phi23=((1+(visc2/visc3)^0.5 (Mg3/Mg2)^0.25)^2)/(Sqrt[8]*(1+(Mg2/Mg3))^0.5);
phi24=((1+(visc2/visc4)^0.5 (Mg4/Mg2)^0.25)^2)/(Sqrt[8]*(1+(Mg2/Mg4))^0.5);

phi31=((1+(visc3/visc1)^0.5 (Mg1/Mg3)^0.25)^2)/(Sqrt[8]*(1+(Mg3/Mg1))^0.5);
phi32=((1+(visc3/visc2)^0.5 (Mg2/Mg3)^0.25)^2)/(Sqrt[8]*(1+(Mg3/Mg2))^0.5);
phi34=((1+(visc3/visc4)^0.5 (Mg4/Mg3)^0.25)^2)/(Sqrt[8]*(1+(Mg3/Mg4))^0.5);

phi41=((1+(visc4/visc1)^0.5 (Mg1/Mg4)^0.25)^2)/(Sqrt[8]*(1+(Mg4/Mg1))^0.5);
phi42=((1+(visc4/visc2)^0.5 (Mg2/Mg4)^0.25)^2)/(Sqrt[8]*(1+(Mg4/Mg2))^0.5);
phi43=((1+(visc4/visc3)^0.5 (Mg3/Mg4)^0.25)^2)/(Sqrt[8]*(1+(Mg4/Mg3))^0.5);

kgmix = (y1*kg1 / ((y1*phi11) + (y2*phi12)+ (y3*phi13) + (y4*phi14)))+ (y2*kg2 /
((y1*phi21) + (y2*phi22)+ (y3*phi23) + (y4*phi24)))+ (y3*kg3 / ((y1*phi31)
+(y2*phi32)+ (y3*phi33) + (y4*phi34)))+ (y4*kg4 / ((y1*phi41) + (y2*phi42)+
(y3*phi43) +(y4*phi44)));

hgmix= FullSimplify[kgmix/(delta + (2*gm))](* W/m2 K *)

$$\frac{0.0533323}{4.74826 \times 10^{-6} + \text{delta}}$$

(* TOTAL CONDUCTANCE CALCULATION *)

htotal = hs + hgmix

$$\frac{0.0533323}{4.74826 \times 10^{-6} + \text{delta}} + 0.0808246\, P^{0.94}$$

APPENDIX 10: Mathematica Code to Develop a Thermal Conductance Model for Al 6061-T4 and Pure Al Interface.

```
Clear[mew_He,mew_Xe,mew_Kr,mew_I,Ms,Mg,Mg_He,Mg_Kr,Mg_Xe,Mg_I,Ts,T0,C
0,C1,g1,g2,g3,g4,alpha1,alpha2,alpha3,alpha4,gamma1,gamma2,gamma3,gamma4,kg1,k
g2,kg3,kg4,visc1,visc2,visc3,visc4,cv1,cv2,cv3,cv4,lambda1,lambda2,lambda3,lambda4,
gm,bt,sigma,X,Y,deltaeff,phi11,phi12,phi13,phi14,phi21,phi22,phi23,phi24,phi31,phi32,
phi33,phi34,phi41,phi42,phi43,phi44,kgmix,x1,x2,x2,x3,k1,k2,k3,k4,hgmix,CLAsigmaA
l,CLAsigmaU,kAl,kU,EAl,EU,slopeAl,slopeU,vAl,vU,keff,sigmaeff,tantheta,Eeff,si,hs,P
,htotal,delta,h]

(* ------------------------------------------------------------------------------------------*)
(* Mg and Ms - Molecular weight of gas and solid respectively  in 'g/mol'*)
(* mew - ratio of molecular weights *)
(* alpha - accomodation coefficient *)
(* Ts and T0 - Temp of the solid and reference temp respectively *)
(* g and gm - Temperature jump distance for an individual component and a mixture
respectively *)
(* visc - dynamic viscosity *)
(* kg - thermal conductivity of the individual gas in W/mK *)
(* lambda - mean free path in 'm'*)
(* sigma - surface roughness *)
(* deltaeff - effective gap thickness = delta+2gm *)
(* kgmix - thermal conductivity of the gas mixture in W/mK*)
(* x and y - mass fraction and mole fraction respectively *)
(* gamma - ratio of specific heats *)
(* cv - specific heat at constant volume in J/Kg K *)
(* ------------------------------------------------------------------------------------------*)

H=1080*10^6; (*In Pa *)

CLAsigmaAl=1*10^-6; CLAsigmaalpure=0.1*10^-6;
kAl=154; kalpure=210;
EAl=68.9*10^9; Ealpure=68*10^9;
slopeAl=0.18; (*rad*) slopealpure=0.03; (*rad*)
vAl=0.33;valpure=0.36;

(* Solid spot conductance calculations *)

keff= 2*kAl*kalpure/(kAl+kalpure);

sigmaeff=1.25* Sqrt[ CLAsigmaAl^2 + CLAsigmaalpure^2];

tantheta= Sqrt[ slopeAl^2 + slopealpure^2];
Eeff = 2*(( ((1-vAl^2)/EAl)+ ((1-valpure^2)/Ealpure))^-1);
si= (Eeff/H)*tantheta
```

sigmaeff
1.25623×10^{-6}
(* plasticity index 'si' > 1 =>Mikic's correlation can be used for plastic deformation of asperities *)
hs= 1.13* (keff/ (H^0.94))*(tantheta/sigmaeff)* (P^0.94)
$0.0940763\, P^{0.94}$

(* Input values For Gap Conductance Model *)
(* 1- Helium; 2- Xenon ; 3- Krypton; 4- Iodine *)

Ms=26.981538 *10^-3 ;Mg1=4.003*10^-3;Mg2=131.293*10^-3;Mg3=83.8*10^-3;Mg4=253.809*10^-3; (* Kg/mol *)
(* Data obtained from properties of gases and liquids 5th edition, Bruce E. Poling et.al *)

visc1=21.7*10^-6; visc2=26.17*10^-6; visc3=28.6*10^-6; visc4= 23*10^-6; (* Kg/m s *)

kg1=0.1696; kg2=0.00625; kg3=0.01067; kg4=0.449; (* W/m K*)

gamma1=1.667;gamma2=1.656;gamma3=1.667;gamma4=1.299;

cv1=3120;cv2=97;cv3=151;cv4=226.016; (* J/Kg K *)

lambda1=0.19266*10^-6; lambda2=0.03788*10^-6; lambda3=0.05234*10^-6; lambda4=0.0419*10^-6; (* meter *)

y1=8.56*10^-5; y2=0.8146; y3=0.1136; y4=0.0705;

x1=Mg1/(Mg1+Mg2+Mg3+Mg4);
x2=Mg2/(Mg1+Mg2+Mg3+Mg4);
x3=Mg3/(Mg1+Mg2+Mg3+Mg4);
x4=Mg4/(Mg1+Mg2+Mg3+Mg4);

(*Accomodation coefficients from literature *)

bt=6*sigmaeff;

alpha1=0.53;alpha2=0.86;alpha3=0.861;alpha4=0.73;

(* Temperature jump distance calculation *)

g1=((2-alpha1)/alpha1)*(2/(gamma1+1))*(kg1/(visc1*cv1))*lambda1;
g2=((2-alpha2)/alpha2)*(2/(gamma2+1))*(kg2/(visc2*cv2))*lambda2;
g3=((2-alpha3)/alpha3)*(2/(gamma3+1))*(kg3/(visc3*cv3))*lambda3;
g4=((2-alpha4)/alpha4)*(2/(gamma4+1))*(kg4/(visc4*cv4))*lambda4;

```
gm =
((x1*g1/(Mg1^0.5))+(x2*g2/(Mg2^0.5))+(x3*g3/(Mg3^0.5))+(x4*g4/(Mg4^0.5)))/((x1/(
Mg1^0.5))+(x2/(Mg2^0.5))+(x3/(Mg3^0.5))+(x4/(Mg4^0.5)))
```

$$2.37413 \times 10^{-6}$$

```
(* Gap thickness calculation *)
X= bt/ (2*gm); Y= 1/(0.305+(1/X));
deltaeff = (X/Y)*(2*gm)
```

$$7.04717 \times 10^{-6}$$

```
(* Thermal conductivity of a mixture calculation using Wilke's mixture rule*)

phi11=1;phi22=1;phi33=1;phi44=1;

phi12=(( 1+(visc1/visc2)^0.5 ( Mg2/Mg1)^0.25)^2)/( Sqrt[8]*( 1+(Mg1/Mg2))^0.5);
phi13=(( 1+(visc1/visc3)^0.5 ( Mg3/Mg1)^0.25)^2)/( Sqrt[8]*( 1+(Mg1/Mg3))^0.5);
phi14=(( 1+(visc1/visc4)^0.5 ( Mg4/Mg1)^0.25)^2)/( Sqrt[8]*( 1+(Mg1/Mg4))^0.5);
phi21=(( 1+(visc2/visc1)^0.5 ( Mg1/Mg2)^0.25)^2)/( Sqrt[8]*( 1+(Mg2/Mg1))^0.5);
phi23=(( 1+(visc2/visc3)^0.5 ( Mg3/Mg2)^0.25)^2)/( Sqrt[8]*( 1+(Mg2/Mg3))^0.5);
phi24=(( 1+(visc2/visc4)^0.5 ( Mg4/Mg2)^0.25)^2)/( Sqrt[8]*( 1+(Mg2/Mg4))^0.5);
phi31=(( 1+(visc3/visc1)^0.5 ( Mg1/Mg3)^0.25)^2)/( Sqrt[8]*( 1+(Mg3/Mg1))^0.5);
phi32=(( 1+(visc3/visc2)^0.5 ( Mg2/Mg3)^0.25)^2)/( Sqrt[8]*( 1+(Mg3/Mg2))^0.5);
phi34=(( 1+(visc3/visc4)^0.5 ( Mg4/Mg3)^0.25)^2)/( Sqrt[8]*( 1+(Mg3/Mg4))^0.5);
phi41=(( 1+(visc4/visc1)^0.5 ( Mg1/Mg4)^0.25)^2)/( Sqrt[8]*( 1+(Mg4/Mg1))^0.5);
phi42=(( 1+(visc4/visc2)^0.5 ( Mg2/Mg4)^0.25)^2)/( Sqrt[8]*( 1+(Mg4/Mg2))^0.5);
phi43=(( 1+(visc4/visc3)^0.5 ( Mg3/Mg4)^0.25)^2)/( Sqrt[8]*( 1+(Mg4/Mg3))^0.5);

kgmix = ( y1*kg1 / ((y1*phi11) + (y2*phi12)+ (y3*phi13) + (y4*phi14) ))+  ( y2*kg2 /
((y1*phi21) + (y2*phi22)+ (y3*phi23) + (y4*phi24) ))+  ( y3*kg3 / ((y1*phi31)
+(y2*phi32)+ (y3*phi33) + (y4*phi34) ))+  ( y4*kg4 / ((y1*phi41) + (y2*phi42)+
(y3*phi43) +(y4*phi44) ));

hgmix= FullSimplify[kgmix/(delta + (2*gm)) ](* W/m2 K *)
```

$$\frac{0.0533323}{4.74826 \times 10^{-6} + \text{delta}}$$

```
(* TOTAL CONDUCTANCE CALCULATION *)

htotal = hs + hgmix
```

$$\frac{0.0533323}{4.74826 \times 10^{-6} + \text{delta}} + 0.0940763\ P^{0.94}$$

APPENDIX 11: Abaqus Input File for the Planar Model with Non-Uniform Heating

(The part and the mesh definitions have been omitted to make the presentation of the code concise in this appendix. The description of the part creation along with the mesh information has been provided in the dissertation write-up)

(To run the input file from the command window: abaqus job=**(the name of inp file, without ".inp". To open the input file in the CAE environment: import the model. File → Import → Model. This dialog will accept *.inp files)

```
*Heading
** Job name: FINEMESH-1 Model name: Model-1
** Generated by: Abaqus/CAE 6.10-2
*Preprint, echo=NO, model=NO, history=NO
**
**
** MATERIALS
**
*Material, name=al
*Conductivity
167.,
*Density
2700.,
*Elastic
 6.9e+10, 0.33
*Expansion
 2.34e-05,
*Specific Heat
963.,
*Material, name=uranium
*Conductivity
 27.5,
*Density
19100.,
*Elastic
 2.08e+11, 0.23
*Expansion
 1.39e-05,
*Specific Heat
120.,
**
** INTERACTION PROPERTIES
**
*Surface Interaction, name=IntProp-1
1.,
*Friction
```

```
0.,
*Surface Behavior, pressure-overclosure=HARD
*Gap Conductance
1e+09, 0.
0., 0.1
**
** INTERACTIONS
**
** Interaction: IT-FOIL
*Contact Pair, interaction=IntProp-1, type=SURFACE TO SURFACE
_PickedSurf373, _PickedSurf372
** Interaction: OT-FOIL
*Contact Pair, interaction=IntProp-1, type=SURFACE TO SURFACE
_PickedSurf375, _PickedSurf374
** Interaction: it-ot
*Contact Pair, interaction=IntProp-1, type=SURFACE TO SURFACE
_PickedSurf377, _PickedSurf376
** ----------------------------------------------------------------
**
** STEP: Step-1
**
*Step, name=Step-1, nlgeom=YES
*Coupled Temperature-displacement, creep=none, steady state
1., 1., 1e-07, 1.
**
** BOUNDARY CONDITIONS
**
** Name: XSymm Type: Symmetry/Antisymmetry/Encastre
*Boundary
_PickedSet378, XSYMM
**
** LOADS
**
** Name: foil heat gen   Type: Body heat flux
*Dflux
_PickedSet371, BF, 1.6e+10
**
** INTERACTIONS
**
** Contact Controls for Interaction: IT-FOIL
*Contact Controls, master=_PickedSurf372, slave=_PickedSurf373, stabilize=1.
** Contact Controls for Interaction: OT-FOIL
*Contact Controls, master=_PickedSurf374, slave=_PickedSurf375, stabilize=1.
** Contact Controls for Interaction: it-ot
*Contact Controls, master=_PickedSurf376, slave=_PickedSurf377, stabilize=1.
** Interaction: htc-inner
```

```
*Sfilm
_PickedSurf369, F, 323., 19000.
** Interaction: htc-outer
*Sfilm
_PickedSurf370, F, 323., 19000.
**
** OUTPUT REQUESTS
**
*Restart, write, frequency=0
**
** FIELD OUTPUT: F-Output-1
**
*Output, field, variable=PRESELECT
**
** HISTORY OUTPUT: H-Output-1
**
*Output, history, variable=PRESELECT
*End Step
```

APPENDIX 12: Abaqus Input File for the Hydroforming and Irradiation Model

(The part and the mesh definitions have been omitted to make the presentation of the code concise in this appendix. The description of the part creation along with the mesh information has been provided in the dissertation write-up)

(To run the input file from the command window: abaqus job=**(the name of inp file, without ".inp". To open the input file in the CAE environment: import the model. File → Import → Model. This dialog will accept *.inp files)

```
*Heading
** Job name: Ar1 Model name: Ar
** Generated by: Abaqus/CAE 6.12-2
*Preprint, echo=NO, model=NO, history=NO
**
** PARTS
**
*Part, name=foil
*Node
(* foil part definitions omitted to maintain brevity *)
*Element, type=CPE8RT
(* element definitions omitted to maintain brevity *)
*Nset, nset=Set-2, generate
(* include node definitions here*)
*Elset, elset=Set-2, generate
(* include element set numbers/definitions here *)
*Elset, elset=_foil-inner_S4, internal
(* include element set numbers/definitions here *)
*Elset, elset=_foil-inner_S2, internal
(* include element set numbers/definitions here *)
*Surface, type=ELEMENT, name=foil-inner
(* include selected surface definitions here *)
*Elset, elset=_foil-outer_S2, internal
(* include element set numbers/definitions here *)
*Elset, elset=_foil-outer_S4, internal
(* include element set numbers/definitions here *)
*Surface, type=ELEMENT, name=foil-outer
(* include selected surface definitions here *)
** Section: foil
*Solid Section, elset=Set-2, material=uranium-plastic
*End Part
**
*Part, name="inner tube"
*Node
(* part definitions omitted to maintain brevity *)
*Element, type=CPE8RT
```

```
(* element definitions omitted to maintain brevity *)
*Nset, nset=Set-2, generate
(* include node set numbers/definitions here *)
*Elset, elset=Set-2, generate
(* include element set numbers/definitions here *)
*Elset, elset=_IT-inner_S4, internal
(* include element set numbers/definitions here *)
*Elset, elset=_IT-inner_S2, internal
(* include element set numbers/definitions here *)
*Surface, type=ELEMENT, name=IT-inner
(* include selected surface definitions here *)
*Elset, elset=_IT-outer_S2, internal
(* include element set numbers/definitions here *)
*Elset, elset=_IT-outer_S4, internal
(* include element set numbers/definitions here *)
*Surface, type=ELEMENT, name=IT-outer
(* include selected surface definitions here *)
** Section: inner tube
*Solid Section, elset=Set-2, material=Al6061-Plastic
*End Part
**
*Part, name="outer tube"
*Node
(* part definitions omitted to maintain brevity *)
*Element, type=CPE8RT
(* element definitions omitted to maintain brevity *)
*Nset, nset=Set-3, generate
(* include node set numbers/definitions here *)
*Elset, elset=Set-3, generate
(* include element set numbers/definitions here *)
*Elset, elset=_OT-outer_S2, internal
(* include element set numbers/definitions here *)
*Elset, elset=_OT-outer_S4, internal
(* include element set numbers/definitions here *)
*Surface, type=ELEMENT, name=OT-outer
(* include selected surface definitions here *)
*Elset, elset=_OT-inner_S4, internal
(* include element set numbers/definitions here *)
*Elset, elset=_OT-inner_S2, internal
(* include element set numbers/definitions here *)
*Surface, type=ELEMENT, name=OT-inner
(* include selected surface definitions here *)
** Section: outer tube
*Solid Section, elset=Set-3, material=Al6061-Plastic
*End Part
**
```

```
**
** ASSEMBLY
**
*Assembly, name=Assembly
**
*Instance, name="inner tube-1", part="inner tube"
*End Instance
**
*Instance, name=foil-1, part=foil
*End Instance
**
*Instance, name="outer tube-1", part="outer tube"
*End Instance
**
*Nset, nset=Set-1, instance="inner tube-1"
*Nset, nset=Set-1, instance=foil-1
*Nset, nset=Set-1, instance="outer tube-1"
*Nset, nset=Set-2, instance="inner tube-1"
*Nset, nset=Set-2, instance="outer tube-1"
*Nset, nset=Set-3, instance="inner tube-1"
*Nset, nset=Set-3, instance=foil-1
*Nset, nset=Set-3, instance="outer tube-1"
*Nset, nset=Set-4, instance="inner tube-1"
*Nset, nset=Set-4, instance=foil-1
*Nset, nset=Set-4, instance="outer tube-1"
*Nset, nset=Set-5, instance="inner tube-1", generate
*Nset, nset=Set-5, instance=foil-1, generate
*Nset, nset=Set-5, instance="outer tube-1", generate
*Elset, elset=Set-5, instance="inner tube-1", generate
*Elset, elset=Set-5, instance=foil-1, generate
*Elset, elset=Set-5, instance="outer tube-1", generate
*Nset, nset=Set-6, instance=foil-1, generate
*Elset, elset=Set-6, instance=foil-1, generate
*Nset, nset=Set-7, instance=foil-1, generate
*Elset, elset=Set-7, instance=foil-1, generate
*Nset, nset=Set-8, instance="inner tube-1"
*Nset, nset=Set-8, instance=foil-1
*Nset, nset=Set-8, instance="outer tube-1"
*Nset, nset=Set-9, instance="inner tube-1"
*Nset, nset=Set-9, instance=foil-1
*Nset, nset=Set-9, instance="outer tube-1"
*Nset, nset=Set-10, instance=foil-1, generate
*Elset, elset=Set-10, instance=foil-1, generate
*Elset, elset=_m_Surf-1_S4, internal, instance="inner tube-1", generate
*Elset, elset=_m_Surf-1_S2, internal, instance="inner tube-1", generate
*Surface, type=ELEMENT, name=m_Surf-1
```

```
*Elset, elset=_s_Surf-1_S2, internal, instance="outer tube-1", generate
*Elset, elset=_s_Surf-1_S4, internal, instance="outer tube-1", generate
*Surface, type=ELEMENT, name=s_Surf-1
*Elset, elset=_Surf-3_S2, internal, instance="outer tube-1"
(* include element set numbers/definitions here *)
*Elset, elset=_Surf-3_S4, internal, instance="outer tube-1"
(* include element set numbers/definitions here *)
*Surface, type=ELEMENT, name=Surf-3
*Elset, elset=_Surf-4_S4, internal, instance="inner tube-1"
(* include element set numbers/definitions here *)
*Elset, elset=_Surf-4_S2, internal, instance="inner tube-1"
(* include element set numbers/definitions here *)
*Surface, type=ELEMENT, name=Surf-4
*Elset, elset=_Surf-5_S2, internal, instance="outer tube-1"
(* include element set numbers/definitions here *)
*Elset, elset=_Surf-5_S4, internal, instance="outer tube-1"
(* include element set numbers/definitions here *)
*Surface, type=ELEMENT, name=Surf-5
*Elset, elset=_m_Surf-6_S4, internal, instance="inner tube-1", generate
*Elset, elset=_m_Surf-6_S2, internal, instance="inner tube-1", generate
*Surface, type=ELEMENT, name=m_Surf-6
*Elset, elset=_s_Surf-6_S2, internal, instance="outer tube-1", generate
*Elset, elset=_s_Surf-6_S4, internal, instance="outer tube-1", generate
*Surface, type=ELEMENT, name=s_Surf-6
*Elset, elset=_m_Surf-8_S4, internal, instance=foil-1
(* include element set numbers/definitions here *)
*Elset, elset=_m_Surf-8_S2, internal, instance=foil-1
(* include element set numbers/definitions here *)
*Surface, type=ELEMENT, name=m_Surf-8
*Elset, elset=_s_Surf-8_S2, internal, instance="inner tube-1"
(* include element set numbers/definitions here *)
*Elset, elset=_s_Surf-8_S4, internal, instance="inner tube-1"
(* include element set numbers/definitions here *)
*Surface, type=ELEMENT, name=s_Surf-8
*Elset, elset=_m_Surf-10_S2, internal, instance=foil-1
(* include element set numbers/definitions here *)
*Elset, elset=_m_Surf-10_S4, internal, instance=foil-1
(* include element set numbers/definitions here *)
*Surface, type=ELEMENT, name=m_Surf-10
*Elset, elset=_s_Surf-10_S4, internal, instance="outer tube-1"
(* include element set numbers/definitions here *)
*Elset, elset=_s_Surf-10_S2, internal, instance="outer tube-1"
(* include element set numbers/definitions here *)
*Surface, type=ELEMENT, name=s_Surf-10
*Elset, elset=_Surf-12_S4, internal, instance="inner tube-1"
(* include element set numbers/definitions here *)
```

```
*Elset, elset=_Surf-12_S2, internal, instance="inner tube-1"
(* include element set numbers/definitions here *)
*Surface, type=ELEMENT, name=Surf-12
*Elset, elset=_Surf-13_S2, internal, instance="outer tube-1"
(* include element set numbers/definitions here *)
*Elset, elset=_Surf-13_S4, internal, instance="outer tube-1"
(* include element set numbers/definitions here *)
*Surface, type=ELEMENT, name=Surf-13
*Elset, elset=_m_Surf-14_S4, internal, instance=foil-1
(* include element set numbers/definitions here *)
*Elset, elset=_m_Surf-14_S2, internal, instance=foil-1
(* include element set numbers/definitions here *)
*Surface, type=ELEMENT, name=m_Surf-14
*Elset, elset=_s_Surf-14_S2, internal, instance="inner tube-1"
(* include element set numbers/definitions here *)
*Elset, elset=_s_Surf-14_S4, internal, instance="inner tube-1"
(* include element set numbers/definitions here *)
*Surface, type=ELEMENT, name=s_Surf-14
*Elset, elset=_m_Surf-16_S2, internal, instance=foil-1
(* include element set numbers/definitions here *)
*Elset, elset=_m_Surf-16_S4, internal, instance=foil-1
(* include element set numbers/definitions here *)
*Surface, type=ELEMENT, name=m_Surf-16
*Elset, elset=_s_Surf-16_S4, internal, instance="outer tube-1"
(* include element set numbers/definitions here *)
*Elset, elset=_s_Surf-16_S2, internal, instance="outer tube-1"
(* include element set numbers/definitions here *)
*Surface, type=ELEMENT, name=s_Surf-16
*Elset, elset=_m_Surf-18_S4, internal, instance="inner tube-1", generate
*Elset, elset=_m_Surf-18_S2, internal, instance="inner tube-1", generate
*Surface, type=ELEMENT, name=m_Surf-18
*Elset, elset=_s_Surf-18_S2, internal, instance="outer tube-1", generate
*Elset, elset=_s_Surf-18_S4, internal, instance="outer tube-1", generate
*Surface, type=ELEMENT, name=s_Surf-18
*Elset, elset=_Surf-20_S4, internal, instance="inner tube-1"
(* include element set numbers/definitions here *)
*Elset, elset=_Surf-20_S2, internal, instance="inner tube-1"
(* include element set numbers/definitions here *)
*Surface, type=ELEMENT, name=Surf-20
*Elset, elset=_Surf-21_S2, internal, instance="outer tube-1"
(* include element set numbers/definitions here *)
*Elset, elset=_Surf-21_S4, internal, instance="outer tube-1"
(* include element set numbers/definitions here *)
*Surface, type=ELEMENT, name=Surf-21
*End Assembly
**
```

```
** MATERIALS
**
*Material, name=Al6061-Plastic
*Conductivity
167.,
*Density
2700.,
*Elastic
6.89e+10, 0.33
*Expansion
2.34e-05,
*Plastic
2.97854e+08,          0.
3.03817e+08, 0.000103788
3.12636e+08, 0.000203785
3.14828e+08, 0.000303384
3.18827e+08, 0.000466394
3.20234e+08, 0.000552785
3.21799e+08, 0.000608999
3.22592e+08, 0.000731266
3.23178e+08, 0.000858794
3.23667e+08, 0.000971875
3.24081e+08, 0.00108532
3.28852e+08, 0.00200756
3.29762e+08, 0.00204261
3.30583e+08, 0.00401162
3.31514e+08, 0.00511611
3.32279e+08, 0.00602954
3.33093e+08, 0.00701644
3.33968e+08, 0.008079
3.34803e+08, 0.00909294
3.35637e+08, 0.0101208
3.36457e+08, 0.011144
3.37167e+08, 0.0120147
3.38029e+08, 0.0130966
3.38808e+08, 0.0140844
3.39581e+08, 0.0150898
3.40346e+08, 0.0160675
3.41153e+08, 0.0171126
3.4187e+08,   0.0180507
3.42642e+08, 0.0190953
3.43421e+08, 0.0201244
3.47061e+08, 0.0250944
3.50529e+08, 0.030057
3.53853e+08, 0.0350468
3.57066e+08, 0.0401315
```

3.59996e+08, 0.0450281
3.62781e+08, 0.0500108
3.65415e+08, 0.0550523
3.67808e+08, 0.0600356
3.70049e+08, 0.0651016
3.72034e+08, 0.070092
3.73799e+08, 0.0750486
3.75406e+08, 0.0800535
3.77033e+08, 0.0853327
3.78426e+08, 0.0900701
3.79805e+08, 0.0950171
3.81142e+08, 0.100062
3.92367e+08, 0.157004
4.02426e+08, 0.223144
4.11107e+08, 0.300105
4.20111e+08, 0.405465
4.26544e+08, 0.500775
4.31495e+08, 0.587787
4.32908e+08, 0.615186
4.36645e+08, 0.693147
4.37748e+08, 0.71784
4.40713e+08, 0.788457
4.41609e+08, 0.81093
4.44795e+08, 0.896088
4.45512e+08, 0.916291
4.48697e+08, 1.0116
*Material, name=uranium-plastic
*Conductivity
27.5,
*Density
19100.,
*Elastic
2.06327e+11, 0.23
*Expansion
1.39e-05,
*Plastic
1.11e+08, 0.
2.32e+08, 0.001
2.99e+08, 0.003
3.36e+08, 0.005
3.63e+08, 0.007
3.94e+08, 0.01
**
** INTERACTION PROPERTIES
**
*Surface Interaction, name=contact-assembly

```
1.,
*Friction
0.,
*Surface Behavior, no separation, pressure-overclosure=HARD
*Gap Conductance
1e+09,   0.
0., 0.01
*Surface Interaction, name=contact-irrad
1.,
*Friction
0.,
*Surface Behavior, pressure-overclosure=HARD
*Gap Conductance
1e+09,   0.
0., 0.01
**
** INTERACTIONS
**
** Interaction: IT-OT
*Contact Pair, interaction=contact-assembly, type=SURFACE TO SURFACE
s_Surf-1, m_Surf-1
** Interaction: Inner-Foil-Irradiation
*Contact Pair, interaction=contact-irrad, type=SURFACE TO SURFACE
s_Surf-14, m_Surf-14
** Interaction: Inner-Outer-Irradiation
*Contact Pair, interaction=contact-irrad, type=SURFACE TO SURFACE
s_Surf-18, m_Surf-18
** Interaction: Outer-Foil-Irradiation
*Contact Pair, interaction=contact-irrad, type=SURFACE TO SURFACE
s_Surf-16, m_Surf-16
** Interaction: foil-innertube
*Contact Pair, interaction=contact-assembly, type=SURFACE TO SURFACE
"inner tube-1".IT-outer, foil-1.foil-inner
** Interaction: foil-outertube
*Contact Pair, interaction=contact-assembly, type=SURFACE TO SURFACE
"outer tube-1".OT-inner, foil-1.foil-outer
** ----------------------------------------------------------------
**
** STEP: Coupled-assembly
**
*Step, name=Coupled-assembly, nlgeom=YES, inc=1000
*Coupled Temperature-displacement, creep=none, steady state
1., 1., 1e-09, 1.
**
** BOUNDARY CONDITIONS
**
```

```
** Name: xSymm Type: Symmetry/Antisymmetry/Encastre
*Boundary
Set-1, XSYMM
** Name: xsymm2 Type: Symmetry/Antisymmetry/Encastre
*Boundary
Set-2, XSYMM
** Name: ysymm1 Type: Symmetry/Antisymmetry/Encastre
*Boundary
Set-8, YSYMM
** Name: ysymm2 Type: Symmetry/Antisymmetry/Encastre
*Boundary
Set-9, YSYMM
**
** LOADS
**
** Name: internal pressure   Type: Pressure
*Dsload
"inner tube-1".IT-inner, P, 3.6e+07
**
** INTERACTIONS
**
** Contact Controls for Interaction: IT-OT
*Contact Controls, master=m_Surf-1, slave=s_Surf-1, stabilize=1.
** Interaction: Inner-Foil-Irradiation
*Model Change, type=CONTACT PAIR, remove
s_Surf-14, m_Surf-14
** Interaction: Inner-Outer-Irradiation
*Model Change, type=CONTACT PAIR, remove
s_Surf-18, m_Surf-18
** Interaction: Outer-Foil-Irradiation
*Model Change, type=CONTACT PAIR, remove
s_Surf-16, m_Surf-16
** Contact Controls for Interaction: foil-innertube
*Contact Controls, master=foil-1.foil-inner, slave="inner tube-1".IT-outer, stabilize=1.
** Contact Controls for Interaction: foil-outertube
*Contact Controls, master=foil-1.foil-outer, slave="outer tube-1".OT-inner, stabilize=1.
**
** OUTPUT REQUESTS
**
*Restart, write, frequency=0
**
** FIELD OUTPUT: F-Output-1
**
*Output, field
*Node Output
CF, NT, RF, RFL, U
```

```
*Element Output, directions=YES
E, HFL, LE, PE, PEEQ, PEMAG, S, THE
*Contact Output
CDISP, CSTRESS
**
** HISTORY OUTPUT: H-Output-1
**
*Output, history, variable=PRESELECT
*End Step
** ----------------------------------------------------------------
**
** STEP: Relieve Pressure
**
*Step, name="Relieve Pressure", nlgeom=YES
*Coupled Temperature-displacement, creep=none, steady state
1., 1., 1e-05, 1.
**
** LOADS
**
** Name: internal pressure   Type: Pressure
*Dsload, op=NEW
**
** OUTPUT REQUESTS
**
*Restart, write, frequency=0
**
** FIELD OUTPUT: F-Output-1
**
*Output, field
*Node Output
CF, NT, RF, RFL, U
*Element Output, directions=YES
E, HFL, LE, PE, PEEQ, PEMAG, S, THE
*Contact Output
CDISP, CSTRESS
**
** HISTORY OUTPUT: H-Output-1
**
*Output, history, variable=PRESELECT
*End Step
** ----------------------------------------------------------------
**
** STEP: Irradiation
**
*Step, name=Irradiation, nlgeom=YES
*Coupled Temperature-displacement, creep=none, steady state
```

```
1., 1., 1e-09, 1.
**
** LOADS
**
** Name: HEAT GEN   Type: Body heat flux
*Dflux
Set-10, BF, 1.6e+10
**
** INTERACTIONS
**
** Interaction: IT-OT
*Model Change, type=CONTACT PAIR, remove
s_Surf-1, m_Surf-1
** Interaction: Inner-Foil-Irradiation
*Model Change, type=CONTACT PAIR, add
s_Surf-14, m_Surf-14
** Contact Controls for Interaction: Inner-Foil-Irradiation
*Contact Controls, master=m_Surf-14, slave=s_Surf-14, stabilize=1.
** Interaction: Inner-Outer-Irradiation
*Model Change, type=CONTACT PAIR, add
s_Surf-18, m_Surf-18
** Contact Controls for Interaction: Inner-Outer-Irradiation
*Contact Controls, master=m_Surf-18, slave=s_Surf-18, stabilize=1.
** Interaction: Outer-Foil-Irradiation
*Model Change, type=CONTACT PAIR, add
s_Surf-16, m_Surf-16
** Contact Controls for Interaction: Outer-Foil-Irradiation
*Contact Controls, master=m_Surf-16, slave=s_Surf-16, stabilize=1.
** Interaction: foil-innertube
*Model Change, type=CONTACT PAIR, remove
"inner tube-1".IT-outer, foil-1.foil-inner
** Interaction: foil-outertube
*Model Change, type=CONTACT PAIR, remove
"outer tube-1".OT-inner, foil-1.foil-outer
** Interaction: InnerHTC
*Sfilm
Surf-20, F, 323., 19000.
** Interaction: OuterHTC
*Sfilm
Surf-21, F, 323., 19000.
**
** OUTPUT REQUESTS
**
*Restart, write, frequency=0
**
** FIELD OUTPUT: F-Output-1
```

```
**
*Output, field
*Node Output
CF, NT, RF, RFL, U
*Element Output, directions=YES
E, HFL, LE, PE, PEEQ, PEMAG, S, THE
*Contact Output
CDISP, CSTRESS
**
** HISTORY OUTPUT: H-Output-1
**
*Output, history, variable=PRESELECT
*End Step
```

APPENDIX 13: Abaqus Input File for the Draw-Plug Based Irradiation Model

(The part and the mesh definitions have been omitted to make the presentation of the code concise in this appendix. The description of the part creation along with the mesh information has been provided in the dissertation write-up)

(To run the input file from the command window: abaqus job=**(the name of inp file, without ".inp". To open the input file in the CAE environment: import the model. File → Import → Model. This dialog will accept *.inp files)

```
*Heading
** Job name: interf-1 Model name: interf
** Generated by: Abaqus/CAE 6.12-2
*Heading
** Job name: interf-1 Model name: interf
** Generated by: Abaqus/CAE 6.12-2
*Preprint, echo=NO, model=NO, history=NO
**
** PARTS
**
*Part, name="Ni foil"
*Node
(* foil part definitions omitted to maintain brevity *)
*Element, type=CAX4RT
(* element definitions omitted to maintain brevity *)
*Nset, nset=Set-1, generate
*Elset, elset=Set-1, generate
*Nset, nset=Set-15, generate
*Elset, elset=Set-15, generate
** Section: Nickel
*Solid Section, elset=Set-15, material=Nickel
*End Part
**
*Part, name=foil
*Node
(* foil part definitions omitted to maintain brevity *)
*Element, type=CAX4RT
(* element definitions omitted to maintain brevity *)
*Nset, nset=Set-1, generate
*Elset, elset=Set-1, generate
*Nset, nset=Set-24, generate
*Elset, elset=Set-24, generate
*Elset, elset="_foil inner_S2", internal, generate
*Surface, type=ELEMENT, name="foil inner"
*Elset, elset="_foil outer_S4", internal, generate
*Surface, type=ELEMENT, name="foil outer"
```

```
** Section: Uranium
*Solid Section, elset=Set-24, material=URANIUM
*End Part
**
*Part, name=innertube
*Node
(* foil part definitions omitted to maintain brevity *)
*Element, type=CAX4RT
 (* element definitions omitted to maintain brevity *)
*Nset, nset=Set-1
*Elset, elset=Set-59, generate
 2101,  3600,     1
*Nset, nset=Set-60, generate
    1,  4149,     1
*Elset, elset=Set-60, generate
    1,  3900,     1
*Elset, elset=_INNERcoolant_S3, internal
*Elset, elset=_INNERcoolant_S2, internal, generate
 *Surface, type=ELEMENT, name=INNERcoolant
*Elset, elset="_recess reg- inner_S4", internal, generate
*Surface, type=ELEMENT, name="recess reg- inner"
*Elset, elset=_upper_S3, internal, generate
 3851,  3900,     1
*Surface, type=ELEMENT, name=upper
_upper_S3, S3
*Elset, elset=_lower_S3, internal, generate
 3701,  3750,     1
*Surface, type=ELEMENT, name=lower
** Section: Al6061-T6
*Solid Section, elset=Set-60, material=Al6061-T6
*End Part
**
*Part, name=outertube
*Node
(* foil part definitions omitted to maintain brevity *)
*Element, type=CAX4RT
(* element definitions omitted to maintain brevity *)
*Elset, elset=Set-14
*Nset, nset=Set-21, generate
    1,  4305,     1
*Elset, elset=Set-21, generate
    1,  4080,     1
*Elset, elset="_recess reg-inner_S2", internal, generate
 1000,  1040,    20
*Elset, elset="_recess reg-inner_S4", internal, generate
 1041,  4001,    20
```

```
*Surface, type=ELEMENT, name="recess reg-inner"
*Elset, elset="_recess reg- outer_S4", internal, generate
*Elset, elset="_recess reg- outer_S2", internal, generate
*Surface, type=ELEMENT, name="recess reg- outer"
*Elset, elset=_upper-inner_S2, internal, generate
*Elset, elset=_upper-inner_S4, internal, generate
*Surface, type=ELEMENT, name=upper-inner
*Elset, elset=_OUTERcoolant_S4, internal, generate
*Elset, elset=_OUTERcoolant_S2, internal, generate
*Surface, type=ELEMENT, name=OUTERcoolant
** Section: Al6061-T6
*Solid Section, elset=Set-21, material=Al6061-T6
*End Part
**
*Part, name=plug1048
*Node
(* foil part definitions omitted to maintain brevity *)
*Element, type=CPE8RT
 (* element definitions omitted to maintain brevity *)
*Nset, nset=Set-2, generate
  1,  395,    1
*Elset, elset=Set-2, generate
  1,  357,    1
*Nset, nset=Set-9
*Elset, elset=Set-9
*Nset, nset=Set-12, generate
*Elset, elset=Set-12, generate
** Section: Plug
*Solid Section, elset=Set-12, material="D2 STEEL"
*End Part
**
**
** ASSEMBLY
**
*Assembly, name=Assembly
**
*Instance, name=innertube-1, part=innertube
*End Instance
**
*Instance, name="Ni foil-1", part="Ni foil"
*End Instance
**
*Instance, name=foil-1, part=foil
*End Instance
**
*Instance, name=outertube-1, part=outertube
```

```
*End Instance
**
*Instance, name=plug1048-1, part=plug1048
*End Instance
**
*Nset, nset=Set-74, instance=innertube-1
*Nset, nset=Set-74, instance=outertube-1
*Nset, nset=s_Set-76, instance=innertube-1
*Nset, nset=Set-77, instance=foil-1, generate
*Elset, elset=Set-77, instance=foil-1, generate
*Nset, nset=Set-78, instance=plug1048-1
*Elset, elset=Set-78, instance=plug1048-1
*Nset, nset=Set-79, instance=plug1048-1
*Elset, elset=Set-79, instance=plug1048-1
*Nset, nset=Set-80, instance=plug1048-1
*Elset, elset=Set-80, instance=plug1048-1, generate
*Nset, nset=Set-81, instance=plug1048-1, generate
*Elset, elset=Set-81, instance=plug1048-1, generate
*Nset, nset=Set-82, instance=innertube-1
*Nset, nset=Set-82, instance=outertube-1
*Elset, elset=Set-82, instance=innertube-1
*Elset, elset=Set-82, instance=outertube-1, generate
*Nset, nset=s_Set-83, instance=innertube-1
*Nset, nset=Set-84, instance="Ni foil-1", generate
*Nset, nset=Set-84, instance=foil-1, generate
*Elset, elset=Set-84, instance="Ni foil-1", generate
*Elset, elset=Set-84, instance=foil-1, generate
*Nset, nset=Set-85, instance=foil-1, generate
*Elset, elset=Set-85, instance=foil-1, generate
*Nset, nset=Set-98, instance=plug1048-1, generate
*Elset, elset=Set-98, instance=plug1048-1, generate
*Nset, nset=Set-99, instance=plug1048-1
*Elset, elset=Set-99, instance=plug1048-1, generate
*Nset, nset=Set-100, instance=plug1048-1
*Elset, elset=Set-100, instance=plug1048-1, generate
*Nset, nset=Set-101, instance=plug1048-1
*Elset, elset=Set-101, instance=plug1048-1
*Nset, nset=Set-102, instance=plug1048-1
*Elset, elset=Set-102, instance=plug1048-1
*Nset, nset=Set-103, instance=innertube-1, generate
*Elset, elset=Set-103, instance=innertube-1, generate
*Nset, nset=Set-104, instance=outertube-1, generate
*Elset, elset=Set-104, instance=outertube-1, generate
*Elset, elset=_s_Surf-76_S3, internal, instance=innertube-1
*Elset, elset=_s_Surf-76_S2, internal, instance=innertube-1, generate
*Surface, type=ELEMENT, name=s_Surf-76
```

*Elset, elset=_m_Surf-78_S2, internal, instance=innertube-1
*Elset, elset=_m_Surf-78_S4, internal, instance=innertube-1
*Surface, type=ELEMENT, name=m_Surf-78
*Elset, elset=_s_Surf-78_S4, internal, instance="Ni foil-1"
*Elset, elset=_s_Surf-78_S2, internal, instance="Ni foil-1"
*Elset, elset=_s_Surf-78_S3, internal, instance="Ni foil-1"
*Surface, type=ELEMENT, name=s_Surf-78
*Elset, elset=_m_Surf-80_S2, internal, instance="Ni foil-1", generate
*Elset, elset=_m_Surf-80_S4, internal, instance="Ni foil-1"
*Surface, type=ELEMENT, name=m_Surf-80
*Elset, elset=_s_Surf-80_S1, internal, instance=foil-1, generate
*Elset, elset=_s_Surf-80_S2, internal, instance=foil-1, generate
*Elset, elset=_s_Surf-80_S3, internal, instance=foil-1, generate
*Surface, type=ELEMENT, name=s_Surf-80
*Elset, elset=_m_Surf-82_S4, internal, instance=foil-1, generate
*Surface, type=ELEMENT, name=m_Surf-82
*Elset, elset=_s_Surf-82_S2, internal, instance="Ni foil-1", generate
*Surface, type=ELEMENT, name=s_Surf-82
*Elset, elset=_m_Surf-84_S3, internal, instance="Ni foil-1"
*Elset, elset=_m_Surf-84_S4, internal, instance="Ni foil-1", generate
*Surface, type=ELEMENT, name=m_Surf-84
*Elset, elset=_s_Surf-84_S4, internal, instance=outertube-1, generate
*Surface, type=ELEMENT, name=s_Surf-84
*Elset, elset=_m_Surf-86_S3, internal, instance=innertube-1, generate
*Surface, type=ELEMENT, name=m_Surf-86
*Elset, elset=_m_Surf-88_S3, internal, instance=innertube-1, generate
*Surface, type=ELEMENT, name=m_Surf-88
*Elset, elset=_m_Surf-90_S4, internal, instance=innertube-1, generate
*Surface, type=ELEMENT, name=m_Surf-90
*Elset, elset=_s_Surf-91_S3, internal, instance="Ni foil-1"
*Elset, elset=_s_Surf-91_S2, internal, instance="Ni foil-1", generate
*Surface, type=ELEMENT, name=s_Surf-91
*Elset, elset=_m_Surf-92_S4, internal, instance=innertube-1
*Elset, elset=_m_Surf-92_S2, internal, instance=innertube-1, generate
*Surface, type=ELEMENT, name=m_Surf-92
*Elset, elset=_s_Surf-92_S2, internal, instance="Ni foil-1"
*Elset, elset=_s_Surf-92_S4, internal, instance="Ni foil-1", generate
*Surface, type=ELEMENT, name=s_Surf-92
*Elset, elset=_m_Surf-94_S2, internal, instance=innertube-1
*Elset, elset=_m_Surf-94_S4, internal, instance=innertube-1, generate
*Surface, type=ELEMENT, name=m_Surf-94
*Elset, elset=_s_Surf-94_S4, internal, instance="Ni foil-1"
*Elset, elset=_s_Surf-94_S2, internal, instance="Ni foil-1", generate
*Surface, type=ELEMENT, name=s_Surf-94
*Elset, elset=_s_Surf-96_S4, internal, instance=outertube-1, generate
*Surface, type=ELEMENT, name=s_Surf-96

*Elset, elset=_s_Surf-97_S2, internal, instance=outertube-1, generate
*Elset, elset=_s_Surf-97_S4, internal, instance=outertube-1, generate
*Surface, type=ELEMENT, name=s_Surf-97
*Elset, elset=_s_Surf-99_S2, internal, instance=outertube-1, generate
*Surface, type=ELEMENT, name=s_Surf-99
*Elset, elset=_s_Surf-101_S4, internal, instance=outertube-1, generate
*Surface, type=ELEMENT, name=s_Surf-101
*Elset, elset=_m_Surf-103_S2, internal, instance=outertube-1, generate
*Surface, type=ELEMENT, name=m_Surf-103
*Elset, elset=_m_Surf-104_S4, internal, instance=innertube-1, generate
*Surface, type=ELEMENT, name=m_Surf-104
*Elset, elset=_s_Surf-104_S2, internal, instance="Ni foil-1", generate
*Surface, type=ELEMENT, name=s_Surf-104
*Elset, elset=_s_Surf-106_S3, internal, instance="Ni foil-1"
*Elset, elset=_s_Surf-106_S2, internal, instance="Ni foil-1", generate
*Surface, type=ELEMENT, name=s_Surf-106
*Elset, elset=_m_Surf-107_S2, internal, instance=innertube-1
*Elset, elset=_m_Surf-107_S4, internal, instance=innertube-1, generate
*Surface, type=ELEMENT, name=m_Surf-107
*Elset, elset=_s_Surf-107_S4, internal, instance="Ni foil-1"
*Elset, elset=_s_Surf-107_S2, internal, instance="Ni foil-1", generate
*Surface, type=ELEMENT, name=s_Surf-107
*Elset, elset=_m_Surf-109_S2, internal, instance=innertube-1, generate
*Elset, elset=_m_Surf-109_S4, internal, instance=innertube-1
*Surface, type=ELEMENT, name=m_Surf-109
*Elset, elset=_s_Surf-109_S2, internal, instance="Ni foil-1"
*Elset, elset=_s_Surf-109_S4, internal, instance="Ni foil-1", generate
*Surface, type=ELEMENT, name=s_Surf-109
*Elset, elset=_m_Surf-111_S3, internal, instance=innertube-1, generate
*Surface, type=ELEMENT, name=m_Surf-111
*Elset, elset=_s_Surf-111_S4, internal, instance=outertube-1, generate
*Surface, type=ELEMENT, name=s_Surf-111
*Elset, elset=_s_Surf-113_S2, internal, instance=outertube-1, generate
*Surface, type=ELEMENT, name=s_Surf-113
*Elset, elset=_m_Surf-115_S4, internal, instance="Ni foil-1", generate
*Surface, type=ELEMENT, name=m_Surf-115
*Elset, elset=_s_Surf-115_S4, internal, instance=outertube-1, generate
*Surface, type=ELEMENT, name=s_Surf-115
*Elset, elset=_m_Surf-117_S2, internal, instance="Ni foil-1", generate
*Elset, elset=_m_Surf-117_S4, internal, instance="Ni foil-1"
*Surface, type=ELEMENT, name=m_Surf-117
*Elset, elset=_s_Surf-117_S1, internal, instance=foil-1, generate
*Elset, elset=_s_Surf-117_S2, internal, instance=foil-1, generate
*Elset, elset=_s_Surf-117_S3, internal, instance=foil-1, generate
*Surface, type=ELEMENT, name=s_Surf-117
*Elset, elset=_m_Surf-119_S4, internal, instance=foil-1, generate

*Surface, type=ELEMENT, name=m_Surf-119
*Elset, elset=_s_Surf-119_S2, internal, instance="Ni foil-1", generate
*Surface, type=ELEMENT, name=s_Surf-119
*Elset, elset=_Surf-121_S3, internal, instance=innertube-1
*Elset, elset=_Surf-121_S2, internal, instance=innertube-1, generate
*Surface, type=ELEMENT, name=Surf-121
*Elset, elset=_Surf-122_S4, internal, instance=outertube-1, generate
*Elset, elset=_Surf-122_S2, internal, instance=outertube-1, generate
*Surface, type=ELEMENT, name=Surf-122
*Elset, elset=_m_Surf-123_S2, internal, instance=plug1048-1, generate
*Elset, elset=_m_Surf-123_S3, internal, instance=plug1048-1, generate
*Surface, type=ELEMENT, name=m_Surf-123
*Elset, elset=_m_Surf-124_S3, internal, instance="Ni foil-1"
*Elset, elset=_m_Surf-124_S4, internal, instance="Ni foil-1", generate
*Surface, type=ELEMENT, name=m_Surf-124
*Elset, elset=_m_Surf-125_S2, internal, instance=plug1048-1, generate
*Elset, elset=_m_Surf-125_S3, internal, instance=plug1048-1, generate
*Surface, type=ELEMENT, name=m_Surf-125
*Elset, elset=_m_Surf-126_S3, internal, instance=innertube-1, generate
*Surface, type=ELEMENT, name=m_Surf-126
*Elset, elset=_s_Surf-127_S2, internal, instance=outertube-1, generate
*Elset, elset=_s_Surf-127_S4, internal, instance=outertube-1, generate
*Surface, type=ELEMENT, name=s_Surf-127
*Elset, elset=_m_Surf-128_S3, internal, instance=innertube-1, generate
*Surface, type=ELEMENT, name=m_Surf-128
*Elset, elset=_m_Surf-129_S4, internal, instance=outertube-1, generate
*Surface, type=ELEMENT, name=m_Surf-129
*Elset, elset=_m_Surf-130_S3, internal, instance=innertube-1, generate
*Surface, type=ELEMENT, name=m_Surf-130
*Elset, elset=_s_Surf-130_S4, internal, instance=outertube-1, generate
*Surface, type=ELEMENT, name=s_Surf-130
*Elset, elset=_m_Surf-132_S3, internal, instance=innertube-1, generate
*Surface, type=ELEMENT, name=m_Surf-132
*Elset, elset=_m_Surf-133_S1, internal, instance=foil-1, generate
*Elset, elset=_m_Surf-133_S2, internal, instance=foil-1, generate
*Elset, elset=_m_Surf-133_S3, internal, instance=foil-1, generate
*Elset, elset=_m_Surf-133_S4, internal, instance=foil-1, generate
*Surface, type=ELEMENT, name=m_Surf-133
*Elset, elset=_s_Surf-133_S2, internal, instance="Ni foil-1"
*Elset, elset=_s_Surf-133_S4, internal, instance="Ni foil-1"
*Surface, type=ELEMENT, name=s_Surf-133
*Elset, elset=_m_Surf-135_S4, internal, instance="Ni foil-1"
*Elset, elset=_m_Surf-135_S2, internal, instance="Ni foil-1"
*Elset, elset=_m_Surf-135_S3, internal, instance="Ni foil-1"
*Surface, type=ELEMENT, name=m_Surf-135
*Elset, elset=_s_Surf-136_S2, internal, instance=innertube-1

```
*Elset, elset=_s_Surf-136_S4, internal, instance=innertube-1
*Surface, type=ELEMENT, name=s_Surf-136
*Elset, elset=_m_Surf-140_S2, internal, instance=plug1048-1, generate
*Elset, elset=_m_Surf-140_S3, internal, instance=plug1048-1, generate
*Surface, type=ELEMENT, name=m_Surf-140
*Elset, elset=_Surf-141_S2, internal, instance=innertube-1
*Elset, elset=_Surf-141_S4, internal, instance=innertube-1
*Elset, elset=_Surf-141_S4, internal, instance=outertube-1, generate
*Surface, type=ELEMENT, name=Surf-141
*Elset, elset=_Surf-142_S3, internal, instance=innertube-1
*Elset, elset=_Surf-142_S2, internal, instance=innertube-1, generate
*Surface, type=ELEMENT, name=Surf-142
*Elset, elset=_Surf-143_S4, internal, instance=outertube-1, generate
*Elset, elset=_Surf-143_S2, internal, instance=outertube-1, generate
*Surface, type=ELEMENT, name=Surf-143
*Surface, type=NODE, name=s_Set-76_CNS_, internal
*Surface, type=NODE, name=s_Set-83_CNS_, internal
*End Assembly
*Amplitude, name=AMP-1, definition=SMOOTH STEP
          0.,          0.,        0.001,          1.,          1.,          1.
**
** MATERIALS
**
*Material, name=Al6061-T6
*Conductivity
167.,
*Density
2700.,
*Elastic
 6.89e+10, 0.33
*Expansion
 2.36e-05,
*Plastic
 2.97854e+08,       0.
 3.03817e+08, 0.000104
 3.12636e+08, 0.000204
 3.14828e+08, 0.000303
 3.18827e+08, 0.000466
 3.20234e+08, 0.000553
 3.21799e+08, 0.000609
 3.22592e+08, 0.000731
 3.23178e+08, 0.000859
 3.23667e+08, 0.000972
 3.24081e+08,  0.00109
 3.28852e+08,  0.00201
 3.29762e+08,  0.00204
```

3.30583e+08, 0.00401
3.31514e+08, 0.00512
3.32279e+08, 0.00603
3.33093e+08, 0.00702
3.33968e+08, 0.00808
3.34803e+08, 0.00909
3.35637e+08, 0.0101
3.36457e+08, 0.0111
3.37167e+08, 0.012
3.38029e+08, 0.0131
3.38808e+08, 0.0141
3.39581e+08, 0.0151
3.40346e+08, 0.0161
3.41153e+08, 0.0171
3.4187e+08, 0.0181
3.42642e+08, 0.0191
3.43421e+08, 0.0201
3.47061e+08, 0.0251
3.50529e+08, 0.0301
3.53853e+08, 0.035
3.57066e+08, 0.0401
3.59996e+08, 0.045
3.62781e+08, 0.05
3.65415e+08, 0.0551
3.67808e+08, 0.06
3.70049e+08, 0.0651
3.72034e+08, 0.0701
3.73799e+08, 0.075
3.75406e+08, 0.0801
3.77033e+08, 0.0853
3.78426e+08, 0.0901
3.79805e+08, 0.095
3.81142e+08, 0.1
3.92367e+08, 0.157
4.02426e+08, 0.223
4.11107e+08, 0.3
4.20111e+08, 0.405
4.26544e+08, 0.501
4.31495e+08, 0.588
4.32908e+08, 0.615
4.36645e+08, 0.693
4.37748e+08, 0.718
4.40713e+08, 0.788
4.41609e+08, 0.811
4.44795e+08, 0.896
4.45512e+08, 0.916

```
 4.48697e+08,     1.01
*Material, name="D2 STEEL"
*Conductivity
20.,
*Density
7700.,
*Elastic
 2.1e+11, 0.3
*Material, name=Nickel
*Conductivity
 60.7,
*Density
8800.,
*Elastic
 2.07e+11, 0.31
*Expansion
 1.31e-05,
*Material, name=URANIUM
*Conductivity
 27.5,
*Density
19050.,
*Elastic
 2.08e+11, 0.23
*Expansion
 1.39e-05,
*Plastic
 1.11e+08,    0.
 2.32e+08, 0.001
 2.99e+08, 0.003
 3.36e+08, 0.005
 3.63e+08, 0.007
 3.94e+08,  0.01
*Swelling
 2.48e-08,
**
** INTERACTION PROPERTIES
**
*Surface Interaction, name=INTPROP-1
1.,
*Friction
0.,
*Surface Behavior, no separation, pressure-overclosure=HARD
*Gap Conductance
 1e+09,   0.
   0., 0.01
```

```
*Surface Interaction, name=IRRAD
1.,
*Friction
0.,
*Surface Behavior, pressure-overclosure=HARD
*Gap Conductance
1e+09,   0.
0., 0.01
*Surface Interaction, name="IRRAD-Aluminum Aluminum"
1.,
*Friction
0.,
*Surface Behavior, pressure-overclosure=HARD
*Gap Conductance
18790.1,     0.
4938.93,  1e-06
646.93,  1e-05
66.76, 0.0001
6.7,  0.001
0.67,   0.01
0.07,    0.1
0.,     1.
*Gap Conductance, pressure
18790.1,     0.
18796.8,   100.
18848.,  1000.
19294.2, 10000.
23180.5,100000.
57028.9,  1e+06
351836.,  1e+07
2.9195e+06,  1e+08
*Surface Interaction, name="IRRAD-Aluminum Ni"
1.,
*Friction
0.,
*Surface Behavior, pressure-overclosure=HARD
*Gap Conductance
18790.1,     0.
4938.93,  1e-06
646.93,  1e-05
66.76, 0.0001
6.7,  0.001
0.67,   0.01
0.07,    0.1
0.,     1.
*Gap Conductance, pressure
```

18790.1,   0.
18792.9,   100.
18814.1, 1000.
18999., 10000.
20609.5,100000.
34635.7, 1e+06
156799., 1e+07
1.2208e+06, 1e+08
*Surface Interaction, name="IRRAD-Ni Uranium"
1.,
*Friction
0.,
*Surface Behavior, pressure-overclosure=HARD
*Gap Conductance
18790.1,   0.
4938.93, 1e-06
646.93, 1e-05
66.76, 0.0001
6.7, 0.001
0.67,   0.01
0.07,   0.1
0.,   1.
*Gap Conductance, pressure
 18790.1,   0.
 18790.6,   100.
 18793.9, 1000.
 18822.9, 10000.
 19075.8,100000.
 21278.3, 1e+06
 40460.9, 1e+07
 207535., 1e+08
*Surface Interaction, name=WELD
1.,
*Friction
0.,
*Surface Behavior, no separation, pressure-overclosure=HARD
*Gap Conductance
 1e+09,   0.
   0., 0.01
**
** INTERACTIONS
**
** Interaction: IRRAD-innertube-nickel
*Contact Pair, interaction="IRRAD-Aluminum Ni", type=SURFACE TO SURFACE
s_Surf-136, m_Surf-135
** Interaction: IRRAD-it-ot-base

*Contact Pair, interaction="IRRAD-Aluminum Aluminum", type=SURFACE TO SURFACE
s_Surf-111, m_Surf-111
** Interaction: IRRAD-it-ot-top
*Contact Pair, interaction="IRRAD-Aluminum Aluminum", type=SURFACE TO SURFACE
s_Surf-113, m_Surf-132
** Interaction: IRRAD-nickel-outertube
*Contact Pair, interaction="IRRAD-Aluminum Ni", type=SURFACE TO SURFACE
s_Surf-115, m_Surf-124
** Interaction: IRRAD-uranium-nickel-2
*Contact Pair, interaction="IRRAD-Ni Uranium", type=SURFACE TO SURFACE
s_Surf-133, m_Surf-133
** Interaction: MP-innertube-nickel
*Contact Pair, interaction=INTPROP-1, type=SURFACE TO SURFACE
s_Surf-91, m_Surf-90
** Interaction: MP-innertube-nickel-base
*Contact Pair, interaction=INTPROP-1, type=SURFACE TO SURFACE
s_Surf-94, m_Surf-94
** Interaction: MP-innertube-nickel-top
*Contact Pair, interaction=INTPROP-1, type=SURFACE TO SURFACE
s_Surf-92, m_Surf-92
** Interaction: MP-it-ot-base
*Contact Pair, interaction=INTPROP-1, type=SURFACE TO SURFACE
s_Surf-127, m_Surf-88
** Interaction: MP-it-ot-top
*Contact Pair, interaction=INTPROP-1, type=SURFACE TO SURFACE
s_Surf-97, m_Surf-126
** Interaction: MP-nickel-outertube
*Contact Pair, interaction=INTPROP-1, type=SURFACE TO SURFACE
s_Surf-84, m_Surf-84
** Interaction: MP-nickel-uranium-1
*Contact Pair, interaction=INTPROP-1, type=SURFACE TO SURFACE
s_Surf-80, m_Surf-80
** Interaction: MP-plug-innertube
*Contact Pair, interaction=INTPROP-1, type=SURFACE TO SURFACE
s_Surf-76, m_Surf-140
** Interaction: MP-uranium-nickel-2
*Contact Pair, interaction=INTPROP-1, type=SURFACE TO SURFACE
s_Surf-82, m_Surf-82
** Interaction: RP-it-ot-base
*Contact Pair, interaction=INTPROP-1, type=SURFACE TO SURFACE
s_Surf-130, m_Surf-130
** Interaction: RP-it-ot-base-weld
*Contact Pair, interaction=WELD, type=SURFACE TO SURFACE
s_Set-76_CNS_, m_Surf-103

```
** Interaction: RP-it-ot-top
*Contact Pair, interaction=INTPROP-1, type=SURFACE TO SURFACE
s_Surf-99, m_Surf-128
** Interaction: RP-it-ot-top-weld
*Contact Pair, interaction=WELD, type=SURFACE TO SURFACE
s_Set-83_CNS_, m_Surf-129
** ----------------------------------------------------------------
**
** STEP: Move plug
**
*Step, name="Move plug", nlgeom=YES, inc=10000
*Coupled Temperature-displacement, creep=none, steady state
0.001, 1., 1e-12, 1.
**
** BOUNDARY CONDITIONS
**
** Name: Plug velocity Type: Velocity/Angular velocity
*Boundary, amplitude=AMP-1, type=VELOCITY
Set-99, 2, 2, 0.160726
** Name: U2 zero Type: Displacement/Rotation
*Boundary
Set-82, 2, 2
** Name: Vel1-Zero Type: Velocity/Angular velocity
*Boundary, amplitude=AMP-1, type=VELOCITY
Set-102, 1, 1
** Name: Vel3-Zero Type: Velocity/Angular velocity
*Boundary, amplitude=AMP-1, type=VELOCITY
Set-101, 6, 6
**
** INTERACTIONS
**
** Interaction: IRRAD-innertube-nickel
*Model Change, type=CONTACT PAIR, remove
s_Surf-136, m_Surf-135
** Interaction: IRRAD-it-ot-base
*Model Change, type=CONTACT PAIR, remove
s_Surf-111, m_Surf-111
** Interaction: IRRAD-it-ot-top
*Model Change, type=CONTACT PAIR, remove
s_Surf-113, m_Surf-132
** Interaction: IRRAD-nickel-outertube
*Model Change, type=CONTACT PAIR, remove
s_Surf-115, m_Surf-124
** Interaction: IRRAD-uranium-nickel-2
*Model Change, type=CONTACT PAIR, remove
s_Surf-133, m_Surf-133
```

```
** Interaction: RP-it-ot-base
*Model Change, type=CONTACT PAIR, remove
s_Surf-130, m_Surf-130
** Interaction: RP-it-ot-base-weld
*Model Change, type=CONTACT PAIR, remove
s_Set-76_CNS_, m_Surf-103
** Interaction: RP-it-ot-top
*Model Change, type=CONTACT PAIR, remove
s_Surf-99, m_Surf-128
** Interaction: RP-it-ot-top-weld
*Model Change, type=CONTACT PAIR, remove
s_Set-83_CNS_, m_Surf-129
**
** OUTPUT REQUESTS
**
*Restart, write, frequency=1
**
** FIELD OUTPUT: F-Output-1
**
*Output, field
*Node Output
CF, NT, RF, RFL, U
*Element Output, directions=YES
CFAILURE, DAMAGEC, DAMAGEFC, DAMAGEFT, DAMAGEMC, DAMAGEMT,
DAMAGESHR, DAMAGET, DMICRT, E, EE, ERPRATIO, HFL, HSNFCCRT,
HSNFTCRT, HSNMCCRT
HSNMTCRT, JK, LE, PE, PEEQ, PEMAG, S, SDEG, SHRRATIO, THE
*Contact Output
BDSTAT, CDISP, CRSTS, CSDMG, CSMAXSCRT, CSMAXUCRT, CSQUADSCRT,
CSQUADUCRT, CSTRESS, DBS, DBSF, DBT, EFENRRTR, ENRRT, OPENBC
**
** HISTORY OUTPUT: H-Output-1
**
*Output, history, variable=PRESELECT
*End Step
** ----------------------------------------------------------------
**
** STEP: Remove Plug and Weld
**
*Step, name="Remove Plug and Weld", nlgeom=YES
*Coupled Temperature-displacement, creep=none, steady state
1., 1., 1e-05, 1.
**
** BOUNDARY CONDITIONS
**
** Name: Plug velocity Type: Velocity/Angular velocity
```

*Boundary, amplitude=AMP-1, type=VELOCITY
Set-99, 2, 2
**
** INTERACTIONS
**
** Interaction: MP-it-ot-base
*Model Change, type=CONTACT PAIR, remove
s_Surf-127, m_Surf-88
** Interaction: MP-it-ot-top
*Model Change, type=CONTACT PAIR, remove
s_Surf-97, m_Surf-126
** Interaction: RP- Remove Plug
*Model Change, remove
Set-98,
** Interaction: RP-it-ot-base
*Model Change, type=CONTACT PAIR, add
s_Surf-130, m_Surf-130
** Interaction: RP-it-ot-base-weld
*Model Change, type=CONTACT PAIR, add
s_Set-76_CNS_, m_Surf-103
** Interaction: RP-it-ot-top
*Model Change, type=CONTACT PAIR, add
s_Surf-99, m_Surf-128
** Interaction: RP-it-ot-top-weld
*Model Change, type=CONTACT PAIR, add
s_Set-83_CNS_, m_Surf-129
**
** OUTPUT REQUESTS
**
*Restart, write, frequency=1
**
** FIELD OUTPUT: F-Output-1
**
*Output, field
*Node Output
CF, NT, RF, RFL, U
*Element Output, directions=YES
CFAILURE, DAMAGEC, DAMAGEFC, DAMAGEFT, DAMAGEMC, DAMAGEMT,
DAMAGESHR, DAMAGET, DMICRT, E, EE, ERPRATIO, HFL, HSNFCCRT,
HSNFTCRT, HSNMCCRT
HSNMTCRT, JK, LE, PE, PEEQ, PEMAG, S, SDEG, SHRRATIO, THE
*Contact Output
BDSTAT, CDISP, CRSTS, CSDMG, CSMAXSCRT, CSMAXUCRT, CSQUADSCRT,
CSQUADUCRT, CSTRESS, DBS, DBSF, DBT, EFENRRTR, ENRRT, OPENBC
**
** HISTORY OUTPUT: H-Output-1

```
**
*Output, history, variable=PRESELECT
*End Step
** ----------------------------------------------------------------
**
** STEP: Irrad
**
*Step, name=Irrad, nlgeom=YES, inc=100000
*Coupled Temperature-displacement, creep=none, steady state
1., 1., 1e-12, 1.
**
** LOADS
**
** Name: CHG-inner   Type: Body heat flux
*Dflux
Set-103, BF, 2.7e+07
** Name: CHG-outer   Type: Body heat flux
*Dflux
Set-104, BF, 2.7e+07
** Name: CP- inner tube inner surf   Type: Pressure
*Dsload
Surf-142, P, 590000.
** Name: CP-outer tube outer surf   Type: Pressure
*Dsload
Surf-143, P, 590000.
** Name: FGP   Type: Pressure
*Dsload
Surf-141, P, 47740.
** Name: heat gen   Type: Body heat flux
*Dflux
Set-85, BF, 1.6e+10
**
** INTERACTIONS
**
** Interaction: IRRAD-innertube-nickel
*Model Change, type=CONTACT PAIR, add
s_Surf-136, m_Surf-135
** Contact Controls for Interaction: IRRAD-innertube-nickel
*Contact Controls, master=m_Surf-135, slave=s_Surf-136, stabilize=1.
** Interaction: IRRAD-it-ot-base
*Model Change, type=CONTACT PAIR, add
s_Surf-111, m_Surf-111
** Contact Controls for Interaction: IRRAD-it-ot-base
*Contact Controls, master=m_Surf-111, slave=s_Surf-111, stabilize=1.
** Interaction: IRRAD-it-ot-top
*Model Change, type=CONTACT PAIR, add
```

s_Surf-113, m_Surf-132
** Contact Controls for Interaction: IRRAD-it-ot-top
*Contact Controls, master=m_Surf-132, slave=s_Surf-113, stabilize=1.
** Interaction: IRRAD-nickel-outertube
*Model Change, type=CONTACT PAIR, add
s_Surf-115, m_Surf-124
** Contact Controls for Interaction: IRRAD-nickel-outertube
*Contact Controls, master=m_Surf-124, slave=s_Surf-115, stabilize=1.
** Interaction: IRRAD-uranium-nickel-2
*Model Change, type=CONTACT PAIR, add
s_Surf-133, m_Surf-133
** Contact Controls for Interaction: IRRAD-uranium-nickel-2
*Contact Controls, master=m_Surf-133, slave=s_Surf-133, stabilize=1.
** Interaction: MP-innertube-nickel
*Model Change, type=CONTACT PAIR, remove
s_Surf-91, m_Surf-90
** Interaction: MP-innertube-nickel-base
*Model Change, type=CONTACT PAIR, remove
s_Surf-94, m_Surf-94
** Interaction: MP-innertube-nickel-top
*Model Change, type=CONTACT PAIR, remove
s_Surf-92, m_Surf-92
** Interaction: MP-nickel-outertube
*Model Change, type=CONTACT PAIR, remove
s_Surf-84, m_Surf-84
** Interaction: MP-nickel-uranium-1
*Model Change, type=CONTACT PAIR, remove
s_Surf-80, m_Surf-80
** Interaction: MP-plug-innertube
*Model Change, type=CONTACT PAIR, remove
s_Surf-76, m_Surf-140
** Interaction: MP-uranium-nickel-2
*Model Change, type=CONTACT PAIR, remove
s_Surf-82, m_Surf-82
** Interaction: RP-it-ot-base
*Model Change, type=CONTACT PAIR, remove
s_Surf-130, m_Surf-130
** Interaction: RP-it-ot-top
*Model Change, type=CONTACT PAIR, remove
s_Surf-99, m_Surf-128
** Interaction: IRRAD-HTC in
*Sfilm
Surf-121, F, 323., 19000.
** Interaction: IRRAD-HTCout
*Sfilm
Surf-122, F, 323., 19000.

```
**
** OUTPUT REQUESTS
**
*Restart, write, frequency=0
**
** FIELD OUTPUT: F-Output-1
**
*Output, field
*Node Output
CF, NT, RF, RFL, U
*Element Output, directions=YES
CFAILURE, DAMAGEC, DAMAGEFC, DAMAGEFT, DAMAGEMC, DAMAGEMT,
DAMAGESHR, DAMAGET, DMICRT, E, EE, ERPRATIO, HFL, HSNFCCRT,
HSNFTCRT, HSNMCCRT
HSNMTCRT, JK, LE, PE, PEEQ, PEMAG, S, SDEG, SHRRATIO, THE
*Contact Output
BDSTAT, CDISP, CRSTS, CSDMG, CSMAXSCRT, CSMAXUCRT, CSQUADSCRT,
CSQUADUCRT, CSTRESS, DBS, DBSF, DBT, EFENRRTR, ENRRT, OPENBC
**
** HISTORY OUTPUT: H-Output-1
**
*Output, history, variable=PRESELECT
*End Step
```

APPENDIX 14: Abaqus Input File for the Control Blade Analysis

(The part and the mesh definitions have been omitted to make the presentation of the code concise in this appendix. The description of the part creation along with the mesh information has been provided in the dissertation write-up)

(To run the input file from the command window: abaqus job=**(the name of inp file, without ".inp". To open the input file in the CAE environment: import the model. File → Import → Model. This dialog will accept *.inp files)

```
*Heading
** Job name: U1U30PROFILEBK98 Model name: U1U30PROFILEBK98
** Generated by: Abaqus/CAE 6.10-2
*Preprint, echo=NO, model=NO, history=NO
**
** PARTS
** (* part definition omitted in this section to make the code concise and clear *)
**
** MATERIALS
**
*Material, name=Al1100
*Conductivity
 186.4,
*Density
2713.,
*Elastic
 6.9e+10, 0.33
*Expansion
 2.36e-05,
*Specific Heat
1120.,
*Material, name=boral
*Conductivity
98.,
*Density
2481.,
*Elastic
 6.2053e+10, 0.23
*Expansion
 1.97e-05,
*Specific Heat
1380.,
**
** INTERACTION PROPERTIES
**
*Surface Interaction, name=IntProp-1
```

1.,
*Friction
0.,
*Surface Behavior, no separation, pressure-overclosure=HARD
*Gap Conductance
 1e+09, 0.
0., 0.1
**
** INTERACTIONS
**
** Interaction: gc
*Contact
*Contact Inclusions, ALL EXTERIOR
*Contact Property Assignment
, , IntProp-1
*Surface Property Assignment, property=GEOMETRIC CORRECTION
**
** STEP: Step-1
**
*Step, name=Step-1, nlgeom=YES
*Coupled Temperature-displacement, creep=none, steady state
1., 1., 1e-05, 1.
**
** BOUNDARY CONDITIONS
**
** Name: BC-1 Type: Displacement/Rotation
*Boundary
_PickedSet1184, 1, 1
_PickedSet1184, 3, 3
** Name: BC-2 Type: Displacement/Rotation
*Boundary
_PickedSet1185, 1, 1
_PickedSet1185, 3, 3
** Name: BC-3 Type: Displacement/Rotation
*Boundary
_PickedSet1186, 1, 1
_PickedSet1186, 3, 3
** Name: BC-4 Type: Displacement/Rotation
*Boundary
_PickedSet1187, 1, 1
_PickedSet1187, 3, 3
** Name: BC-5 Type: Displacement/Rotation
*Boundary
_PickedSet1188, 1, 1
_PickedSet1188, 3, 3
** Name: BC-6 Type: Displacement/Rotation

```
*Boundary
_PickedSet1189, 1, 1
_PickedSet1189, 3, 3
** Name: BC-7 Type: Displacement/Rotation
*Boundary
_PickedSet1190, 1, 1
_PickedSet1190, 3, 3
** Name: BC-8 Type: Displacement/Rotation
*Boundary
_PickedSet1191, 1, 1
_PickedSet1191, 3, 3
** Name: BC-9 Type: Displacement/Rotation
*Boundary
_PickedSet1192, 1, 1
_PickedSet1192, 3, 3
** Name: BC-10 Type: Displacement/Rotation
*Boundary
_PickedSet1193, 1, 1
_PickedSet1193, 3, 3
**
** LOADS
**
** Name: LEFT EDGE   Type: Body heat flux Using Field: LEFT EDGE
*Dflux, op=NEW (* check chapter 12 for the body flux equation definition *)
**
** INTERACTIONS
**
** Interaction: htc1
*Sfilm
_PickedSurf933, F, 325., 1000.
** Interaction: htc2
*Sfilm
_PickedSurf934, F, 325., 1000.
**
** OUTPUT REQUESTS
**
*Restart, write, frequency=0
**
** FIELD OUTPUT: F-Output-1
**
*Output, field, variable=PRESELECT
**
** HISTORY OUTPUT: H-Output-1
**
*Output, history, variable=PRESELECT
*End Step
```

REFERENCES

1. S.M. Seidlin, L.D. Marinelli, E. Oshry, "Radioactive Iodine Therapy: Effect on Functioning Metastases of Adenocarcinoma of Thyroid," *JAMA*, **132**, pp. 838-847, 1946.
2. A. Georges, O. Bersillion, J. Blachot, A.H. Wapstra, "The NUBASE Evaluation of Nuclear and Decay Properties," *Nuclear Physics A (Atomic Mass Data Center)*, **729**, pp. 3-128, 2003.
3. E. Segre, C.S.Wu, "Some Fission Products of Uranium," *Physical Review*, **57 (6)**, pp. 552-552, 1940.
4. L. Sorensen, M. Archambault, "Visualization of the Liver by Scanning with Mo-99 (Molybdate) as tracer," *Journal of Laboratory and Clinical Medicine*, **62**, pp. 330-340, 1963.
5. C.W. Allen, R.A. Butler, C.A. Jarousse, J.L. Falgoux, "Feasibility Development Program, LEU Foil Plate Target for the Production of Molybdenum-99," *RERTR International Meeting*, Prague, Czech Republic, 2007.
6. G.F. Vandegrift, C. Conner, G.L. Hofman, R.A. Leonard, A. Mutalib, J. Sedlet, D.E. Walker, T.C. Wiencek, J.L. Snelgrove, "Modification of Targets and Processes for Conversion of Mo-99 Production from High- to Low-Enriched Uranium," *Industrial and Engineering Chemistry. Research*, **39**, pp. 3140-3145, 2000.
7. J.A. Smaga, J. Sedlet, C. Conner, M.W. Liberatore, D.E. Walker, D.G. Wygmans, G.F. Vandegrift, " Electroplating Fission Recoil Barriers onto LEU Metal Foils for Mo-99 Production Targets," *Proceedings of the XXth International Meeting*

on Reduced Enrichment for Research and Test Reactors, Jackson Hole, WY, 1997.

8. K.K. Turner, "*The Thermal-Mechanical Analysis of Targets for the High Volume Production of Molybdenum-99 Using a Low-Enriched Uranium Metal Foil [PhD Dissertation]*," University of Missouri, Columbia, MO, 2012.
9. National Research Council, 2009, *Medical Isotope Production Without Highly Enriched Uranium*, The National Academies Press, Washington, D.C.
10. C.V. Madhusudhana, *Thermal Contact Conductance*, Springer, New York, NY, 1996.
11. US. Department of Energy, *DOE Fundamentals Handbook- Nuclear Physics and Reactor Theory,* **2**, pp. 48-58, 1993.
12. Missouri University Research Reactor, *User's Guide- University of Missouri Research Reactor Facility*, Columbia, MO, 1969.
13. C. Conner, E.F. Lewandowski, J.L. Snelgrove, M.W. Liberatore, D.E. Walker, T.C. Wiencek, D.J. McGrann, G.L. Hofman, G.F. Vandegrift, "Development of Annular Targets for {sup 99} MO Production," *Proceedings of the 1999 International Meeting on Reduced Enrichment for Research and Test Reactors*, Budapest, Hungary, 1999.
14. A. Mutalib, B. Purwadi, H.G. Adang, L. Hotman, M. Kadarisman, A. Sukmana, Sriyono. A. Suripto, H. Nasution, D.L. Amin, A. Basiran, A. Gogo, D. Sunaryadi, T. Taryo, G.F. Vandegrift, G.L. Hofman, C. Conner, J. Sedlet, D. Walker, R.A. Leonard, E.L. Wood, T.C. Wiencek, J.L. Snelgrove, "Full Scale Demonstration of the Cintichem Process for the Production of Molybdenum-99 using a Low

Enriched Uranium Target," *International Meeting on Reduced Enrichment for Research and Test Reactors,* Sao Paulo, Brazil, 1999.

15. G. Yeoh, "*Consideration of U-foil/Aluminum wall gap of 30μm for engineering specification purposes,*" 2004.
16. B.B. Mikic, "*Thermal Contact Resistance [PhD Dissertation]*," Massachusetts Institute of Technology, Cambridge, MA, 1966.
17. C.W. Allen, G.L. Solbrekken," Feasibility Study -2, Production of Fission Product Using the LEU- Modified Cintichem Process- Thermal Hydraulic Analysis," *Technical Data Report (TDR-0104)*, Missouri University Research Reactor, Columbia , Missouri, 2007.
18. T.M. Donlevy, P.J. Anderson, D. Beattie, B. Braddock, S. Fulton, R. Godfrey, R. Law, S. McNiven, P. Sirkka, G. Storr, D. Wassink, A. Wong, G. Yeoh, G., "Low-Enrichment Mo-99 Target Development Program at ANSTO," *Proceedings of the International Meeting on Reduced Enrichment for Research and Test Reactors*, Bariloche, Argentina, 2002.
19. B.C. Lee, C.S. Lee, H. Kim, "Physics Study for a LEU MO Target Irradiation at HANARO," *Proceedings of the International Meeting on Reduced Enrichment for Research and Test Reactors*, Chicago, Illinois, 2002.
20. A. Mushtaq, M. Iqbal, I.H. Bokhari, T. Mahmood, T. Mahmood, Z. Ahmad, Q. Zaman, "Neutronics and Thermal Hydraulic Analysis for Production of Fission Molybdenum-99 at Pakistan Research Reactor-1," *Annals of Nuclear Energy*, **35**, pp. 345-352, 2008.

21. A. Mushtaq, M. Iqbal, I.H. Bokhari, T. Mahmood, T. Mahmood, "Low Enriched Uranium Foil Plate Target for the Production of Fission Molybdenum-99 in Pakistan Research Reactor-1", *Nuclear Instruments and Methods in Physics Research B*, **267**, pp. 1109-1114, 2009.

22. K.K. Turner, G.L. Solbrekken, C.W. Allen , " Thermal-Mechanical Analysis of Varying Boundary Conditions on a LEU Foil based Molybdenum-99 Plate Processing Target, *"Proceedings of the ASME International Mechanical Engineering Congress and Exposition(IMECE 2010)*, Vancouver, British Columbia, Canada, 2010.

23. S.G. Govindarajan, G.L. Solbrekken, C.W. Allen, "Thermal Mechanical Analysis of a Low-Enriched Uranium Foil Based Annular Target for the Production of Molybdenum-99," *Proceedings of the ASME 2012 International Mechanical Engineering Congress and Exposition (IMECE2012)*, Houston, Texas, 2012.

24. S.G. Govindarajan, B.S. Graybill, P.F. Makarewicz, Z. Xie, G.L. Solbrekken, "Assembly and Irradiation Modeling of Residual Stresses in Low-Enriched Uranium Foil Based Annular Targets for Molybdenum-99 Production," *Science and Technology of Nuclear Installations*, Article Id: 673535, 2013.

25. C.V. Madhusudhana, "Thermal Conductance of Cylindrical Joints," *International Journal of Heat and Mass Transfer*, **42**, pp. 1273-1287, 1999.

26. C.V. Madhusudhana, L.S. Fletcher, "Solid Spot Thermal Conductance of Zircaloy-2/Uranium Dioxide Interfaces," *J.Nucl Sci Eng*, **83**, pp. 327-332, 1981.

27. C.V. Madhusudhana, L.S. Fletcher, "Thermal Conductance of Cylindrical Contacts," *Proceedings of the eighth Canadian congress on applied mechanics*, New Brunswick, Canada. pp. 755-756, 1981.

28. T.R. Hsu, W.K. Tam, "On Thermal Contact Resistance of Compound Cylinders," *AIAA 14th Thermophysics Conf. Paper 79-1069.* American Institute of Aeronautics and Astronautics, New York, 1979.

29. A.M. Ross, R.L. Stoute, "Heat Transfer Coefficient Between UO2 and Zircaloy-2,"*Atomic Energy of Canada, Ltd., Report CRFD-1075*, Ottawa, Ontario, Canada, 1962.

30. I.I. Novikov, L.S. Kokorev, N.N. Del'vin, N.N., "Experimental Heat Exchange Between Co-axial Cylinders in Vacuum," *Atomnaya Energiya*, **32**, pp. 474-475, 1972.

31. T.F. Lemczyk, M.M. Yovanovich, "New Models and Methodology for Predicting Thermal Contact Resistance in Compound Cylinders and Finned Tubes," *Heat Transfer Engineering*, **8**, pp. 35-42, 1987.

32. N. Milosevic, M. Raynaud, K. Maglic, "Estimation of Thermal Contact Resistance Between the Materials of a Double Layer Sample Using the Laser Flash Method," *Inverse Problems in Engineering*, **10**, pp. 85-103, 2002.

33. K.K. Turner, G.L. Solbrekken, C.W. Allen, "Thermal-Mechanical Analysis of Annular Target Design For High Volume Production of Molybdenum-99 Using Low Enriched Uranium ", *Proceedings of the ASME International Mechanical Engineering Congress and Exposition(IMECE 2009)*, Lake Buena Vista , Florida, 2009.

34. S.G. Govindarajan, G.L. Solbrekken, "Effect of Interfacial Conductance on the Thermal Stresses in a Low-Enriched Uranium Foil Based Annular Target for the Production of Molybdenum-99, *Transactions of the American Nuclear Society*, **109**, Washington, D.C, pp. 511-514, 2013.

35. B.B. Mikic, "Thermal Contact Conductance: Theoretical Considerations," International Journal of Heat and Mass Transfer, **17**, pp. 205-214, 1974.

36. C.W. Allen, "Calculation of Fission Gas Inventory during U-Foil Irradiation," *Technical Data Report (TDR-0111)*, Missouri University Research Reactor, Columbia, Missouri, 2007.

37. K.C. Jane, Z.Y.Lee, "Thermoelasticity of Multi Layered Cylinders," Journal *of Thermal Stresses*, **22**, pp. 57-74, 1999.

38. Y.C. Yang. H.L. Lee, "Coupled Thermoelasticity of an Infinitely Long Triple Layer Annular Cylinder," *Journal of Thermal Stresses*, **29**, pp. 229-244, 2001.

39. C.I. Hung, C.K. Chen, Z.Y. Lee, "Thermoelastic Transient Response of Multilayered Hollow Cylinders with Initial Interface Pressure," *Journal of Thermal Stresses*, **24**, pp. 987-1006, 2001.

40. M. Comninou, J. Dundurs, "On Lack of Uniqueness in Heat Conduction through a Solid to Solid Contact," *Journal of Heat Transfer*, **102**, pp. 319-32, 1980.

41. R.W. Zimmerman, M.P. Lutz, "Thermal Stresses and Thermal Expansion in a Uniformly Heated Functionally Graded Cylinder," *Journal of Thermal Stresses*, **22**, pp. 177-178, 1999.

42. P.F. Makarewicz, S.G. Govindarajan, G.L. Solbrekken, "Experimental Testing of Annular Target Surrogates for the Production of Molybdenum-99," *Proceedings*

of the ASME 2012 International Mechanical Engineering Congress & Exposition, Paper IMECE2012-87783, Houston, Texas, 2012.

43. K.K. Turner, G.L. Solbrekken, C.W. Allen, "Thermal Mechanical Response of a Non-Uniformly Heated nominally Flat and Curved LEU Foil based Molybdenum-99 Production Targets, *Transactions of the American Nuclear Society*, **107**, San Diego, California, pp. 91-94, 2012.
44. R.S. Barnes, A.T. Churchman, G.C. Curtis, V.W. Eldred, J.A. Enderby, A.J.E. Foreman, O.S. Plail, S.F. Pugh, G.N. Walton, L.M. Wyatt, " Swelling and Inert Gas Diffusion in Irradiated Uranium," *Proceedings of the Second United Nations International Conference on the Peaceful Uses of Atomic Energy*, **5**, UNITED NATIONS, Geneva, pp. 543-565, 1958.
45. J.F. Saltsman, "Theoretical Analysis of Swelling Characteristics of Cylindrical Uranium Dioxide Fuel Pins With a Niobium-1-Percent-Zirconium Clad," *NASA Technical Memorandum*, Lewis Research Center, Cleveland, Ohio, 1978.
46. R.G. Robal, T.N. Tambling, "Unrestrained Swelling of Uranium Nitride Fuel Irradiated at Temperatures from 1100 to 1400 K," *NASA Technical Memorandum*, Lewis Research Center, Cleveland, Ohio, 1973.
47. G.L. Hofman, J. Rest, J.L. Snelgrove, "Irradiation Behavior of Uranium Oxide-Aluminum Dispersion Fuel," Proceedings of the International Meeting on Reduced Enrichment for Research and Test Reactors, Seoul, Korea, 1996.
48. C.L. Angerman, W.R. McDonell, "Irradiation Behavior of Uranium Fuel Tubes in a Pressurized Water Reactor," *Nuclear Science and Engineering*, **28**, pp. 42-50, 1967.

49. R.D. Leggett,B. Mastel, T.K. Bierlein, “Irradiation Behavior of High Purity Uranium,” *Metallurgy Research Reactor & Fuels Laboratory*, Hanford Atomic Products Operation, Richland, Washington, 1963.

50. R.W. Hobbs, *Personal Communication*, Research Reactors Division, Oak Ridge National Lab, Oak Ridge, TN.

51. F.J. Stubbs, G.N. Walton, “Emission of Active Rare Gases from Fissile Material During Irradiation with Slow Neutrons. Experimental Technique and Identification of Gases,” *Proceedings of the International Conference on the Peaceful Uses of Atomic Energy*, **7**, UNITED NATIONS, Geneva, pp. 163-168, 1956.

52. R.P. Mikesell, R.B. Scott, “Heat Conduction Through Insulating Supports in Very Low Temperature Equipment,” *J Res, US Natl Bureau Standards*, **57**, pp. 371-378, 1956.

53. L.S. Fletcher, R.G. Miller, “Thermal Conductance of Gasket Material for Spacecraft Joints,”*AIAA 11th Aerospace Sciences Meeting*, Washington, D.C, January 10-12, 1973.

54. G.L. Solbrekken, A.S. El-Gizawy, C.W. Allen, “Engineering design of LEU Foil Based Target for High Volume Production of Moly-99,” *International Meeting on Reduced Enrichment for Research and Test Reactors,* 2008.

55. A.S. El-Gizawy, J.K. Berlin, B.S. Graybill, “Robust Design of Assembly Process of Targets Carrying LEU Foils for Production of Mo-99,” *ANS Winter Meeting and Nuclear Technology Expo, Technical Conference Proceedings: The Status of Global Nuclear Deployment*, Washington, DC, USA, 2011.

56. “Abaqus FEA,” D S Simulia. © Dassault Systemes 2002-2014.

57. J. Scott, “*Thermal Hydraulic Optimization for High Production of Low-Enriched Uranium Based Molybdenum-99 (Master’s Thesis)*,”University of Missouri, Columbia, Missouri, 2009.

58. F.P. Incropera, D.P. DeWitt, T.L. Bergman, A.S.Lavine, *Fundamentals of Heat and Mass Transfer*, 6th Edition, John Wiley & Sons, 2007.

59. P.W. Dittus and L.M.K. Boelter, “Heat Transfer in Automobile Radiators of the Tubular Type,” *Univ. California Pub.Eng.***2**(13), Oct. 17, 1930, pp. 443-461; reprinted in *Int. Comm. Heat Mass Transfer*, **12**, (1985) 3-22.

60. R.P. Govoro, “*Flow Characterization of the N-1 Channel to Determine Water Velocity and Maximum Coolant Capacity [Undergraduate Honors Research]*,” University of Missouri, Columbia, Missouri, 2008.

61. S. Timoshenko, J.N. Goodier, *Theory of Elasticity*, McGraw Hill Book Company, pp. 410-413, 1951.

62. B.A. Boley, J.H. Weiner, *Theory of Thermal Stresses*, Dover Publications Inc, New York, NY, pp. 272-281, 1960.

63. A.C. Ugural, F.K. Fenster, *Advanced Strength and Applied Elasticity*, Elsevier, New York, NY, pp. 255-256, 1975.

64. R.K.S Racha, *Damage Characterization of Four Wrought Aluminum Alloys [MS Thesis]*, Tennessee Technological University, 2008.

65. G.R. Caskey Jr., “Memo to P.H. Permar,” *Technical Division Savannah River Laboratory*, Aiken, SC, USA, 1965.

66. N. Srinivasan., Y.V.R.K Prasad., "Characterization of Dynamic Recrystallization in Nickel Using Processing Map for Hot Deformation," Mat. Sci. Tech, **8**, p. 206, 1992.

67. R.C. Reid., J.M. Prausnitz., B.E. Poling., The Properties of Gases and Liquids, 4th Edition, McGraw-Hill, Inc., NY, pp. 37-40, 79-80 and Appendix A, 1987.

68. G.L. Hofman., T.C. Wiencek., E.L. Wood., J.L. Snelgrove., A. Suripto., H. Nasution., D. Lufti-Amin., A. Gogo., " Irradiation Tests of Mo-99 Isotope Production Employing Uranium Metal Foils," International Meeting on Reduced Enrichment for Research and Test Reactors, Seoul, South Korea, 1996.

69. C.W. Allen., "Assessment of Fission Gas Release During LEU Foil Target Irradiation and Disassembly," *Technical Data Report (TDR-0112)*, Missouri University Research Reactor, Columbia, Missouri, 2008.

70. J. Ozeroff., "Atomic Displacements Produced by Fission Fragments and Fission Neutrons in Matter," General Electric Company- Knolls Atomic Power Laboratory, Schenectady, NY, 1949.

71. Y.S. Kim., G.L. Hofman., "Fission Product Induced Swelling of U-Mo Alloy Fuel," Journal of Nuclear Materials, **419**, pp. 291-301, 2011.

72. D. Tabor., "A Simplified Account of Surface Topography and the Contact Between Solids," *Wear*, **32(2)**, pp. 269-271, 1975.

73. R.H. Vickerman., R. Harris., "The Thermal Conductivity and Temperature Jump Distance of Gas Mixtures," *Transactions of the American Nuclear Society*, **22**, p. 523, 1975.

74. C.R. Wilke., "A Viscosity Equation for Gas Mixtures," *Journal of Chemical Physics*, **18**, pp. 517-519, 1950.

75. J.C. McKibben., Safety Analysis Report, Missouri University Research Reactor (MURR), **1**, 2006.

76. S.C. Meguid., J.C. Stranart., J. Heyerman, "On the Layered Micromechanical Three-Dimensional Finite Element Modeling of Foam Filled Columns," Finite Element in Analysis and Design, **40**, pp. 1035-1057, 2004.

77. S.G. Govindarajan, J.A. Moreland, G.L. Solbrekken, C. McKibben, N. Peters, "BORAL Control Blade Thermal Mechanical Analysis," *Proceedings of the 5th International Symposium on Material Testing Reactors*, Columbia, MO, October 22nd- 25th , 2012.

78. BORAL® Composite Standard Specifications, SP-BORA-001en, Rev. 10-17-08, Ceradyne Canada, ULC.

79. Hazards Summary Report, University of Missouri Research Reactor Facility, February, 1966.

80. X-5 Monte Carlo Team, "MCNP-A General Monte Carlo N-Particle Transport Code, Version 5 Volume I, II, III," LA-UR-03-1987/LA-CP-03-0245/LA-CP-03-0284, Los Alamos National Laboratory, 2003.

81. N.J. Peters, J.C. McKibben, K. Kutikkad, W.H. Miller, " Refining the Accuracy of Predicting Physics Parameters at Research Reactors due to the Limitations in Energy Balance Method using MCNP and ENDF Evaluations," *Nuclear Science and Engineering, ANS Nucl. Sci and Eng*, 171, pp. 210-219, 2012.

82. N.J. Peters, *Personal Communication*, Missouri University Research Reactor, Columbia, MO.

83. MURR, BORAL Control Blade Drawing # 54802, University of Missouri Research Reactor Facility, Columbia, MO.

84. MURR, Control Blade Mount -Old GE Drawing # 107C4659, University of Missouri Research Reactor Facility, Columbia, MO.

VITA

Srisharan Govindarajan is from the southern city of Chennai in India. After graduating with a B'Tech degree in mechanical engineering from the SRM University in 2008, he started working towards his MS degree in mechanical engineering at the University of Missouri in Columbia, under the guidance of Dr. Gary Solbrekken. His research focused on developing thermal-mechanical solutions to support the safe irradiation of annular targets under high heat fluxes. He obtained his MS degree in December 2011, and started working towards his PhD degree in mechanical engineering in 2012. His PhD dissertation centered on developing thermal-mechanical solutions for internal heat generating applications, such as nuclear reactor control blades and foil based irradiation targets. Srisharan had the opportunity to work as a thermal-stress analysis intern at the Oak Ridge National Laboratory, as a part of the Advanced Short Term Research Opportunity program sponsored by the Oak Ridge Institute of Science and Education in Oak Ridge, Tennessee. Here he performed thermal-stress safety calculations for foil based targets that were to be irradiated. Apart from publishing articles in journals and conference proceedings, he has also co-authored a book chapter along with his dissertation supervisor Dr. Gary Solbrekken.